Quantifying redox metabolism in the plant metabolic network

Edward Smith

Department of Plant Sciences

Magdalen College

Thesis submitted for the degree of

Doctor of Philosophy

University of Oxford

Trinity term 2021

Abstract

The aim of this thesis was to develop and evaluate methods for quantifying redox metabolism in plants. Current methods suffer from a lack of: quantitative measurement; specificity between different redox carriers; and subcellular resolution. Three approaches were explored to address these limitations including, deuterium labelling, genetically encoded fluorescent biosensors for redox metabolites, and isotopically non-stationary metabolic flux analysis (INST-MFA). Deuterium labelling strategies for quantifying NADPH production fluxes were found to be ineffective in plants due to hydrogen exchange between NADPH and water, catalysed by flavin-enzymes. Fluorescent biosensors were effective at quantifying changes in NADH:NAD^+ ratios and NADPH concentrations in *Arabidopsis* leaves, and identified dynamic responses to pathogen elicitation, hypoxia, nitrogen supply and menadione treatment. INST-MFA using [^{13}C]glucose was used to quantify changes in subcellular fluxes of heterotrophic *Arabidopsis* cells under menadione induced oxidative stress; major changes in flux through anaplerotic reactions were identified and coenzyme balancing suggested the majority of biosynthetic NADPH demand could be met by isocitrate dehydrogenase. Of the methods evaluated, INST-MFA has the potential to make the largest contribution to quantifying redox metabolism in plants by providing measurement of specific subcellular fluxes, although this approach remains limited by a lack of coenzyme specificity. Further development of fluorescent biosensors to allow quantitative calibration will provide critical information for kinetic or thermodynamic models of plant metabolism. The methods developed in this thesis provide a set of tools for quantifying redox metabolism in plants that can be applied to improve our fundamental understanding of plant biology and meet biotechnological aims.

Acknowledgments

First and foremost, I'd like to thank my supervisors Professors Nick Kruger, George Ratcliffe and James McCullagh for all their help and support over the course of this DPhil. It has been a privilege to work with you and I could not have asked for better supervisors.

Thanks to Markus Schwarzländer and all the members of his group for teaching me about biosensors and making me feel so welcome during my visit to Münster. I really appreciate your generous and open approach to science, and I am looking forward to building on our collaboration in the future. Thanks to Joshua Rabinowitz and all the members of his group, particularly Zhaoyue Zhang for your advice about deuterium labelling and giving me so much of your time. Thanks to Boon Leong Lim for sharing plant material and Xinyu Fu and Berkley Walker for help with INST-MFA data analysis.

I'd like to thank everyone in Oxford who has supported me both in and out of the lab. Thanks to Lee Sweetlove and all the members of your group for including me in your science and social activities. Thanks to Pedro and Rita for keeping the biochemistry lab running smoothly and thanks to everyone in the mass spec facility for teaching me everything I know about LC-MS. In particular, thanks to John Walsby-Tickle, Elisabete Pires, Ingvild Hvinden, David Hauton, and James Wickens for always being free to help.

I'd like to thank the Department of Plant Sciences for maintaining such a positive work environment and like to acknowledge the Interdisciplinary Biosciences Doctoral Training Partnership (BBSRC) for funding this research and providing me with some great friends.

Finally, thanks to Lottie for being so supportive and understanding, and for reminding me that life doesn't always depend on plant metabolism.

Contents

Abstract ..... **i**

Acknowledgments ..... **ii**

Chapter 1: Introduction **1**

1.1 Redox metabolism 1

1.2 Redox carriers 1

1.3 Redox regulation of proteins by post translational modification 8

1.4 Balancing redox metabolism 9

1.5 Quantifying redox metabolism is necessary for metabolic engineering 14

1.6 Quantifying the redox metabolism of pyridine nucleotides 15

1.7 Research objectives 20

Chapter 2: Materials and methods **22**

2.1 Plant material 22

2.2 Metabolite extraction 23

2.3 Liquid Chromatography Mass Spectrometry 24

2.4 INST-MFA of heterotrophic *Arabidopsis* cell cultures 26

2.5 Analysis of deuterium labelling 30

2.6 Analysis of fluorescent biosensors 34

Chapter 3: Isotopically non-stationary metabolic flux analysis of heterotrophic *Arabidopsis* cell cultures **37**

3.1 Introduction 37

3.2 Results 42

3.3 Discussion 69

3.4 Conclusion 79

Chapter 4: Limitations of deuterium labelled substrates for quantifying NADPH metabolism in heterotrophic *Arabidopsis* cell cultures 80

4.1 Introduction 80

4.2 Results 81

4.3 Discussion 97

4.4 Conclusion 100

Chapter 5: Fluorescent biosensors for redox metabolites 102

5.1 Introduction 102

5.2 Results 107

5.3 Discussion 129

5.4 Conclusion 145

Chapter 6: General discussion 146

6.1 Quantifying redox metabolism in plants 146

6.2 Future work 152

6.3 Conclusion 155

References 156

Appendix A 198

A.1 Effect of cell extraction method on metabolite peak area and recovery 198

A.2 Glycosyl labelling of UDP glucose 200

A.3 Complete labelling timecourses 202

A.4 Relative 2-Oxoglutarate abundance 204

A.5 Model definition and net fluxes of heterotrophic *Arabidopsis* cell cultures 205

A.6 Coenzyme stoichiometries 213

A.7 Comparison of predicted and measured isotopologue abundances 216

A.8 Validation of PLSDA 217

A.9 Flux map of control vs menadione treated *Arabidopsis* cell cultures 219

A.10 Net flux probability distributions 220

A.11 Comparison of SS-MFA vs INST-MFA 228

Appendix B 229

B.1 Confocal images of biosensor subcellular localisation 229

Chapter 1: Introduction

1.1 Redox metabolism

Redox metabolism is fundamental to all life, but despite this, our understanding remains limited by the lack of selective and sensitive techniques available for studying it. The aim of this thesis is to develop and evaluate new methods for quantifying redox metabolism in plants. Greater understanding of redox metabolism in plants is vital for future advances in genetic engineering aiming to increase plant productivity or use plants for biotechnology.

Almost all life ultimately derives energy from sunlight. Photosynthesis uses the energy from the sun to oxidise water, generating high energy electrons that are used to do chemical work (Nelson and Junge, 2015). The resulting reducing power can either be directly used for physiological processes or be used to fix CO_2 into organic molecules that are subsequently oxidised, or used to build biomass, by both photoautotrophic and heterotrophic organisms. This interconversion of energy between different forms is mediated by redox reactions which transfer electrons from one compound to another, changing the oxidation state of the atoms involved. The electrons can take many paths as they move from high to low redox potentials and it is these different routes that drive the biochemical diversity of life (Horn, 2021).

Redox metabolism can involve reactions which convert substrates to products as well as redox-based post translational modifications (PTMs) of proteins. Redox reactions are pervasive throughout the metabolism of plants with ~1/3 of enzyme catalysed reactions involving oxidoreductases (Horn, 2021; Schläpfer et al., 2017). A salient feature of the reactions catalysed by oxidoreductases is the involvement of common redox carriers which act as energy couplers between different reactions.

1.2 Redox carriers

If every reduction reaction had to be directly linked to the primary oxidation of water or organic substrates, then metabolism would be severely limited in terms of spatial organisation

and catalytic diversity. Instead, redox reactions are mediated through a diverse set of carrier molecules including pyridine nucleotides, quinones, flavins, metalloproteins and thiol containing proteins and peptides. These molecules act as reversible electron acceptors and donors allowing redox reactions to be separated in space and time, and permitting metabolism to dynamically adapt to changing needs. Redox carriers with highly specialised roles also exist within specific protein complexes such as chlorophyl and pheophytin in photosystem II. However, the purpose of these molecules is to catalyse the transfer of electrons within specific individual reaction mechanisms rather than acting as hubs connecting multiple different reduction and oxidation reactions. It is these central hubs of redox metabolism that will be considered in the following sections.

1.2.1 Small molecule redox carriers

Apart from molecular oxygen, nicotinamide adenine dinucleotide (NAD) and the phosphorylated form, nicotinamide adenine dinucleotide phosphate (NADP), are the redox carriers most commonly used by oxidoreductase enzymes (Horn, 2021; Schläpfer et al., 2017). The reason for the high prevalence of NAD(P)(H) in biological redox reactions lies in the physiological range of possible redox potentials from -380 mV to -250 mV which allows NAD(P)(H) to optimally match the redox transformations most commonly found in cellular metabolism (Jinich et al., 2018). The involvement of specific redox cofactors in oxidoreductases is defined by conserved binding sites, with many NAD(P)(H) dependent enzymes sharing the conserved Rossman fold (Rao and Rossmann, 1973). Despite NADP(H) and NAD(H) having identical standard reduction potentials, enzymes are often specific to NAD(H) or NADP(H) with the phosphate group of NADP(H) facilitating specific binding interactions (Baker et al., 1992). The ability of enzymes to differentiate between NAD(H) and NADP(H) is vital to metabolism, allowing diverse reactions to proceed simultaneously and providing additional metabolic flexibility. The primary role of NAD(H) is to transfer electrons from the oxidation of substrates into the mitochondrial electron transport chain, generating the proton gradient required to synthesise ATP (Schertl and Braun, 2014). NADPH provides a supply of reducing power for

biosynthesis, oxidative stress responses and maintenance of thiol redox networks (Foyer and Noctor, 2009). These catabolic and anabolic roles are reflected in the ratios of reduced to oxidised forms, with a ratio of $NADPH:NADP^+$ greater than one and a ratio of $NADH:NAD^+$ less than one generally observed (Heineke et al., 1991; Igamberdiev and Gardeström, 2003; Szal et al., 2008). The importance of pyridine nucleotides goes beyond just energy metabolism as pyridine nucleotides also have both intra- and extracellular signalling roles, affecting gene expression, protein modification, and cell death and survival (Gakière et al., 2018a; Hashida et al., 2009; Hunt et al., 2004). In this way, pyridine nucleotides are able to link redox metabolism to gene expression and signalling pathways, but their primary roles as redox carriers will be considered in this thesis.

Flavins are another type of soluble redox carrier; derived from riboflavin and including flavin mononucleotide (FMN) and flavin adenine dinucleotide (FAD). Flavins can undergo one or two electron reductions (Massey, 2000) allowing them to link processes such as the two electron oxidation of NADH by mitochondrial complex I which then transfers single electrons to the chains of Fe-S clusters within the same complex (Berrisford and Sazanov, 2009; Rich and Maréchal, 2012). Reduced flavins in solution are rapidly oxidised in the presence of oxygen and so are almost always associated with enzymes either covalently or non-covalently (Massey, 2000). The protein structure can affect the redox potential of the flavin group, allowing flavoproteins to mediate a wide range of electron transfers between different redox couples (Nogués et al., 2004).

Quinones are a diverse class of redox carriers derived from aromatic compounds by addition of C=O groups. The lipid soluble ubiquinone and plastoquinone are components of the mitochondrial and photosynthetic electron transport chains respectively, responsible for transferring electrons between protein complexes (Liu and Lu, 2016). Other quinones in plants are water soluble and act as defence compounds against herbivory through redox cycling and production of reactive oxygen species (ROS) (Bhonwong et al., 2009).

1.2.2 Protein and peptide redox carriers

Proteins and peptides can also act as redox carriers either via metal cofactors or thiol groups. Metal cofactors can facilitate redox transfers via the various oxidation states of bound metals including iron, molybdenum, copper, and manganese. Ferredoxin, plastocyanin and cytochromes are metalloproteins which act as redox carriers rather than having specific catalytic functions as oxidoreductases. Ferredoxin contains an 2Fe-2S cluster and is important for photosynthesis, nitrogen and sulfur assimilation and reducing thioredoxin (Fukuyama, 2004; Hanke and Mulo, 2013). Plastocyanin is a copper containing redox carrier protein that links photosystem II to photosystem I (Höhner et al., 2020). Cytochromes are heme containing proteins some of which are soluble, and some are membrane bound, with cytochrome *c* forming an integral part of the mitochondrial electron transport chain by transferring electrons from complex III to complex IV (Welchen and Gonzalez, 2016).

Other redox proteins and peptides use thiol chemistry to mediate the transfer of electrons whereby sulfur atoms of cysteine residues can be oxidised to form disulfides.

$$2\ RSH \rightleftharpoons RS{-}SR + 2H^{+} + 2e^{-}$$

Thioredoxins are a family of small thiol-containing proteins which are important for reducing thiol groups in specific target proteins to modulate their activity, with protein surface interactions between thioredoxins and target proteins creating specificity in the thioredoxin redox network (Meyer et al., 2012). Thioredoxins are reduced themselves by thioredoxin reductases which transfer electrons from either ferredoxin or NADPH to thioredoxin (Jacquot et al., 1994).

Glutathione (GSH) is a tripeptide which can be reversibly oxidised and combined with a second glutathione molecule to form a disulfide (GSSG). Glutathione is a highly abundant redox carrier in plant cells, with cytoplasmic concentrations measured up to 3.5 mM (Meyer et al., 2001). Glutathione has a major role in ROS detoxifying systems as well as providing electrons for thiol switching of proteins via glutaredoxin (Meyer et al., 2012; Noctor et al., 2012). Glutathione is maintained in a highly reduced state by glutathione reductase which uses reductant

from NADPH and is vital for efficient photosynthesis and protection from ROS (Kubo et al., 1993; Müller-Schüssele et al., 2020; Zuccarelli and Freschi, 2018).

1.2.3 Subcellular compartmentation of redox carriers

Subcellular compartments can possess distinct redox states due to the selective permeability of membranes to the mobile soluble redox carriers, glutathione, and pyridine nucleotides. Transport mechanisms can be specific to oxidised or reduced forms of redox couples allowing the flow of electrons between compartments to be controlled by specific transport proteins or indirect shuttle mechanisms (Figure 1.1).

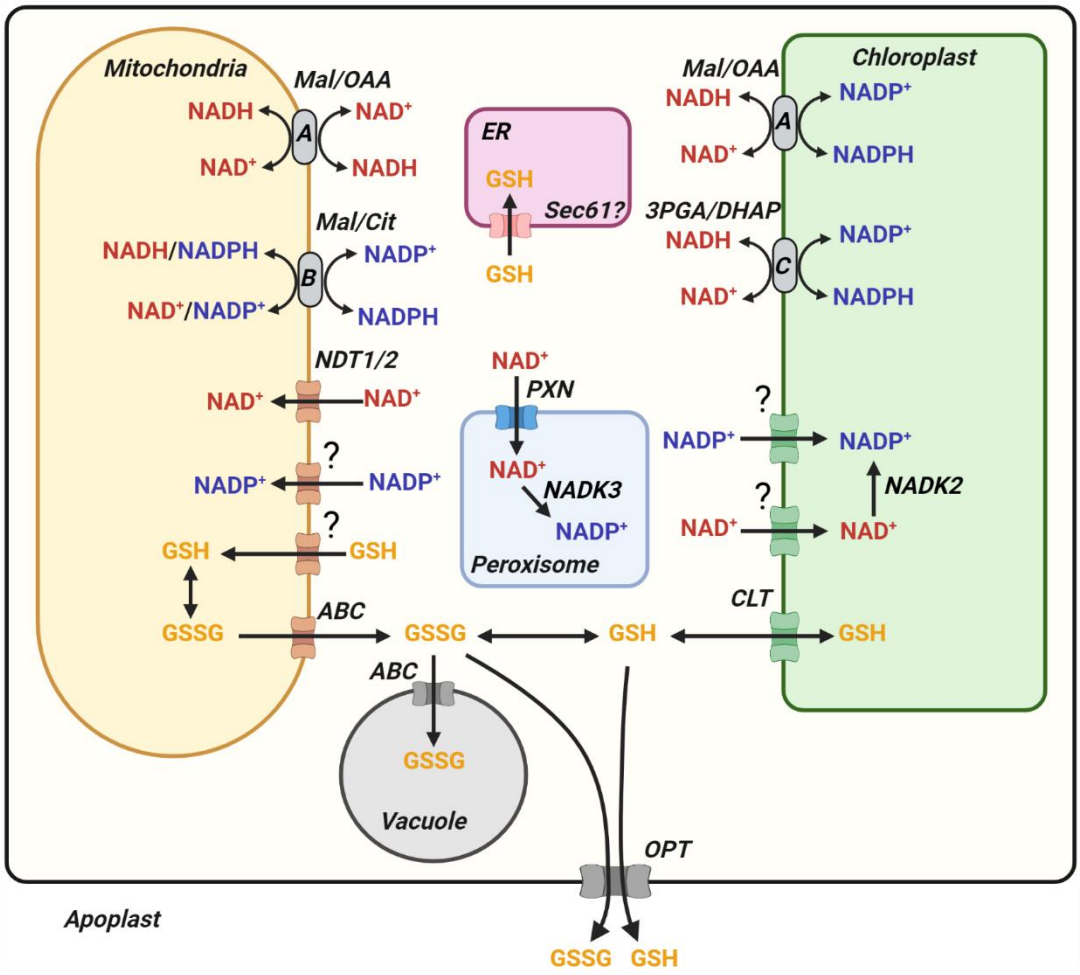

Figure 1.1. Subcellular compartmentation and transport of glutathione and pyridine nucleotides. **A**) Oxaloacetate/malate translocator. **B**) Tricarboxylate/dicarboxylate transporter **C**) Triose-phosphate-translocator. NDT – nicotinamide adenine dinucleotide transporter, ABC – ATP binding cassette, OPT – oligopeptide transporter, CLT - chloroquinone-like transporter, PXN - peroxisomal nucleotide transporter, NADK – NAD kinase, ER – endoplasmic reticulum **?)** - potential but as yet uncharacterised transporter. Created with BioRender.com

Glutathione transporters have been identified in the tonoplast, plasma membrane and chloroplast envelope (Foyer et al., 2001; Jamaï et al., 1996; Schneider et al., 1992). Oligopeptide transporters can transport GSH and GSSG across the plasma membrane along with other small peptides. Glutathione can pass between the chloroplast and cytosol through specific chloroquinone resistance transporter-like (CLT) transporters which can also transport the glutathione precursor γ-glutamylcysteine (γ-EC) (Maughan et al., 2010). ATP-binding cassette (ABC) family transporters can transport GSSG and other glutathione conjugates from the mitochondria to the cytosol (Schaedler et al., 2014) or from the cytosol to the vacuole (Lu et al., 1998). Sequestration of GSSG into the vacuole is a mechanism to maintain a high cytosolic GSH:GSSG ratio under conditions of oxidative stress (Queval et al., 2011). Concentrations of glutathione and ratios of GSH:GSSG differ substantially between different compartments and under different conditions demonstrating that, although glutathione can move between compartments, it is not in equilibrium. The redox state of the glutathione pool in each compartment will be the product of the different processes contributing to its oxidation and reduction as well as specific import or export of GSH and GSSG. For example, the glutathione redox potential (E_{GSH}) of mitochondria is more oxidised than that of the cytosol (Schaedler et al., 2014) and is much more variable in the chloroplast stroma compared to the cytosol under changing light conditions (Haber and Rosenwasser, 2020; Müller-Schüssele et al., 2020). The glutathione redox potential is also much more oxidised in the endoplasmic reticulum (ER) compared to the cytosol and can affect the glutathionylation status of proteins (Aller et al., 2013). The mechanism of glutathione transport into the ER is currently not known in plants. It is possible that glutathione passively diffuses via Sec6,1 which has been shown to be a glutathione specific transporter in yeast (Ponsero et al., 2017), and is also present in the *Arabidopsis* genome.

Pyridine nucleotides are not membrane permeable and only transporters for NAD^+ have been identified in plants. Three NAD^+ transporters exist, two targeted to the inner mitochondrial membrane (NDT1 and NDT2) (Feitosa-Araujo et al., 2020a; Luo et al., 2019; de Souza Chaves et al., 2019) and one to the peroxisomal membrane (PXN) (Agrimi et al., 2012). NDT1 and NDT2

are antiporters and can exchange NAD^+ for nucleotides such as ADP or AMP, or NAD precursors including nicotinic acid mononucleotide (NaMN), nicotinamide mononucleotide (NMN) and nicotinic acid adenine dinucleotide (NaAD) (Palmieri et al., 2009). GFP-fusion studies in tobacco protoplasts originally located NDT1 to the chloroplast membrane (Palmieri et al., 2009) but recent evidence from stably transformed *Arabidopsis* plants showed exclusive mitochondrial localisation (de Souza Chaves et al., 2019). Chloroplasts must also be able to import NAD^+ or its precursors which are synthesised in the cytosol (Gakière et al., 2018b), but the mechanism remains unclear. Neither NDT1 or NDT2 transport $NADP^+$ or NADPH and therefore NAD-kinase is presumably necessary to maintain the NADP(H) pool in the chloroplasts and peroxisomes (Li et al., 2018). The NAD(P)(H) concentration in the ER has yet to be measured in plants and, to date, no ER localised pyridine nucleotide transporter has been identified. It is possible that NAD(P)(H) are not required in the plant ER and therefore an ER localised transporter for pyridine nucleotides may not exist in plants.

The impermeability of compartments to reduced forms of the pyridine nucleotides allows distinct redox states to exist in different compartments. For example, the $NADH:NAD^+$ ratio is greater in the mitochondria compared to the cytosol, favouring the oxidation of NADH for proton pumping across the inner mitochondrial membrane (Igamberdiev and Gardeström, 2003; Szal et al., 2008). Although reduced pyridine nucleotides cannot be directly transported across membranes, indirect transport of reducing equivalents is facilitated by shuttle mechanisms which rely on transporters and dehydrogenases in different compartments such as the malate/oxaloacetate shuttle, malate/aspartate shuttle, triose phosphate/3-phosphoglycerate shuttle (Heineke et al., 1991; Journet et al., 1981; Selinski and Scheibe, 2018) and citrate valve (Igamberdiev, 2020) (Figure 1.1). These shuttle mechanisms are particularly important in illuminated photosynthetic cells as they can export excess reductant from the chloroplast to other compartments maintaining efficient photosynthetic electron flux (Scheibe, 2004; Selinski and Scheibe, 2018; Shameer et al., 2019). The transport of reducing equivalents between compartments via shuttle mechanisms adds an additional level of flexibility and complexity to

plant redox metabolism by linking the transport of reductant to fluxes through central carbon metabolism. This compartmented nature of redox metabolism means that any method for quantifying redox processes must be compartment-specific.

1.3 Redox regulation of proteins by post translational modification

As well as electrons being transferred between different redox carriers, electrons can also be transferred onto proteins via redox post-translational modifications (Buchanan and Balmer, 2005; Friso and Van Wijk, 2015; Martí et al., 2020; Mock and Dietz, 2016; Ruiz-May et al., 2019). Redox PTMs include carbonylation, sulfhydration, nitrosylation, hydroxylation, glutathionylation and the formation of disulfide bonds. These modifications can lead to a range of effects including inactivation, activation, translocation, oligomizeration and proteolytic processing of proteins. The range of possible oxidation states of sulfur make cysteine residues the major targets of redox modification in proteins, with their reactivity tuned by the local protein structure and electrostatic environment (Couturier et al., 2013; Waszczak et al., 2015). Cysteine residues can react either directly with ROS such as H_2O_2, or with other cysteine residues to form intra- or intermolecular disulfide bonds. The oxidation state of a particular cysteine residue, which can in turn affect protein function, is defined by the protein structure, the concentrations of specific electron donors/acceptors and the kinetics of the interaction which can be affected by other competing redox processes. Therefore, protein redox PTMs provide a link between redox metabolism and protein activity, affecting signalling pathways, gene expression and enzyme activity. The classical example of redox PTM modulating enzyme activity is the activation of Calvin cycle enzymes by the ferredoxin/thioredoxin system which links the availability of reductant to carbon fixation (Schürmann and Buchanan, 2008). Redox PTMs can also affect gene expression by modulating the activity of transcription factors (Dietz, 2014). For example, homeodomain transcription factors which control shoot development in *Arabidopsis* are regulated by three conserved cysteine residues which are reduced by thioredoxin (Comelli and Gonzalez, 2007). Advances in protein mass spectrometry have made comprehensive quantification of redox

PTMs possible across the proteome, providing a system wide view of the interaction of redox metabolism with proteins (Mock and Dietz, 2016).

1.4 Balancing redox metabolism

The many possible interactions between redox carriers, oxidoreductase enzymes and redox PTMs must be balanced to maintain metabolic function. Demands for reductant for biosynthesis and cellular maintenance must be matched with the available supply for optimal growth while avoiding the potentially damaging effects of excess reductant. However, despite the connections between different redox carriers, they are not in equilibrium and there is no unifying cellular redox state which defines the balance between supply and demand for reductant (Potters et al., 2010). A cellular redox state is not a generalisable quantitative parameter, instead redox metabolism is specific to the redox couples which accept/donate electrons at biologically relevant rates through enzyme catalysed reactions. The different *in vivo* redox potentials of the NADH:NAD^+ and NADPH:$NADP^+$ couples exemplify this, as despite the identical standard reduction potentials of NAD(H) and NADP(H), their different concentrations lead to distinct redox potentials (Heineke et al., 1991; Herber and Santarius, 1965; Igamberdiev and Gardeström, 2003; Szal et al., 2008; Wigge et al., 1993). An overarching cellular redox state or complete equilibration between all redox couples would not allow the simultaneous oxidation and reduction of substrates for anabolism and catabolism to occur in the same subcellular compartments at the same time. Therefore, it is critical to evaluate redox carriers separately and not to make a cell wide generalisation of redox state. The pyridine nucleotides, NAD(P)(H), are involved in >650 oxidoreductase reactions (Horn, 2021; Schläpfer et al., 2017) and support the reduction of other redox couples including glutathione, thioredoxin, and ascorbate. Therefore, understanding pyridine nucleotide metabolism is a prerequisite for understanding redox metabolism in plants. NADPH is of particular importance to biosynthesis and stress tolerance in plants, which are the major targets of metabolic engineering, and therefore the following sections focus primarily on NADPH metabolism.

1.4.1 NADPH demands

Demands for NADPH can be divided into biosynthetic and maintenance processes where biosynthesis results in the net synthesis of biomass and maintenance encompasses all other process which consume NADPH.

NADPH is required for assimilation of carbon, nitrogen and sulfur as well as biosynthesis of amino acids, lipids, and secondary metabolites. The production of carbohydrates via the Calvin cycle is the major sink for NADPH in photosynthesising cells as 3-phosphoglycerate is reduced to glyceraldehyde 3-phosphate (Calvin and Benson, 1948; Walker et al., 2020). Different forms of bioavailable nitrogen require different sources of reductant with cytosolic nitrate reductase consuming NADH (Lee, 1980), plastidic nitrite reductase requiring NADPH or reduced ferredoxin (Joy and Hageman, 1966; Ramaro et al., 1981) and glutamate synthase (GOGAT) requiring NADH or reduced ferredoxin in the plastids (Miflin and Lea, 1976). Nitrogen assimilation represents the largest biosynthetic demand for NADPH in heterotrophic plant cell cultures (Masakapalli et al., 2010, 2013, 2014) and can consume up to 23% of NADPH generated by photosynthetic linear electron flow, depending on the nitrogen source available (Walker et al., 2020). Fatty acid biosynthesis occurs in the plastid and requires reductant from one NADPH and one NADH for the addition of each two carbon unit to the acyl chain by acetyl-CoA carboxylase and fatty acid synthetase (Rawsthorne, 2002; Slabas and Fawcett, 1992). Most plant tissues make trace amounts of lipids to support membranes but seeds can produce much larger quantities reaching up to 80% of dry weight in some species (Voelker and Kinney, 2001). The biosynthesis of some amino acids requires an input of reductant from NADPH including arginine, cysteine, isoleucine, leucine, lysine, methionine, phenylalanine, proline, threonine, tryptophan, valine, and glutamate (Schläpfer et al., 2017). Finally, due to the structural diversity of plant secondary metabolites, secondary metabolic pathways often require a reduction step at some point, with the reductant most commonly being derived from NADPH (Horn, 2021). The magnitude of these different demands for NADPH will vary depending on the tissue type, developmental stage, and external conditions but precise measurements of

biosynthetic reductant demands can be made based on biomass output fluxes and stoichiometries of reactions, assuming turnover of end products is minimal.

A major maintenance role of NAPDH is in preserving the balance of reactive oxygen species (ROS) which are an inevitable consequence of metabolism in an oxygenic environment. The antioxidant systems for balancing ROS have been extensively reviewed (Foyer and Noctor, 2009, 2011, 2020; Noctor and Foyer, 1998; Noctor et al., 2012; Pandey et al., 2015) but there two important features. Firstly, antioxidant systems require a source of reductant which is typically supplied by NAPDH. Secondly, ROS have important signalling roles and their production can also be dependent on the activity of NADPH oxidases which rely on reductant supplied by NADPH (Sagi and Fluhr, 2006; Suzuki et al., 2011). Therefore, an adequate supply of NADPH is necessary for maintaining optimal ROS levels. ROS are the partially reduced or excited forms of oxygen that are more reactive than native oxygen including superoxide ($O_2^{\bullet-}$), hydrogen peroxide (H_2O_2), hydroxyl radical ($OH^{\bullet}$) and singlet oxygen ($^1O_2$) (Halliwell and Gutteridge, 2015a). ROS can cause damage to cells by oxidising essential cellular components including DNA, RNA, proteins and membrane lipids (Halliwell and Gutteridge, 2015b). Different ROS are removed by different antioxidant systems including superoxide dismutase, which converts $O_2^{\bullet-}$ to H_2O_2; catalase, which converts H_2O_2 to water; and peroxidases, which detoxify H_2O_2 to water using reductant from various redox carriers including glutathione, ascorbate and thioredoxins. Ascorbate which has been oxidised to monodehydroascorbate can be regenerated via the ascorbate-glutathione cycle which comprises monodehydroascorbate reductase (MDHAR), dihydroascorbate reductase (DHAR) and glutathione reductase (GR) (Foyer and Halliwell, 1976). MDHAR and GR require reductant from NADPH to drive the cycle and regenerate GSH and ascorbate which have been oxidised to detoxify H_2O_2 (Hossain et al., 1984; Kubo et al., 1993). Ultimately, the reductant supporting glutathione, ascorbate, thioredoxins and peroxiredoxins can be derived from NADPH and therefore adequate NADPH supply underpins the antioxidant capacity of cells.

Although excessive or unbalanced ROS production can be damaging, ROS also form the basis of many signalling pathways in plants and other organisms (Mittler, 2017). Priming plants with the direct application of ROS or ROS inducing agents can even improve plant performance and growth (González-Bosch, 2018; Hossain et al., 2015). ROS production from NADPH oxidases (NOX) has been implicated in signalling pathways important for development and growth as well as abiotic and biotic stress responses (Hu et al., 2020; Marino et al., 2012; Miller et al., 2009; Sun et al., 2019; Wang et al., 2018). NADPH oxidases are transmembrane proteins which generate extracellular superoxide radicals which can be converted to H_2O_2 and O_2 by SOD. NOX could potentially represent a large NADPH demand under specific conditions although absolute quantification of the NADPH demand from NOX activity has not been reported.

Protein thiol networks are also supported by reductant from NADPH. Thioredoxin and glutaredoxin modulate the switching of thiol groups in proteins and require an input of reductant which ultimately comes from NADPH, either to reduce thioredoxin reductase or glutathione disulfide (Meyer et al., 2012). Thiol switching processes are mediated by specific enzymes but the thermodynamic driving force for reducing disulfide bonds needs to be available, and this is supplied by NADPH.

Photosynthetic organisms face a unique challenge in controlling the input of reductant from photosynthetic electron transport as they are sessile organisms. Despite this, plants have several mechanisms for decreasing the incident light absorbed. These include long term adaptation such as leaf area, leaf position and photosystem antenna size (Anderson et al., 1995), as well as medium term adaptations such as leaf and chloroplast movement (Koller, 1990; Wada, 2013). Furthermore, plants are able to dissipate light energy prior to electron transport through non-photochemical quenching where light energy is dissipated as heat (Papageorgiou and Govindjee, 2014). However, reductant demand and supply can change rapidly and potentially become mismatched. Therefore, plants have evolved various mechanisms to dissipate excess reducing power resulting from the unavoidable absorption of light (Scheibe, 2019; Scheibe et al., 2005; Walker et al., 2020). These include routes of alternative electron flow such as cyclic

electron transport, which uses reductant to produce ATP in place of NADPH, and the water-water cycle, which consumes NADPH via a cyclic reaction involving ascorbate and glutathione (Miyake, 2010). Plant mitochondria also possess additional sinks for NAD(P)H via the activity of alternative dehydrogenases (Rasmusson et al., 2004) and the alternative oxidase (Lambers, 1982). Together these enzymes dissipate excess NAD(P)H as heat and therefore represent a maintenance demand for reductant.

Maintenance costs are much more difficult to quantify than biosynthetic requirements as they are not associated with the formation of easily quantifiable output metabolites. Maintenance costs can be indirectly estimated by subtracting the biosynthesis costs from the total NADPH production rate, assuming the system is at a metabolic steady state (Cheung et al., 2013). However, maintenance costs during non-steady state conditions, which could occur during acute biotic or abiotic stresses, are more difficult to quantify.

1.4.2 NADPH supply

In plants, NAD(P) is synthesized *de novo* from aspartate as well as being recovered by salvage mechanisms (Gakière et al., 2018b; Hashida et al., 2009; Noctor et al., 2006). Although non-redox reactions which consume NAD(H) and NADP(H) are important for plant development and stress responses (Gakière et al., 2018a), the role of these coenzymes in redox metabolism depends on the conversion between the oxidised and reduced forms (Figure 1.2). The redox couples are oxidised and reduced rapidly, with a half-life of <1 s (Arrivault et al., 2009), as many different reactions simultaneously contribute to their oxidation or reduction. This redox cycling occurs much faster than synthesis or breakdown, and therefore any individual NAD(P)(H) molecule will likely be oxidised and reduced many times in its lifetime.

In photosynthetic plant tissues, ferredoxin-$NADP^+$ reductase (FNR, EC 1.18.1.2) transfers electrons from photosystem I via ferredoxin to $NADP^+$. NADPH is also produced in both heterotrophic and autotrophic tissues by the oxidation of carbon substrates via enzymes including: glucose-6-phosphate dehydrogenase (G6PDH, EC 1.1.1.49), 6-phosphogluconate dehydrogenase (6PGDH, EC 1.1.1.44), NADP-isocitrate dehydrogenase (NADP-IDH, EC

1.1.1.42), NADP-malate dehydrogenase (NADP-MDH, EC 1.1.1.37), NADP-malic enzyme (NADP-ME, EC 1.1.1.40), methylenetetrahydrofolate dehydrogenase (MTHFD, EC 1.5.1.5) (Gorelova et al., 2017a) and non-phosphorylating glyceraldehyde 3-phosphate dehydrogenase (GAPDH, EC 1.2.1.9) as well as other aldehyde dehydrogenases (Missihoun et al., 2018). NADPH can also be generated from NADH via the phosphorylation of NADH by NAD kinases using ATP (Chai et al., 2005, 2006; Turner et al., 2004). Genetic studies knocking out or overexpressing specific sources of NADPH provide evidence that they make variable and potentially significant contributions to total NADPH production (Corpas and Barroso, 2014; Mhamdi and Noctor, 2015; Mhamdi et al., 2010; Voll et al., 2012; Wakao et al., 2008). However, the relative contributions of the different sources have yet to be accurately quantified.

1.5 Quantifying redox metabolism is necessary for metabolic engineering

Understanding and quantifying the different sources and sinks of reductant is a prerequisite for effective metabolic engineering, to ensure any modifications to metabolism do not detrimentally affect cellular redox balance (Chen et al., 2014; Liu et al., 2018; Park and Choi, 2017; Wang et al., 2013). Numerous examples of redox balancing strategies exist from engineering microorganisms (de Arroyo Garcia and Jones, 2020; Chemler et al., 2010; Chen et al., 2014; Harth et al., 2020; King and Feist, 2014; Qiao et al., 2017; Wang et al., 2013; Yukawa et al., 2020; Zhao et al., 2017a), but a lack of quantitative understanding of redox metabolism in plants means that rational strategies for balancing coenzymes in the latter systems have not been explored in depth.

Modifying the supply of reducing power has the potential to improve photosynthetic productivity (Kramer and Evans, 2011), nitrogen use efficiency (Foyer et al., 2011), and yield in crops under stress (Zinta et al., 2016). For example, drought stress tolerance and resistance to *Phytophthora nicotianae* was improved in tobacco by increasing the capacity for cytosolic NADPH production by expressing a plastidic isoform of G6PDH in the cytosol (Scharte et al., 2009). Similarly, salt tolerance was improved in *Arabidopsis* by overexpressing a cytosolic

G6PDH from soybean (Jin et al., 2021). Yields were increased in both *Arabidopsis* and tobacco by introduction of cytochrome c_6 from red algae. This stimulated higher rates of photosynthetic electron transport compared to wild type plants which relied solely on plastocyanin to transfer electrons between the Cyt b_6f complex and PSI (Chida et al., 2007; López-Calcagno et al., 2020). Cytochrome c_6 was found to be more efficient than plastocyanin resulting in higher levels of the products of the photosynthetic electron transport chain, NADPH and ATP (Chida et al., 2007). In contrast, increasing NAPDH oxidation capacity, rather than NADPH production can also be a valid strategy for metabolic engineering, highlighting the complex nature of redox balancing. For example, expression of cyanobacterial flavodoxin and a soluble ferredoxin-$NADP^+$ reductase provided an additional route for electron flow in chloroplasts, alleviating overreduction of the photosynthetic electron transport chain which can occur under oxidative stress conditions (Giró et al., 2011). Although these examples highlight the potential benefits of engineering redox metabolism in plants, further progress will require a network view of the optimal modifications to make and the consequences of these on plant fitness in field conditions. To achieve this goal, tools are needed for quantifying redox metabolism in plants.

1.6 Quantifying the redox metabolism of pyridine nucleotides

Redox metabolism is defined by the flow of electrons between specific metabolites, redox carriers, and macromolecules. Understanding redox metabolism requires information about where electrons are going and at what rate. Redox metabolism is specific to individual redox carriers and within individual compartments, so methods need to provide compartment- and redox carrier-specific information. Several experimental techniques are available which provide varying degrees of information including genetic studies of enzyme overexpression/knockdown, measurement of protein PTMs, measurement of redox carrier concentrations, and flux analysis based on extracellular rates and isotope labelling. The pyridine nucleotides are the most widely used redox carriers and therefore discussion will focus on methods for quantifying pyridine nucleotide metabolism, but the same principles apply to all redox carriers.

The involvement of NAD(P)(H) in metabolism can be described in several ways (Figure 1.2). Both the total concentration, and the concentrations of specific reduced/oxidised forms are important for signalling and regulation (Gakière et al., 2018a; Hashida et al., 2009; Hunt et al., 2004). The redox potentials, defined by the relative concentrations of reduced/oxidised forms and influenced by local pH, are important for determining reaction directionality and the flow of reducing power. The rate of interconversion between reduced and oxidised forms (the redox flux) is important for energy metabolism and redox homeostasis (Corpas and Barroso, 2014). Finally, synthesis and breakdown of NAD(P)(H) is important for post translational protein modification, gene expression, and cell death and survival (Gakière et al., 2018a; Hashida et al., 2009; Hunt et al., 2004). These parameters are related but can vary separately from each other, and therefore accurate quantification of each of these parameters is vital for fully understanding NAD(P)(H) metabolism.

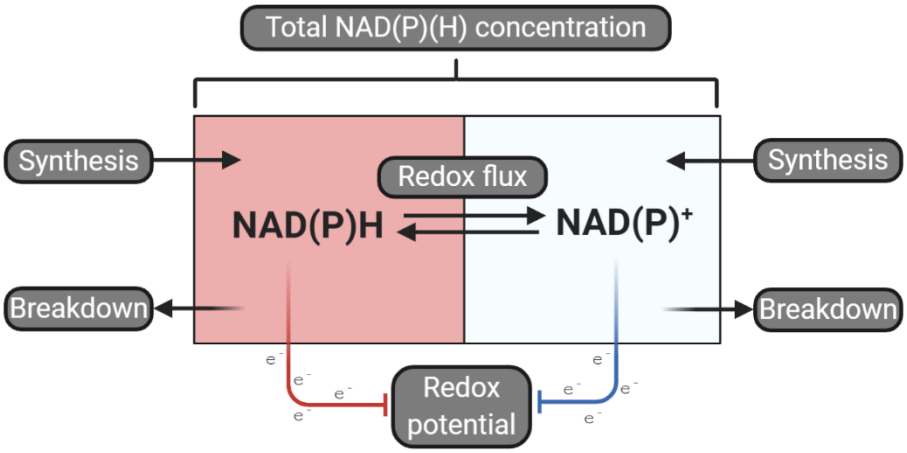

Figure 1.2. The different parameters associated with the redox couples NADP(H) and NAD(H) at a metabolic steady state including: the concentration of $NAD(P)^+$ or NAD(P)H, the redox potential, the rate of interconversion between reduced and oxidised forms or the redox flux, and the synthesis/breakdown flux. Steady state redox and synthesis/breakdown fluxes can vary separately from the concentrations of NAD(P)(H). The total pool size of NAD(P)(H) can vary separately from NAD(P)H:$NAD(P)^+$ ratio. The redox potential is dependent on the NAD(P)H:$NAD(P)^+$ ratio and pH but independent of total concentrations or fluxes. It is likely that changes in one parameter will be associated with changes in other parameters, particularly in the transition to a new metabolic steady state. However, fluxes, total concentrations and ratios can vary separately and should be measured independently to gain a full understanding of NAD(P)(H) metabolism. Created with BioRender.com

1.6.1 Enzyme abundance and activity

Transcript or protein levels of enzymes producing and consuming NAD(P)H can be quantified under different conditions. Expression levels of NADPH producing dehydrogenases have been shown to change under a variety of stress conditions (reviewed in Corpas and Barroso, 2014). For example, expression of $NADP^+$-IDH increases in *Arabidopsis* roots under salt stress (Leterrier et al., 2012) and $NADP^+$-ME expression and activity both increase in tobacco under drought stress (Hýsková et al., 2014). The metabolic network can be further perturbed by knocking down/out or overexpressing specific proteins. Knocking out different sources of NADPH under non-stress conditions generally has little effect, demonstrating the flexibility and redundancy of the metabolic network (Chai et al., 2006; Mhamdi and Noctor, 2015; Mhamdi et al., 2010; Voll et al., 2012; Wakao et al., 2008). This also highlights the limitation of using genetic studies to infer information about metabolic function as a lack of phenotype does not necessarily mean that a gene lacks an important function. Advantageously, protein information

can be compartment specific by identifying subcellular localisation sequences (Sperschneider et al., 2017) or using fluorescent tags (Tanz et al., 2013), or immunolocalization (Sauer and Friml, 2010). Quantifying transcript or protein levels is necessary for defining the metabolic network within which redox metabolism operates, but it cannot provide quantitative information about the flow of reducing power through the metabolic network necessary for understanding the metabolic phenotype (Fernie and Stitt, 2012).

1.6.2 Measuring concentrations

Measuring the concentrations of pyridine nucleotides or other redox carriers can provide some of the basic information needed to describe their redox metabolism and is required to predict the direction of electron flow based on thermodynamics. Changes in concentration over time or between two conditions show that redox metabolism has been perturbed in some way, either by a change in the activity or abundance of certain enzymes and/or a change in the availability of substrates or consumption of products. Specific and separate measurements of $NADP^+$, NADPH, NAD^+ and NADH are important for understating their redox metabolism due to their distinct roles. Analytical methods can provide specific metabolite quantification, but analysis of whole cell extracts lacks subcellular resolution (Lu et al., 2018; Zhang et al., 2020). Subcellular fractionation methods go some way to overcoming this limitation, but methods can be laborious and still give incomplete resolution of subcellular compartments (Dietz, 2017). Fluorescent biosensors offer a potential solution to these problems, providing compartment specific real time information about metabolite concentrations or redox potentials. Recently several fluorescent biosensors for NADPH and NADH:NAD^+ have been expressed in plants (Lim et al., 2020; Steinbeck et al., 2020) and these will be explored further in Chapter 5. However, quantifying concentrations alone does not inform about the fluxes which ultimately define the metabolic phenotype (Fell, 2005; Kruger and Ratcliffe, 2009) and therefore application of flux analysis methods to redox metabolism should also be explored.

1.6.3 Flux analysis

Redox fluxes can be measured at the inputs or outputs of the metabolic network and where a single process dominates the flux. For example, the electron flux into the photosynthetic electron transport chain can be quantified by the oxygen evolution from photosystem II which can be measured using ^{18}O labelling methods (Gauthier et al., 2018). More commonly, fluorescence measurements of photosystem II are used to estimate the rate of linear electron flux, although these are often based on assumptions about incident photon absorbance and the fraction of photosystem II, which may not always be accurate (Baker, 2008). Similarly, the electron flux through the mitochondrial electron transport chain can be measured from the oxygen uptake rate of isolated mitochondria (Jacoby et al., 2015). However, these inputs and outputs of electrons represent the net product of many different possible routes of electron flow, and fluxes through the intermediate reactions which make up redox metabolism cannot be quantified from the major input and output fluxes alone.

Isotope labelling and metabolic flux analysis (MFA) is able to quantify fluxes throughout the metabolic network, including redox reactions, and provide the quantitative network-orientated view necessary for understanding plant metabolism (Kruger and Ratcliffe, 2015; Kruger et al., 2012). ^{13}C-MFA can only follow the fate of carbon atoms, but redox fluxes which involve the transfer of electrons can still be indirectly estimated where these are associated with carbon transformations. Therefore, ^{13}C-MFA can estimate balances of cofactor production and consumption including NADPH, NADH and ATP. Furthermore, metabolic flux analysis can be compartment specific by analysing labelling of compartment-specific metabolites such as cell wall- or starch-derived glucose moieties (Allen et al., 2007). Flux analysis has the potential to provide the quantitative flux information necessary for understanding redox metabolism in plants, but current application of MFA to plants suffers from two limitations: reliance on isotopic steady state analyses which requires long labelling timecourses that cannot capture short lived changes in metabolism, and ambiguity in coenzyme specificity of reactions when following carbon flow alone.

Most metabolic flux analyses in plants have used isotopic steady state MFA (SS-MFA) to quantify intracellular fluxes (Allen and Young, 2013; Alonso et al., 2011; Iyer et al., 2008; Kruger et al., 2012; Lonien and Schwender, 2009; Masakapalli et al., 2010, 2013, 2014; Williams et al., 2008). An alternative method which overcomes the isotopic steady state requirement, isotopically non-stationary metabolic flux analysis (INST-MFA), can quantify fluxes over shorter timescales but, to date, its application in plants has been limited (Ma et al., 2014; Xu et al., 2021). NADPH demands can change rapidly in response to external stimuli such as pathogen infection, drought, flooding, or fluctuating light, and therefore it is useful to understand how the metabolic network can meet these more transient and potentially larger demands. INST-MFA provides network wide quantitative flux measurements over timescales relevant to these transient changes in redox metabolism, and therefore there is a pressing need to apply INST-MFA to quantify redox metabolism in plants.

Redox reactions involving NAD(P)(H) involve the transfer of electrons as hydride ions and therefore isotopically labelled hydrogen (^{2}H, deuterium) can be used to quantify fluxes through these reactions. Methods using deuterium labelled substrates to quantify redox fluxes through specific coenzymes have been developed in mammalian cells (Chen et al., 2019a; Fan et al., 2014; Ghergurovich et al., 2020; Lewis et al., 2014; Liu et al., 2016; Zhang et al., 2017), but are yet to be applied to plants. The distinct roles of NADP(H) and NAD(H) (see section 1.2.1) mean that specific quantification of their fluxes is important for understanding redox metabolism. However, ^{13}C-MFA cannot distinguish between reactions which could use either NADP(H) or NAD(H). Therefore, there is a pressing need to apply deuterium labelling methods to plants to overcome the limitations of ^{13}C-MFA and quantify fluxes through specific redox coenzymes.

1.7 Research objectives

Our understanding of redox metabolism in plants remains limited by the tools we have available for quantitative measurement of subcellular concentrations and fluxes of specific redox

carriers. Therefore, the aim of this thesis is to develop and evaluate novel methods for quantifying redox metabolism in plants. To achieve this, I will pursue the following objectives:

1. Develop isotopically non-stationary ^{13}C-metabolic flux analysis in heterotrophic *Arabidopsis* cell cultures to quantify fluxes under changing demands for NADPH (Chapter 3).

2. Develop deuterium labelling strategies for quantification of specific coenzyme fluxes in heterotrophic *Arabidopsis* cell cultures (Chapter 4).

3. Evaluate fluorescent biosensors as tools for real time *in vivo* quantification of redox carrier concentrations and ratios (Chapter 5).

Chapter 2: Materials and methods

2.1 Plant material

2.1.1 *Arabidopsis* cell cultures

Cell suspensions of *Arabidopsis thaliana* (ecotype *Landsberg erecta*) were cultured in MS medium at pH 5.8 containing 30 g/L glucose, 0.5 mg/L 1-naphthaleneacetic acid, and 0.05 mg/L kinetin as described by Williams et al. (Williams et al., 2008). Cultures were grown in sterile 250 mL Erlenmeyer flasks, sealed with a double layer of aluminium foil, on an orbital shaker running at 120 rpm in complete darkness at 22 °C. The cell line was maintained by weekly subculturing 15 mL of cell culture into 100 mL of fresh medium. Liquid cell cultures were used for INST-MFA experiments.

Deuterium labelling experiments required transfer of plant material to deuterated media with minimal metabolic perturbation and carryover from growth media. Therefore a method for growing cell cultures on easily transferable filter paper disks was modified from Horsch et al. (Horsch et al., 1980) and Scholten et al. (Scholten, 1980). Filter paper cultures of *Arabidopsis thaliana* were maintained on 42.4 mm diameter Whatman No. 1 filter papers in 5 cm diameter Petri dishes containing 5 mL MS agar (0.5% w/v) at pH 5.8 with 30 g/L glucose, 0.5 mg/L 1-naphthaleneacetic acid, and 0.05 mg/L kinetin at 22 °C. Dishes were sealed with a layer of Micropore (3M) tape and grown in complete darkness. 2 mL of 4-d-old liquid cultures was collected on filter papers using a Buchner funnel and concentrated by weak vacuum before the cells and filter paper were transferred directly to agar plates. Filter paper cultures were then grown for 4 d (unless otherwise specified) before use in isotopic labelling experiments.

2.1.2 Transgenic plants

Seeds of transgenic *Arabidopsis thaliana* (Col-0) were kindly donated by Markus Schwarzländer (University of Münster, Germany) and Boon Leon Lim (University of Hong Kong, Hong Kong). Plants expressing Peredox-mCherry were generated as described in Steinbeck et al., (2020). Cyt-iNapC-B, Cyt-iNap1, cyt-iNap4, cyt-SoNar, plast-iNapC, plast-

iNap1, plast-iNap4, plast-SoNar, perox-iNapC, perox-iNap1 and perox-iNap4 plants were generated as described in Lim et al., (2020). SoNar and iNap sensors were originally developed by Yi Yang (East China University of Science and Technology, China) (Tao et al., 2017; Zhao et al., 2015). Seeds for plants expressing cyt-iNapC-A and cyt-iNap2 were donated by MS who transformed these by amplifying the coding sequence of iNap from Tao et al., (2017) and transferring into a pB7WG2 vector (Karimi et al., 2002). *Agrobacterium tumefaciens* mediated transformation of *Arabidopsis thaliana* (Col-0) was performed by the floral dip method (Clough and Bent, 1998). Transformants were selected based on the resistance marker for phosphinothricin and sensor fluorescence.

Arabidopsis seedling were grown on vertical plates of half strength MS media with 1% (w/v) sucrose, 0.01% (w/v) myoinositol, 0.9% (w/v) agar and 10 mM 2-(*N*-morpholino)ethanesulfonic acid (MES buffer), pH 5.7 (KOH). Seedlings were cultivated under long day conditions, 16 h light, 8 h dark at 21 °C after stratification for 2-4 d in the dark at 4 °C. Seedlings were individually transferred to soil after 5 d and grown under greenhouse conditions (16 h light, 8 h dark) for analysis of leaf disks once plants were 4- to 6-weeks old.

2.2 Metabolite extraction

2.2.1 DCM:HCl and 80% MeOH extraction of liquid cell cultures

5 ml of 4-d-old *Arabidopsis* cell culture (~300 – 500 mg fresh weight) was rapidly filtered under vacuum (<10 s) onto Whatman No. 1 filter papers and cells scraped into 1.35 ml of 2:1 DCM:EtOH or 80% MeOH on dry ice (-78 °C). 150 µl of 60 mM HCL was added to the DCM:EtOH samples and cells vortexed for 10 s. Samples were centrifuged at 20,000 x g for 10 min (4 °C). For DCM:EtOH extracts 400 µl of the aqueous phase stored on ice whilst pH was measured and 45 µl 0.48 M HCL was added to reduce the pH to < 2.5. Samples were then filtered using 10 KDa MWCO filters (Amicon), transferred to glass LCMS vials and stored at -80 °C before analysis by IC-MS.

2.2.2 MeOH:AcN extraction of filter-paper cell cultures

Under green light, cells were scraped from filter papers into a 2 mL screw-cap microfuge tube, weighed, and an appropriate volume of ice-cold extraction solvent (1:1 MeOH:AcN) was added in a ratio of cell fresh weight (mg) to extraction solvent (µL) of 1:1.5 (unless otherwise stated). The tube was then vortexed for 5 s and submerged in liquid nitrogen before being centrifuged for 20 min at 20,000× g at 4 °C. The supernatant was then filtered through 10 KDa MWCO filters (Amicon) before being transferred to Waters total recovery LC-MS vials and either analysed immediately or stored at −80 °C.

2.3 Liquid Chromatography Mass Spectrometry

2.3.1 Ion exchange – quadrupole-orbitrap MS (Qexactive)

An ion-exchange chromatography method was adapted from Walsby-Tickle et al., 2020. Metabolite extracts were analysed using a Thermo Scientific ICS-5000+ ion chromatography system coupled directly to a Q-Exactive Hybrid Quadrupole-Orbitrap mass spectrometer with a HESI II electrospray ionization source (Thermo Scientific, San Jose, CA, USA). The ICS-5000+ HPLC system incorporated an electrolytic anion generator (KOH) which was programmed to produce a 5–100 mM OH- gradient over 37 min to facilitate ion chromatography. An inline electrolytic suppressor removed hydroxide ions and cations from the post-column eluent prior to MS analysis (Thermo Scientific Dionex AERS 500). A 10 µL partial loop injection was used for all analyses and the chromatographic separation was performed using a Thermo Scientific Dionex IonPac AS11-HC 2 × 250 mm, 4 µm particle size column with a Dionex Ionpac AG11-HC 4 µm 2 × 50 guard column inline. The flow rate was 0.25 mL/min. The total run time was 37 min and the hydroxide ion gradient was: 0 min, 0 mM; 1 min, 0 mM; 15 min, 60 mM; 25 min, 100 mM; 30 min, 100 mM; 30.1 min, 0 mM; 37 min, 0 mM. Analysis was performed in negative ion mode using a scan range from 60 to 900 and resolution set to 70,000. The tune file source parameters were: Sheath gas flow 60 mL/min; auxiliary gas flow 20 mL/min; spray voltage 3.6 V; capillary temperature 320 °C ; S-lens RF value 70; heater temperature 450 °C . Automatic

gain control target was set to 1×10^6 and the maximum injection time value was 250 ms. The column temperature was maintained at 30 °C.

2.3.2 Ion-pairing reverse phase – triple quadrupole MS (Quattro Micro)

An ion-pairing reverse phase chromatography method was modified from Buescher et al., 2010. Compounds were separated using a silica based reverse phase C18 column (Waters Cortecs T3, 1.6 μm, 2.1 × 100 mm). The mobile phase solvent A was 10 mM tributylamine, 10 mM acetic acid, 2 mM acetyl acetone, 5% (v/v) methanol all in Milli-Q water and solvent B was propan-2-ol. The chromatographic gradient was: 0 min, 100% A, 0.35 mL/min; 3 min, 92% A, 0.35 mL/min; 5 min, 92% A. 0.35 mL/min; 10 min 87% A, 0.35 mL/min; 10.5 min, 87% A, 0.15 mL/min; 12 min 20% A, 0.15 mL/min; 18 min, 20% A, 0.12 mL/min; 21 min, 100% A, 0.15 mL/min; 22 min, 100% A, 0.35 mL/min. The column temperature was maintained at 40 °C. MS analysis was performed using a Quattro-Micro triple quad MS (Waters, Milford, MA, USA) in negative ion mode using single ion monitoring for each compound and isotopologue. The source parameters were: desolvation gas flow 190 L/hr; cone gas flow 20 L/h; capillary voltage 2.7 V; source temperature 150 °C; desolvation temperature 390 °C; cone voltage 20 V.

2.3.3 Zic-cHILIC – quadrupole time-of-flight MS (Xevo-G2-XS)

Compounds were separated using a Zic-cHILIC (3 μm, 100 Å, 150 × 2.1 mm) column (Merck, Kenilworth, NJ, USA). The mobile phase solvent A was 20 mM ammonium acetate in water and solvent B was 100% acetonitrile (AcN). The flow rate was 0.4 mL/min and the gradient was: 0 min, 30% A; 1 min, 30% A; 10 min, 40% A; 10.5 min, 60% A; 15 min, 60% A; 15.5 min, 30% A; 19 min 30% A. The injection volume was 2 μL using partial loop injection in a 10 μL loop. The column temperature was maintained at 40 °C. MS analysis was performed using a Xevo-G2-XS (Waters, Milford, MA, USA) quadrupole time-of-flight (q-TOF) mass spectrometer in negative mode, scan range from 50 to 900. Source parameters were: desolvation gas flow 750 L/h; cone gas flow 50 L/hr; capillary voltage 2.5 V; source temperature 150 °C; desolvation temperature 300 °C; cone voltage 40 V; source offset 80 V.

2.4 INST-MFA of heterotrophic *Arabidopsis* cell cultures

2.4.1 Menadione treatment H_2-DCFDA ROS analysis

Liquid cell cultures were assayed by incubating 4-d-old cell suspension culture with 60 µM or 200 µM menadione or EtOH control for 6 h before adding 2.5 µM H_2-DCFDA. End point fluorescence was measured (excitation 504 nm, emission 529 nm) after 1.5 h. Background fluorescence was monitored using cells incubated without H_2-DCFDA and by measuring the fluorescence of the dye in the presence of menadione and MS media but without any cells.

2.4.2 [$^{13}C_6$]glucose labelling

Menadione dissolved in EtOH was added to 115 ml of 4-d-old heterotrophic *Arabidopsis* cell cultures to 60 µM (0.065% EtOH v/v) and incubated for 6 h in the dark. A cell sample was taken before the addition of labelled glucose. [$^{13}C_6$]glucose dissolved in MS media was added to give a ~60% proportion of labelled:unlabelled glucose and a final concentration of ~120 mM glucose. The precise amount of labelled glucose to add was calculated based on the media glucose concentration prior to labelling. Cells were incubated in the dark for 4 h and samples taken at 0, 0.5, 1, 2, 4, 8, 10, 15, 20, 30, 60, 120, 270 min using the DCM:EtOH extraction method (2.2.1). Care was taken to minimise light exposure by using minimal green lighting.

2.4.3 Mass isotopologue distribution measurement and natural abundance correction

LC-MS data was analysed using El-Maven software (Agrawal et al., 2019) and compounds identified using an in-house database of authentic standards (Walsby-Tickle et al., 2020). Mass isotopologue distributions (MIDs) were corrected for natural abundance of heavy isotopes using AccuCor (Su et al., 2017).

2.4.4 UDP-glucose deconvolution

The MID of UDP was deconvoluted from the MID of UDP-glucose using least squares fitting implemented in MATLAB (Appendix A.2).

2.4.5 Hierarchical clustering of atom enrichment

Hierarchical clustering analysis was performed on the fractional atom enrichment for each metabolite using the clustergram function in MATLAB. Fractional atom enrichment is the probability that any one carbon atom is isotopically labelled calculated using Equation 1. Where a_i is the fractional abundance of isotopologues containing i heavy isotopes and n is the total number of carbon atoms in the molecule.

$$\sum_{i=1}^{n} \frac{(a_i.\ i)}{n} \tag{1}$$

Equation 1. Fractional atom enrichment. a_i is the fractional abundance of isotopologues containing i heavy isotopes and n is the total number of carbon atoms in the molecule.

2.4.6 Model construction and flux estimation

Metabolic modelling was performed using the Isotopomer Network Compartmental Analysis software package (INCA v1.9, http://mfa.vueinnovations.com, Vanderbilt University) (Young, 2014) implemented in MATLAB 2019b. A network of carbon atom transitions was defined based on the model of central carbon metabolism of heterotrophic *Arabidopsis* cell cultures described in Masakapalli et al., 2014. The full model definition is in Appendix A.5. Pseudo fluxes were added to describe mixing of subcellular pools of metabolites upon extraction or mixing of pre-existing unlabelled pools of certain metabolites. Modelling inputs included isotopic labelling timecourses for 18 metabolites extracted at 0, 0.5, 1, 2, 4, 8, 10, 15, 20, 30, 60, 120, 270 min, biosynthetic output fluxes and the isotopic composition of the media. Mass isotopologue distributions were corrected for the presence of naturally abundant heavy isotopes using AccuCor (Su et al., 2017). Fluxes were estimated using a Levenberg-Marquardt optimization algorithm (Levenberg, 1944) to minimize the differences between the measured and simulated mass isotopologue distributions by minimising the sum of squared residual (SSR) which is weighted by the individual measurement variance (Young, 2014). The greater the SSR the worse the data fits the model, the smaller the SSR the better the model describes the data. A

fit is accepted if the SSR falls within a range defined by Equation 2 where (n-p) is the degrees of freedom (DOF):

$$\chi^2_{\alpha/2}(n-p), \chi^2_{1-\alpha/2}(n-p) \quad (2)$$

Equation 2. Chi-square test to determine if model fit should be accepted. If sum of squared residuals is with the bounds defined by the equation, then the fit is accepted. n is the number of independent measurements, p is the number of fitted parameters and α is the threshold p-value at which the fit is rejected.

Free parameters were iteratively updated to identify a best-fit solution. 32 random initial restarts were performed to identify a global best fit. The best fit was confirmed by parameter continuation (see 2.4.7 Flux map statistical analysis).

Consistent errors for each measured mass isotopologue at each timepoint within each experiment were determined by systematically varying the error and recalculating the SSR. Mol% errors were set to a minimum value for MIDs ≤ 0.5mol% and scaled linearly up to a maximum error for MIDs ≥ 25 mol% (Young, 2014). The maximum error was set 0.7 mol% larger than the minimum error. The scaling of errors for MIDs ≤ 25mol% is to avoid setting overly large errors on small isotopologue measurements.

2.4.7 Flux map statistical analysis

Two methods were used to estimate the precision of flux estimation, parameter continuation and Monte Carlo simulation. Parameter continuation was performed using the continuate function in INCA to generate 95% CI for each parameter. This function measures the sensitivity of the SSR to variation in each individual parameter (Antoniewicz et al., 2006). Any improvements in the best-fit solution identified during parameter continuation were retained in subsequent analyses. Monte Carlo simulation was also performed to determine parameter uncertainty and compare the probability distributions of parameter estimates between control and menadione treated cells. To perform Monte Carlo simulations, the best-fit set of parameters is used to generate multiple synthetic datasets which are perturbed by gaussian noise based on the measurement errors. Each synthetic dataset is then refitted to generate a set of optimal parameters. Repeating this process many times generates a probability distribution for each

parameter. 1000 rounds of Monte Carlo simulation were run using the 'montecarlo' function in INCA based on the method described by Press and Vetterling (1992) (Young, 2014).

Significant differences between parameters in control and menadione flux maps were calculated by comparing the 83.4% confidence intervals which is equivalent to a significance of P = 0.05, if variance between the two groups is equal (Austin and Hux, 2002; Knol et al., 2011). Comparing two means involves comparing two sources of variability in contrast to comparing a mean to a constant value where there is only once source of variability. Therefore, narrower confidence intervals must be evaluated to establish if there is a significant difference between two distributions. For any parameters with unequal variances the confidence intervals to compare for a 95% probability the model parameters are different, were calculated by Equation 3 (Knol et al., 2011).

$$\left[1 - 2 \times \Phi\left(-1.96 \times \frac{\sqrt{1+\rho^2}}{1+\rho}\right)\right] \times 100\% \tag{3}$$

Equation 3. Formula to calculate the confidence intervals to compare in order to establish a difference between two independent groups with a 95% confidence. ρ represents the ratio of standard deviations and Φ represents the standard normal cumulative distribution function. See Knol et al., 2011 for a full derivation of this equation.

The confidence intervals were calculated from Monte Carlo simulations by ranking the parameter estimates in ascending order and discarding appropriate number of values form the top and bottom. For example, the top and bottom 8.3% of values are discarded for an 83.4% confidence interval and the top and bottom 2.5% values for the 95% confidence interval.

Principle component analysis (PCA) and partial least squares discriminant analysis (PLSDA) were performed on 1000 Monte Carlo simulations for control and menadione treated cells using MetaboAnalyst, an online implementation of R for metabolomics (Chong et al., 2019; R Core Team, 2020). Free net fluxes were scaled by mean centring and dividing by the standard deviation and used as variables for PCA and PLSDA. Pool size estimates, exchange fluxes and pseudo fluxes describing the mixing of compartmented or metabolically inactive pools of metabolites were excluded from analysis. Principle component analysis was performed using the

prcomp package in R (R Core Team, 2020). Partial least squares-discriminant analysis (PLSDA) was performed using the pls package in R (Mevik and Wehrens, 2007). See Appendix A.8 for further details and validation of PLSDA.

2.4.8 High performance parallel computation

INST-MFA is computationally intensive and therefore parameter estimations, parameter continuation and Monte Carlo simulation were performed using a parallel processing cluster at the University of Oxford Advanced Research Computing (ARC) facility (Richards, 2015). Parallel jobs were submitted using the SLURM job scheduler. The parallel job submission script was modified from the implementation described in Xu et al., 2021.

2.5 Analysis of deuterium labelling

2.5.1 Simulating NADPH redox active hydride labelling

A MATLAB script was written to compute the effect of changing each parameter on the measured NADPH redox active hydride labelling. The script is based on a correction factor for the deuterium kinetic isotope effect (Equation 4) and the calculation of the relative contribution of a pathway to total NADPH production (Equation 5) based on (Fan et al., 2014; Zhang et al., 2017).

$$C_{KIE} = \frac{V_H}{V_D} + x\left(1 - \frac{V_H}{V_D}\right) \quad (4)$$

Equation 4. Correction factor for deuterium kinetic isotope effect. $^{V_H}/_{V_D}$ is the preference of the enzyme for hydrogen over deuterium. x is the substrate labelling fraction.

$$\text{Fraction}_{NADPH\ from\ oxPPP} = 2 \times \left(\frac{[^2H]\text{NADPH}}{\text{Total NADPH}}\right) \times \left(\frac{[^2H]\text{G6P}}{\text{Total G6P}}\right)^{-1} \times \left(1 - H_{exchange}\right)^{-1} \times C_{KIE} \quad (5)$$

Equation 5. Calculation of the contribution of the oxPPP to total NADPH production. Terms in brackets are the fractional labelling of NADPH redox active hydride, fractional labelling of G6P at C1 and the correction factor for water exchange of NADPH redox active hydride. C_{KIE} is the correction factor for the deuterium kinetic isotope effect.

2.5.2 Redox active hydride labelling

Calculation of NADPH redox active hydride labelling (Equation 6) was adapted from Fan et al., 2014.

Observed MID vector of $NADP^+$ from a labelled sample where a_N is the proportion of isotopologues containing N heavy isotopes:

$$NADP^+{}_{labelled} = \begin{bmatrix} M+0 \\ M+1 \\ M+2 \end{bmatrix} \equiv \begin{bmatrix} a_0 \\ a_1 \\ a_2 \end{bmatrix}$$

The observed MID vector of NADPH from the same labelled sample as $NADP^+{}_{labelled}$ described in terms of $NADP^+{}_{labelled}$ and the parameter x:

$$NADPH_{labelled} = \begin{bmatrix} M+0 \\ M+1 \\ M+2 \end{bmatrix} = \begin{bmatrix} a_0(1-x) \\ a_1(1-x) + a_0x \\ a_2(1-x) + a_1x \end{bmatrix} \cdot \frac{1}{1-(a_2x)} \quad (6)$$

Equation 6. The relationship between the observed MID of NADPH and NADP+ from the same sample. $M+N$ is the observed proportion of isotopologues containing N heavy isotopes. x is the fractional enrichment of the redox active hydride of NADPH.

2.5.3 *In vitro* oxPPP labelling

The reaction mix contained 20 mM NH_4HCO_3 (pH 8.0), 5 mM $MgCl_2$, 0.5 mM $NADP^+$, 0.5 mM ATP, 0.2 mM glucose (either unlabelled or [1-^{2}H] labelled glucose at 98% isotopic purity; Cambridge Isotope Laboratories, Andover, MA, USA), 0.5 U/mL hexokinase (*S. cerevisiae*), 0.5 U/mL glucose 6-phosphate dehydrogenase (*L. mesenteroides*), 0.5 U/mL 6-phosphogluconate dehydrogenase (*S. cerevisiae*) and 2.5 U/mL glutathione reductase (S. cerevisiae). Aliquots (200 µL) of reaction mix were incubated at room temperature for 4 h in a 96-well plate reader. Absorbance at 340 nm was monitored to ensure the reaction was complete. 200 µL of reaction mixture was then added to 800 µL of 4 °C quenching buffer (1:1 MeOH:AcN) centrifuged for 15 min at 20,000× g at 4 °C and the supernatant stored at −80 °C before analysis by LC-MS.

2.5.4 *In vitro* NADPH–water exchange by glutathione reductase

0.7 mM NADPH was incubated at room temperature in an aqueous reaction mixture containing 2.5 mM Tris-Cl (pH 7.6), 5 mM NaCl, 8.5 U/mL glutathione reductase and 75% D2O. After 40 min, 200 μL of reaction mixture was added to 800 μL of 4 °C quenching buffer (1:1 MeOH:AcN with or without 0.625% (v/v) formic acid) and incubated on dry ice for 20 min. Samples were then centrifuged for 15 min at 20,000× g at 4 °C and the supernatant placed in autosampler vials for immediate analysis by LC-MS.

2.5.5 *In vivo* D_2O labelling

Four-day-old heterotrophic *Arabidopsis* filter paper cultures were washed with liquid MS media containing 30 g/L glucose, 0.5 mg/L 1-naphthaleneacetic acid, and 0.05 mg/L kinetin and 45% D_2O. Cells were then either immediately extracted or transferred to MS agar plates containing 45% D_2O and extracted at 0.5, 1, 2 and 4 h post transfer to deuterated media.

2.5.6 *In vivo* [1-^{2}H]glucose labelling and 6-AN treatment

Four-day-old heterotrophic *Arabidopsis* filter paper cultures were transferred to MS agar plates with or without 10 mM 6-AN and incubated for 20 h before being transferred to MS agar plates containing 100% [1-^{2}H]glucose (30 g/L) (98% isotopic purity; Cambridge Isotope Laboratories, Andover, MA, USA) and 10 mM 6-AN. Cells were then incubated in the dark and metabolites extracted at 0.5, 1 and 2 h post transfer to deuterated media.

2.5.7 Proteomic analysis of cell extract

Four-day-old heterotrophic *Arabidopsis* filter paper cultures were extracted as described in section 2.2.2 and the MWCO filter concentrate was analysed via tryptic digest proteomics. Samples were reduced with 10 mM dithiothreitol (DTT) for 40 min at 56 °C before alkylation in 20 mM iodoacetamide (IAA) for 30 min in the dark at room temperature. Samples were reduced again with 3 uL of 85 mM DTT for 10 min in the dark at room temperature to eliminate excess IAA. Samples were then precipitated with six volumes of ice-cold acetone and incubated overnight at −20 °C before centrifugation at 15,000× g for 10 min at 4 °C. The pellet was dried in

air for no more than 5 min before resuspension in 50 mM ammonium bicarbonate. Trypsin was then added in a 1:50 (w/w) ratio of trypsin:sample protein and incubated overnight at 37 °C. A second trypsin digestion was performed with a 1:100 (w/w) ratio in 80% acetonitrile and incubated at 37 °C for three hours. The reaction was stopped by addition of 5% formic acid and the sample dried using a vacuum centrifuge. The peptides were resolubilised in 15 µL of 0.1% formic acid.

Resulting tryptic peptides were analysed on a NanoAcquity-UPLC system (Waters) connected to an Orbitrap Elite mass spectrometer (Thermo Fischer Scientific) possessing an EASY-Spray nano-electrospray ion source (Thermo Fischer Scientific). The peptides were trapped on an in-house packed guard column (75 µm i.d. × 20 mm, Acclaim PepMap C18, 3 µm, 100 Å) using solvent A (0.1% formic acid in water) at a pressure of 140 bar. The peptides were separated on an EASY-spray Acclaim PepMap® analytical column (75 µm i.d. × 50 mm, RSLC C18, 3 µm, 100 Å) using a linear gradient (length: 100 min, 3% to 60% solvent B (0.1% formic acid in acetonitrile), flow rate: 300 nL/min). The separated peptides were electrosprayed directly into the mass spectrometer operating in a data-dependent mode using a CID based method. Full scan MS spectra (scan range 350–1500 m/z, resolution 120,000, AGC target 1×10^6, maximum injection time 250 ms) and subsequent CID MS/MS spectra (AGC target 5×10^4, maximum injection time 100 ms) of the 10 most intense peaks were acquired in the Ion Trap. CID fragmentation was performed at 35% of normalized collision energy and the signal intensity threshold was kept at 500 counts. The CID method used performs beam-type CID fragmentation of the peptides.

Data analysis was performed with Peaks 8.5 (Bioinformatics Solutions Inc., Waterloo, ON, Canada) The raw MS file was searched against the respective protein sequence. Trypsin with a maximum number of 3 missed cleavages and one unspecific end was selected as the protease. Carbamidomethylation (cysteine), oxidation (methionine), deamination (asparagine, glutamine) were set as variable modifications. Precursor mass tolerance was set as 15 ppm and fragment mass tolerance for CID was set to 0.8 Da.

2.5.8 PaxDB quantitative proteome analysis

Data from PaxDB (Wang et al., 2015) was associated with data from Uniprot (Bateman et al., 2017) to identify the relative abundance of proteins that contain NADP(H) and FAD binding sites. PaxDB data for 37 *A. thaliana* and 40 *H. sapiens* cell line proteomes were downloaded from PaxDB as .csv files. PaxDB identifiers were matched to Uniprot accession numbers which were then used to download information about the proteins. Proteins which were associated with both "FAD" and "NADP" keywords were identified as being flavin enzymes, potentially capable of catalysing hydrogen exchange between NADPH and water. The relative abundance of these proteins was summed to give a total abundance of NADP-flavin enzymes in each proteome.

2.5.9 Compartmentation simulation

A linear model was created in MATLAB consisting of seven variable parameters: fractional amount of cytosolic G6P, 0.85 (Heise et al., 2015); fractional amount of cytosolic NADPH, 0.5 (Heineke et al., 1991; Igamberdiev and Gardeström, 2003); fractional NADPH production in the cytosol, 0.18 (Masakapalli et al., 2014); fraction of cytosolic NADPH production from oxPPP, 1.0 (Masakapalli et al., 2014); fraction of plastidic NADPH production from oxPPP, 0.9; fractional labelling of cytosolic G6P, 0.5; and fractional labelling of plastidic G6P, 0.4. Each parameter was varied between 0 and 1 whilst all other parameters were fixed. Note that plastidic G6P labelling fractions greater than cytosolic G6P labelling were omitted, as it was assumed all plastidic G6P is derived from cytosolic G6P.

2.6 Analysis of fluorescent biosensors

2.6.1 Confocal microscopy

Confocal laser scanning microscopy of 3- to 5-day old *Arabidopsis* seedlings was performed using a AXIO imager 2 upright microscope (Zeiss) with a LSM 880 laser scanning module (Zeiss) and a 40x water immersion objective. For iNap and SoNar imaging, fluorescence was measured from emission at 500-540 nm by sequential excitation at 405 nm and 488 nm with

an open pinhole at 2.39 airy units. Chlorophyl fluorescence was measured from emission at 627-700 nm by excitation at 488 nm. MitoTracker Orange fluorescence was recoded from emission at 566-611 nm by excitation at 561 nm.

MitoTracker Orange (ThermoFisher scientific) staining was performed according to the manufacturer's instructions. MitoTracker Orange dissolved in DMSO was diluted to 250 nM in half strength MS media, pH 5.8 (KOH) and seedlings incubated in this staining solution for 10 min. Seedlings were washed with half strength MS media pH 5.8 (KOH) before analysis by confocal microscopy.

2.6.2 Plate reader fluorescence assay

Fluorescence measurements were performed using a CLARIOstar microplate reader (BMG labtech). 5 mm disks of fully expanded rosette leaves of 4- to 6-week-old *Arabidopsis* were cut using a leaf punch (avoiding the mid-vein) and placed upside down in the bottom of 96 well plates containing 200 µl of assay buffer: 10mM MES, pH 5.8, 5 mM KCl, 10 mM $MgCl_2$, 10 mM $CaCl_2$. Fluorescence was monitored at the appropriate wavelengths for the particular sensor (Table 2.1) using top-optics, a focal height adjusted between 6 to 8 mm, and orbital averaging with 4 mm diameter and 70 microflashes per well. Leaf disks were incubated in the dark for a minimum of 1 h before treatments were added. Sample sizes in figure legends represent the total number of leaf disks in each condition. Within each experiment leaf disks were cut from at least two plants grown in identical conditions and distributed equally between different treatment and control groups.

Fluorescence of Col-0 *Arabidopsis* leaf disks was subtracted for each of the wavelengths for each biosensor. The ratio of background corrected data was then taken for each biosensor. For iNap1,2,4, and SoNar the $R_{420/482}$ was divided by the $R_{420/482}$ of identically treated iNapC leaf disks. Ratios are $\log_{10}$ transformed before plotting to restore symmetry to ratios above and below one.

Table 2.1. Fluorescent wavelengths used for biosensors.

	Fluorescent signal 1		**Fluorescent signal 2**	
	Excitation (nm)	**Emission (nm)**	**Excitation (nm)**	**Emission (nm)**
SoNar and iNap1,2,4,C	420 ± 15	520 ± 20	482 ± 8	520 ± 15
Peredox-mCherry	400 ± 8	530 ± 20	570 ± 10	610 ± 8
cpYFP	400 ± 8	530 ± 20	482 ± 8	530 ± 20
GRX1-roGFP2	400 ± 8	530 ± 20	482 ± 8	530 ± 20
ATeam	435 ± 10	485 ± 10	435 ± 10	540 ± 8

Chapter 3: Isotopically non-stationary metabolic flux analysis of heterotrophic *Arabidopsis* cell cultures

3.1 Introduction

3.1.1 ^{13}C flux analysis for quantifying redox metabolism

^{13}C metabolic flux analysis allows quantification of subcellular fluxes and can be used to estimate rates of redox coenzyme production and consumption (Fuhrer and Sauer, 2009; Masakapalli et al., 2010, 2013, 2014; Rühl et al., 2012a). For example, steady state MFA (SS-MFA) has shown that the oxidative pentose phosphate pathway (oxPPP) cannot supply sufficient reductant for biosynthesis in heterotrophic *Arabidopsis* cells and therefore other sources must make a significant contribution (Masakapalli et al., 2010). Furthermore, the oxPPP flux has been shown to vary independently of the reductant demand for biosynthesis (Masakapalli et al., 2013), consistent with the idea that it is not the sole source of NADPH. In both *Arabidopsis* and *S. cerevisiae* cell cultures, flux distributions are balanced in terms of NADPH supply and biosynthetic demand only if it is assumed that isocitrate dehydrogenase (IDH) generates NADPH rather than NADH (Masakapalli et al., 2010, 2013, 2014; Suarez-Mendez et al., 2016). Duplicate pathways and ambiguity in coenzyme specificity of certain enzymes *in vivo* can create uncertainty in this coenzyme balancing (Fuhrer and Sauer, 2009; Masakapalli et al., 2010, 2013, 2014; Suarez-Mendez et al., 2016). However, by examining which assumptions are necessary for metabolic supply to meet demand, the potential importance of different coenzyme sources can be quantified.

Previous studies in heterotrophic *Arabidopsis* cell cultures examined long term changes in nutrient composition such as phosphate limitation or variation in inorganic nitrogen supply (Masakapalli et al., 2013, 2014). However, demands for redox coenzymes could change much more rapidly or transiently in response to external stimuli such as pathogen infection, drought, flooding, or fluctuating light, and therefore it is important to understand how the metabolic network can meet these more transient and potentially larger demands on redox metabolism.

3.1.2 INST-MFA can quantify transient metabolic steady states

Most metabolic flux analysis in plant cell cultures has been based on steady state MFA in which metabolites reach an isotopic steady state before analysis. Such systems typically require days for protein derived amino acids to reach the required isotopic steady state (Masakapalli et al., 2010, 2013, 2014; Williams et al., 2008). A metabolic steady state must be maintained over this period and therefore SS-MFA is not suitable for studying more short lived metabolic steady states. Dynamic labelling experiments in which label incorporation is measured before achieving an isotopic steady state can quantify fluxes with shorter labelling timecourses. Kinetic flux profiling (KFP) and isotopically non-stationary-MFA (INST-MFA) are two techniques for quantifying fluxes from dynamic labelling data. KFP and INST-MFA both use a differential equation model to fit isotopic labelling data to metabolic fluxes. KFP fits the decay of the unlabelled fraction (M0) and the subcellular metabolite concentrations, without accounting for the higher mass isotopologues (M1, M2, etc.) (Heise et al., 2015; Szecowka et al., 2013; Yuan et al., 2008). INST-MFA makes use of the full mass isotopologue distribution of each metabolite and can therefore quantify fluxes based on atom rearrangement and labelling patterns as well as the rates of label incorporation (Wiechert and Nöh, 2005). The additional labelling information used in INST-MFA improves flux resolution and removes the requirement for measurement of metabolite concentrations to deduce fluxes (Adebiyi et al., 2015; Ma et al., 2014; Xu et al., 2021; Young et al., 2011) and therefore INST-MFA is a more informative technique than KFP.

INST-MFA has been applied to study photosynthetic metabolism in the leaves of *Arabidopsis* and *Camelina sativa* as well as cyanobacteria (Adebiyi et al., 2015; Jazmin et al., 2017; Ma et al., 2014; Xu et al., 2021). INST-MFA has not yet been applied to heterotrophic plant cell cultures. Compared to INST-MFA in leaves, flux analysis in cell cultures has several advantages as cells can be easily and rapidly extracted, and labelled substrates and chemical treatments can be easily applied in a controlled manner. A prerequisite for both SS-MFA and INST-MFA is a homogenous population of cells that have identical flux phenotypes, because isotopically labelled metabolites from individual cells are mixed during extraction. Compared to

mature leaves cell cultures are likely to be more homogenous but it is possible that flux distributions may differ between individual cells in a population depending on their age, cell cycle stage or if undergoing autophagy. The potential impact of cell type heterogeneity on INST-MFA of leaves has not yet been thoroughly explored and therefore cell cultures may offer a more tractable experimental system for evaluating INST-MFA as a tool for quantifying redox metabolism, compared to intact plants or leaves.

Compared to SS-MFA, INST-MFA requires substantially greater experimental and computational effort and therefore consideration of optimal experimental design is important (Nöh and Wiechert, 2006; Nöh et al., 2006; Wiechert and Nöh, 2005). Experimentally, metabolism must be quenched, and metabolites extracted over short timescales (30 s), with sufficient measurements to capture labelling dynamics before isotopic steady state is reached. Computational optimisation of sampling times and labelled substrates is possible but requires prior knowledge of fluxes and metabolite concentrations which is not always available for the system being studied. Rapid metabolic quenching is vital for measuring labelling of central carbon intermediates as their half-lives are typically <60 s and often considerably shorter (Arrivault et al., 2009). This is less of an issue for SS-MFA in which proteogenic amino acids are analysed which have much slower turnover times. INST-MFA of photoautotrophic cyanobacteria has made use of quenching in cold buffer and centrifugation to separate cells from the media (Jazmin et al., 2017). Care must be taken to ensure there is no metabolite leakage during quenching and therefore rapid filtration is another possible method (Krall et al., 2009)

The computational requirements for INST-MFA are greater than SS-MFA. INST-MFA adds a time component to data and therefore a system of ordinary differential equations must be solved in comparison to the linear equations of SS-MFA. The model size and number of measurements affect the time taken to optimise the flux solution. Therefore, INST-MFA is not applicable to genome scale models and certain model simplifications and assumptions are necessary to reduce the size of the model. Estimation of parameter uncertainties can be performed in parallel and therefore high-performance computing with access to many compute nodes can

greatly increase the speed of analyses. Despite the additional effort, INST-MFA is theoretically feasible in heterotrophic *Arabidopsis* cell cultures and is ultimately necessary for analysing metabolic steady states which cannot be maintained for days.

3.1.3 Menadione increases reductant demand

To perturb the metabolic network and identify changes in redox metabolism associated with increased demand for reductant, menadione has proven to be an effective treatment in plants (Baxter et al., 2007a; Lehmann et al., 2009; Schwarzländer et al., 2009; Sweetlove et al., 2002). Menadione is a redox active quinone which can be metabolised by flavoenzymes including mitochondrial NADH: ubiquinone reductase, ubiquinol: cytochrome c reductase and microsomal NADPH-cytochrome P-450 reductase (Thor et al., 1982) (Figure 3.1). Metabolism of menadione generates intracellular superoxide radicals and increases metabolic demand for NADPH both directly, and through subsequent detoxification of ROS (Figure 3.1) (Baxter et al., 2007a; Sweetlove et al., 2002; Thor et al., 1982). Previous work in heterotrophic *Arabidopsis* cell cultures treated with 60 µM menadione identified metabolomic, transcriptomic and ^{13}C labelling changes (Baxter et al., 2007a). Changes observed were consistent with inhibition of the TCA cycle enzymes, aconitase, pyruvate dehydrogenase and 2-oxoglutarate dehydrogenase which are known to be affected by oxidative damage (Baxter et al., 2007a; Millar and Leaver, 2000; Verniquet et al., 1991). An increase in the concentration, and rate of ^{13}C label incorporation into gluconate (presumed to be derived from 6PG) was also observed following menadione treatment, suggesting an increase in flux through the oxPPP. However, although qualitative interpretations could be made about likely changes in flux, precise quantification of fluxes was not attempted and therefore the relative contributions of different pathways to maintaining NADPH supply could not be determined.

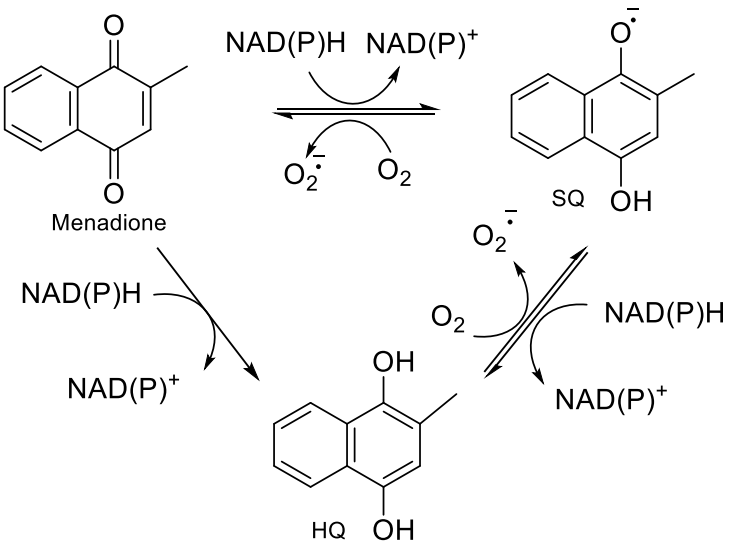

Figure 3.1. Mechanism of NADPH consumption and superoxide radical formation by menadione. SQ - semiquinone, HQ-hydroquinone. Adapted from *(Thor et al., 1982)*.

The aim of this chapter is to quantify how the plant metabolic network responds to increased NADPH demand. To achieve this, I optimised a metabolite extraction method for quantifying central carbon metabolites over the short timecourses required for INST-MFA. Menadione treatment was used to increase the demand for NADPH and isotopic labelling using [$^{13}C_6$]glucose was performed. Data was fitted to a model of central carbon metabolism and differences in the flux phenotype between control and menadione treated cells identified. The resulting flux maps were used to explore the effect of menadione treatment on coenzyme turnover.

3.2 Results

3.2.1 Optimised metabolite extraction for central carbon intermediates

INST-MFA requires quantification of mass isotopologue distributions (MIDs) of central carbon metabolites at defined time points following the supply of a labelled substrate to the cells. Inaccuracies in measurement of MIDs can lead to poorly resolved fluxes, particularly for low abundance isotopologues (Mairinger et al., 2018). Increasing the concentration of metabolites in samples used for analysis can improve the accuracy of MID measurement and therefore the extraction method used for subsequent analysis was optimised. Low pH extraction can help to quench metabolism by inhibiting enzymatic activity, liberate bound metabolites from proteins and prevent chemical degradation of some compounds (Gil et al., 2015). Therefore, a low pH (<2.5) biphasic extraction using dichloromethane (DCM) and ethanol (EtOH) was compared to extraction using 80% MeOH without any pH adjustment. To establish if cell disruption by bead milling improved metabolite extraction from plant cell cultures, the effect of homogenisation with glass and metal beads was also tested.

DNA concentration can be used as an approximate indicator of cell lysis, and therefore to establish the effect of extraction method on cell lysis, DNA concentration was measured using

absorbance at 260 nm (Figure 3.2A).

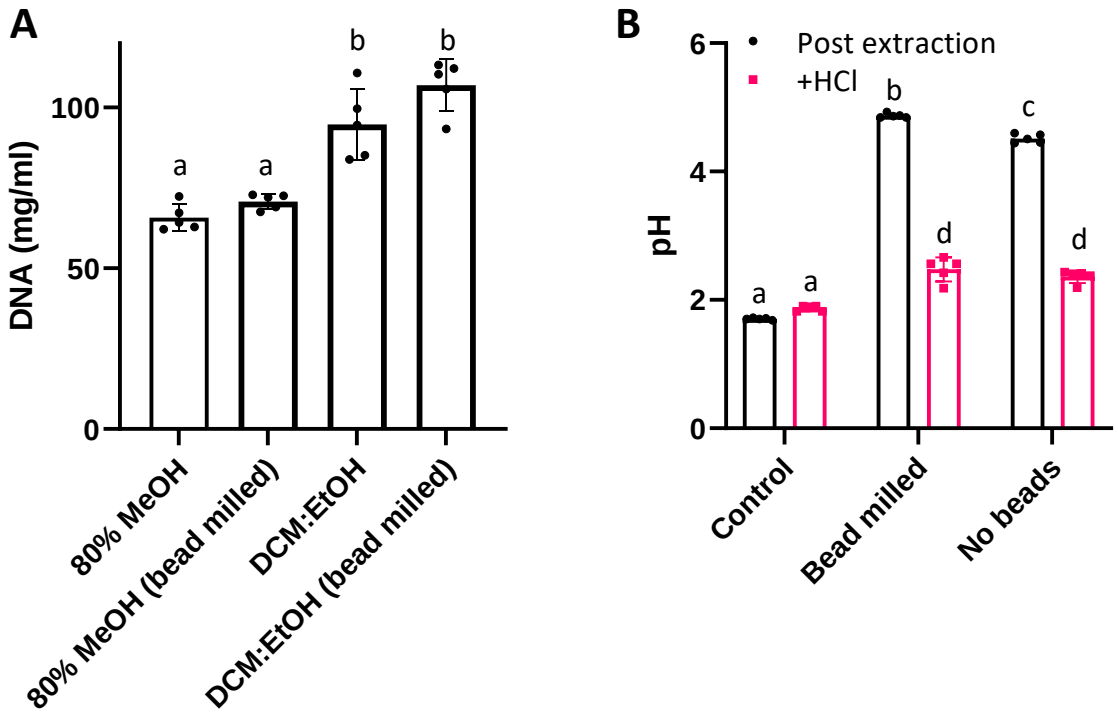

Figure 3.2. Comparison of metabolite extraction methods. A) The effect of extraction method on DNA concentration in extracts of *Arabidopsis* cell cultures. DNA concentration was measured by absorbance at 260 nm. B) The pH of metabolite extracts from DCM:EtOH extraction method both immediately after extraction (black bars) and after addition of 125 µl 60 mM HCl (pink bars). 125 µl of water was added to control samples in place of HCl. Different letters indicate significant differences, one-way ANOVA followed by Tukey test $P < 0.05$. Values are the mean ± SD n = 5.

Figure 3.2A shows DCM:EtOH extraction resulted in a significantly higher DNA concentration compared to 80% MeOH extraction. Bead milling did not cause a significant increase in DNA concentration in either extraction method, suggesting cells are sufficiently lysed using organic solvent alone.

Extraction with DCM:EtOH and HCl lowers the pH of the sample but the extracted cell contents can have buffering capacity and therefore additional HCl can be added to the extract to decrease the pH to < 2.5. To quantify the change in pH after extraction and addition of a further 125 µl of 60 mM HCl the pH was measured using a pH probe (Figure 3.2B). The plant cell extract increased the pH of the extraction solvent from pH 1.7, before addition of plant cells, to

pH 4.8 immediately after extraction (Figure 3.2B). Addition of 125 µl of 60 mM HCl was required to decrease the pH back to <2.5. Bead milling caused a slightly larger increase in pH immediately following extraction. Figure 3.2B shows the plant cell extract contains considerable buffer capacity, necessitating addition of HCl after the initial extraction to maintain a low pH in the extracted sample. Reliable pH measurement of 80% MeOH samples could not be made due to the high organic solvent content of the sample.

To identify which extraction method produced the highest concentration of metabolites for subsequent analysis of mass isotopologue distributions, ion-chromatography-mass spectrometry (IC-MS) was used to quantify the relative abundance of compounds of interest (Figure 3.3).

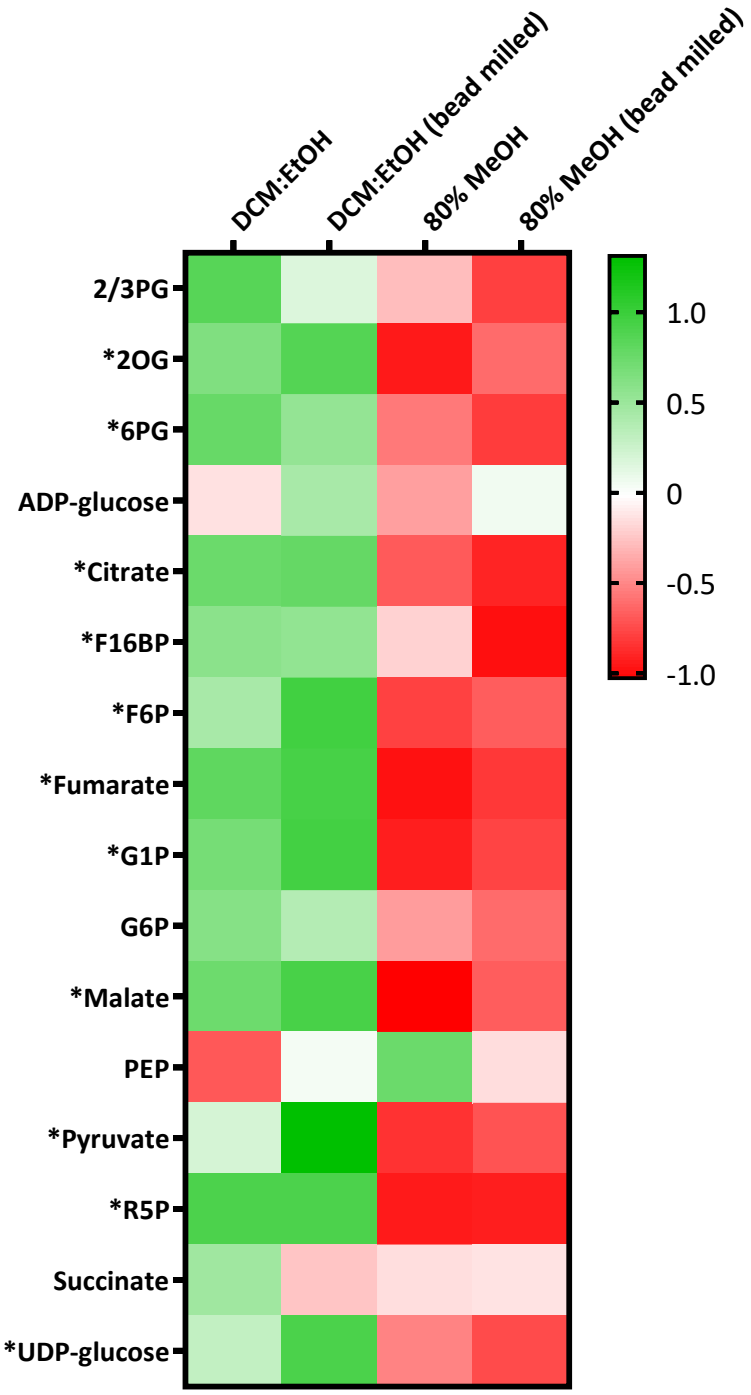

Figure 3.3. The effect of extraction method on metabolite concentration of central carbon metabolites extracted from heterotrophic *Arabidopsis* cell cultures. Cell cultures were extracted using DCM:EtOH + HCl or 80% MeOH extraction methods with or without bead milling. Peak areas for each metabolite were scaled by mean centring and dividing by their standard deviation, n = 5. * indicates a significant difference between extraction methods, ANOVA, $P < 0.05$.

Figure 3.3 shows DCM:EtOH extraction produced significantly larger or equivalent peak areas compared to 80% MeOH extraction for all compounds of interest. Bead milling had a minor

effect on metabolite extraction compared to the choice of extraction solvent. Subsequent analysis used DCM:EtOH extraction due to the improved peak area and metabolite recovery. Raw peak area and recovery data for individual metabolites are presented in Appendix A.1.

3.2.2 Menadione treatment induced oxidative load

To increase the metabolic demand for NADPH, cell cultures were treated with menadione. To confirm menadione treatment induced an oxidative load without exceeding the ROS detoxifying capacity of *Arabidopsis* cell cultures, cells were incubated with 60 µM or 200 µM menadione for 6 h and ROS production quantified using H_2-DCFDA, a dye which becomes fluorescent when deacetylated by intracellular esterases and oxidised by various ROS (Gomes et al., 2005) (Figure 3.4).

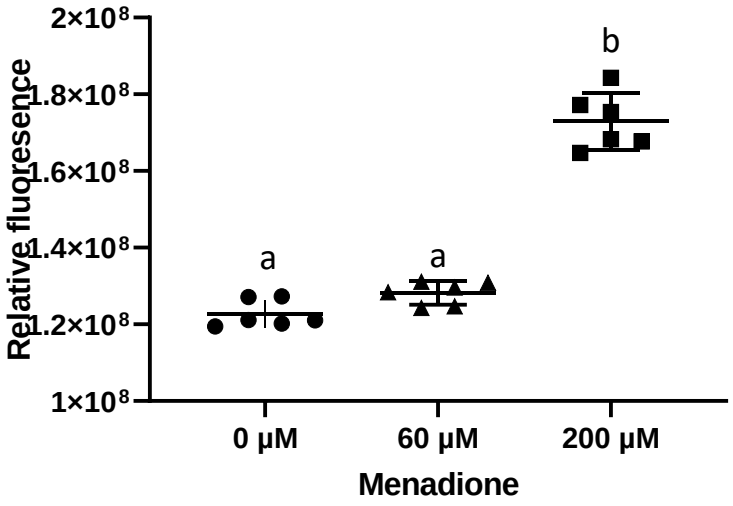

Figure 3.4. Effect of menadione on ROS production in 4-d-old heterotrophic *Arabidopsis* cell cultures quantified by H_2-DCFDA fluorescence. Cells were incubated with menadione for 6 h prior to measurement. Values are the mean ± SD, n = 6. Different letters represent a significant difference, one-way ANOVA followed by Tukey test $P < 0.05$.

Incubation of cell cultures with 200 µM menadione for 6 h caused a significant increase in H_2-DCFDA fluorescence (Figure 3.4). 60 µM menadione did not cause a significant increase in H_2-DCFDA fluorescence compared to an EtOH treated control, suggesting that although menadione induced increased ROS production, the cellular ROS detoxifying systems were not overwhelmed. Previous analyses of heterotrophic *Arabidopsis* cell cultures treated with 60 µM

menadione identified a decrease in aconitase activity, which is sensitive to oxidative damage (Verniquet et al., 1991), as well as metabolomic and transcriptomic changes consistent with an increased oxidative load (Baxter et al., 2007a). Subsequent analysis used 60 µM menadione to increase the cellular NADPH demand without exceeding the capacity of the metabolic network to remove reactive oxygen species and for consistency with previous analysis of heterotrophic *Arabidopsis* cell cultures (Baxter et al., 2007a).

3.2.3 [$^{13}C_6$]glucose labelling

To introduce isotopic label to the cell cultures for subsequent flux analysis, a bolus of [$^{13}C_6$]glucose was added to the growth media after 6 h treatment with 60 µM menadione or to untreated control cells. The proportion of labelled glucose in the media was confirmed by LC-MS of media samples taken during the labelling timecourse Table 3.1.

Table 3.1. Proportion of [$^{13}C_6$]glucose in media measured by LC-MS of media samples taken from heterotrophic *Arabidopsis* cell cultures after addition of [$^{13}C_6$]glucose.

	%[$^{13}C_6$]glucose in media	
Replicate	**Control**	**Menadione**
A	62.5	59.8
B	62.8	60.6
C	65.3	66.1

Table 3.1 shows there was variation in the proportion of labelled glucose in the media between biological replicates. This can be accurately accounted for during flux analysis by defining the proportion of labelled substrate in each replicate.

The incorporation of ^{13}C into metabolites was quantified using ion chromatography mass spectrometry (IC-MS). Average isotopic enrichment was calculated, corrected for the natural abundance of heavy isotopes and normalised to the proportion of labelled glucose in the media. To identify closely associated metabolites and visualise the labelling data, hierarchical clustering was performed on the average isotopic enrichments for each metabolite (Figure 3.5).

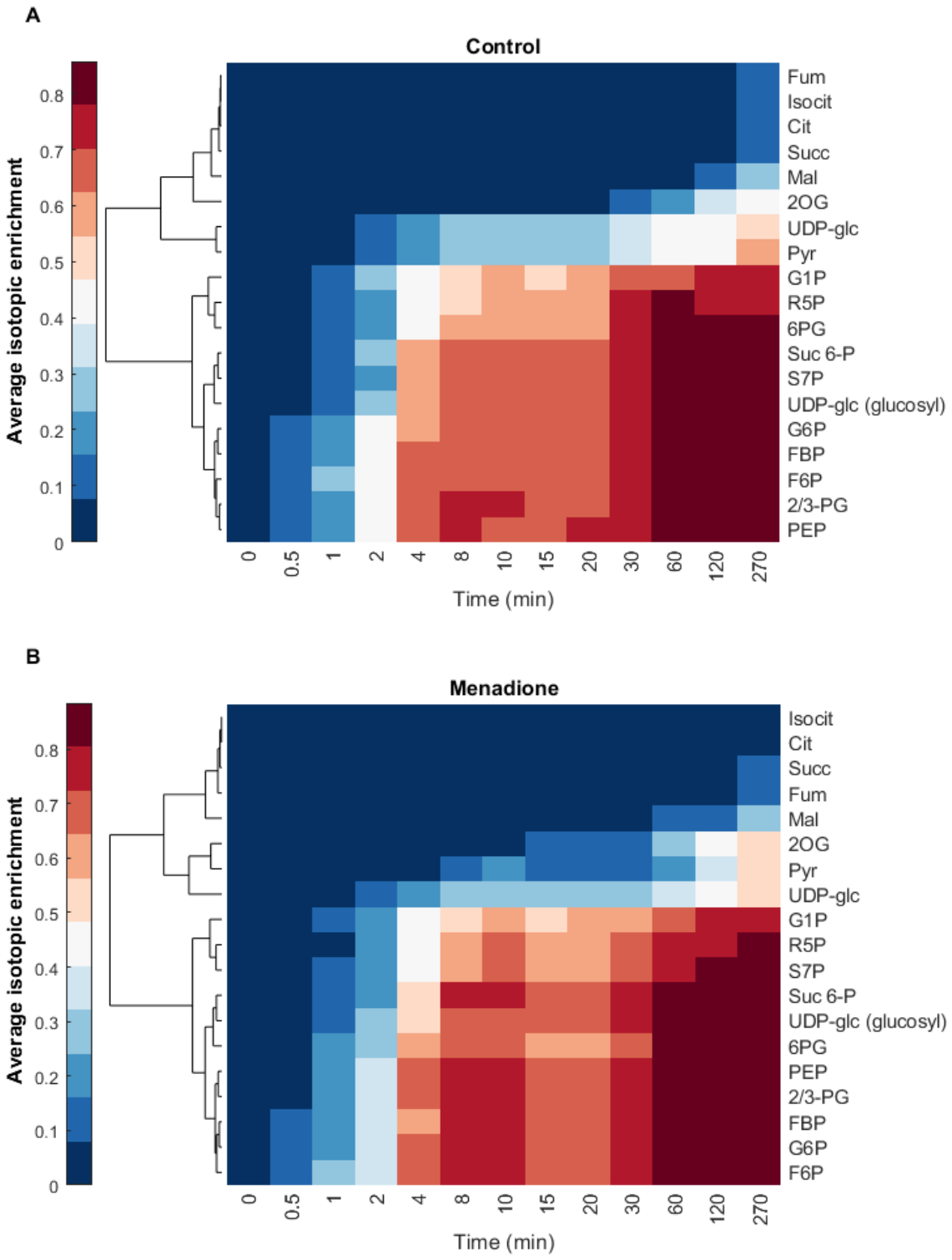

Figure 3.5. Hierarchical clustering of average isotopic enrichment in central carbon metabolites extracted from 4-d-old heterotrophic *Arabidopsis* cell cultures following supply of [$^{13}C_6$]glucose. A) Control cells. B) Cells treated with 60 µM menadione for 6 h before addition of [$^{13}C_6$]glucose. Values are corrected for the abundance of [$^{13}C_6$]glucose in the media and are the mean of three replicates.

Figure 3.5 shows similar clustering of metabolite labelling timecourses in control and menadione treated cells. Glycolytic intermediates are labelled fastest followed by the pentose phosphate pathway and starch/sucrose synthesis intermediates with TCA intermediates labelled the slowest (Figure 3.5). Average isotopic enrichment does not reach the isotopic enrichment of the media for any metabolite, suggesting the presence of either pre-existing unlabelled and metabolically inactive pools of metabolites, or an input of unlabelled carbon from an internal source such as vacuolar sugars. To accommodate these possibilities, an unlabelled input of glucose, and unlabelled metabolically inactive pools of highly abundant organic acids, were incorporated into the flux models used for subsequent analysis (see Appendix A.5 for full model definition). In both control and menadione treated cells a small fluctuation in the average isotopic enrichment occurred between 4-15 minutes in the more rapidly labelled metabolites, with isotopic enrichment increasing and then decreasing slightly (Figure 3.5). This effect is more pronounced in the menadione treated cells (Figure 3.5B).

The average isotopic enrichment showed metabolites incorporated label over time and clustered in expected groups, but further information about the underlying fluxes is contained in the individual mass isotopologue distributions of each metabolites (Figure 3.6-8, Appendix A.3). Overall, the time-courses of changes in MIDs for individual metabolites were similar for menadione-treated and untreated cell cultures (Figure 3.6-8).

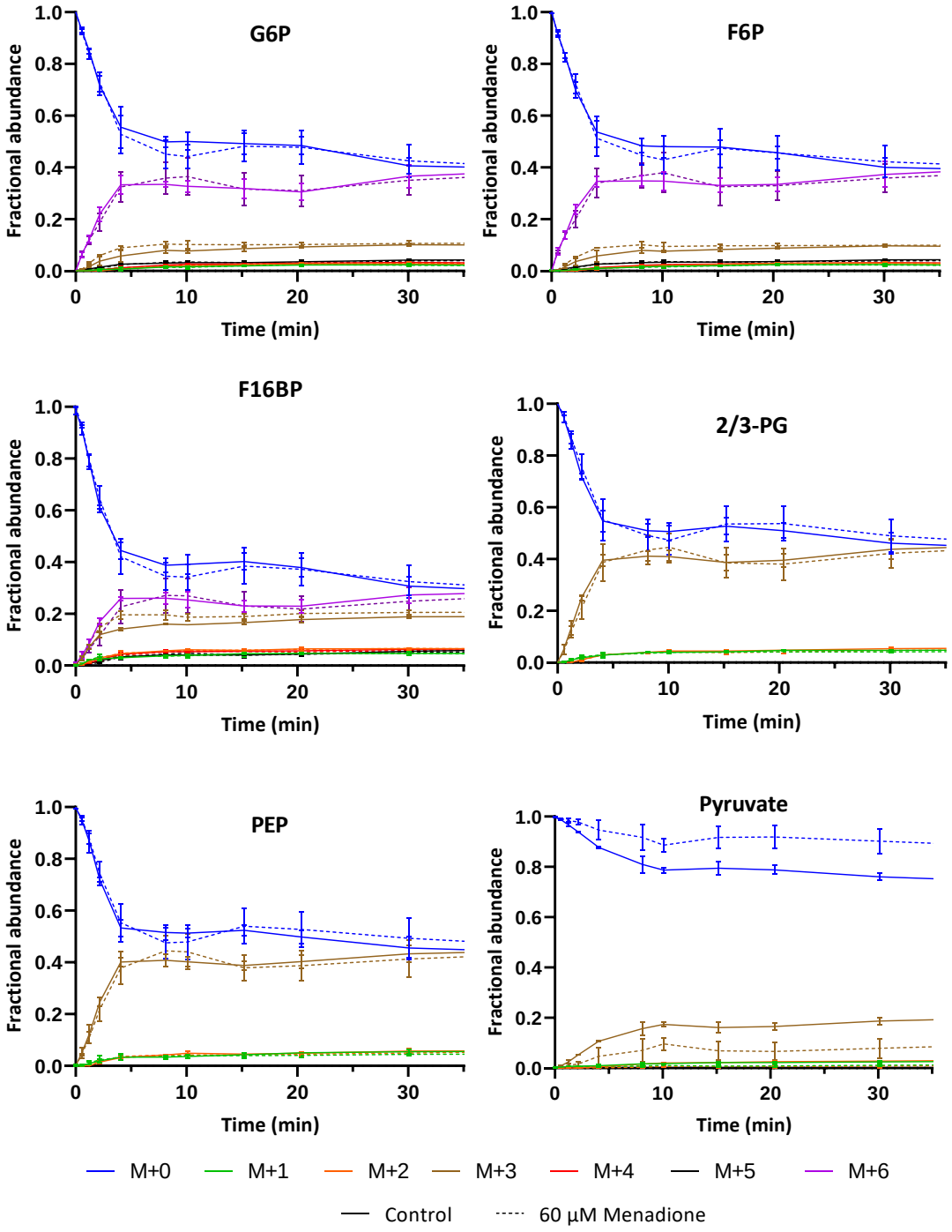

Figure 3.6. Mass isotopologue distributions of glycolytic intermediates after supply of [$^{13}C_6$]glucose to heterotrophic *Arabidopsis* cell cultures following 6 h treatment with 60 µM menadione. MID's are corrected for natural abundance of heavy isotopes. Values are the mean ± SD n = 3.

Figure 3.6 shows M+6 and M+3 isotopologues dominated glycolytic intermediates as fully labelled hexose phosphates were mixed with unlabelled triose phosphates at FBPase. M+3 G6P and F6P were identified after 30 s of labelling indicating substantial exchange flux between

triose- and hexose- phosphates. M+5 G6P and F6P were identified after 30 s which could be derived from carbon rearrangements in the non-oxidative section of the pentose phosphate pathway. M+1 and M+2 isotopologues were also present after 1 min in all intermediates. Pyruvate was labelled much more slowly than upper glycolytic intermediates suggesting either a large relative pool size or input into pyruvate from other sources such as malate which was labelled more slowly than PEP (Figure 3.7). M+1 pyruvate was present after 30s in both control and menadione treated samples, probably partially derived from M+1 PEP. M+2 pyruvate was only detected after 2 minutes, likely derived from malate which has been formed via the TCA cycle. Menadione treatment caused pyruvate to be labelled more slowly across all isotopologues. This may be caused by an increased pyruvate concentration and/or an increased flux into pyruvate from malate relative to PEP.

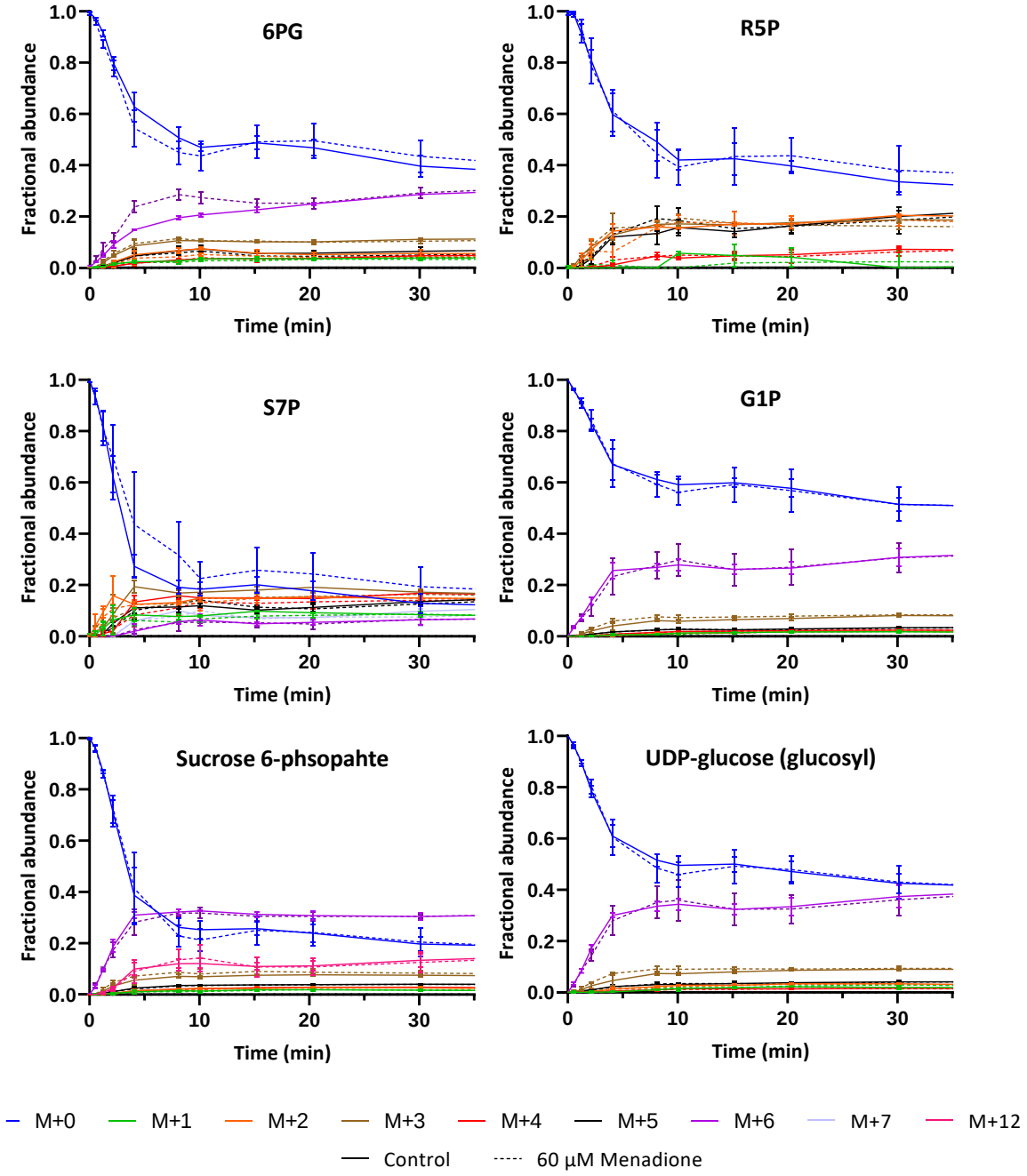

Figure 3.7. Mass isotopologue distributions of pentose phosphate pathway and starch/sucrose biosynthesis intermediates following supply of [$^{13}C_6$]glucose to heterotrophic *Arabidopsis* cell cultures following 6 h treatment with 60 µM menadione. MID's are corrected for natural abundance. Values are the mean ± SD n = 3.

Label incorporation into 6PG was similar to its precursor, G6P, but with the proportion of M+1, M+2, M+4 and M+5 isotopologues increasing more rapidly and to a larger extent in 6PG (Figure 3.7). Separate subcellular pools of G6P and 6PG and duplication of G6PDH in the plastid and cytosol may explain these differences. Menadione treatment caused faster increase in the

proportion of M+6 6PG, suggesting a larger oxPPP flux caused by the increased demand for NADPH. R5P was labelled in similar proportions in M+2, M+3 and M+5 isotopologues. M+5 and M+3 R5P likely comes directly from hexose phosphates via the oxPPP. M+3 R5P could also be derived from triose phosphates in the non-oxidative PPP. After two minutes all possible isotopologues of S7P were identified which could be derived from the non-oxidative PPP and scrambling between pentose and triose phosphates. G1P is derived from G6P and involved in cytosolic sucrose synthesis and plastidic starch synthesis. The proportion of M+6 and M+3 G1P increased at a similar rate to G6P although to a lesser extent, possibly due to an input of unlabelled G1P from an existing pool of unlabelled starch or sucrose. UDP-glucose and sucrose 6-phosphate are precursors of sucrose synthesis specifically in the cytosol. Labelling of UDP was deconvoluted from UDP-glucose labelling to reveal the labelling specifically in the glucosyl moiety (Appendix A.2). The labelling pattern of the glucosyl moiety of UDP-glycose closely resembled G6P with the major contribution from M+3 and M+6 isotopologues. Differences in G1P and UDP-glucose labelling may derive from separate plastidic and cytosolic G1P pools. M+6 and M+12 were the major labelled isotopologues of sucrose 6-phosphate which are derived from the combination of M+6 hexose phosphate precursors. The initial rate and pattern of labelling in sucrose 6-phosphate was similar to its precursors F6P and UDP-glucose.

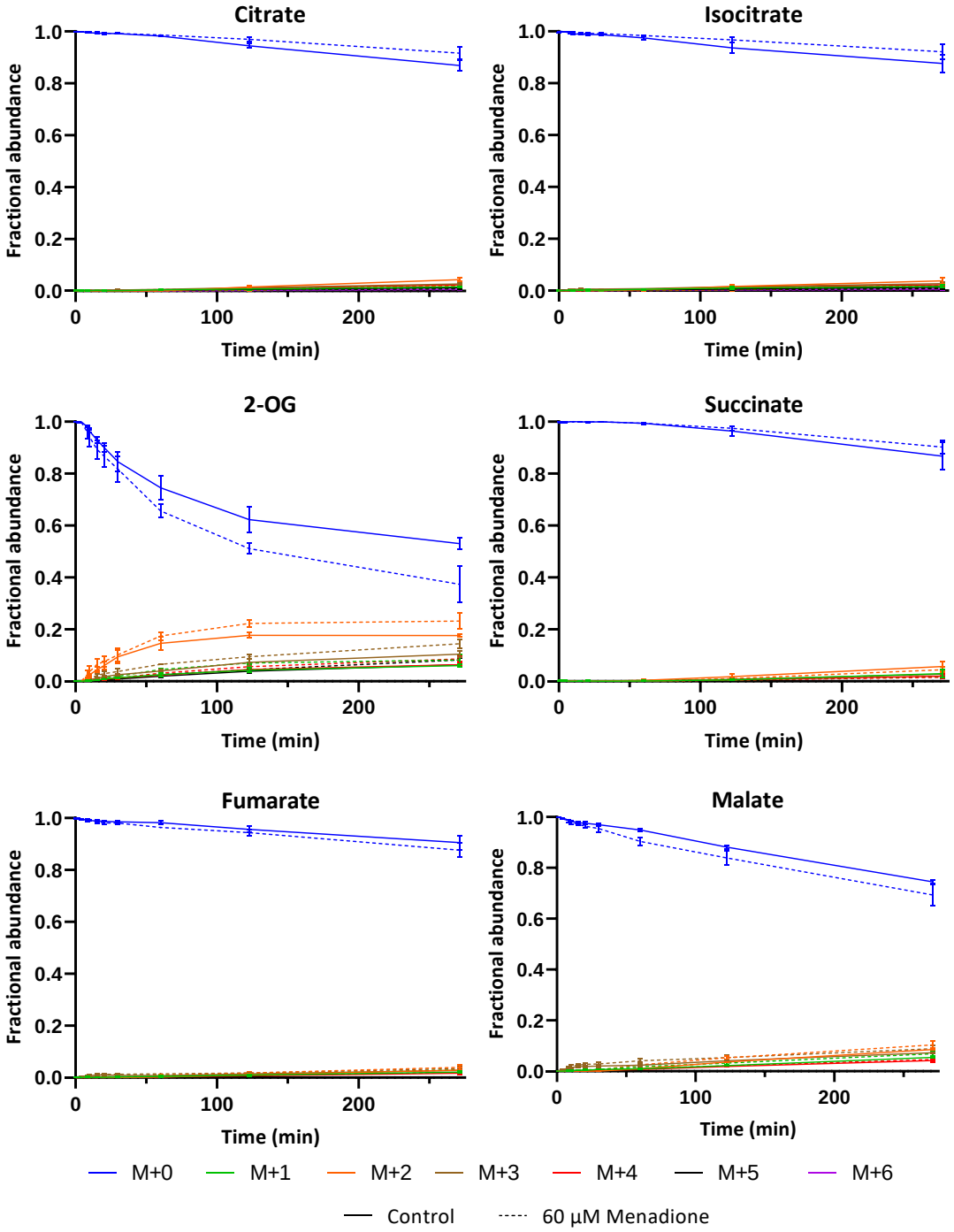

Figure 3.8. Mass isotopologue distributions of TCA cycle intermediates following supply of [$^{13}C_6$]glucose to heterotrophic *Arabidopsis* cell cultures following 6 h treatment with 60 µM menadione. MID's are corrected for natural abundance. Values are the mean ± SD n = 3.

M+3 and M+2 were the predominant labelled isotopologues in TCA intermediates (Figure 3.8). M+3 labelling is likely derived from OAA formed from M+3 labelled PEP by PEP-carboxylase (PEPC). The major labelled isotopologue of malate, fumarate, citrate and isocitrate

was initially M+3 before M+2 labelling begins to make up an increasing proportion after 30-60 min. M+2 isotopologues are derived from M+2 acetyl CoA resulting from M+3 pyruvate entering the TCA cycle. 2OG was labelled faster than its precursor, isocitrate, suggesting multiple separate pools of isocitrate are present that are not in equilibrium with the isocitrate that 2OG is formed from. Vacuolar stores of TCA intermediates could explain the observed labelling pattern. M+2 was the major form of labelled 2OG, probably derived from mitochondrial M+2 isocitrate. Menadione treatment increased the rate and extent of label incorporation into 2OG. Inhibition of aconitase by ROS induced by menadione treatment may lead to a decrease in flux from citrate to isocitrate to 2OG, causing a decrease in 2OG concentration and subsequently faster increase in the proportion of labelled 2OG. Analysis of 2OG abundance from the relative total peak area summed across all mass isotopologues was consistent with this, showing lower levels of 2OG in menadione treated cells (Appendix A.4). Labelling in succinate was predominantly M+2, likely from TCA cycle flux from 2OG. No initial M+3 labelling was observed in succinate unlike other TCA cycle intermediates.

3.2.4 INST-MFA model construction

Estimation of subcellular fluxes using INST-MFA requires an accurate model of carbon atom transitions that can be sufficiently constrained by the available measurements to quantify fluxes of interest. A model of core carbon metabolism was constructed building on previous SS-MFA of identical heterotrophic *Arabidopsis* cell cultures (Masakapalli et al., 2014) (Appendix A.5). The model consisted of glycolysis, pentose phosphate pathway, anaplerosis, TCA cycle, and biomass synthesis pathways for starch, sucrose, cell wall, and amino acids. Inclusion of these major pathways was supported from qualitative analyses of the isotopic labelling patterns (Figure 3.6-8) and hierarchical clustering of time-courses (Figure 3.5). Model inputs included labelled glucose from the media as well as an input of unlabelled glucose assumed to be derived from vacuolar sugars. This was necessary to explain the difference between average isotopic enrichment in the media and in metabolites that reached an isotopic steady state after 1 h (Figure

3.5). An unlabelled input of CO_2 was also included in the model to account for mixing between cellular and atmospheric CO_2 (Masakapalli et al., 2013, 2014).

Subcellular compartmentation included the cytosol, mitochondria, and plastid. Some metabolites were assigned to specific compartments such as glycolytic and pentose phosphate pathway intermediates. Analyses of metabolites such as UDP-glucose, which is exclusively cytosolic (Szecowka et al., 2013), can provide compartment specific information and constrain compartmented fluxes. The oxidative PPP (oxPPP) was duplicated in the cytosol and plastids whereas the non-oxidative steps were exclusively localised to the plastid, consistent with previous SS-MFA and biochemical evidence (Kruger and von Schaewen, 2003; Masakapalli et al., 2010). Transketolase and transaldolase from the non-oxidative pentose phosphate pathway were described as half reactions to account for their enzyme reaction mechanisms and lack of specificity (Kruger and von Schaewen, 2003; Masakapalli et al., 2010). In contrast, some metabolites and reactions were not assigned to specific compartments due to an inability to quantify compartment specific labelling data which can cause a lack of flux determinability. Reactions such as those catalysed by malate dehydrogenase and isocitrate dehydrogenase were grouped into single reactions despite the existence of separate compartment specific isozymes, in order to increase flux determinability at the expense of compartment specific information (Masakapalli et al., 2010, 2013, 2014; Williams et al., 2008).

To minimise the computational requirement and increase the indefinability of fluxes, further model simplifications and omissions were made. Calvin cycle and photorespiratory reactions were excluded as *Arabidopsis* cell cultures were maintained in darkness. Reactions which carry relatively small fluxes were also excluded such as secondary metabolism and nucleic acid synthesis (Rontein et al., 2002). Some reactions were omitted as they could not be defined from the available labelling data such as the GABA shunt, which produces identical labelling patterns to the conversion of 2-OG to succinate via the TCA cycle. Sucrose cycling was also omitted due to inability to separately quantify cytosolic and vacuolar sugars (Kruger et al., 2007).

Compared to the previous SS-MFA model several additional features were required for INST-MFA. To accommodate the measurement of additional metabolic intermediates metabolites were added to linear pathways such as PEP, 2/3PG, Ru5P and isocitrate. Instantaneous mixing reactions were included to account for the subcellular mixing which occurs during metabolite extraction. Dilution reactions were also added for organic acids such as fumarate, citrate, and malate which are present as large unlabelled pools in the vacuole (Ohnishi et al., 2018; Szecowka et al., 2013), consistent with the slower labelling rates observed (Figure 3.5,Figure 3.8).

Output fluxes were defined from Masakapalli et al., (2014) based on [U-^{14}C]glucose labelling and biomass composition analyses and fitted as individual measurements with associated experimental errors (Appendix A.6. Table A.3). Identical output fluxes were used for both control and menadione treated cells based on the fact that 60 µM induced only a mild oxidative load (Figure 3.4) and due to the difficulty in quantifying biomass outputs fluxes during the relatively short lived metabolic steady state following menadione treatment.

3.2.5 Flux estimation

To determine fluxes in central carbon metabolism the free flux and pool size parameters were iteratively fitted to the [$^{13}C_6$]glucose labelling timecourses and biomass output fluxes. The model was simultaneously fitted to data from three biological replicates for each condition. Preliminary analysis was unable to achieve a statistically acceptable fit between the model and the data and therefore factors affecting model fitting were explored including cell heterogeneity and isotopologue measurement uncertainties.

It was observed that the heterotrophic *Arabidopsis* cells clumped together (Figure 3.9). To explore the potential impact of this on flux estimation by INST-MFA, the time-course of labelled substrate uptake measured from samples of a heterogeneous cell cultures was modelled Figure 3.10A) and the simulated data used for flux estimation (Figure 3.10B).

Figure 3.10A shows the exponential decay in the unlabelled fraction of a labelled substrate imported into cells form the media. Clumping of cells may result in a delay in the time taken for the labelled substrate to reach cells in the centre of the clump. The resulting labelling

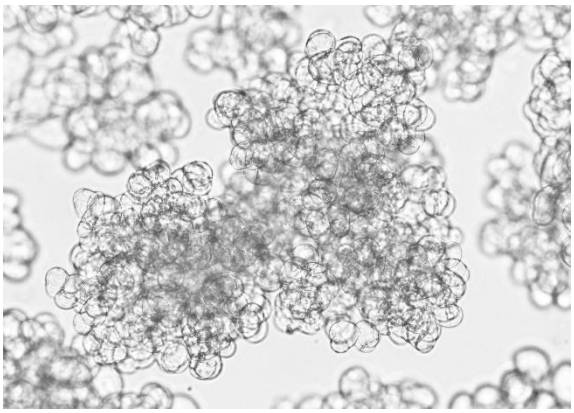

Figure 3.9. 4-d-old heterotrophic *Arabidopsis* cell cultures imaged using brightfield microscopy.

timecourse, measured upon extraction of a metabolite from the population of cells, is a weighted average of these delayed labelling timecourses based on the size of each population of cells. The weighting depends on the structure of the groups of cells. For example, if the clumps of cells approximated to spheres (Figure 3.10A dashed line) then the size of each population would decrease towards the centre of the sphere with the relationship $4\pi r^2$. The delayed labelling timecourse had a sigmoidal shape in contrast to the exponential decay expected in a homogenous cell population (Figure 3.10A).

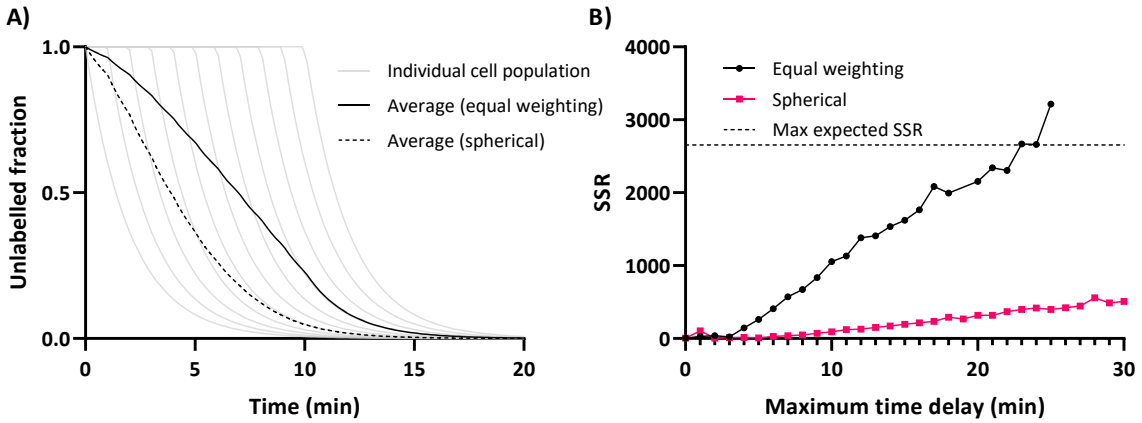

Figure 3.10. Effect of heterogenous cell populations and delayed substrate uptake on flux analysis. **A)** Simulated effect of a heterogenous population of cells on the labelling of cellular metabolites. 11 populations of cells were simulated with a delay in the time taken for the labelled substrate to reach the cells (grey lines). The average isotopic enrichment from metabolites extracted from the cells is the weighted average of the individual populations assuming there are an equal number of cells in each population (solid black line), or cells are arranged in a 3D sphere where the majority of cells are on the outside and the size of each population decreases with the distribution $4\pi r^2$ (dashed black line). **B)** The effect of a heterogenous cell population causing delayed labelled glucose uptake on flux estimation. An idealised dataset of metabolite labelling time-courses with no delay in labelled substrate uptake was initially simulated. Increasing amounts of delay in labelled glucose uptake were added to the simulated data representing a heterogenous population of cells. Fluxes were estimated using the simulated data and the sum of squared residuals (SSR) calculated using INCA.

To quantify the effect of a delay in the uptake of labelled substrate on the fitting procedure of ISNT-MFA, an idealised dataset was simulated with no measurement error and delays in labelled glucose uptake from 0 – 30 min simulated based on equal weightings or a spherical distribution of cells. Fluxes were then estimated based on the modified dataset and the sum of squared residuals (SSR) between the simulated measurements and the flux model were calculated (Figure 3.10B). Delayed label incorporation in a heterogenous population of cells increases the residual of flux estimation (Figure 3.10B). Assuming cells are clustered in spheres, a delay of up to 5 min causes a minimal increase in the SSR (<10). Delays of up to 30 min still cause relatively small increases in the SSR (<500). Therefore, short delays in glucose uptake are unlikely to cause a lack of fit in flux estimations.

The effect of measurement error on model fitting was also explored by adjusting the measurement error of the experimental data to a fixed value across different timepoints and

metabolites and calculating the SSR after flux estimation (Figure 3.11). As measurement error was increased the total residuum decreased (Figure 3.11). A larger error was required to achieve an accepted fit for menadione treated cells compared to control cells, reflecting the larger variation in the measurements between the three biological replicates in the menadione treated cells. Differences in the measurement error of individual mass isotopologues and time points from biological replicates can cause overly tight fitting of free parameters to specific time points or isotopologues, as the residual for each measurement is weighted by its standard error. Therefore, defining consistent errors across time points and isotopologues avoided biasing the fitting procedure to a small number of measurements and allowed a statistically acceptable fit between the data and the free parameters to be achieved.

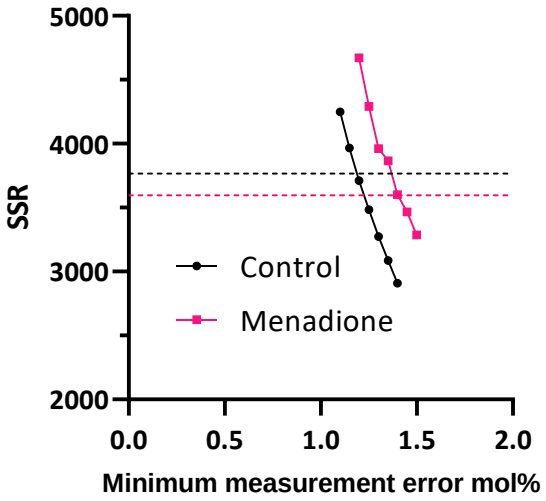

Figure 3.11. The effect of measurement error on flux estimation residual for control (black circles) and menadione (pink squares) cell cultures. Dashed lines represent the maximum SSR required for an accepted fit. Mol% errors were set to a minimum value for MIDs ≤ 0.5mol% and scaled linearly up to a maximum error for MIDs ≥ 25 mol% (Young, 2014). The maximum error was set 0.7 mol% larger than the minimum error. X-axis is the minimum error value defined for MIDs ≤ 0.5 mol%. SSR – sum of squared residuals.

Measurement errors were fixed, and the best-fit fluxes estimated for control and menadione treated cells. Model parameters are described in Table 3.2. Differences in the isotopologue measurements, total free parameters, degrees of freedom and critical χ^2 value between control and menadione treated cells are due to two missing samples in menadione

treated cells (10 min Replicate A, 60 min Replicate B), otherwise the models are identical. The resulting best fit flux estimates for control and menadione treated cells are represented as flux maps (Figure 3.12, Appendix A.9) and individual values are listed in Table 3.3 and Appendix A.5.

Table 3.2. Summary of characteristics of best-fit flux models for control cells and cells treated with 60 µM menadione. Each model was simultaneously fitted to three independent labelling datasets from independent cell cultures. Mol% errors were set to a minimum value for MIDs ≤ 0.5mol% and scaled linearly up to a maximum error for MIDs ≥ 25 mol% (Young, 2014). The maximum error was set 0.7 mol% larger than the minimum error. Flux measurements were defined as biomass outputs from Masakapalli et al., 2014. MS norms refer to the scaling factors applied to mass isotopologues to account for any missing or anomalous mass isotopologue measurements (Young, 2014).

Model parameter	**Control**	**Menadione**
Isotopologue measurements	4418	4218
Measurement error	1.20 – 1.90 mol%	1.45 – 2.15 mol%
Flux measurements	30	30
Total free parameters	847	815
MS norms	698	666
Number of free fluxes	96	96
Number of free pool sizes	53	53
Degrees of freedom	3601	3433
Total residuum (SSR)	3758.0	3353.0
Critical χ^2 value (p = 0.05)	3601.0 – 3769.2	3272.5 – 3597.3

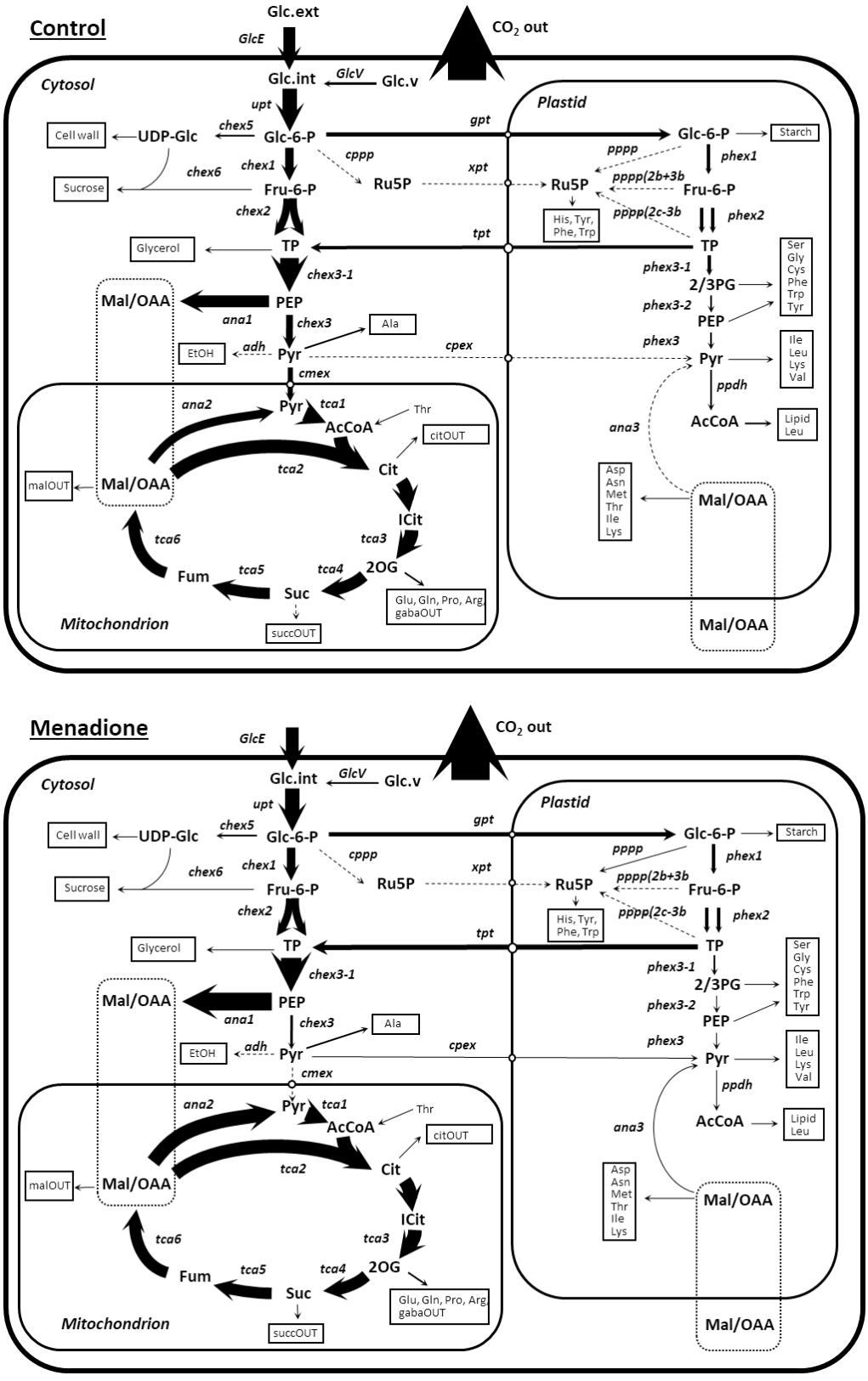

Figure 3.12. Flux maps of central carbon metabolism in heterotrophic *Arabidopsis* cell cultures treated with 60 µM menadione for 6 h or an untreated control. Fluxes were deduced using INST-MFA following supply of [$^{13}C_6$]glucose. Arrow thickness is proportional to relative molar flux. Fluxes < 1% of glucose uptake rate are indicated by dashed arrows. Arrow labels refer to values in Table 3.3.

Table 3.3. Global best-fit flux estimates for heterotrophic *Arabidopsis* cell cultures treated with 60 µM menadione for 6 h or an untreated control. Fluxes were deduced using INST-MFA following supply of [$^{13}C_6$]glucose. Fluxes are the molar flux relative to glucose uptake ± SD (SD is estimated from a linear approximation). The 95% confidence intervals (italics) of free fluxes were determined by Monte Carlo simulation (lower bound – upper bound). Bold values indicate a significant difference ($P < 0.05$, non-overlapping 83.4% confidence intervals calculated by Monte Carlo simulation). See Appendix A.5 for the complete set of flux values and reaction definitions.

Flux	Equation	Relative molar flux	
		Control	Menadione
Hexose/triose phosphate metabolism			
upt	GLC.int -> G6P.c	1.000 ± 0.000	1.000 ± 0.000
		1.000 – 1.000	*1.000 – 1.000*
Glcv	**GLC.v -> GLC.int**	**0.162 ± 0.002**	**0.113 ± 0.005**
		0.156 – 0.167	***0.102 – 0.122***
chex1	G6P.c <-> F6P.c	0.599 ± 0.005	0.587 ± 0.034
		0.555 – 0.646	*0.533 – 0.654*
chex2	FBP.c <-> TP.c + TP.c	0.540 ± 0.005	0.529 ± 0.041
		0.486 – 0.606	*0.460 – 0.608*
chex3-1	TP.c <-> 3PG.c	1.315 ± 0.009	1.417 ± 0.158
		1.210 – 1.540	*1.267 – 1.559*
chex3	**PEP.c -> PYR.c**	**0.477 ± 0.007**	**0.173 ± 0.215**
		0.380 – 0.633	***0.090 – 0.342***
phex1	G6P.p <-> F6P.p	0.237 ± 0.005	0.246 ± 0.036
		0.199 – 0.279	*0.182 – 0.291*
phex2	FBP.p <-> TP.p + TP.p	0.233 ± 0.005	0.243 ± 0.028
		0.196 – 0.274	*0.184 – 0.291*
phex3-1	TP.p <-> 3PG.p	0.222 ± 0.007	0.119 ± 0.146
		0.067 – 0.249	*0.039 – 0.181*
phex3-2	3PG.p <-> PEP.p	0.145 ± 0.006	0.043 ± 0.044
		0.020 – 0.176	*0.030 – 0.106*
phex3	PEP.p -> PYR.p	0.121 ± 0.006	0.020 ± 0.044
		0.000 – 0.151	*0.008 – 0.082*
Pentose phosphate pathway			
cppp1	G6P.c -> 6PG.c	0.000 ± 0.000	0.000 ± 0.004
		0.000 – 0.000	*0.000 – 0.010*
pppp1	6PG.p -> Ru5P.p + CO2	0.004 ± 0.002	0.007 ± 0.038
		0.002 – 0.022	*0.004 – 0.043*
pppp2a	R5P.p + TKC2.p <-> S7P.p	0.004 ± 0.001	0.005 ± 0.013
		0.002 – 0.010	*0.003 – 0.018*

ppppp2b	E4P.p + TKC2.p <-> F6P.p	-0.008	±	0.001	-0.007	±	0.013
		-0.011	*–*	*0.010*	*-0.009*	*–*	*0.018*
ppppp2c	X5P.p <-> TP.p + TKC2.p	-0.004	±	0.001	-0.002	±	0.025
		-0.007	*–*	*0.008*	*-0.004*	*–*	*0.025*
ppppp3a	S7P.p <-> E4P.p + TAC3.p	0.004	±	0.001	0.005	±	0.013
		0.002	*–*	*0.010*	*0.003*	*–*	*0.018*
ppppp3b	TP.p + TAC3.p <-> F6P.p	0.004	±	0.001	0.005	±	0.013
		0.002	*–*	*0.010*	*0.003*	*–*	*0.018*
Transporters/exchanges							
cmex	**PYR.c -> PYR.m**	**0.373**	**±**	**0.006**	**0.000**	**±**	**0.181**
		0.257	***–***	***0.428***	***0.000***	***–***	***0.191***
cpex	PYR.c -> PYR.p	0.000	±	0.010	0.070	±	0.178
		0.000	*–*	*0.143*	*0.000*	*–*	*0.109*
gpt	G6P.c <-> G6P.p	0.303	±	0.007	0.315	±	0.034
		0.259	*–*	*0.346*	*0.250*	*–*	*0.367*
tpt	TP.c <-> TP.p	-0.239	±	0.009	-0.363	±	0.157
		-0.428	*–*	*-0.169*	*-0.482*	*–*	*-0.226*
Tricarboxylic acid cycle							
tca1	PYR.m -> CO2 + AcCoA	0.998	±	0.005	1.008	±	0.162
		0.862	*–*	*1.131*	*0.835*	*–*	*1.130*
tca2	AcCoA + MAL -> CIT	0.972	±	0.004	0.982	±	0.152
		0.858	*–*	*1.111*	*0.842*	*–*	*1.144*
tca3	ICIT -> CO2 + AKG	0.943	±	0.004	0.953	±	0.152
		0.829	*–*	*1.083*	*0.812*	*–*	*1.115*
tca4	AKG -> CO2 + SUCCCoA	0.811	±	0.004	0.821	±	0.152
		0.695	*–*	*0.953*	*0.680*	*–*	*0.982*
tca5	SUCC <-> FUM	0.801	±	0.005	0.811	±	0.153
		0.684	*–*	*0.941*	*0.670*	*–*	*0.976*
tca6	FUM <-> MAL	0.804	±	0.005	0.814	±	0.153
		0.687	*–*	*0.944*	*0.672*	*–*	*0.980*
Anaplerotic fluxes							
ana1	**PEP.c + CO2 <-> MAL**	**0.838**	**±**	**0.008**	**1.243**	**±**	**0.338**
		0.769	***–***	***1.026***	***1.001***	***–***	***1.401***
ana2	**MAL -> PYR.m + CO2**	**0.625**	**±**	**0.006**	**1.008**	**±**	**0.172**
		0.541	***–***	***0.769***	***0.741***	***–***	***1.116***
ana3	MAL -> PYR.p + CO2	0.000	±	0.007	0.020	±	0.169
		0.000	*–*	*0.076*	*0.007*	*–*	*0.074*
CO2out	CO2 -> CO2.eff	2.678	±	0.008	2.698	±	0.221
		2.306	*–*	*3.078*	*2.273*	*–*	*3.101*
Starch synthesis							

phex4/5	G6P.p <-> G1P.p	0.061 ± 0.006	0.063 ± 0.015
		0.032 – 0.089	*0.033 – 0.092*
Sucrose synthesis			
chex4/5	G6P.c <-> G1P.c	0.098 ± 0.004	0.097 ± 0.016
		0.068 – 0.125	*0.067 – 0.130*
chex6	F6P.c + UDPG -> S6P	0.059 ± 0.004	0.058 ± 0.015
		0.030 – 0.085	*0.028 – 0.090*

Figure 3.12 and Table 3.3 summarise the deduced flux distributions within central carbon metabolism in menadione-treated and untreated cell cultures. Menadione treatment caused a significant decrease in flux through pyruvate kinase (chex3) and an increase in flux through PEP carboxylase (ana1) and malic enzyme (ana2). Flux through the plastidic pentose phosphate pathway also increased in menadione treated cells although the flux remained small relative to glucose uptake. Flux through plastidic malic enzyme (ana3) increased in menadione treated cells but the flux was small relative to mitochondrial malic enzyme (ana2). Import of cytosolic pyruvate into plastids (cpex) increased in menadione treated cells and direct import of pyruvate into mitochondria (cmex) was significantly decreased. Input of unlabelled glucose (GlcV) was significantly smaller in menadione treated cells. Output fluxes to biomass were constrained to the same values and are therefore similar in control and menadione treated cells. TCA cycle and upper glycolytic fluxes were similar between control and menadione treated cells. Exchange fluxes were also estimated for reversible reactions and are detailed in Appendix A.5A.5. Note that the biological meaning of apparent exchange fluxes can be difficult to interpret depending on the precise enzyme reaction mechanism involved and labelled substrate used (Beard and Qian, 2007; Wiechert, 2007).

To identify statistically significant differences in flux distributions, Monte Carlo simulations were performed based on the global best fit flux maps. Multiple estimates for each flux are generated by adding Gaussian noise to each measurement based on the measurement error and then re-fitting the fluxes (see Appendix A.10 for probability distributions of each flux). Two approaches were used to determine significantly different fluxes (methods 2.4.7). Overlap

between 83.4% confidence intervals and multivariate statistics using principal component analyses (PCA) and partial least squares discriminant analysis (PLSDA). PCA and PLSDA were performed on the free net fluxes to identify if flux distributions could be separated in control and menadione treated cells and to identify any outliers from Monte Carlo simulation (Figure 3.13).

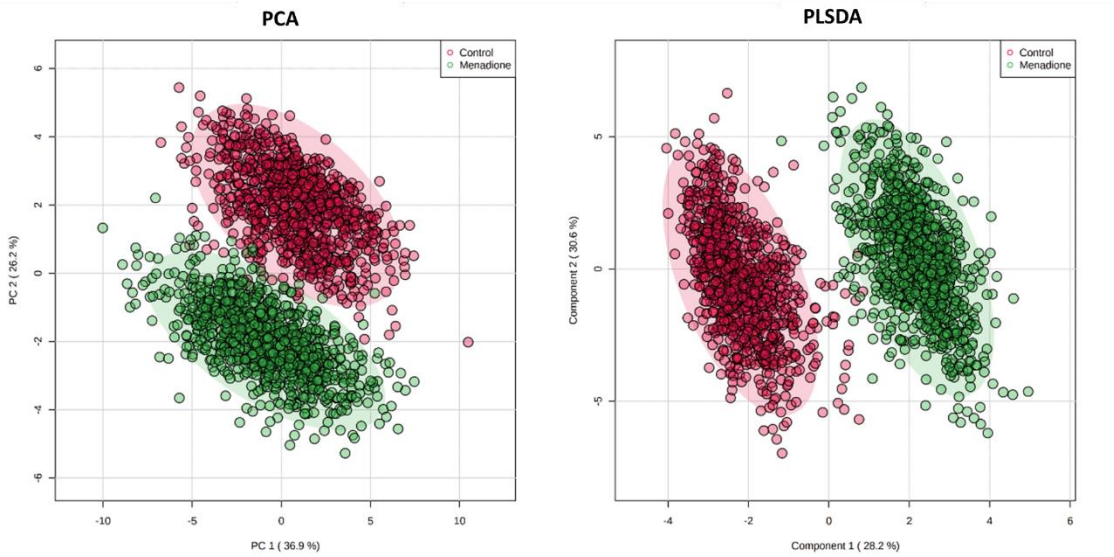

Figure 3.13. Principal component analysis (PCA) and partial least squares discriminant analysis (PLSDA) of 1000 Monte Carlo simulations of fluxes from control (red) and menadione (green) treated cell cultures. Fluxes were mean centred and scaled to unit variance. Shaded regions represent 95% confidence interval. Values in brackets on the axis describe proportion of the variation in the data described by the top two principal components. Only free, net fluxes of central carbon metabolism were included in the analysis. Biomass output fluxes, exchange fluxes, pool sizes and pseudo fluxes for mixing of compartmented or unlabelled pools were excluded.

Figure 3.13 shows that PCA could differentiate between the fluxes in control and menadione treated cells and none of the Monte Carlo simulations are obvious outliers. PSLDA showed clear separation between the groups, as expected from the PCA analysis (See Appendix A.8 for PLSDA model validation). To identify which fluxes contributed to the PLSDA separation, variable importance projection (VIP) scores were ranked for each free net flux parameter (Figure 3.14).

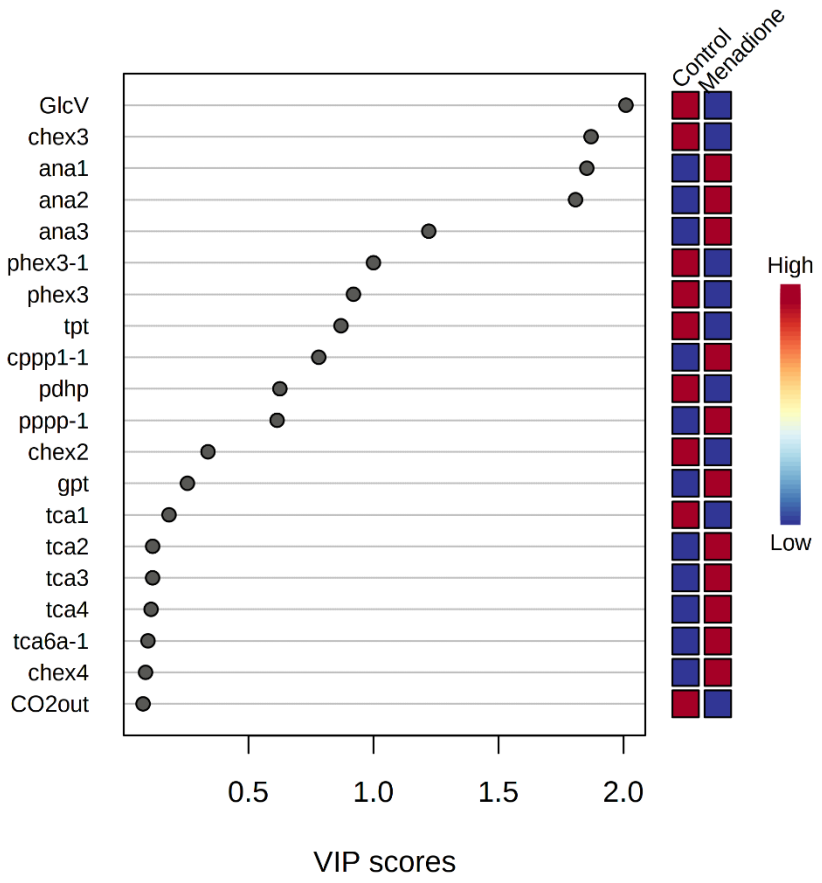

Figure 3.14 Variable importance in projection (VIP) scores from PLSDA analysis of 1000 Monte Carlo simulations of fluxes from control and menadione treated cell cultures. Fluxes were mean centred and scaled to unit variance. Only free, net fluxes of central carbon metabolism were included in the analysis. Biomass output fluxes, exchange fluxes, pool sizes and pseudo fluxes for mixing of compartmented or unlabelled pools were excluded.

VIP scores identify GlcV, chex3, ana1 and ana2 as making the largest contributions to distinguishing between flux distributions between control and menadione treated cells, in agreement with comparison of the confidence intervals (Table 3.3). TCA cycle fluxes and CO_2 efflux do not contribute to separation of the groups confirming these fluxes were not significantly affected by menadione treatment.

3.2.6 Coenzyme balancing

To assess the ability of the network to satisfy the metabolic demand for the coenzymes ATP, NADH and NADPH, fluxes were multiplied by the stoichiometries of coenzyme producing and consuming reactions (Appendix A.6, Table A.2). Reactions such as those catalysed by

glutamate synthase (GOGAT) and IDH carry relatively large fluxes and could produce/consume NADPH or NADH depending on the relative involvement of different isozymes. The effect on coenzyme balance of coenzyme specificity was evaluated by assuming complete specificity for NADH or NADPH for GOGAT and IDH and quantifying the net surplus or deficit of NADPH production in meeting the biosynthetic demands (Figure 3.15).

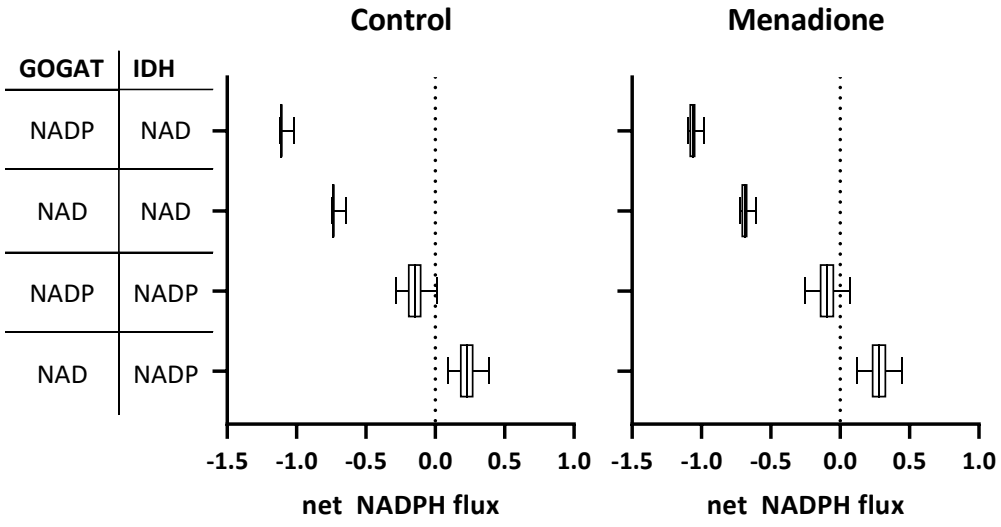

Figure 3.15. Comparison of coenzyme balance for NADPH in systems with differing coenzyme specificities of GOGAT and IDH. Total rates of NADPH production by the central metabolic network and consumption by biomass production were calculated assuming complete NAD- or NADP- specificity for GOGAT and IDH in various combinations. Values > 0 represent excess production of NADPH relative to biosynthetic demands, values < 0 represent a deficit of NADPH to meet biosynthetic demand. Error bars represent 95% confidence intervals calculated from Monte Carlo simulations of global best fit flux maps.

Figure 3.15 shows that NADPH-IDH was required for catabolic production of NADPH to meet the biosynthetic demand regardless of the coenzyme specificity of GOGAT. Cells could meet the biosynthetic demand for NADPH if GOGAT is NADPH-specific but with very little remaining NADPH production for possible maintenance processes. Assuming GOGAT is entirely NADH-specific and IDH is entirely NADP-specific resulted in production of NAPDH in excess of the requirement for biosynthesis, which could be used to support maintenance processes. NADPH production was similar in control and menadione treated cells.

Table 3.4. Coenzyme balance for heterotrophic *Arabidopsis* cells treated with 60 µM menadione. Assuming NADP-IDH and NADH-GOGAT. ATP requirement for biosynthesis assumes all amino acid exports are converted into protein. Values in italics in brackets are 95% confidence intervals calculated by Monte Carlo simulation of global best fit flux maps (lower bound – upper bound). [a]ATP potentially generated from oxidative phosphorylation assuming NADH not required for biosynthesis generates 2.5 ATP/NADH. Bold values represent a significant difference ($P < 0.05$, non-overlapping 83.4% CI)

Metabolite	**Molar flux (relative to glucose uptake)**		
	Requirement for biomass	**Generated by network**	
		Control	**60 µM Menadione**
ATP	2.12	**1.17**/10.3[a] *(0.93 – 1.43)*	**0.81**/10.15[a] *(0.59-1.07)*
NADH	0.57	4.68 *(4.08 – 5.25)*	4.62 (*3.97 – 5.23)*
NADPH	0.76	0.95 (*0.83 – 1.12)*	0.99 (0.87 – 1.19)

Table 3.4 shows that the ATP requirement for biosynthesis cannot be met by substrate level phosphorylation. However, the deficit could be covered by ATP generated via oxidative phosphorylation from the excess NADH not directly used for biosynthesis. NADPH production can meet the biosynthetic demand in both control and menadione treated cells assuming GOGAT is NADH specific and IDH is NADPH specific. ATP production from substrate level phosphorylation is significantly lower in menadione treated cells (55% of biosynthetic demand) compared to control (38% of biosynthetic demand). The difference between control and menadione treated cells is largely due to the decrease in flux through pyruvate kinase, which produces ATP (chex3, Table 3.3).

3.3 Discussion

3.3.1 INST-MFA quantified fluxes in heterotrophic *Arabidopsis* cell cultures

INST-MFA was able to quantify fluxes in heterotrophic *Arabidopsis* cell cultures and identify changes in flux caused by menadione treatment. Previous flux analyses in heterotrophic *Arabidopsis* cell cultures have been made using SS-MFA based on parallel labelling experiments with [1-^{13}C]glucose, [2-^{13}C]glucose and [$^{13}C_6$]glucose and measurement of MIDs by GC-MS and

positional isotopologues by NMR of organic acids and proteogenic amino acids (Masakapalli et al., 2010, 2013, 2014; Williams et al., 2008). In this thesis, INST-MFA was used based on the labelling timecourse of metabolites of central carbon metabolism following supply of [$^{13}C_6$]glucose measured by LC-MS. The cell line, growth media, growth conditions and biomass output constraints in this study were identical to those used in previous SS-MFA of heterotrophic *Arabidopsis* cell cultures (Masakapalli et al., 2014). Overall, the flux distribution measured by INST-MFA is similar to previously published steady state flux maps (Appendix A.11), although this may be expected due to the similar network structure and biosynthetic constraints. Nevertheless, INST-MFA flux maps show a number of differences including larger glycolytic flux, smaller PPP flux, less pyruvate import into mitochondria and plastids, and larger anaplerotic fluxes through PEPC and mitochondrial ME (Appendix A.11). Net CO_2 efflux relative to glucose uptake was similar between the two methods. The different flux distributions may be caused by changes in the cell line over time as seven years of continuous subculturing could lead to substantial genetic changes (Pucker et al., 2019). However, it is more likely that the differences in fluxes are due to the experimental method than changes in the cell cultures as fundamentally different information is used to deduce fluxes in SS-MFA compared to INST-MFA and flux identifiability can be different between the two methods (Nöh and Wiechert, 2006).

The flux distributions estimated based on iterative modelling are generally supported by qualitative interpretation of the MIDs of the measured metabolites. For example, the rapid appearance of M+3 malate (Figure 3.8) supports large flux through PEPC which is confirmed by the modelled fluxes (chex3, Table 3.3, Figure 3.12). In contrast, the low flux through the oxPPP estimated by INST-MFA is somewhat surprising considering the rapid labelling of 6PG and R5P which is consistent with substantial oxPPP flux.

To further explore the accuracy of the flux estimations the potential effect of cell heterogeneity was explored. Heterotrophic *Arabidopsis* cell cultures are callus cells and grow in clumps of multiple cells which may lead to heterogenous rates of labelled glucose uptake in a population of cells. Simulating the effect of heterogenous cell populations on the rate of labelled

glucose uptake (Figure 3.10) showed that a delay in glucose uptake leads to a more sigmoidal label uptake curve. G6P and F6P are labelled fastest following supply of labelled glucose and therefore most closely represent the rate that labelled glucose is taken up by cells. Delays in glucose uptake would cause M+0 labelling curves to have a sigmoidal shape but this is not the case (Figure 3.6), suggesting labelled glucose is efficiently mixed and reaches all cells within the first labelling timepoint at 30 s.

Unlike SS-MFA, INST-MFA is more sensitive to perturbations following supply of isotopically labelled substrate as metabolites are extracted within 30 s. Exchanging growth media by filtration, centrifugation or sedimentation can cause metabolic perturbation and was previously shown to cause a large decrease in ascorbate concentration in heterotrophic *Arabidopsis* cells, potentially due to oxidative stress induced by handling of cell cultures (Baxter et al., 2007a). To avoid metabolic perturbation from complete media exchange, a bolus of labelled glucose was added to cell cultures increasing the media glucose concentration from ~60 mM to ~120 mM. Since plant plasma membrane glucose transporters have K_m values for glucose in the range 0.01 – 2 mM (Büttner, 2007), it is likely that glucose uptake will be fully saturated both before and after addition of labelled glucose and therefore there will be only a minimal effect on metabolic fluxes. However, the change in average isotopic enrichment of metabolites over time does not show the expected exponential pattern but instead shows a fluctuation between 4-15 min (Figure 3.5). The only way to explain the initial increase and then decrease in the isotopic enrichment of a metabolite is for there to be an increase in the input flux from an unlabelled precursor. These changes in flux distribution could be caused by a change in oxygen availability as the foil lid of the flask was removed, which has previously been shown to restrict oxygen availability to the culture media (Williams et al., 2008). Perturbation of fluxes may also have been caused by the osmotic change as the external glucose concentration is doubled during addition of labelled media. This may induce transitory changes in sugar export from unlabelled vacuolar stores. The differential equation model fitted to the data cannot account for the observed

fluctuation and therefore it may contribute to the uncertainty in flux estimates by requiring larger measurement errors to achieve a statistically acceptable fit.

3.3.2 Menadione differentially affects fluxes throughout the metabolic network

Metabolomics and analysis of the metabolism of [^{13}C]glucose have previously suggested that treatment of heterotrophic *Arabidopsis* cell cultures with 60 µM menadione inhibits flux through the TCA cycle, increases flux through the pentose phosphate pathway and decreases concentrations of amino acids (Baxter et al., 2007a). However, absolute fluxes were not quantified to confirm this. In this chapter, INST-MFA of menadione treated cell cultures showed that TCA cycle flux was maintained after menadione treatment, with increased input of cytosolic OAA and malate into the TCA cycle relative to cytosolic pyruvate (Figure 3.12). Baxter et al., (2007), report decreased rates of label incorporation into TCA cycle intermediates during 6 h incubation with [$^{13}C_6$]glucose, and equate this to decreased TCA cycle flux. However, results in this chapter demonstrate that menadione treatment decreased the rate of label incorporation into pyruvate (Figure 3.6) which may cause the decreased labelling of TCA cycle intermediates observed by Baxter et al., (2007). This highlights the benefit of integrating metabolite labelling data into a flux model and the challenges associated with attempting to interpret individual rates of label incorporation without taking a system-wide perspective.

The lack of TCA cycle inhibition shown by INST-MFA is surprising considering the sensitivity of certain TCA cycle enzymes to oxidative stress and specifically menadione treatment (Baxter et al., 2007a; Lehmann et al., 2012; Obata et al., 2011; Sweetlove et al., 2002). Aconitase which catalyses conversion of citrate to isocitrate was shown to be rapidly inactivated by H_2O_2 as well as menadione treatment (Baxter et al., 2007a; Lehmann et al., 2012; Obata et al., 2011; Sweetlove et al., 2002; Verniquet et al., 1991). However, no significant change in flux from citrate to isocitrate (represented by tca3, Table 3.3) was observed using INST-MFA. The lipoic acid containing subunits of the pyruvate dehydrogenase complex (PDC) and 2-oxoglutarate dehydrogenase complex (OGDC) can also be inhibited by lipid peroxidation products generated by excess ROS (Millar and Leaver, 2000; Obata et al., 2011; Sweetlove et al., 2002). However,

flux from 2OG to succinate and from pyruvate to acetyl CoA (tca1 and tca4, Table 3.3) were unchanged after menadione treatment. Despite no measured change in flux through PDC or OGDC the labelling timecourses of the precursors, pyruvate and 2OG, were affected by menadione treatment with an increase in the rate of label incorporation into pyruvate and a decrease in the rate of label incorporation into 2OG (Figure 3.6, Figure 3.8). This suggests that menadione treatment did have an effect on metabolism around pyruvate and 2OG but this did not result in significant changes in TCA cycle flux.

The flux from PEP to pyruvate catalysed by pyruvate kinase (PK) and subsequent import of pyruvate into mitochondria was significantly decreased after menadione treatment (Figure 3.12, Table 3.3). Mammalian and yeast PK are known to be regulated by Cys oxidation to inhibit glycolysis and divert flux into the oxPPP under oxidative stress (Grüning et al., 2011; McDonagh et al., 2009; Soares et al., 2011). However, there is no such evidence in plants and a previous study of *Arabidopsis* roots showed pyruvate kinase (PK) was unaffected by menadione treatment (Lehmann et al., 2012). INST-MFA showed flux was diverted into cytosolic PEPcarboxylase to allow glycolytic and TCA cycle flux to be maintained following menadione treatment. Increased mitochondrial ME flux maintained the supply of pyruvate within the mitochondria. This alternative route of carbon entry into the mitochondria is at the cost of one ATP by substrate level phosphorylation but there is still sufficient supply to meet biosynthetic demand (Table 3.4).

Flux through plastidic malic enzyme (ME) (ana3, Figure 3.12, Table 3.3) also increased following menadione treatment. *Arabidopsis* contains six isoforms of ME, three cytosolic NADP-ME and a plastidic NADP-ME (Wheeler et al., 2005), and two mitochondrial NAD-ME (Tronconi et al., 2008). NADP-ME has been shown to play a role in oxidative stress tolerance (Chen et al., 2019b) but, from the changes in flux presented in Table 3.3, plastidic ME makes only a very small contribution (<2%) to the total rate of NADPH production under stress conditions. Adding all six possible isoforms of ME would reduce the flux determinability of these reactions and therefore the model was simplified by including just mitochondrial NAD-ME (ana2) and plastidic NADP-ME (ana3). An additional reaction from malate to cytosolic pyruvate

representing cytosolic NADP-ME could be added to the model, but distinguishing between cytosolic and mitochondrial ME flux may be difficult without relevant compartmented measurements of malate and pyruvate labelling. Label incorporation into a reporter metabolite such as alanine, which is synthesised from cytosolic pyruvate, could potentially help resolve this flux.

The flux phenotype observed by INST-MFA in this chapter may be the response to a very mild oxidative stress, showing flux through the TCA cycle could be maintained by bypassing pyruvate kinase. It's possible that the TCA cycle flux had recovered after 6 h treatment with menadione whereas previous studies supplied labelled glucose and menadione at the same time (Baxter et al., 2007a). A necessary requirement of INST-MFA is that fluxes and intermediate metabolite concentrations are constant over time (Nöh and Wiechert, 2006; Wiechert and Nöh, 2005). Therefore, a 6 h treatment was used in this study to ensure a metabolic steady state was achieved before labelled substrate was applied, as supported by Previous metabolomic analysis of heterotrophic *Arabidopsis* cell cultures following 6 h treatment with 60 µM menadione (Baxter et al., 2007a).

Identical biomass output fluxes, based on [U-^{14}C]glucose labelling and biomass composition analyses of untreated *Arabidopsis* cell cultures (Masakapalli et al., 2014), were used to constrain the flux estimation of both control and menadione treated cells. Previous analysis of identical cell cultures showed 4 h treatment with 50 µM menadione caused a significant increase in output flux to acidic soluble compounds and a significant increase in flux into sucrose (potentially due to sucrose cycling) but there was no significant effect on fluxes to into basic compounds, other soluble sugars, starch, protein or cell wall components (Garlick, 2002). This analysis did not quantify biomass outputs into individual compounds based on the biomass composition of the cells which would be required for constraining the INST-MFA model. Due to the fact that the perturbed metabolic steady state in menadione treated cells is likely to be short lived, it is difficult to estimate biomass output fluxes precisely at the point the ^{13}C labelling experiment is started (6 h after menadione treatment). The biomass composition of amino acids

could be measured following menadione treatment but unless all proteins were turned over in this time, the biomass composition will reflect the biomass outputs over a longer period, including prior to the menadione treatment. Therefore, in the absence of reliable biomass output measurements identical output fluxes were defined for both control and menadione treated cells, meaning that the differences in flux were defined by differences in isotopic labelling timecourses.

The contribution of the biomass constraints to the flux estimates could be further explored, although the computational demands of the non-linear statistical analysis for INST-MFA are considerable and therefore this analysis was not attempted in this thesis. Estimation of the contribution of biomass output constraints on the estimated fluxes can be made using local variances but these can fail to accurately capture the non-linear relationship between measurements and fluxes (Antoniewicz et al., 2006). The importance of biomass constraints for ^{13}C-MFA remains an open question that requires further analysis as, theoretically, flux estimations can be determined without biomass constraints, if the unknown fluxes of interest remain overdetermined by the available measurements.

3.3.3 Coenzyme balancing

Menadione increased the demand for NADPH but there was no significant increase in total NADPH production estimated from carbon flux through NADPH producing reactions (Table 3.4). The majority of NADPH production was provided by IDH, assuming it is NADP-specific, with <1% contribution from the oxPPP. This contrasts with previous steady state flux maps of heterotrophic *Arabidopsis* cell cultures which showed ~40% of the NADPH produced was derived from the oxPPP (Masakapalli et al., 2013, 2014). oxPPP flux did increase in menadione treated cells, qualitatively supported by an increase in the rate of 6PG labelling (Figure 3.6), but the total oxPPP flux remained <1.5% of glucose uptake rate (Figure 3.12, Table 3.3).

One of the largest biosynthetic demands for reductant comes from nitrogen assimilation via the GS/GOGAT cycle. Two isoforms of GOGAT are found in plants, Fd-GOGAT and NADH-GOGAT. NADPH can act as a source of reductant for Fd-GOGAT via ferredoxin NADP

reductase, supported by evidence that oxPPP activity increases with supply of ammonium, dependent on protein synthesis (Esposito et al., 2005). The activities of the two isoforms of GOGAT vary with light, tissue and developmental stage with plastidic Fd-GOGAT more associated with nitrogen assimilation in illuminated leaves (Matoh and Takahashi, 1982; Wallsgrove et al., 1982) and plastidic NADH-GOGAT associated with non-photosynthetic tissues such as roots (Kojima et al., 2014; Lancien et al., 2002; Watanabe et al., 1996). Proteomic analysis of *Arabidopsis* cell cultures in the light showed expression of both isoforms of GOGAT but no data are available for cell cultures in the dark (Mergner et al., 2020). Transcript abundance of ferredoxin NADP-reductase was significantly decreased upon menadione treatment of heterotrophic *Arabidopsis* cell cultures (Baxter et al., 2007a), which may be a mechanism to decrease flux through Fd-GOGAT. The coenzyme specificity of GOGAT can have a large effect on the NADPH balance of cells (Figure 3.15). If GOGAT is exclusively NADPH specific, then additional sources of NADPH must be present for catabolic NADPH production to exceed the biosynthetic demand, even if IDH is assumed to be completely NADP-specific. Alternative sources of NADPH could be derived from carbon fluxes not considered in the current model or from transhydrogenation of NADH to NADPH (Bykova and Møller, 2001; Bykova et al., 1999).

One carbon metabolism could contribute to NADPH production via methylenetetrahydrofolate dehydrogenase (MTHFDH) which was shown to be important for oxidative stress response in *Arabidopsis* (Gorelova et al., 2017a). Changes in transcript abundance in genes associated with folate metabolism were also identified in *Arabidopsis* cell cultures treated with menadione, including an increase in At3g12290, encoding MTHFDH (Baxter et al., 2007a). Various catabolic reactions generate one-carbon derivatives of tetrahydrofolate (THF) which are then converted between different oxidation states (Gorelova et al., 2017b; Hanson et al., 2000). These different one carbon intermediates were not identified by the LC-MS analysis used in this study and therefore fluxes between them could not be resolved. Therefore in both the ISNT-MFA model presented in this chapter, and previous steady state analyses, one carbon metabolism was simplified to a generic one carbon metabolite (CX).

However, even if it is assumed all flux from serine to glycine (gly Table A.1) generated methylene-THF that was oxidised to make NADPH, this would only contribute 2.6% of total NAPDH production in both control and menadione treated cells. The relatively small flux through one carbon metabolism and lack of change with menadione treatment suggest one carbon metabolism is unlikely to be a major contributor to maintaining NADPH balance in this system.

Another potential source of NADPH could be the cytosolic conversion of glyceraldehyde 3-phsopahte to 3-phosphoglycerate. Two enzymes can potentially catalyse this reaction, cytosolic NAD-dependent glyceraldehyde 3-phosphate dehydrogenase (GAPDH) and the cytosolic NADP-dependent non-phosphorylating glyceraldehyde 3-phosphate dehydrogenase (GAPN). Differential redox regulation of GAPN and GAPDH suggests flux is diverted through the NADPH producing reaction during oxidative stress (Piattoni et al., 2013; Schneider et al., 2018) and knockout mutants of GAPN showed increased sensitivity to oxidative stress (Rius et al., 2006). GAPDH is also localised to the nucleus and mitochondria during oxidative stress where it serves a moonlighting role regulating gene expression and stress signalling pathways (Sweetlove et al., 2002; Zaffagnini et al., 2013). The flux from cytosolic triose-phosphates to 3PG (chex3-1, Table 3.3) could potentially meet the entire biosynthetic NADPH demand if flux was diverted through GAPN. Biosynthetic ATP demands could still be met by oxidative phosphorylation of NADH to make up for the loss of ATP production from GAPDH. Although it is unlikely that GAPN exclusively converts GAP to 3PG, an increase of just 58% in the proportion of flux through GAPN relative to GAPDH would be sufficient to meet the biosynthetic demand for NADPH.

As well as direct production of optimal proportions of NADH and NADPH, transhydrogenation could interconvert between coenzymes to achieve a balanced supply. Unlike prokaryotes or mammals, which use soluble or membrane bound transhydrogenase to convert between NADPH and NADH (Rydström, 2006; Sauer et al., 2004), genes for such proteins have not been identified in plants. Transhydrogenase-like activity has still been measured in plant mitochondria (Bykova and Møller, 2001; Bykova et al., 1999) but this is likely via cycling

reactions between dehydrogenases with differing coenzyme specificity rather than a specific transhydrogenase protein. In photosynthetic tissues in the light, the plastidic NADP-MDH and mitochondrial and cytosolic NAD-MDH act as a transhydrogenase system by exporting the reducing equivalents generated as NAPDH in the chloroplasts to form NADH in the cytosol or mitochondria (Selinski and Scheibe, 2018). Reversal of the malate valve to transfer reductant from NADH to $NADP^+$ could potentially meet an increased demand for plastidic NADPH from mitochondrial or cytosolic NADH. Similarly, transhydrogenation could occur via IDH isoforms with mitochondrial NAD-IDH consuming NADH to generate isocitrate which is then oxidised by NADP-IDH in other compartments. In embryos of developing *B.napus* ^{13}C-labelling analyses supports flux from 2OG to citrate via isocitrate which could potentially support transhydrogenation (Schwender et al., 2006).

The INST-MFA presented in this chapter could not resolve fluxes though isozymes of MDH and IDH in different compartments. For simplicity and to help resolve fluxes around the anaplerotic node of PEP, pyruvate, malate and OAA, malate/OAA were modelled as a single pool assumed to be in rapid equilibrium between different compartments (Kappelmann et al., 2016). Similarly, citrate and isocitrate were modelled as single pools in rapid equilibrium across different compartments. Net flux through IDH could be estimated (tca 3, Table 3.3), but the flux through isozymes in different compartments, which could potentially produce different coenzymes, was not resolved.

A final method of conversion from NADH to NADPH could be direct phosphorylation of NADH. *Arabidopsis* contain an NADH kinase (NADK3) which can use ATP to generate NADPH from NADH therefore operating effectively as a transhydrogenase (Turner et al., 2005). NADK3 was shown to be important for oxidative stress response with knockout plants showing decreased levels of NADPH and reduced glutathione compared to wild type plants after treatment with methyl viologen (Chai et al., 2006). Unfortunately, flux through this reaction, which involves transfer of a phosphate group rather than any carbon atoms, cannot be quantified by ^{13}C-flux analysis.

In summary, INST-MFA of heterotrophic *Arabidopsis* cell cultures showed coenzyme requirements for NADPH could not be met by the oxPPP, consistent with previous SS-MFA of the same cell cultures (Masakapalli et al., 2010, 2013, 2014) and in contrast to the common assumption that the oxPPP is the major source of NADPH in heterotrophic cells (Kruger and von Schaewen, 2003). IDH is also considered to make a substantial contribution to NADPH supply but could only balance the network if IDH was assumed to exclusively generate NADPH (Figure 3.15, Table 3.4). For NADPH production to exceed the biosynthetic requirement and to supply maintenance processes such as detoxifying ROS, then either ammonium assimilation via GOGAT must use reductant provided by NADH, or alternative sources of NADPH must be present. These could include one carbon metabolism, non-phosphorylating glyceraldehyde 3-phosphate dehydrogenase, possible indirect transhydrogenation though cycling of MDH or IDH, or phosphorylation of NADH by NADH kinase. Menadione treatment did not cause an apparent increase in total NADPH production suggesting either demand was not increased or one of the aforementioned NADPH producing mechanisms supports the increased NADPH demand induced by oxidative stress without changing the total combined rate of NAD^+ and $NADP^+$ reduction.

3.4 Conclusion

INST-MFA can quantify fluxes in heterotrophic *Arabidopsis* cells and resolve the subtle changes in flux associated with mild oxidative stress induced by 60 µM menadione, primarily involving alternative carbon entry into the mitochondria. The potential requirement for alternative sources of NADPH discussed here highlight the ambiguity of carbon-based flux analysis for understanding coenzyme balancing. It is possible for carbon fluxes and total production of reducing equivalents to remain constant, but the specific coenzymes generated to vary by the action of isozymes with differing coenzyme specificity. To overcome the inherent inability of ^{13}C labelling to resolve the ambiguity of NAD(P) fluxes, it is necessary to evaluate alternative strategies for quantifying the rates of metabolism of specific coenzymes.

Chapter 4: Limitations of deuterium labelled substrates for quantifying NADPH metabolism in heterotrophic *Arabidopsis* cell cultures

The following chapter is largely reproduced from Smith et al., (2019) with the permission of the co-authors.

4.1 Introduction

The previous chapter used ^{13}C based flux analysis to quantify the effect of menadione induced oxidative stress on carbon fluxes in central metabolism. However, carbon-based analysis could not quantify specific coenzyme fluxes from pathways where an identical carbon transformation could produce either NADPH or NADH. This is the case for malic enzyme (ME), isocitrate dehydrogenase (IDH) and glyceraldehyde 3-phosphate dehydrogenase and leads to an inability to empirically measure total NADPH and NADH production or consumption. Redox reactions involving pyridine nucleotides transfer hydrogen atoms and electrons and therefore isotopically labelled hydrogen (deuterium) can be used to quantify redox reactions involving NADH and NADPH.

Deuterium-labelled substrates can be supplied to cells to quantify the relative contribution of specific pathways to total NADPH production. In this method a deuterated substrate is supplied to cells and deuterium is transferred onto the redox active hydride of NADPH via a specific pathway. Simultaneously, other NADPH-generating reactions will transfer unlabelled hydrogen onto the redox active hydride of NADPH. Therefore, the proportion of NADPH that has incorporated deuterium reflects the proportion that has been generated by the pathway being probed. By using different deuterated substrates, the contribution of different pathways to total NADPH production can be measured. This method has been successfully applied in mammalian cell cultures to quantify the relative NADPH production of various pathways such as the oxPPP using [1-^{2}H]- or [3-^{2}H]glucose (Chen et al., 2019a; Fan et al., 2014; Ghergurovich et al., 2020; Lewis et al., 2014), methylenetetrahydrofolate dehydrogenase

(MTHFDH) using [2,3,3-^{2}H]serine (Fan et al., 2014) and malic enzyme by using [4-^{2}H]glucose (Liu et al., 2016). Additionally, stimulated Raman scattering microscopy of deuterium labelled lipids can be used to visualise to contribution of different pathways to NADPH production specifically for lipid biosynthesis (Hong et al., 2020). However, analysis is complicated by the activity of flavin enzymes which are able to catalyse the loss of deuterium from the redox active hydride of NADPH to water, via exchange involving flavin groups, requiring an additional correction to be applied (Kazuki et al., 1980; Zhang et al., 2017). This additional consideration means that genetic evidence is still important to support the conclusions of deuterium labelling studies (Chen et al., 2019a).

The aim of this chapter is to use deuterium-labelled substrates to quantify the relative contribution of different pathways to total NADPH production in heterotrophic *Arabidopsis* cell cultures. To achieve this, I used LC-MS to measure deuterium incorporation into NADPH and other metabolites after supply of deuterated glucose or deuterated water (D_2O). The effects of different amounts of substrate labelling and water exchange were simulated to establish their influence on the extent of deuterium incorporation into NADPH from labelled substrates. The effect of compartmentation was also simulated to quantify the effect disequilibrium between subcellular compartments can have on the accuracy of calculations based on whole cell extracts.

4.2 Results

4.2.1 Deuterium labelling *in vitro*

Redox reactions involving NAD(P)H transfer electrons as hydride ions and therefore isotopically labelled hydrogen can be used to directly follow these reactions. The oxPPP produces NADPH from glucose with hydrogen from carbon one or three being directly transferred to NADPH via glucose 6-phosphate dehydrogenase (G6PDH) and 6-phosphogluconate dehydrogenase (6PGDH), respectively (Figure 4.1A). To quantify the proportion of NADPH produced by the oxPPP, relative to all other sources, 1- or 3- deuterated glucose can be supplied to cells and the label incorporation into the redox active hydride of

NADPH measured by LC-MS. To confirm this labelling strategy, [1-^{2}H]glucose was combined with hexokinase (HK), G6PDH and 6PGDH, and the mass isotopologue distribution (MID) of NADPH measured by LC-MS (Figure 4.1C). Supply of [1-^{2}H]glucose to HK and G6PDH resulted in 94.7% ± 2.2% of NADPH incorporating a single deuterium atom (Figure 4.1C). Upon the addition of 6PGDH, half of the NADPH produced was unlabelled as it had been produced by 6PGDH via transfer of unlabelled hydrogen from C3 of 6-phosphogluconate (6-PG). This confirmed that [1-^{2}H]glucose could be used to quantify the proportion of NADPH produced by G6PDH and therefore the oxPPP.

In addition to transfer of deuterium onto NADPH from labelled substrates, the redox active hydride of NADPH can be exchanged with water via a reaction catalysed by flavin-containing enzymes (Figure 4.1B) (Kazuki et al., 1980; Zhang et al., 2017). This occurs as hydrogen is transferred from a non-labile C–H bond in NADPH to a more labile N–H bond in $FADH_2$ (Kazuki et al., 1980; Zhang et al., 2017). This can result in loss of label from the redox active hydride of NADPH following labelling with deuterated substrates such as [1-^{2}H]glucose, leading to an underestimation of the contribution of the oxPPP to total NADPH production. This effect was confirmed *in vitro* by the addition of glutathione reductase (GR), a flavin-containing enzyme, to a mixture of hexokinase (HK) and G6PDH supplied with [1-^{2}H]glucose. This resulted in the production of 100% unlabelled NADPH due to complete equilibration of the redox active hydride with water (Figure 4.1C). To confirm the effect of flavin enzymes, the reciprocal experiment was performed by incubating NADPH with D_2O in the presence of GR (Figure 4.1D). Incubation of NADPH with GR in 75% D_2O in the absence of any other substrates also resulted in near complete equilibration of NADPH with water, with the proportion of NADPH containing one deuterium atom reaching 72.4% ± 1.2%. Together, these two results confirm that the redox active hydride of NAPDH can be exchanged with water and that this reaction can be catalysed by flavin containing enzymes without the need for complete catalytic turnover.

Addition of formic acid to the quenching solvent has been reported to improve the extraction efficiency and stability of NADPH from mammalian cell cultures (Lu et al., 2018).

However, preliminary analysis suggested addition of formic acid caused additional deuterium incorporation into NADPH from D_2O. To quantify the effect of formic acid on H/D exchange between NADPH and D_2O, NADPH was incubated with 75% D_2O and mixed with solvent containing 1:1 MeOH:AcN and 0.625% (v/v) formic acid added before LC-MS analysis (Figure 4.1D). The proportion of NADPH containing one deuterium atom (M+1) increased to 10% ± 0.47% in the absence of any enzymes, confirming that formic acid alone could cause exchange of hydrogen between NADPH and water. NADPH containing two deuterium isotopes was present when NADPH was incubated with GR and then quenched with solvent containing formic acid (Figure 4.1D). This showed that H/D exchange caused by formic acid was at a site distinct from that of GR catalysed exchange, which is at the redox active hydride. Because of the potential for additional H/D exchange, formic acid was omitted from the extraction solvent for subsequent extraction of cell cultures. Overall, the results of these *in vitro* experiments confirmed that [1-^{2}H]glucose could be used to label NADPH via the oxPPP and highlighted the need to correct for the water exchange caused by flavin-containing enzymes.

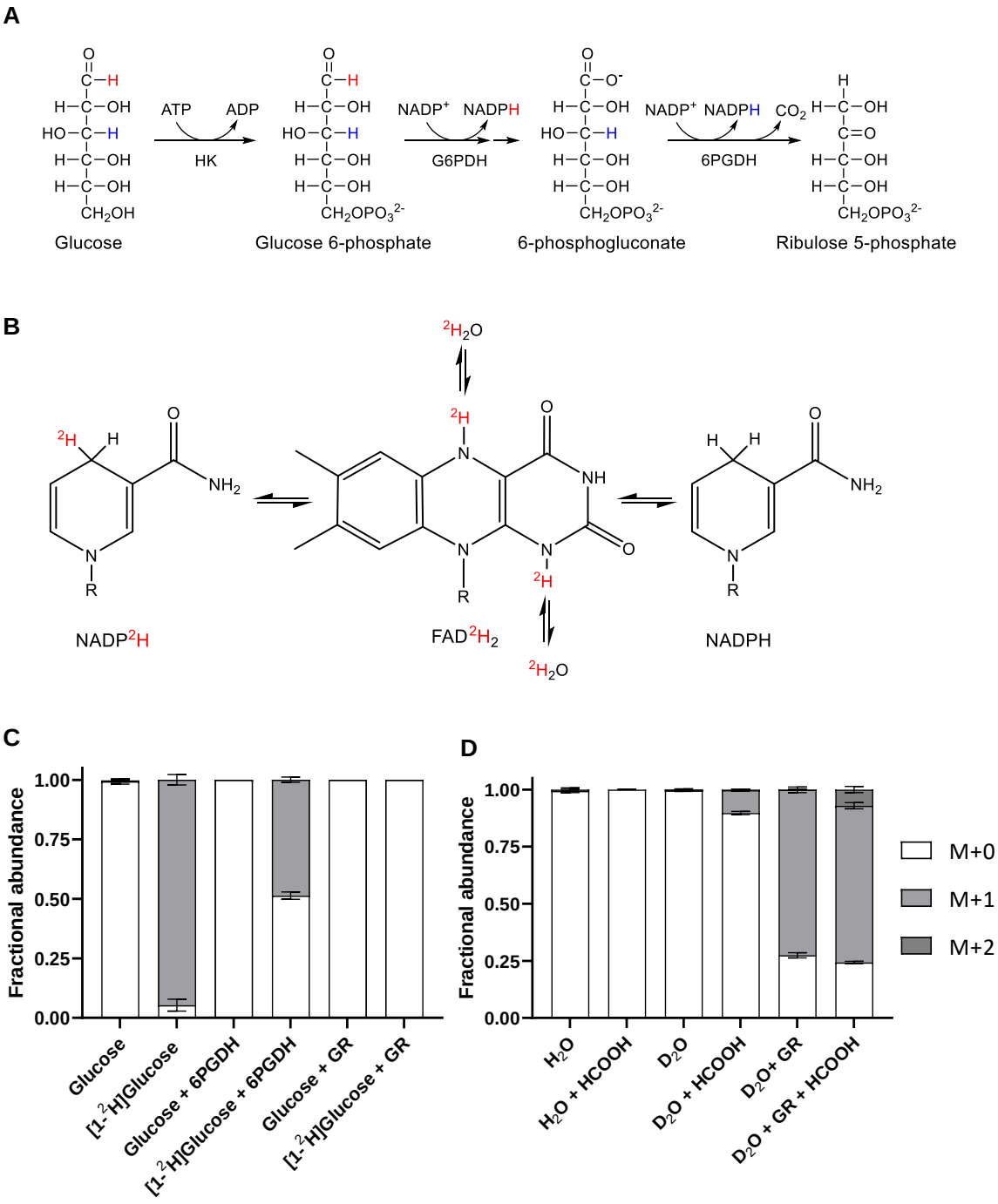

Figure 4.1. Validation of the labelling strategy for quantifying relative NADPH production via the oxPPP. (**A**) The route of deuterium incorporation from 1- (red) or 3- (blue) deuterated glucose into NADPH via hexokinase (HK), glucose 6-phsophate dehydrogenase (G6PDH) or 6-phosphogluconate dehydrogenase (6PGDH). (**B**) The route of hydrogen transfer between NADPH, $FADH_2$ and water catalysed by flavin enzymes. (**C**) Mass isotopologue distribution (MID) of NADPH after 4 h incubation with unlabelled or [1-^{2}H] labelled glucose with hexokinase and G6PDH and in the presence or absence of glutathione reductase (GR) or 6PGDH. (**D**) MID of NADPH after 40 min incubation with GR in either 100% H_2O or 75% D_2O. The reaction was quenched by adding 800 µl of 4 °C quenching solvent, 1:1 MeOH:AcN with or without

0.625% formic acid (HCOOH), to 200 µl of reaction mix. Samples were analysed using Zic-cHILIC chromatography and Xevo G2 XS MS. MIDs are corrected for natural abundance of heavy isotopes using IsoCor (Millard et al., 2012). Values are mean ± SD, n = 3.

4.2.2 Water exchange *in vivo*

To predict if the presence of NADPH-flavin enzymes could cause a significant exchange between NADPH and water in plants, the abundance of NADPH-flavin enzymes was compared in *Arabidopsis thaliana* and *Homo sapiens* proteomes available in PaxDB, an online quantitative proteomic database (Wang et al., 2015) (Figure 4.2). On average, *A. thaliana* proteomes contained more NADPH-flavin enzymes than *H. sapiens (*Mann–Whitney test, $p = 0.0002$), suggesting that flavin-enzyme-catalysed water exchange may be a greater issue in plants than in mammalian cells.

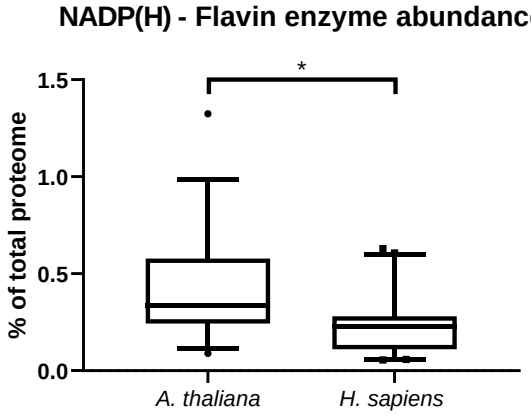

Figure 4.2. Abundance of NADP(H) flavin enzymes in quantitative proteomes of A. *thaliana* and H. *sapiens* from PaxDB (Wang et al., 2015). NADP(H) flavin enzymes were categorized as proteins containing both FAD and NADP(H) binding sites. Data points are from 37 A. *thaliana* proteomes and 40 H. *sapiens* proteomes. Populations are significantly different (Mann-Whitney test, p = 0.0002)

To quantify the hydrogen exchange between NADPH and water via the reaction with flavin-containing enzymes, heterotrophic *Arabidopsis* cells were incubated on media containing 45% D_2O over 4 h and the deuterium incorporation into NADPH and $NADP^+$ quantified by LC-MS. The labelling specifically in the redox active hydride of NADPH was then calculated by deconvoluting the $NADP^+$ mass isotopologue distribution from the NADPH mass isotopologue distribution (Figure 4.3).

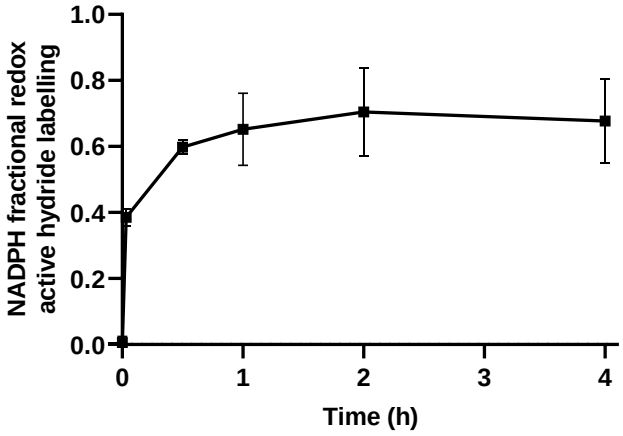

Figure 4.3. NADPH redox active hydride labelling from D_2O. 4-d-old heterotrophic *Arabidopsis* cells were transferred to media containing 45% D_2O and metabolites extracted over 4 h before analysis by ion-pai-reverse-phase (IPRP) chromatography and Quattro Micro MS. Redox active hydride labelling in NADPH was calculated by deconvoluting the $NADP^+$ mass isotopologue distribution from the NADPH mass isotopologue distribution. Values are the mean ± SD, n = 3.

Deuterium was rapidly incorporated into the redox active hydride of NADPH and reached a steady state within 30 min (Figure 4.3), consistent with data from mammalian cell cultures (Zhang et al., 2017). After 1 h, NADPH redox active hydride labelling reached an average of 68% ± 11%. Correcting for the 45% D_2O in the media resulted in an exchange fraction between NADPH and water of 150% ± 24%. An exchange fraction of >100% for a single hydrogen is unexpected but could be explained by exchange of an additional deuterium onto NADPH and not $NADP^+$ at a site separate from the redox active hydride. *In vivo*, $NADP^+$ and NADPH are rapidly interconverted so any deuterium incorporation at sites other than the redox active hydride is accounted for by deconvolution of the MIDs of $NADP^+$ and NADPH. Therefore, the additional exchange may have occurred after metabolism had been quenched and $NADP^+$ and NADPH are no longer rapidly interconverted. Flavin enzymes not effectively inactivated after metabolite extraction could cause this additional exchange and therefore proteomic analysis was performed to identify if any proteins remained in the extract after organic solvent extraction (Figure 4.4). Across four independent cell extracts, 66 flavin-containing, NADPH binding, proteins were identified which may catalyse NADPH–water exchange. There was a significant amount of variability with some proteins only identified in a single sample. This highlights

protein precipitation as a potential source of variability in sample preparation and metabolite extraction. Despite this potential for an additional route of H/D exchange which could occur after metabolic quenching, it is clear that there is extensive exchange between the redox active hydride of NADPH and water, and that this may have implications for the application of deuterium labelling to *Arabidopsis* cell cultures.

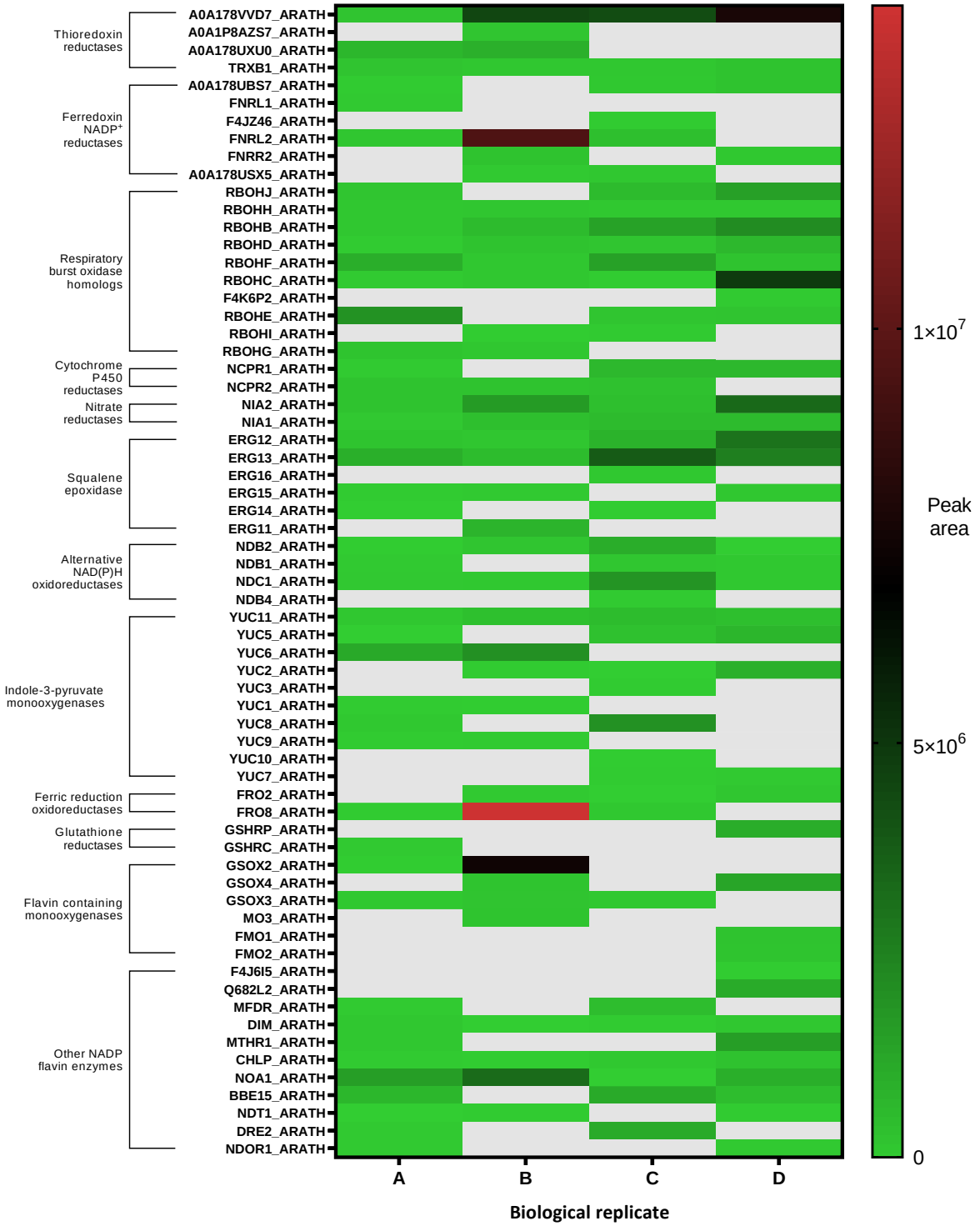

Figure 4.4. The relative abundance of NADP-flavin enzymes identified in heterotrophic *Arabidopsis* cell extracts prior to molecular-weight-cut-off (MWCO) filtration. Cells were extracted using 1:1 MeOH:AcN and filtered using MWCO filters. The filter concentrate was then analysed by trypsin digest proteomics. A-D represent biologically independent replicate samples.

In addition to direct deuterium incorporation into NADPH via flavin-enzyme-catalysed water exchange, deuterium could also be indirectly incorporated into the redox active hydride of NADPH from water via triose phosphates and the oxPPP (Figure 4.5A). Labile hydrogens in the active site of triose phosphate isomerase can exchange with those in water and be transferred onto triose phosphates (Fletcher et al., 1976; Maister et al., 1976; Schleucher et al., 1999). Flux from triose phosphates back to hexose phosphates, as observed using [$^{13}C_6$]glucose in heterotrophic *Arabidopsis* cell cultures (Chapter 3), can then lead to deuterium incorporation into positions within glucose 6-phosphate (G6P) that can be transferred onto NADPH via the oxPPP. This would result in the measured water exchange fraction being dependent on the flux from triose to hexose phosphates and the oxPPP, as well as the rate of flavin-enzyme-catalysed water exchange. Thus, quantifying the extent of labelling of NADPH from D_2O may result in overestimation of the water exchange fraction and calculation of the oxPPP contribution to NADPH production. To determine if this occurred, the MIDs of oxPPP intermediates, G6P, 6PG and Ru5P were measured by LC-MS (Figure 4.5B). The proportion of M+1 and M+2 G6P and 6PG increased over time as deuterium was incorporated from D_2O (Figure 4.5B). Less deuterium was incorporated into Ru5P suggesting that deuterium was transferred onto NADPH from C3 of 6PG via 6PGDH (Figure 4.1A) and therefore not present on Ru5P. This supports the hypothesis that the back flux from triose phosphates to G6P is sufficient to lead to significant label incorporation into NADPH. Ru5P still incorporates deuterium over time (Figure 4.5B), potentially via F6P and transketolases/transaldolases or from the oxPPP via G6P that may also be labelled at C5 (Figure 4.5A).

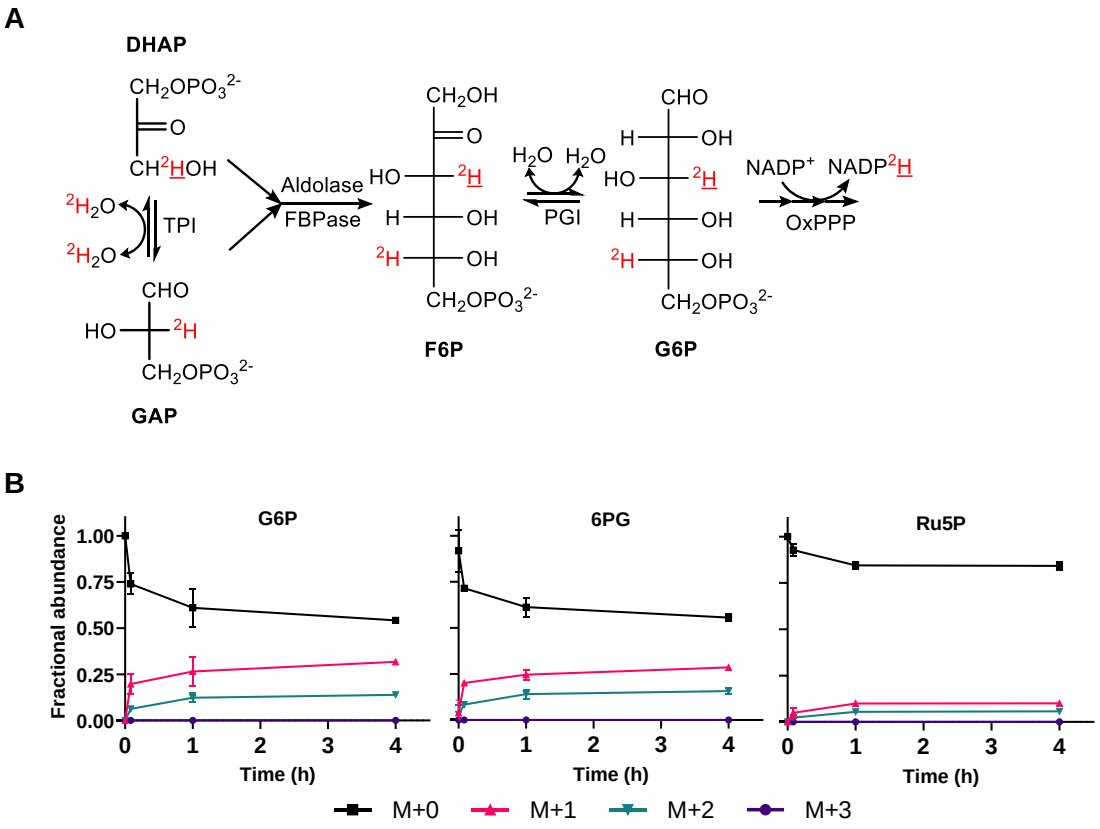

Figure 4.5. Deuterium labelling in pentose phosphate pathway intermediates from triose-/hexose-phosphate exchange following transfer of *Arabidopsis* cells to 45% D_2O. (**A**) The route of deuterium (^2H) incorporation into NADPH via triose phosphate isomerase (TPI) modified from (Schleucher et al., 1999). ^2H represents deuterium which is transferred to the redox active hydride of NADPH (**C**) Mass isotopologue distributions of oxPPP intermediates after incubation of *Arabidopsis* cell cultures on 45% D_2O media for up to 4 h. Samples were analysed using ion-exchange chromatography and Q-Exactive MS and corrected for natural abundance using IsoCor (Millard et al., 2012). Values are the mean ± SD, n = 3.

In summary, incubation of cell cultures on D_2O demonstrated rapid and extensive exchange of the redox active hydride of NADPH with water (Figure 4.3), potentially preventing measurement of deuterium transfer onto the redox active hydride of NADPH from deuterated glucose. In addition, the transfer of deuterium from water to NADPH via triose phosphates and the oxPPP causes overestimation of the water exchange fraction, preventing an accurate estimate of the contribution of the flavin-containing enzymes to water exchange.

4.2.3 [1-^{2}H]Glucose labelling *in vivo*

To establish if [1-^{2}H]glucose can provide specific information about NADPH production from the oxPPP, despite the high rate of water exchange, heterotrophic *Arabidopsis* cells were transferred to media containing 100% [1-^{2}H]glucose and the deuterium incorporation into NADPH and other metabolites was measured by LC-MS (Figure 4.6). The effect of inhibiting the oxPPP using 6-aminonicotinamide (6-AN), an inhibitor of 6PGDH (Garlick et al., 2002; Köhler et al., 1970), was also investigated to determine if the expected NADPH labelling was dependent on the flux through the oxPPP.

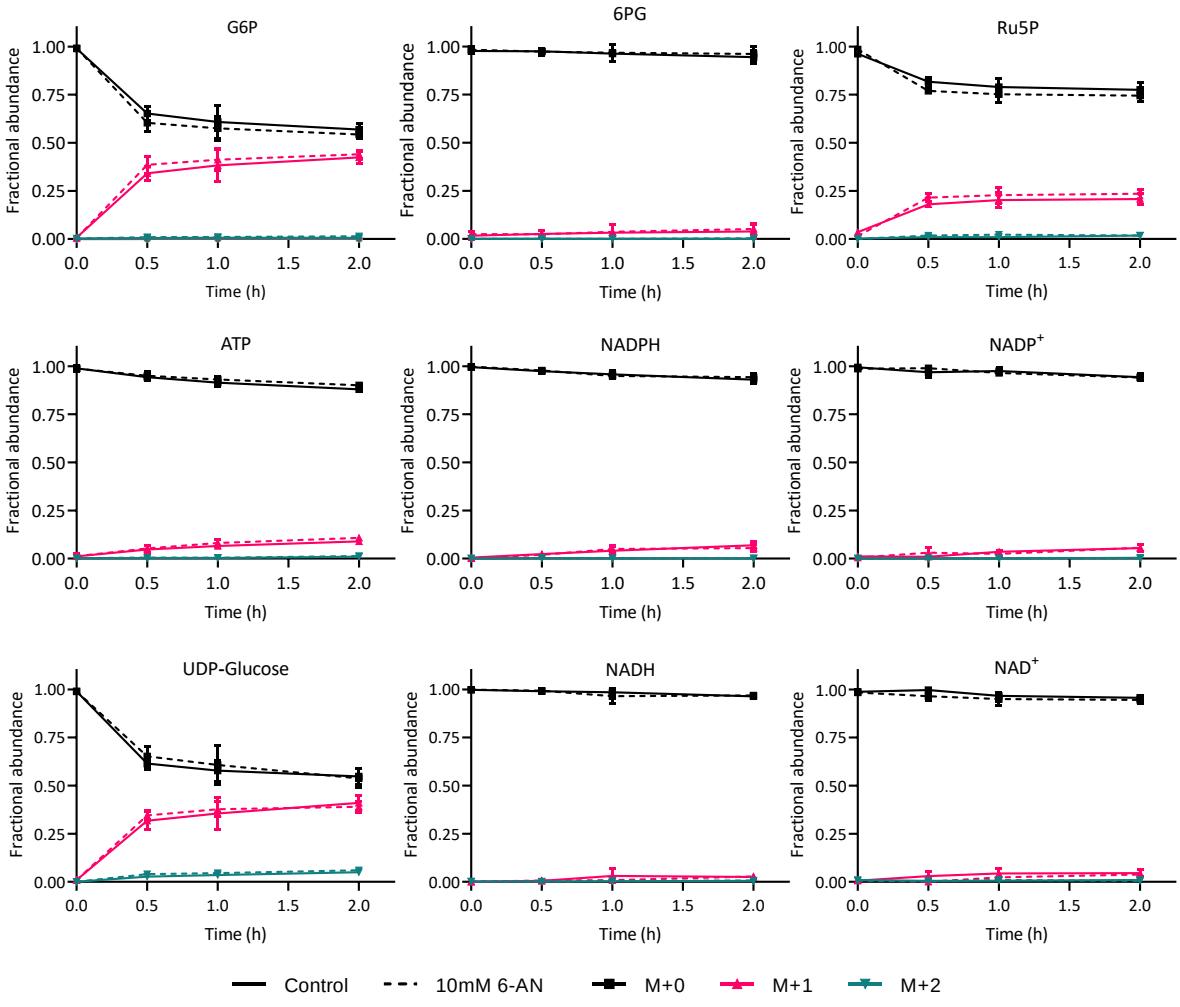

Figure 4.6. Mass isotopologue distributions (MIDs) of metabolites from heterotrophic *Arabidopsis* cell cultures incubated with (- - -) or without (–) 10 mM 6-AN for 20 h before transfer to 100% [1-^{2}H]glucose media for up to 2 h. NAD(P)(H) were quantified using Zic-cHILIC chromatography, Xevo G2 XS MS. Glucose 6-phosphate (G6P), 6-phosphogluconate (6PG), ribulose 5-phosphate (Ru5P), ATP and UDP-

glucose were analysed using ion-exchange chromatography and Qexactive MS. MIDs were corrected for natural abundance using IsoCor (Millard et al., 2012). Values are the mean ± SD, n = 4.

Figure 4.6 shows the incorporation of deuterium over time into oxPPP intermediates. Deuterium is rapidly incorporated into the G6P pool, apparently reaching an isotopic steady state after ~1 h with 43.2 ± 2.7% becoming M+1 labelled. Deuterium was also incorporated into 6PG over time, although to a much lesser extent than G6P. This suggested that deuterium was transferred onto NADPH from G6P and was therefore not present in 6PG. Ru5P showed greater deuterium incorporation than 6PG but less than G6P. Label can be incorporated into Ru5P from glycolytic intermediates and the non-oxidative PPP, similar to the result observed from D_2O labelling (Figure 4.5B).

Label incorporation into Ru5P can lead to downstream labelling of purines and subsequent labelling of the non-redox active hydrogens of NAD(P)(H) from *de novo* synthesis and salvage pathways. NAD is synthesized de novo from aspartate as well as being recycled from various breakdown products (Gakière et al., 2018b). Incorporation of phosphoribosyl phosphonate, derived from ribose 5-phospahte by quinolinate phosphoribosyltransferase, could lead to deuterium incorporation into NAD during *de novo* synthesis. Adenylation of nicotinate mononucleotide (NaMN) using ATP as a substrate could also lead to deuterium incorporation from both *de novo* synthesis and salvage pathways. Following transfer to [1-^{2}H]glucose, deuterium was incorporated into ATP over time as well as NAD^+ and NADH (Figure 4.6). As NADP is synthesised from NAD, this suggested that deuterium was incorporated into the non-redox hydrides of NADP(H) over 2 h.

NADPH can incorporate deuterium into one of two redox active hydrides from [1-^{2}H]glucose via G6PDH (Figure 4.1A). The label incorporation specifically at the redox active hydride of NADPH was calculated by deconvolution of the $NADP^+$ MID from the NADPH MID (Equation 6, Figure 4.7A). Although deuterium was incorporated into both NADPH and $NADP^+$ (Figure 4.7A), labelling of the redox active hydride was not significantly different from zero and did not change over time (one-way ANOVA $p = 0.36$) (Figure 4.7A). Unsurprisingly, inhibition

of the oxPPP by addition of 6-AN had no effect on label incorporation, given that flux through the uninhibited oxPPP did not produce measurable redox active hydride labelling. NADH showed a similar lack of redox hydride labelling (Figure 4.7B), although this was expected as G6PDH is specific to $NADP^+$ (Wakao and Benning, 2005).

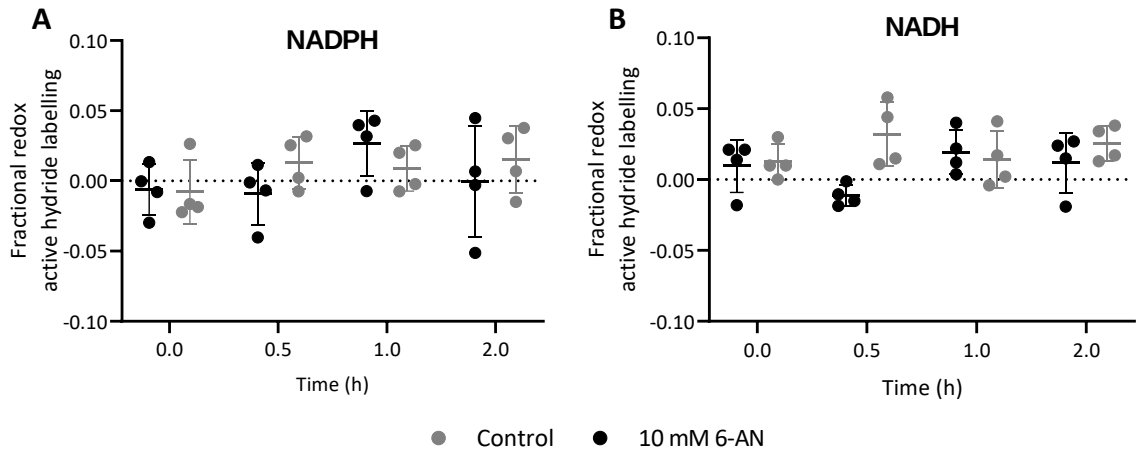

Figure 4.7. Redox active hydride labelling of NADPH and NADH. The effect of 6-AN on NADPH redox active hydride labelling calculated by deconvolution of $NADP^+$ and NADPH MID. Cells were incubated with (•) or without(•) 10 mM 6-AN for 20 h before transfer to 100% [1-^{2}H]glucose media and extracted over 2 h. Samples were analysed using Zic-cHILIC chromatography and Xevo G2 XS MS. Each point is a single biological replicate. Error bars are SD, n = 4.

The ability to measure small amounts of label incorporation depends on the precision of LC-MS analysis. The spectral accuracy of the LC-MS methods used in this study was determined by comparing the MID of unlabelled samples to the expected MID from natural abundance (Figure 4.8). For NADPH extracted from heterotrophic *Arabidopsis* cell cultures, the maximum absolute spectral error of the optimal method using Zic-cHILIC chromatography and Xevo G2 XS mass spectrometry was ± 1.60%, meaning label incorporation lower than this cannot be reliably measured. Ion-pair reverse phase chromatography and Quattro Micro mass spectrometry performed worse with a maximum absolute spectral discrepancy of ± 2.33%.

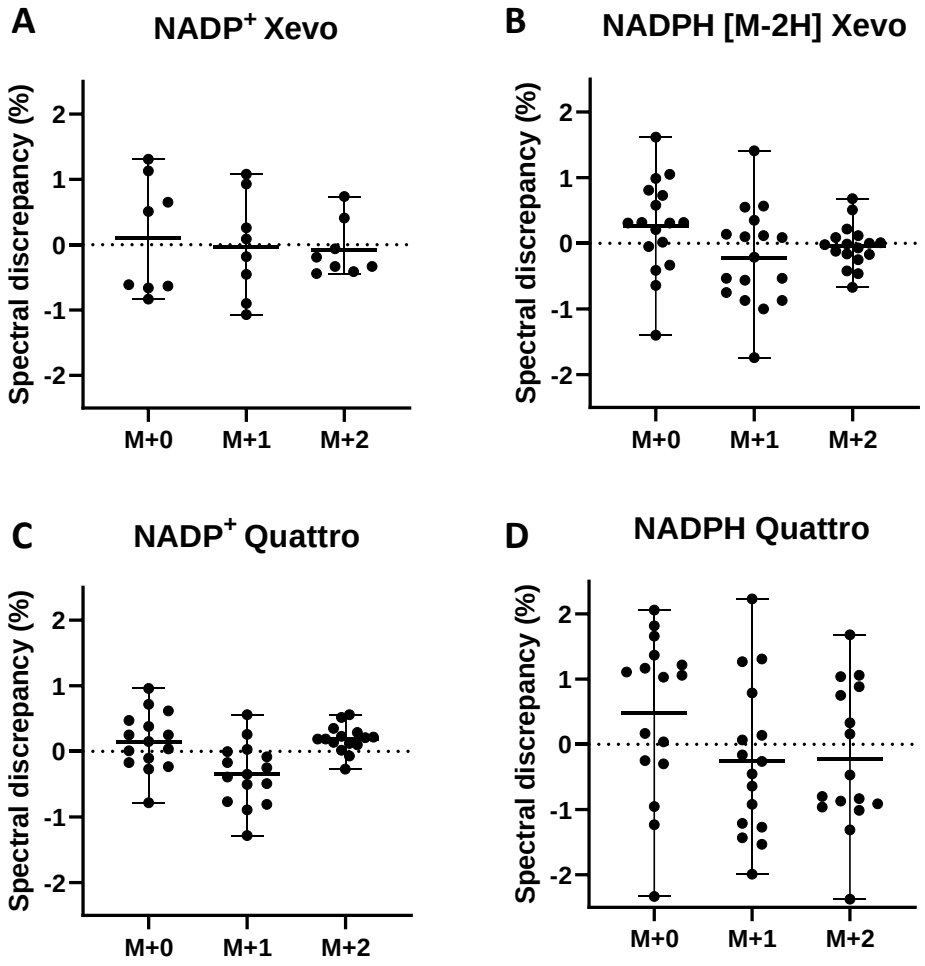

Figure 4.8. Spectral accuracy of NADP(H) mass isotopologue distribution measurement from representative metabolite extracts of heterotrophic *Arabidopsis* cell cultures **A,B**) Zic-cHILIC chromatography and Xevo G2 XS MS **C,D**) Ion-pair reverse phase chromatography and Quattro Micro MS. Spectral discrepancy is the difference between the measured fractional abundance and the predicted fractional abundance from natural abundance of heavy isotopes. Individual values from biological replicates are represented as black circles. Error bars represent maximum and minimum values.

In summary, the data show that there was no net accumulation of deuterium at the redox active hydride of NADPH when [1-^{2}H]glucose was supplied, suggesting that the flux through the oxPPP was much smaller than the rate of flavin-enzyme-catalysed water exchange. Ultimately, the lack of detectable deuterium at the redox hydride of NADPH prevents measurement of the oxPPP contribution to NADPH production in heterotrophic *Arabidopsis* cells under the conditions tested here.

4.2.4 Simulating NADPH Redox Active Hydride Labelling

Deuterium incorporation into the redox active hydride of NADPH is dependent on the contribution of the pathway being measured to total NADPH production, the extent of substrate labelling, the water exchange fraction and the magnitude of any deuterium kinetic isotope effect (KIE) (Equation 4 & 5). To assess the influence of these factors on the label incorporation into NADPH, different values for each of the parameters were simulated and the expected NADPH redox active hydride labelling calculated (Equation 4 & 5).

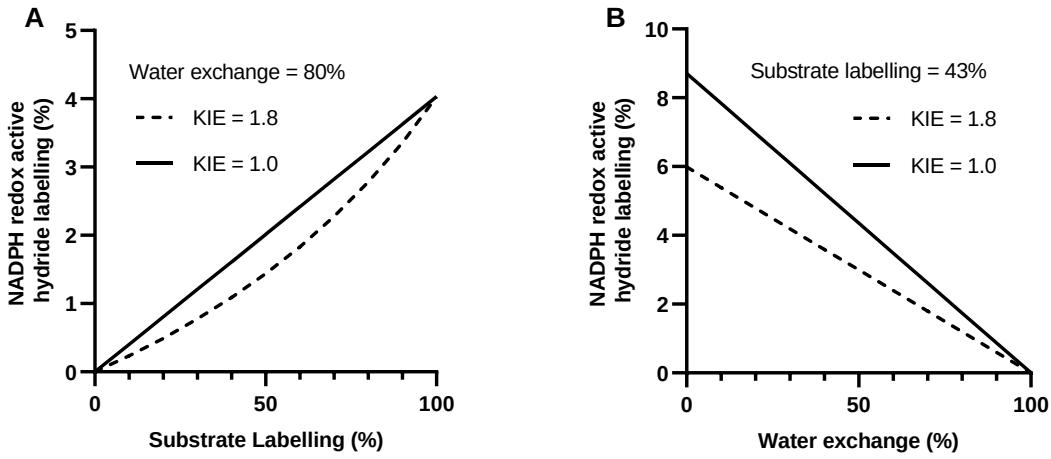

Figure 4.9. The simulated effect of substrate labelling (**A**) and water exchange fraction (**B**) on the NADPH redox active hydride labelling in the presence (---) or absence (–) of a deuterium kinetic isotope effect (KIE) calculated using Equation 4 & 5, methods 2.5.1. The oxPPP contribution to NADPH production was fixed at 40%. **A**) Water exchange was fixed at 80% whilst substrate labelling was varied. **B**) Substrate labelling was fixed at 43% whilst water exchange was varied.

Figure 4.9 shows the effect of different water exchange and substrate labelling fractions on the label incorporation into NADPH, assuming 40% of total cellular NADPH is produced by the oxPPP (Masakapalli et al., 2014). As substrate labelling increases, the NADPH labelling increases (Figure 4.9A) and as water exchange increases, NADPH labelling decreases (Figure 4.9B). The presence of a kinetic isotope effect (KIE) can also decrease the observed NADPH labelling as hydrogen can be preferentially transferred onto NADPH over deuterium. These data highlight the fact that deuterium incorporation into NADPH can be significantly decreased by

high water exchange and low substrate labelling as well as the deuterium kinetic isotope effect, which may differ depending on the enzyme or pathway being analysed.

4.2.5 The effect of subcellular compartmentation

Subcellular compartmentation can affect the interpretation of labelling data from whole cell extracts. Unlike mammalian cells, the oxPPP is present in both the cytosol and plastids of *Arabidopsis* (Kruger and von Schaewen, 2003; Masakapalli et al., 2010) with the potential for different fluxes in each compartment. Depending on the extent of equilibration of substrates and isotopic label between compartments, analysis of whole cell extracts could produce an incorrect estimate of the oxPPP contribution to NADPH production. To identify how subcellular compartmentation could affect the accuracy of the experimental method, a linear model was constructed (Figure 4.10A), and each parameter varied in turn whilst all others remained fixed (Figure 4.10B).

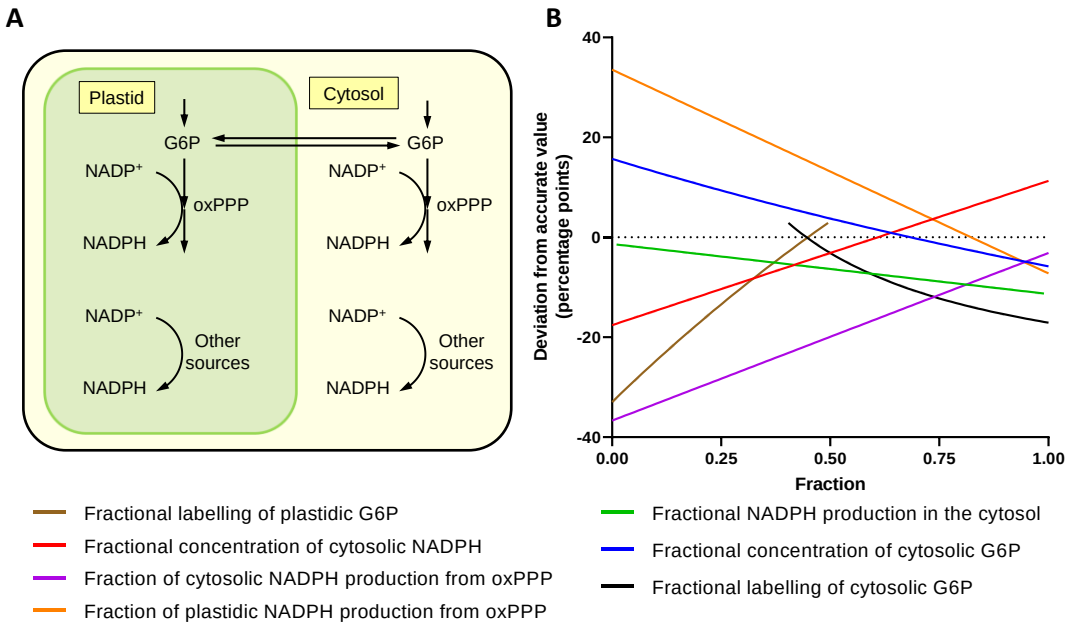

Figure 4.10. The effect of compartmentation on the measurement of the oxPPP contribution to total NADPH production. (**A**) Two compartment model simulating duplicated oxPPP in the cytosol and plastids. (**B**) The deviation of the experimentally measured value for a whole cell extract from the actual value for the oxPPP contribution to total cellular NADPH production. Each parameter was varied between 0 and 1 whilst all other parameters were fixed at the following values: fractional amount of cytosolic G6P, 0.85 (Heise et al., 2015); fractional amount of cytosolic NADPH, 0.5 (Heineke et al., 1991; Igamberdiev and Gardeström, 2003); fractional NADPH production in the cytosol, 0.18 (Masakapalli et al., 2014); fraction

of cytosolic NADPH production from oxPPP, 1.0 (Masakapalli et al., 2014); fraction of plastidic NADPH production from oxPPP, 0.9; fractional labelling of cytosolic G6P, 0.5; and fractional labelling of plastidic G6P, 0.4.

For example, Figure 4.10B shows that if labelling of G6P in the cytosol and plastid does not reach isotopic equilibrium then the measured value of the total oxPPP contribution to NADPH production could be underestimated by up to 30 percentage points (pp). Other parameters also cause deviations (up to 37 pp) depending on how much they differ between compartments. These data highlight the fact that compartmentation can cause variable, non-proportional errors when making calculations based on whole cell extracts, with disequilibrium between cytosolic and plastidic G6P labelling potentially having one of the largest effects.

4.3 Discussion

Deuterium was not detected at the redox active hydride of NADPH after feeding cells with 100% [1-^{2}H]glucose (Figure 4.7A). The lack of redox hydride labelling may be explained by high flavin-enzyme-catalysed water exchange and low substrate labelling, with further complications from triose/hexose phosphate exchange and compartmentation, ultimately confounding the proposed method for measuring the oxPPP contribution to NADPH production in heterotrophic *Arabidopsis* cell cultures.

4.3.1 Flavin-enzyme-catalysed water exchange abolishes detectable labelling from [1-^{2}H]glucose

Flavin enzymes catalyse exchange between NADPH redox active hydride and water via a half reaction that does not require catalytic turnover (Zhang et al., 2017). This was confirmed *in vitro* with glutathione reductase and NADPH in the absence of glutathione, with NADPH completely equilibrating with water (Figure 4.1C,D). In heterotrophic *Arabidopsis* cell cultures, NADPH rapidly incorporated deuterium from D_2O with a water exchange fraction >100% (Figure 4.3). In contrast, mammalian cell cultures show lower water exchange fractions, from 40% to 70% depending on the cell line (Zhang et al., 2017). The higher water-exchange fraction in plants is likely due to a greater abundance of flavin enzymes in *A. thaliana* compared to *H.*

sapiens cell lines, as shown by quantitative proteomic data from PaxDB (Wang et al., 2015) (Figure 4.4). However, the magnitude of the water exchange fraction is ultimately dependent on the relative rates of flavin-enzyme-catalysed water exchange and all other NADPH producing reactions. In some organisms, cell lines, or under certain conditions, the flux through NADPH producing reactions may be slow relative to the flavin-enzyme-catalysed water exchange, preventing detectable accumulation of deuterium at the redox active hydride of NADPH following supply of deuterated substrates, as is the case in heterotrophic *Arabidopsis* cell cultures (Figure 4.7). Deuterium was still incorporated into $NADP^+$ and NADPH (Figure 4.6) at sites other than the redox active hydride most likely from *de novo* synthesis and salvage pathways of NAD metabolism.

4.3.2 Low substrate labelling decreases maximum possible labelling signal

As well as high water exchange, low substrate labelling may also decrease the extent of deuterium incorporation into NADPH below detectable levels (Figure 4.9). In this study, labelling of G6P, the immediate precursor for label transfer to NADPH, reached only 43.2 ± 2.7% M+1 after 2 h (Figure 4.6). This is significantly less than the substrate labelling reported for mammalian cell cultures which ranges from 60% to 100% depending on the cell line and glucose substrate used (Fan et al., 2014; Lewis et al., 2014; Zhang et al., 2017). Deuterium from [1-^{2}H]glucose can be lost due to the reversible interconversion catalysed by a combination of phosphoglucose and phosphomannose isomerases (Ben-Yoseph et al., 1994). Hexose to triose phosphate recycling could also transfer deuterium from carbon one to carbon six of G6P (Fernie et al., 2001). Use of [3-^{2}H]glucose may increase the labelling of G6P by avoiding these losses, although triose-hexose phosphate exchange could still cause loss of deuterium from C3 by exchange with water. In H1299 human cells, use of [3-^{2}H]glucose increased G6P labelling from 68% to 90% (Lewis et al., 2014) although use of [3-^{2}H]glucose did not significantly affect G6P labelling in iBMK cells (Fan et al., 2014). The relatively low level of substrate labelling achieved in *Arabidopsis* cells limits the maximum possible labelling in the redox active hydride of NADPH to 1.9%, assuming a KIE of 1.8 (Shreve and Levy, 1980), an oxPPP contribution of 40%

and a water exchange fraction of 80% (Figure 4.9). This approaches the analytical precision of the LC-MS methodology (Figure 4.8), suggesting that even if the water exchange fraction were lower, accurate measurement of NADPH labelling would remain a challenge.

4.3.3 Metabolic network structure prevents accurate measurement

Although higher rates of NADPH production under certain conditions or in certain cell lines may result in a detectable level of deuterium in the redox active hydride of NADPH, the structure of the plant metabolic network compromises quantitative analysis due to potential overestimation of the water exchange fraction. Cells grown on media containing D_2O can incorporate deuterium into metabolites via any reaction where hydrogen is exchangeable with water. A prominent route in photosynthetic cells is the reduction of $NADP^+$ by ferredoxin-$NADP^+$ reductase, which specifically uses hydrogen from water to produce NADPH. This problem is circumvented in the current study by the use of heterotrophic plant cells and the extraction of metabolites under minimal green light. However, even in heterotrophic tissues, many enzymes in which reaction intermediates possess labile hydrogens such as isomerases, hydratases and aminotransferases, can also incorporate deuterium from water into various metabolites. One such route is via triose phosphate isomerase where deuterium from D_2O can become incorporated onto C3 of DHAP and is retained on C3 of hexose phosphates (Schleucher et al., 1999) (Figure 4.5). *Arabidopsis* cells cultured on 45% D_2O show equivalent labelling patterns in G6P and 6PG but significantly less label incorporation into Ru5P (Figure 4.5), suggesting that deuterium is at C3 of 6PG and specifically transferred to NADPH via 6PGDH. This resulted in NADPH labelling from D_2O being dependent on both flavin-enzyme-catalysed water exchange and triose-phosphate recycling combined with oxPPP flux. Therefore, the water exchange fraction cannot be accurately determined in this system. This is similar to an issue in a mammalian system discussed by Zhang et al., (2017) in which additional deuterium incorporation into malate from D_2O via fumarase is proposed to lead to labelling of NADPH via malic enzyme (ME) and therefore cause overestimation of the water exchange fraction in cells where ME makes a significant contribution to NADPH production. However, fumarase incorporates hydrogen from

water into carbon three of malate (Mescam et al., 2011) but malic enzyme transfers a hydride from carbon two onto NADPH (Tao et al., 2003) meaning that, despite being a rout of deuterium incorporation into the metabolic network, it is not a direct path from water onto NADPH.

Finally, the compartmentation of plant metabolism compromises the accuracy of flux determination from deuterium labelling. In contrast to mammalian cells, the oxPPP in plants is duplicated in the cytosol and plastids (Kruger and von Schaewen, 2003; Masakapalli et al., 2010) and the extent of equilibration between compartments can affect measurements based on whole cell extracts (Figure 4.10). The simple model used in this study was based on just two compartments, whereas in reality, contributions to NADPH supply from the mitochondria and peroxisomes could also affect results, further decreasing the quantitative accuracy of measurements from whole cell extracts. Subcellular deuterium incorporation could potentially be resolved for some metabolites such as G6P where UDP- and ADP-glucose can be used to report on cytosolic and plastidic G6P labelling respectively (Ma et al., 2014). Similar labelling patterns were measured for G6P and UDP-glucose (Figure 4.6), following supply of [1-^{2}H]glucose, suggesting that the G6P from whole cell extracts is representative of the cytosolic pool. This may be due to the relatively high cytosolic concentration of G6P (Gerhardt et al., 1987; Heise et al., 2015; Szecowka et al., 2013), or rapid equilibration between cytosolic and plastidic pools of G6P. However, evidence from ^{13}C MFA of heterotrophic *Arabidopsis* cell cultures shows that cytosolic and plastidic pools of G6P are not in isotopic equilibrium (Masakapalli et al., 2010). Disequilibrium between hexose phosphate pools in different compartments could be quantified by comparing label incorporation in to UDP-glucose and ADP-glucose but unfortunately the concentration of ADP-glucose was too low for reliable analysis in this study.

4.4 Conclusion

Despite the methods explored here having previously been exploited to study redox metabolism in mammalian cell cultures (Chen et al., 2019a; Fan et al., 2014; Lewis et al., 2014; Liu et al., 2016; Zhang et al., 2017), several factors confound the use of the same approach in

plant cells. The plant metabolic network is markedly different from that of mammals, being more compartmented and interconnected. These differences affect the interpretation of deuterium labelling experiments, ultimately preventing the quantitative measurement of the oxPPP contribution to total NADPH production. Low substrate labelling and high water-exchange combine to produce a level of NADPH labelling that is close to, or below, the limit of analytical detection. Even if analytical precision were improved, the accuracy of the estimates is likely to be compromised due to overestimation of the NADPH–water exchange fraction and potential errors introduced by compartmentation. Overall, the findings presented in this chapter provide a framework for establishing deuterium labelling strategies to quantify redox fluxes in organisms other than mammalian cells. Although it is disappointing that the method is not tenable in heterotrophic *Arabidopsis* cell cultures, these tools will hopefully still provide insight into other biological systems in the future.

Chapter 5: Fluorescent biosensors for redox metabolites

5.1 Introduction

The previous two chapters have attempted to address the underlying fluxes supporting redox metabolism in plants through the balanced production and consumption of the redox coenzymes NADH and NADPH. However, in many situations production and consumption of redox coenzymes are not perfectly balanced and their concentrations can change over time (Verhagen et al., 2020). Metabolic networks must adapt to changing conditions and move from one metabolic steady state to another to maintain biological function. Quantifying metabolism during this dynamic phase can be useful for understanding the underlying control structure of metabolism (Ratcliffe and Shachar-Hill, 2006). Various approaches are available for understanding dynamic changes in metabolism including kinetic modelling and dynamic flux analysis (Antoniewicz, 2013; Wahl et al., 2008). Any method to assess dynamics in metabolism requires measurement of metabolite concentrations over time, ideally at subcellular resolution. Even without integration into kinetic models, changes in concentrations can reveal perturbations of metabolism and can be useful for evaluating competing hypotheses. Therefore, quantification of concentrations and redox potentials of the coenzymes NADH and NADPH is useful for understanding redox metabolism in plants.

5.1.1 Quantifying NAD(P)(H) concentrations and ratios

The concentrations of NAD(P)(H) and ratios of reduced and oxidised forms differ considerably between tissues, cells and subcellular compartments, and therefore specific, non-averaged information is key to quantifying NAD(P)(H) metabolism (Heineke et al., 1991; Herber and Santarius, 1965; Igamberdiev and Gardeström, 2003; Szal et al., 2008; Wigge et al., 1993). Analytical methods for quantifying pyridine nucleotides are destructive, relying on total cell extraction and averaging of different NAD(P)(H) pools followed by enzymatic or LC-MS based analysis (Lu et al., 2018; Zhang et al., 2020). Subcellular fractionation methods aim to measure compartment specific concentrations, but artefacts can arise during extraction from exchange

between compartments and interconversion of reduced and oxidised species (Dietz, 2017). Recently developed techniques using rapid affinity purification of organelles attempt to overcome these limitations (Luo et al., 2020), but can still suffer from metabolite loss and rapid redox interconversion during extraction (Niehaus et al., 2020). Non-aqueous fractionation provides the current best estimates of subcellular NAD(P)(H) concentrations by fixing metabolism prior to extraction, but methods are generally laborious, and can still give incomplete resolution of subcellular compartments (Heineke et al., 1991; Herber and Santarius, 1965; Igamberdiev and Gardeström, 2003; Szal et al., 2008; Wigge et al., 1993). Therefore, a non-invasive organelle specific measurement tool is required.

5.1.2 NAD(P)H autofluorescence

The intrinsic autofluorescence of NAD(P)H can provide a dynamic non-invasive measure of total NAD(P)H concentration (Chance et al., 1962; Schaefer et al., 2019). However, application to plants has been limited to measurement of isolated organelles due to the high intensity UV radiation required and interference from other fluorescent components (Kasimova et al., 2006). Additionally, due to the relatively high concentration of NAD(P)H in the mitochondria, quantification of NAD(P)H autofluorescence in other subcellular compartments is challenging. Furthermore, the fluorescence spectra of NADH and NADPH are not distinguishable and the oxidised forms ($NAD(P)^+$) are not fluorescent at all. Recently, fluorescence lifetime imaging has been used to distinguish between protein bound NADPH and NADH (Blacker and Duchen, 2016; Blacker et al., 2014) but this method is technically demanding due to the pulsed UV lasers required, and has not yet been established in plants. Genetically encoded fluorescent biosensors offer a possible solution allowing real-time, non-destructive, measurement of dynamic changes in concentrations of specific metabolites with greater temporal and spatial separation than other methods.

5.1.3 Genetically encoded fluorescent biosensors

Biosensors for many metabolites have been applied to plants (Walia et al., 2018), including sensors for calcium (Walia et al., 2018), potassium (Wang et al., 2020), zinc (Lanquar

et al., 2014), chloride (Lorenzen et al., 2004), pH (Gjetting et al., 2012), glucose (Chaudhuri et al., 2008), glutamate (Toyota et al., 2018), ATP (De Col et al., 2017), phosphate (Sahu et al., 2020), abscisic acid (Waadt et al., 2020), auxin (Herud-Sikimic et al., 2020), gibberellin (Rizza et al., 2017), hydrogen peroxide (Costa et al., 2010) and, glutathione (Schwarzländer et al., 2008) as well as thioredoxin redox potential (Sugiura et al., 2019). The basic principle of metabolite sensitive fluorescent biosensors is to fuse a ligand binding domain to one or two fluorescent proteins, coupling a conformational change upon ligand binding to a change in fluorescence. Two fluorescent signals are required to allow ratiometric analysis which generates an internally normalised signal independent of the biosensor protein expression level. Absolute ligand concentrations can then be calculated by determining the binding and response properties of sensors *in vitro*, and by *in vivo* calibration. The main disadvantages of fluorescent biosensors are the measurement of only a single parameter at a time, the need for genetic transformation, and the risk of potential artefacts caused by pH or inaccurate calibration. The advantages of fluorescent biosensors over analytical methods are: the ability to measure real time kinetics of transient events, such as the initiation of photosynthesis; strict cell type, tissue or compartment specificity through the use of subcellular localisation tags or specific promoters; and exquisite specificity for the analyte they measure. These advantages cannot be achieved with any other method.

5.1.4 SoNar, iNap and Peredox-mCherry are NAD(P)(H) sensors expressed in plants

Just three of the growing number of fluorescent protein-based NAD(P)(H) biosensors (Zhao et al., 2017b) have been expressed in plants so far: two different NADH:NAD^+ ratio sensors, SoNar and Peredox-mCherry; and the NADPH sensors of the iNap family (Lim et al., 2020; Steinbeck et al., 2020) (Figure 5.1). These sensors have already been used to initiate the exploration of several aspects of plant biology including: reductant flow during photosynthesis and photorespiration (Lim et al., 2020), immune responses (Steinbeck et al., 2020), stomatal development (Feitosa-Araujo et al., 2020b), hypoxia (Wagner et al., 2019), and tissue specific differences in pyridine nucleotides (Steinbeck et al., 2020). However, this work has only set a

starting point and there are a number of questions still to be explored, particularly by analysing multiple sensors for redox metabolites in parallel.

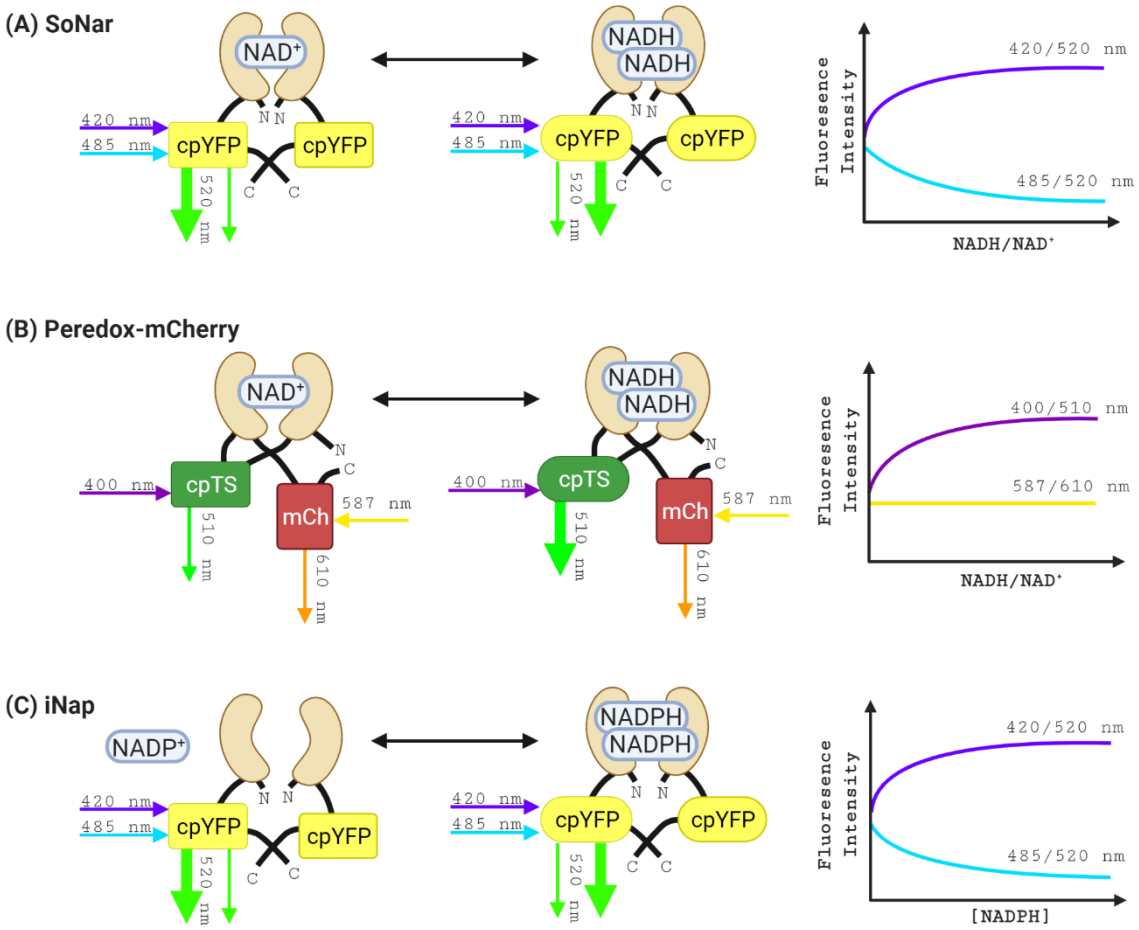

Figure 5.1. The structure and binding properties of SoNar, Peredox-mCherry and iNap. (**A**) SoNar is a dimer made from monomers containing a cpYFP (circularly permuted yellow fluorescent protein) and a Rex domain. The dimer is able to bind both NAD^+ and NADH (Zhao et al., 2015). Binding of NADH causes an increase in cpYFP fluorescence intensity at excitation (Ex) 420 nm/ emission (Em) 520 nm whilst binding of NAD^+ causes an increase in fluorescence intensity at Ex 485 nm/ Em 520 nm. (**B**) Peredox-mCherry is made from a cpTS (circularly permuted T-Sapphire) and two Rex binding domains fused to an mCherry fluorescent protein at the C-terminus (Hung et al., 2011). Binding of NADH causes an increase in fluorescence intensity at Ex 400 nm/ Em 510 nm of cpTS whilst NAD^+ competes for binding but has no direct effect on fluorescence. mCherry fluorescence at Ex 587 nm/ Em 610 nm is insensitive to NAD(H) concentration and provides an internal normalisation. (**C**) iNap is a modified form of SoNar, also made from a cpYFP and Rex domain but mutated to change the binding specificity to bind NADPH only (Tao et al., 2017). Binding of NADPH causes an increase in fluorescence intensity at Ex 420 nm/ Em 520 nm and a decrease in fluorescence intensity at Ex 485 nm/ Em 520 nm. Figure was created with BioRender.com.

5.1.5 Redox metabolites are connected

NADPH and NADH are not in thermodynamic equilibrium but are still connected by kinetically controlled enzyme catalysed reactions. This means that under appropriate conditions electrons can flow from NADH to $NADP^+$ or from NADPH to NAD^+. A major example of this is net export of NADH from chloroplasts in the light via the malate/OAA shuttle (Selinski and Scheibe, 2018). NADPH is consumed to generate malate from OAA in the chloroplasts which is then exported and converted back to OAA in the cytosol to make NADH. The activity of and direction of the malate valve is dependent on the more negative redox potential of NADPH in the chloroplast in the light compared to the redox potential of NADH in the cytosol. SoNar, Peredox-mCherry and iNap all report changes in NAPDH and NADH consistent with the hypothesis of reductant export from chloroplast in the light (Elsässer et al., 2020; Lim et al., 2020; Steinbeck et al., 2020). Other situations may also require interconversion of pyridine nucleotides, or shuttle systems to transport reducing equivalents between subcellular compartments, and fluorescent biosensors could be useful in identifying these.

Along with the pyridine nucleotides, glutathione is also a major player in the redox metabolism of plants (Noctor et al., 2012)(see section 1.2.2). The disulphide form, GSSG, is continually reduced to GSH by glutathione reductase using NADPH (Kubo et al., 1993) and therefore the glutathione redox potential is dependent on an adequate supply of NADPH. Under non-stress conditions glutathione is highly reduced providing reductant for thiol signalling networks as well as detoxifying reactive oxygen species (Gill et al., 2013; Noctor et al., 2012). Biosensors for glutathione redox potential have been established in plants and their use has become more routine than the recently applied NAD(P)(H) sensors (Müller-Schüssele et al., 2021; Schwarzländer et al., 2016). In this chapter I will also use the sensor cyt-GRX1-roGFP2 to measure relative changes in the glutathione redox potential in the cytosol.

By quantifying the concentrations or redox potentials of these metabolites in parallel, connections between compartments and metabolites can be identified as well as coordinated responses to changing external demands. Fundamentally, measuring concentrations alone cannot

quantity the flow of electrons from one metabolite to another. However, by applying treatments which induce specific demands for reductant, correlations between metabolites or compartments can still be informative.

The objective of this chapter is to quantify the effects of redox stress on redox metabolites using genetically encoded fluorescent biosensors, and to compare and evaluate the currently available biosensors for this purpose. To achieve this, I characterised transgenic plants expressing biosensors for NADPH in the cytosol, plastids and peroxisomes, NADH:NAD^+ ratio in the cytosol and plastids, and glutathione redox potential in the cytosol. Leaf disks in the dark were used for all experiments due to the ease of parallel comparison using multiwell fluorometry, and for comparison with previous data employing the same experimental system (Steinbeck et al., 2020; Wagner et al., 2019). To evaluate the effectiveness of the available biosensors, I quantified the effect of treatments which increase the cellular demand for NAPDH including menadione, nitrite, hypoxia and the immune elicitor flg22.

5.2 Results

5.2.1 Fluorescent spectra of biosensors

Transgenic seeds were donated by Boon Leong Lim (BL), University of Hong Kong, and Markus Schwarzländer (MS), University of Münster. Expression of all iNap and SoNar variants was controlled by a CaMV 35S promoter but different expression plasmids were used for cyt-iNap2 and cyt-iNapC-A (donated by MS) compared to the remaining iNap and SoNar lines (donated by BL) (Lim et al., 2020). Expression of Peredox-mCherry was controlled by the *UBIQUITIN10* promoter (Steinbeck et al., 2020). Properties of the biosensors used in this chapter are described in Table 5.1

Table 5.1. Fluorescent biosensors analysed in this chapter. Plast – plastids, Cyt – cytosol, Perox – Peroxisomes. [a]Ex- excitation wavelength (nm), Em – emission wavelength (nm).

Sensor	Metabolite	Kd or mid-point potential	Subcellular localisation	Fluorescence Ex/Em[a]	pH sensitive	Notes	Refence
iNapC	-	-	plast, cyt, perox	420/520 482/520	No Yes	NAD(P)H insensitive control sensor for pH correction of iNap and SoNar	(Lim et al., 2020; Tao et al., 2017)
iNap1	NADPH	0.29 µM	plast, cyt, perox	420/520 482/520	No Yes	High affinity NADPH sensor	(Lim et al., 2020; Tao et al., 2017)
iNap2	NADPH	6 µM	cyt	420/520 482/520	No Yes	Mid-affinity NADPH sensor	(Tao et al., 2017)
iNap4	NADPH	30 µM	plast, cyt, perox	420/520 482/520	No Yes	Low affinity NADPH sensor	(Lim et al., 2020; Tao et al., 2017)
SoNar	NADH:NAD^+	K_{ratio} 0.036	plast, cyt	420/520 482/520	No Yes	True ratio sensor as signal is dependent on both NADH and NAD^+	(Lim et al., 2020; Zhao et al., 2015)
Peredox-mCherry	NADH:NAD^+	K_{ratio} 0.0024	cyt	400/530 570/610	No No	An NADH sensor compensated by NAD^+ concentration – total pool or NAD^+ concentration must be considered	(Steinbeck et al., 2020)
GRX1-roGFP2	E_{GSH}	-270 mV	cyt	400/530 482/530	No No	Thiol based sensor sensitive to glutathione redox potential	(Gutscher et al., 2008)
ATeam	$MgATP^2$	50 µM	cyt	435/485 435/540	No No	FRET-based sensor specific to $MgATP^{2-}$	(Voon et al., 2018)

To confirm the spectral properties of transgenic plants, and that biosensors were expressed at sufficiently high levels for analysis, fluorescence spectra were recorded in leaf disks of 4- to 6-week-old *Arabidopsis* plants using a fluorescence plate reader (Figure 5.2-6).

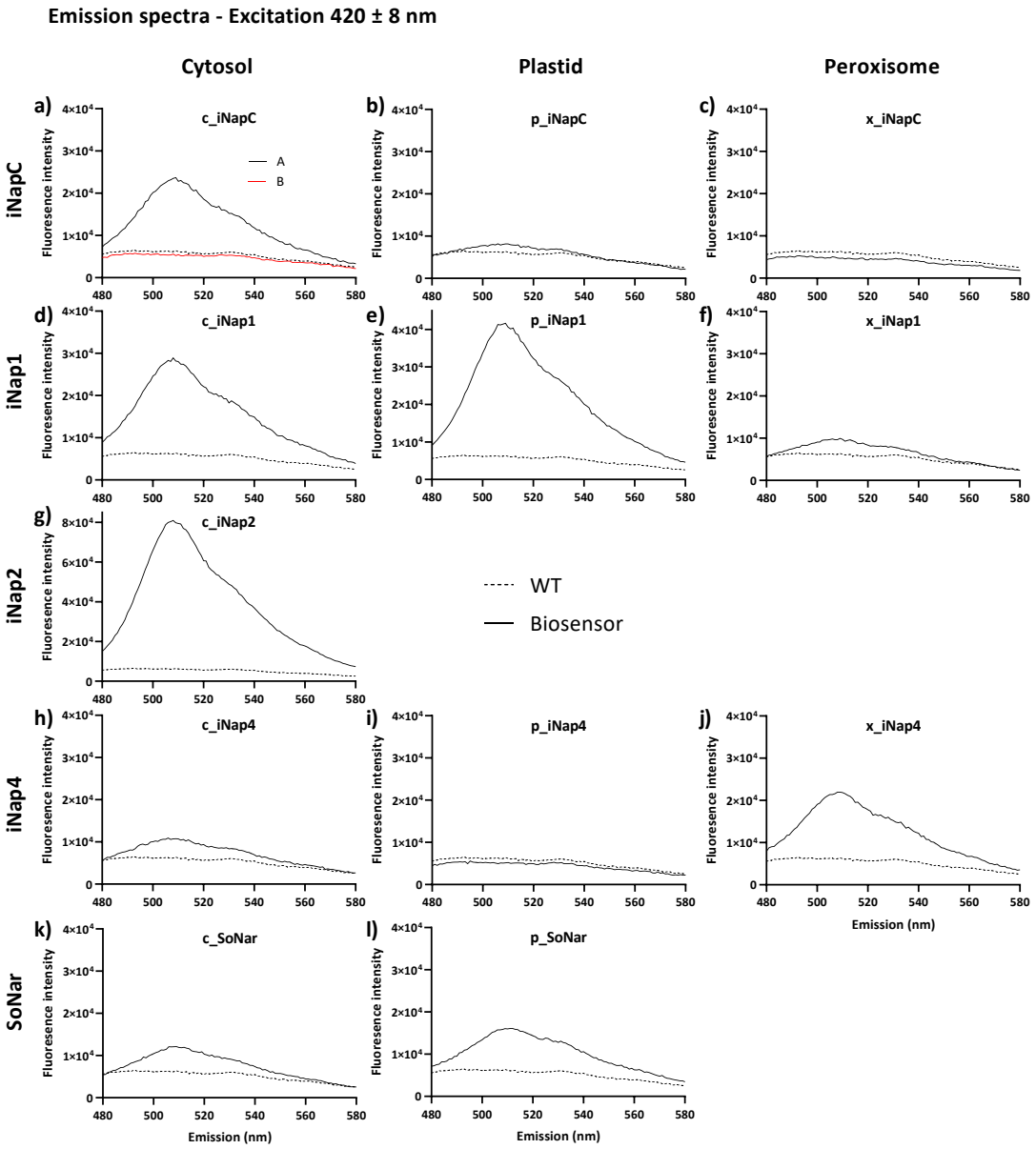

Figure 5.2. Representative emission spectra of iNap and SoNar variants expressed in *Arabidopsis*. Leaf disks of 4- to 6-week old plants were analysed in 96 well plates using a fluorescent plate reader with excitation at 420 ± 8 nm. Emission bandwidth 8 nm, identical signal gain was used across samples. Solid line is transgenic plant expressing biosensor, dashed line is WT control. Two separate transgenic lines of cytosolic iNapC were compared, cyt-iNapC-A black line, cyt-iNapC-B pink line.

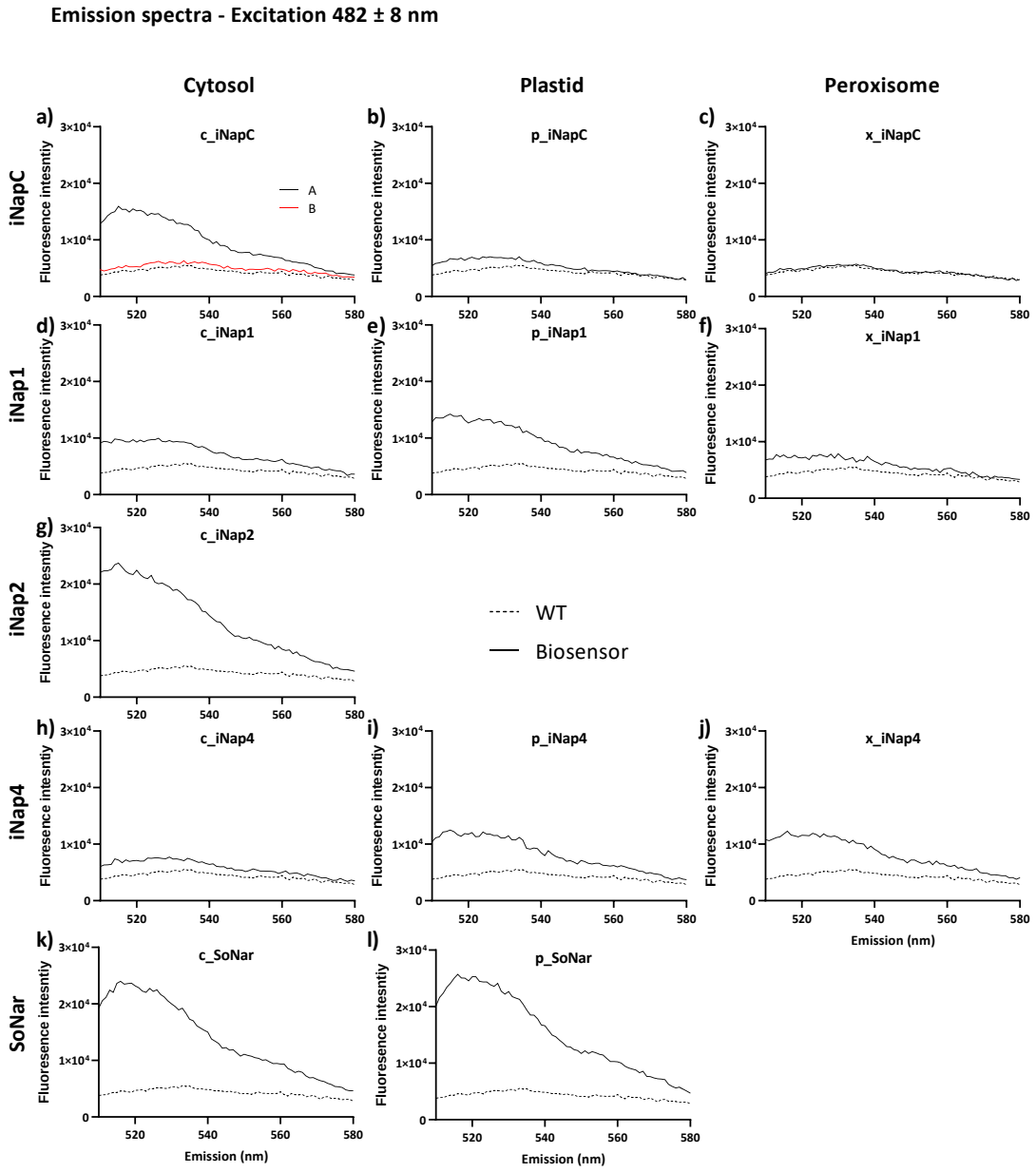

Figure 5.3. Representative emission spectra of iNap and SoNar variants expressed in *Arabidopsis*. Leaf disks of 4- to 6-week old plants were analysed in 96 well plates using a fluorescent plate reader with excitation at 482 ± 8 nm. Emission bandwidth 8 nm. Solid line is transgenic plant expressing biosensor, dashed line is WT control. Two separate transgenic lines of cytosolic iNapC were compared, cyt-iNapC-A black line, cyt-iNapC-B pink line.

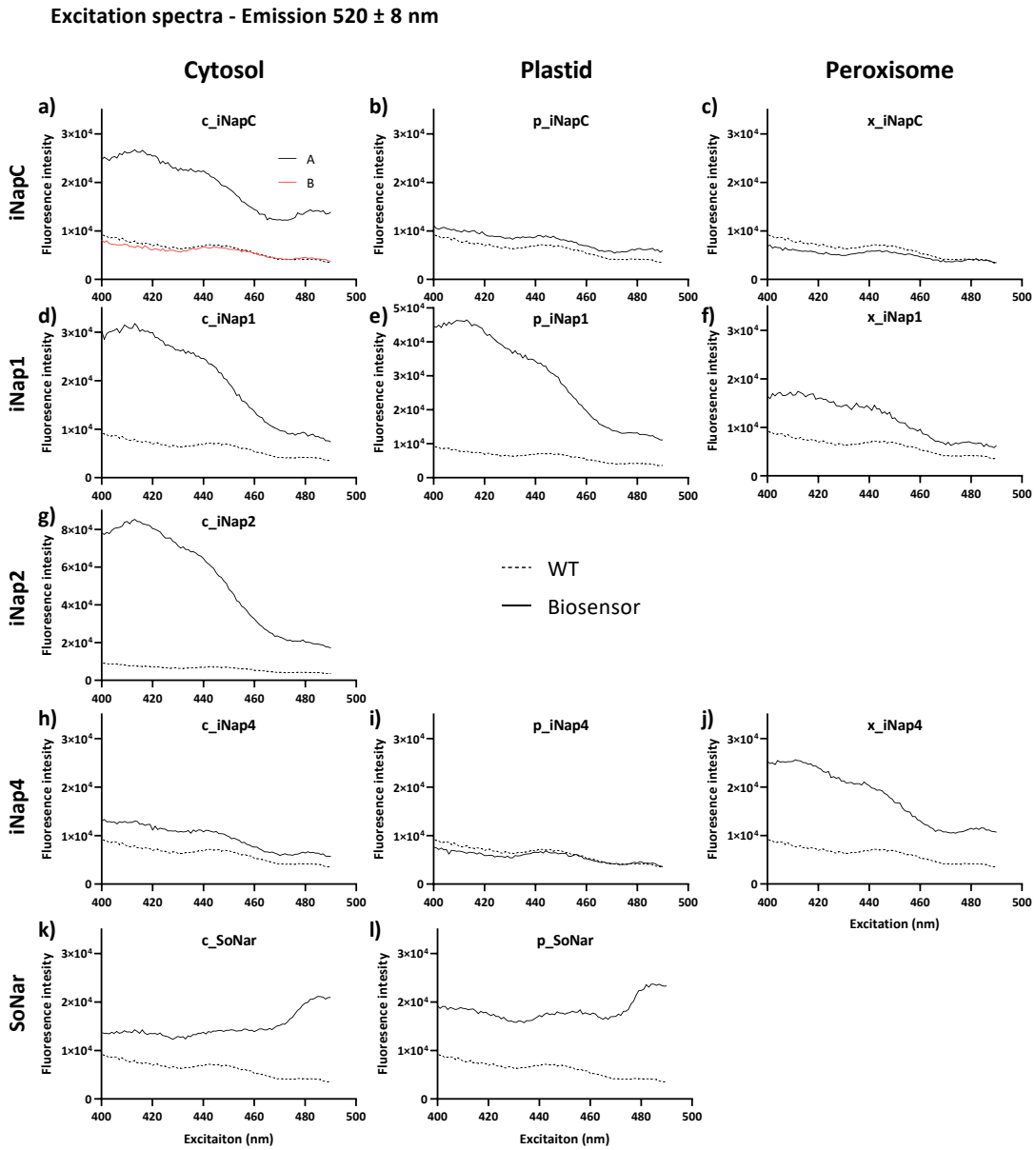

Figure 5.4. Representative excitation spectra of iNap and SoNar variants expressed in *Arabidopsis*. Leaf disks of 4- to 6-week old plants were analysed in 96 well plates using a fluorescent plate reader with emission at 520 ± 8 nm. Excitation bandwidth 8 nm. Solid line is transgenic plant expressing biosensor, dashed line is WT control. Two separate transgenic lines of cytosolic iNapC were compared, cyt-iNapC-A black line, cyt-iNapC-B pink line.

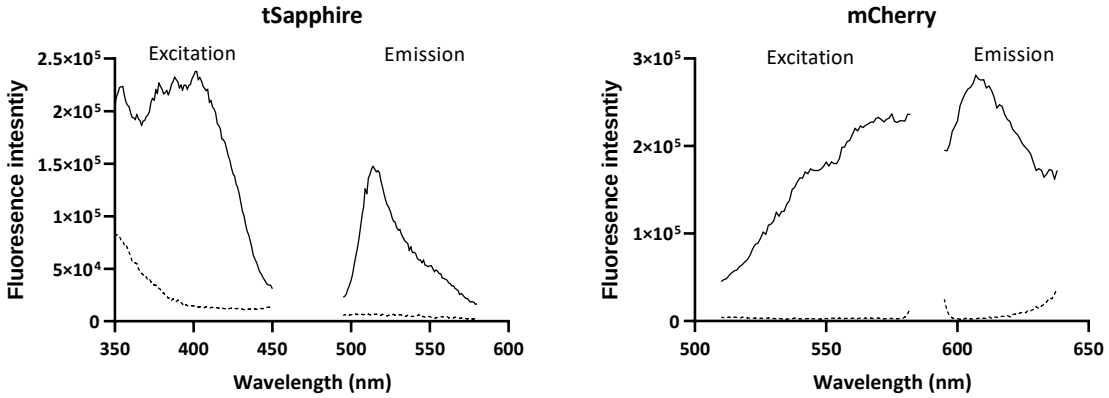

Figure 5.5. Representative fluorescence spectra of Peredox-mCherry in leaf disks of *Arabidopsis*. Leaf disks of 4- to 6- week old plants were analysed in 96 well plates using a fluorescent plant reader. Solid line - transgenic plant, dashed line - WT plant. tSapphire excitation was measured at emission 530 ± 20 nm and emission measured at excitation 400 ± 8 nm. mCherry excitation was measured at emission 610 ± 16 nm and emission measured at excitation 570 ± 10 nm.

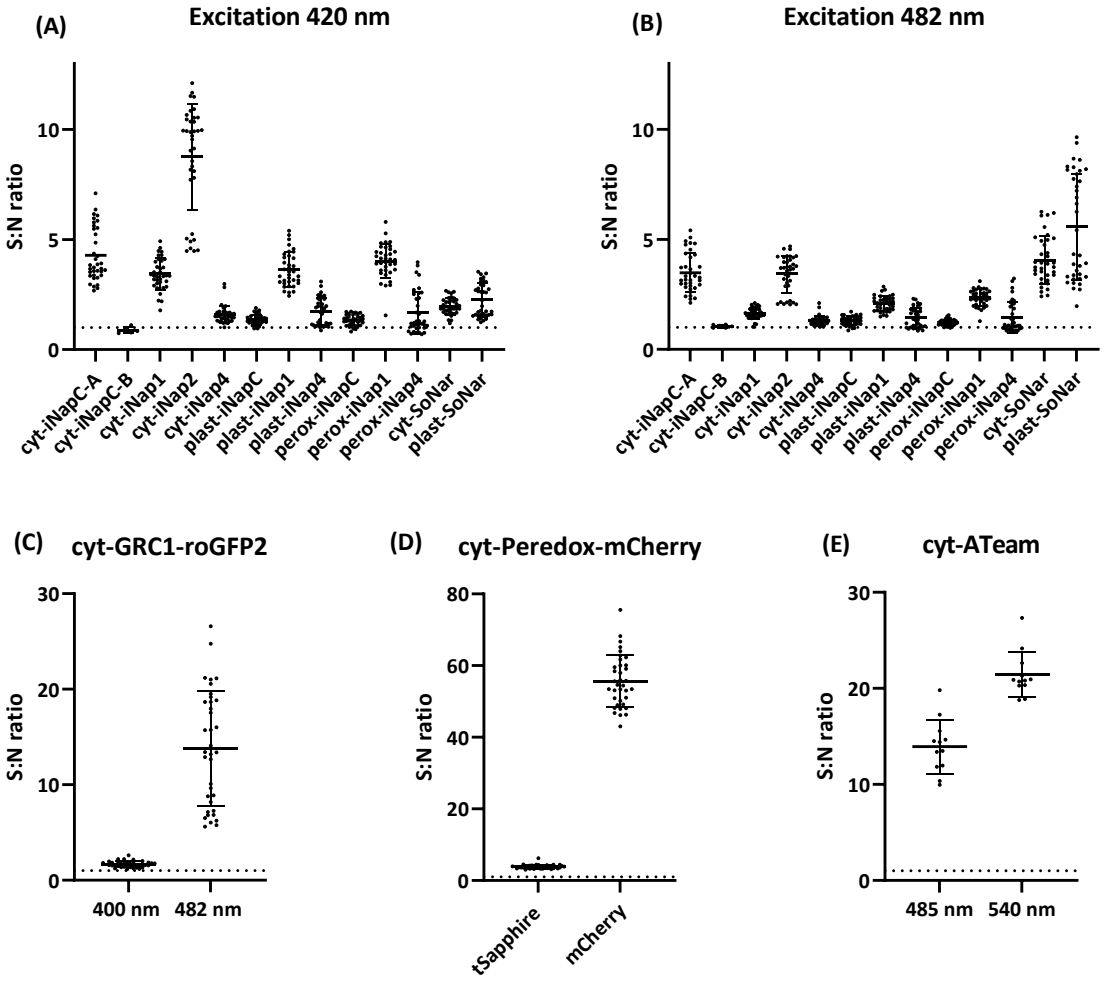

Figure 5.6. Signal:noise (S:N) ratios of fluorescent sensors expressed in *Arabidopsis*. Leaf disks of 4- to 6-week old plants were analysed in 96 well plates using a fluorescent plate reader. **A)** S:N ratio of iNap and SoNar variants from fluorescence intensity at 520 ± 20 nm from excitation at 420 ± 15 nm. **B)** S:N ratio of iNap and SoNar variants from fluorescence intensity at 520 ± 20 nm from excitation at 482 ± 8 nm. **C)** S:N ratio of cyt-GRX1-roGFP2 from fluorescence intensity at 530 ± 20 nm from excitation at 400 ± 8 nm and 482 ± 8 nm. **D)** S:N ratio of cyt-Peredox-mCherry, tSapphire excitation 400 ± 8 nm, emission 530 ± 20 nm and mCherry excitation 570 ± 10 nm, emission 610 ± 8 nm. **E)** S:N ratio of cyt-ATeam from fluorescence intensity at 485 ± 10 nm and 540 ± 8 nm from excitation at 435 ± 10 nm. Noise was defined as the fluorescence of WT Col-0 plants at the same excitation/emission wavelengths as the biosensor. Dashed line represents a S:N ratio of 1. Bars are the mean ± SD $n \geq 6$.

SoNar and iNap have two fluorescence excitation maxima at 420 nm and 482 nm measured by emission at 520 nm (Tao et al., 2017; Zhao et al., 2015) and the majority of transgenic plants expressing these sensors were fluorescent at these expected wavelengths (Figure 5.2-4). However, when comparing the fluorescence signal to the background fluorescence in WT

plants, Cyt-iNap4, plast-iNapC, plast-iNap4, perox-iNapC and perox-iNap4 showed poor signal to noise ratios (Figure 5.6). The low fluorescence of perox-iNapC and plast-iNapC made subsequent pH correction impossible for peroxisomal sensors and added a large amount of variability to plastidic sensors in subsequent experiments. Cyt-iNapC-B was not fluorescent above background at all (Figure 5.6A,B) and therefore subsequent analysis used cyt-iNapC-A. Despite using the same CaMV 35S promoter, the transgenic iNap expressing plants from MS show higher S:N ratios compared to the iNap expressing plants from BL (Figure 5.6). The other sensors used in this chapter, peredox-mCherry, GRX1-roGFP2 and ATeam, all showed much higher S:N ratios than iNap and SoNar expressing plants.

There was substantial variability in overall fluorescence intensity and subsequent signal to noise ratios between plants and between separate leaves within a plant. This highlights the importance of quantifying ratios of fluorescence to internally normalise for variation in sensor expression level between plants or tissues.

5.2.2 Confocal microscopy confirms subcellular localisation of biosensors

Subcellular localisation of biosensors was achieved by fusion to specific targeting sequences, chloroplast transketolase transit peptide (TKTP) from *Nicotiana tabacum* and peroxisomal targeting signal type 1 (SRL) (Lim et al., 2020). Expression of biosensors without specific targeting sequences was used for cytosolic localisation. To confirm the subcellular location of targeted sensors, confocal microscopy was used to quantify fluorescence in different tissues of 3- to 5- day-old *Arabidopsis* seedlings (Appendix B.1). Fluorescence was detected in the expected subcellular location for all sensors. Fluorescence signal intensity of iNapC was very low for cyt-iNapC-B (BL) (Appendix B.1.2). Fluorescence intensity of peroxisomal iNapC was very dim in autotrophic tissues and could only be reliably identified in roots (Appendix B.1.7), consistent with the low signal to noise ratio measured in leaf disks using a fluorescence plate reader (Figure 5.6A,B).

Previous attempts by Lim et al., (2020) and Steinbeck et al., (2020) were unsuccessful in localising biosensors to the mitochondria. Localisation of iNap2 to mitochondria was attempted

by fusing a mitochondrial targeting peptide to the N-terminus of iNap2. *Arabidopsis* seeds from primary agrobacterium-mediated transformation were donated by MS and screened using herbicide selection. Initial screening resulted in a single positive transformant which was propagated, and the progeny were screened for mitochondrial localisation of iNap2 by staining with the mitochondrial stain MitoTracker-Orange (Appendix B.1.16B.1). However, fluorescence was localised to the cytosol and not mitochondria, confirmed by a lack of overlap with the mitochondrial stain (Appendix B.1.16B.1).

5.2.3 Multiwell parallel fluorometry to monitor subcellular redox dynamics

Multiwell fluorometry using a plate reader allows multiple sensors to be analysed simultaneously with parallel controls and replicates (Nietzel et al., 2019a, 2020; Wagner et al., 2019). This allows much greater throughput and more robust comparison compared to analysis using confocal microscopy. Ratiometric analysis is critical to allowing comparison as it provides internal normalisation for differences in sensor expression, tissue amount, and tissue positioning. For each biosensor two fluorescence excitation/emission signals were measured, and background corrected using the fluorescence signal from WT leaf disks not expressing any biosensors, which was recorded in parallel for each experiment and treatment. The ratio between the two fluorescent signals for each biosensor was calculated and $\log_{10}$ transformed to restore symmetry to data for ratios above and below one. iNap and SoNar are sensitive to changes in pH when excited at 482 nm and therefore pH correction using iNapC is required (Lim et al., 2020; Tao et al., 2017; Zhao et al., 2015, 2016b). iNapC is not sensitive to NADPH or NADH and therefore changes in the ratio of fluorescence intensity from excitation at 420 nm and 482 nm ($R_{420/482}$) are dependent only on pH (Lim et al., 2020; Tao et al., 2017). The pH dependence of iNap1-4 and SoNar is identical to the pH dependence of iNapC over a physiologically relevant range (pH 7.0 – 8.2 (Lim et al., 2020; Tao et al., 2017). For pH correction of iNap1-4 and SoNar sensors, the $R_{420/482}$ for each sensor was divided by the $R_{420/482}$ for the corresponding iNapC sensor in the same compartment treated under identical conditions. Identical fluorescence gain settings were used for each sensor to allow comparison of absolute fluorescence ratios between compartments and sensors variants.

To evaluate the effectiveness of the biosensors for quantifying changes in redox metabolites, treatments known to affect redox metabolism including menadione, nitrite, hypoxia and flg22, were applied to leaf disks of *Arabidopsis* plants expressing sensors for; cytosolic, plastidic and peroxisomal NADPH (Figure 5.7-5.11); cytosolic and plastidic NADH:NAD^+ (Figure 5.12, 5.13); and cytosolic glutathione redox potential (Figure 5.14).

5.2.4 iNap sensors detected changes in NADPH

To quantify changes in NADPH, individual fluorescence intensities were measured for multiple iNap sensor variants with different NADPH binding affinities (Figure 5.10, 5.11). The ratio of fluorescence was calculated (Figure 5.8, 5.9) and pH effects were corrected by normalising the fluorescence ratio to the pH insensitive control sensor, iNapC (Figure 5.7).

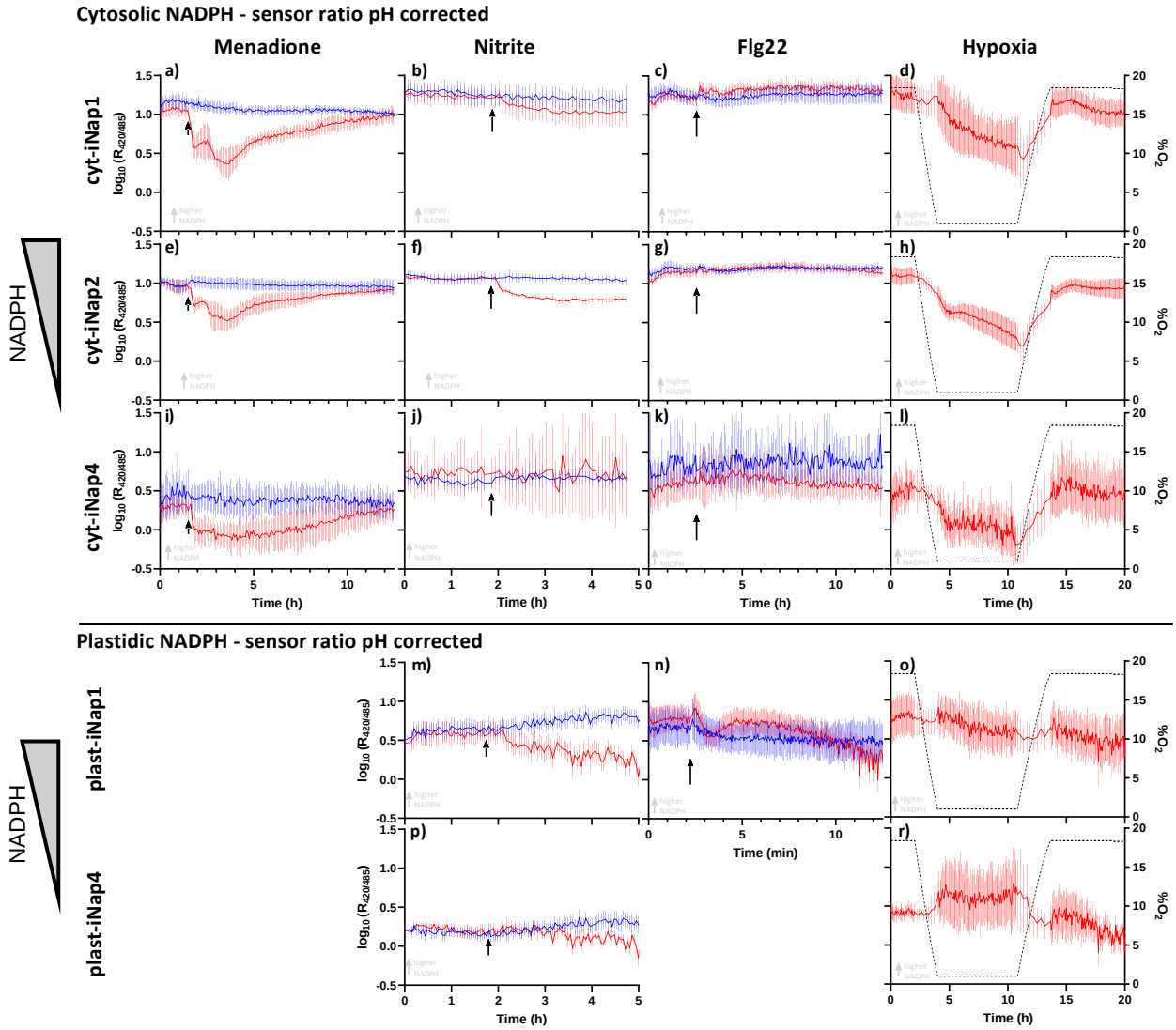

Figure 5.7. Relative NADPH concentration measured by iNap sensors after pH correction in leaf disks of 4- to 6-week-old *Arabidopsis*. Red lines (—) represent treated leaf disks, blue lines (—) represent an equivalent control. Leaf disks were analysed in 96 well plates in a fluorescent plate reader. Fluorescence was measured by emission at 520 ± 20 nm from excitation at 420 ± 15 nm and 482 ± 8 nm. $R_{420/482}$ was normalised to the fluorescence ratio for identically treated iNapC in the same compartment. iNap1, iNap2 and iNap4 were expressed in the cytosol. iNap1 and iNap4 were expressed in the plastids. Menadione concentration was 60 µM, nitrite concentration was 2 mM, flg22 concentration was 1 µM. Oxygen concentration was reduced by flushing the plate reader with nitrogen regulated by an atmospheric control unit. Black arrows indicate the time treatment, or an equivalent control, was added to leaf disks. Values are the mean ± SD n = 5

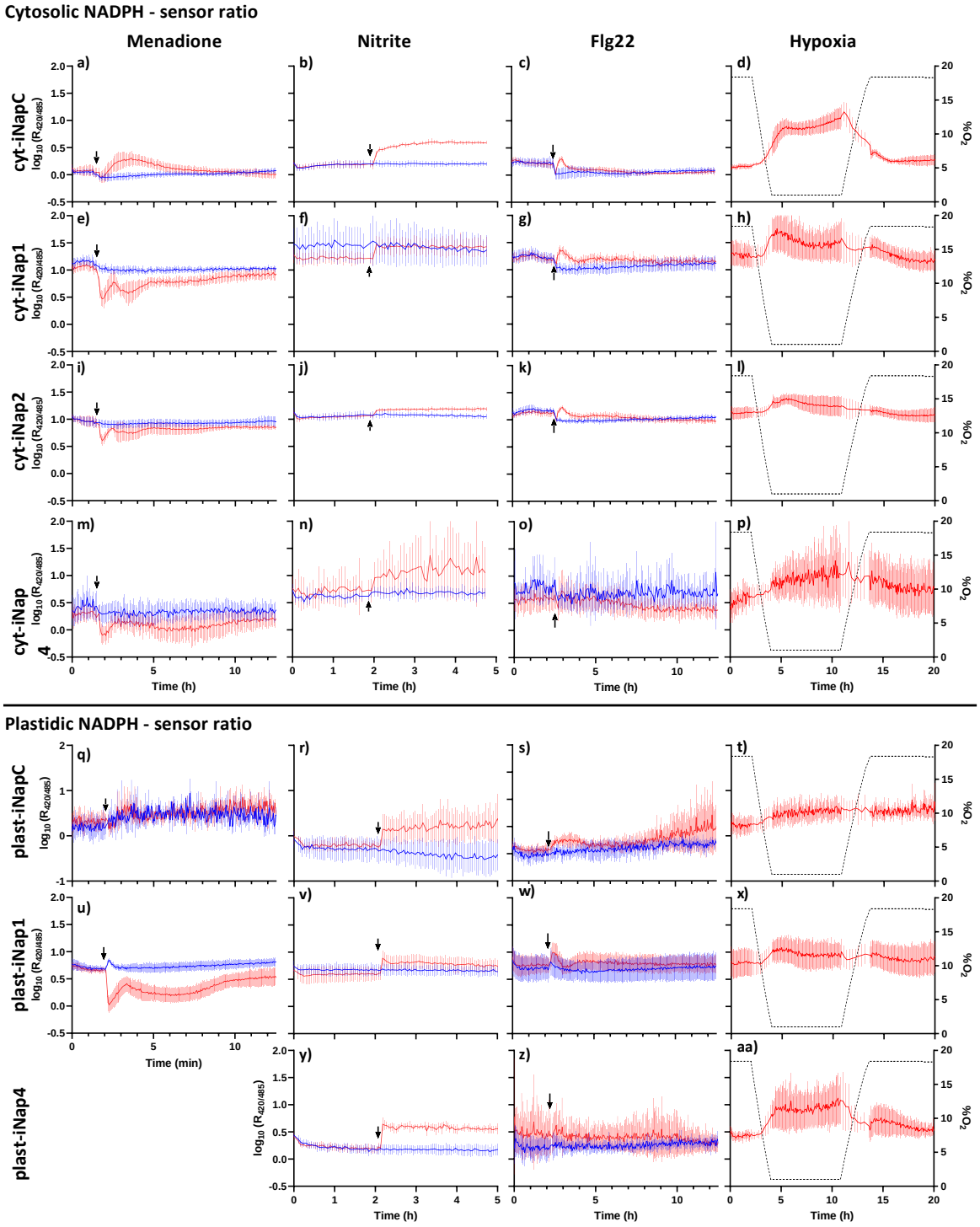

Figure 5.8. Fluorescence ratio ($R_{420/482}$) of iNap expressed in the cytosol and plastids before pH correction with iNapC in leaf disks of 4- to 6-week-old *Arabidopsis*. Red lines (—) represent treated leaf disks, blue lines (—) represent an equivalent control. Leaf disks were analysed in 96 well plates in a fluorescent plate reader. Fluorescence was measured by emission at 520 ± 20 nm from excitation at 420 ± 15 nm and 482 ± 8 nm. iNapC, iNap1, iNap2 and iNap4 were expressed in the cytosol. iNapC, iNap1 and iNap4 were expressed in the plastids. Menadione concentration was 60 µM, nitrite concentration was 2 mM, flg22 concentration was 1 µM. Oxygen concentration was reduced by flushing the plate reader with nitrogen regulated by an atmospheric control unit. Black arrows indicate the time treatment, or an equivalent control, was added to leaf disks. Values are the mean ± SD n = 5

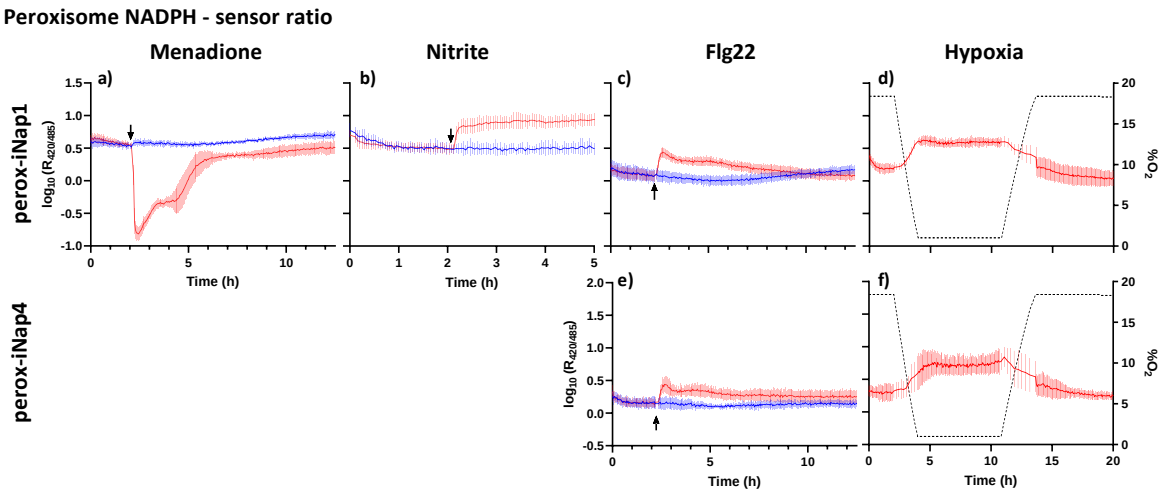

Figure 5.9. Fluorescence ratio ($R_{420/482}$) of iNap1 and iNap4 expressed in the peroxisome before pH correction with iNapC in leaf disks of 4- to 6-week-old *Arabidopsis*. Red lines (—) represent treated leaf disks, blue lines (—) represent an equivalent control. Leaf disks were analysed in 96 well plates in a fluorescent plate reader. Fluorescence was measured by emission at 520 ± 20 nm from excitation at 420 ± 15 nm and 482 ± 8 nm. Menadione concentration was 60 µM, nitrite concentration was 2 mM, flg22 concentration was 1 µM. Oxygen concentration was reduced by flushing the plate reader with nitrogen regulated by an atmospheric control unit. Black arrows indicate the time treatment, or an equivalent control, was added to leaf disks. Values are the mean ± SD n = 5

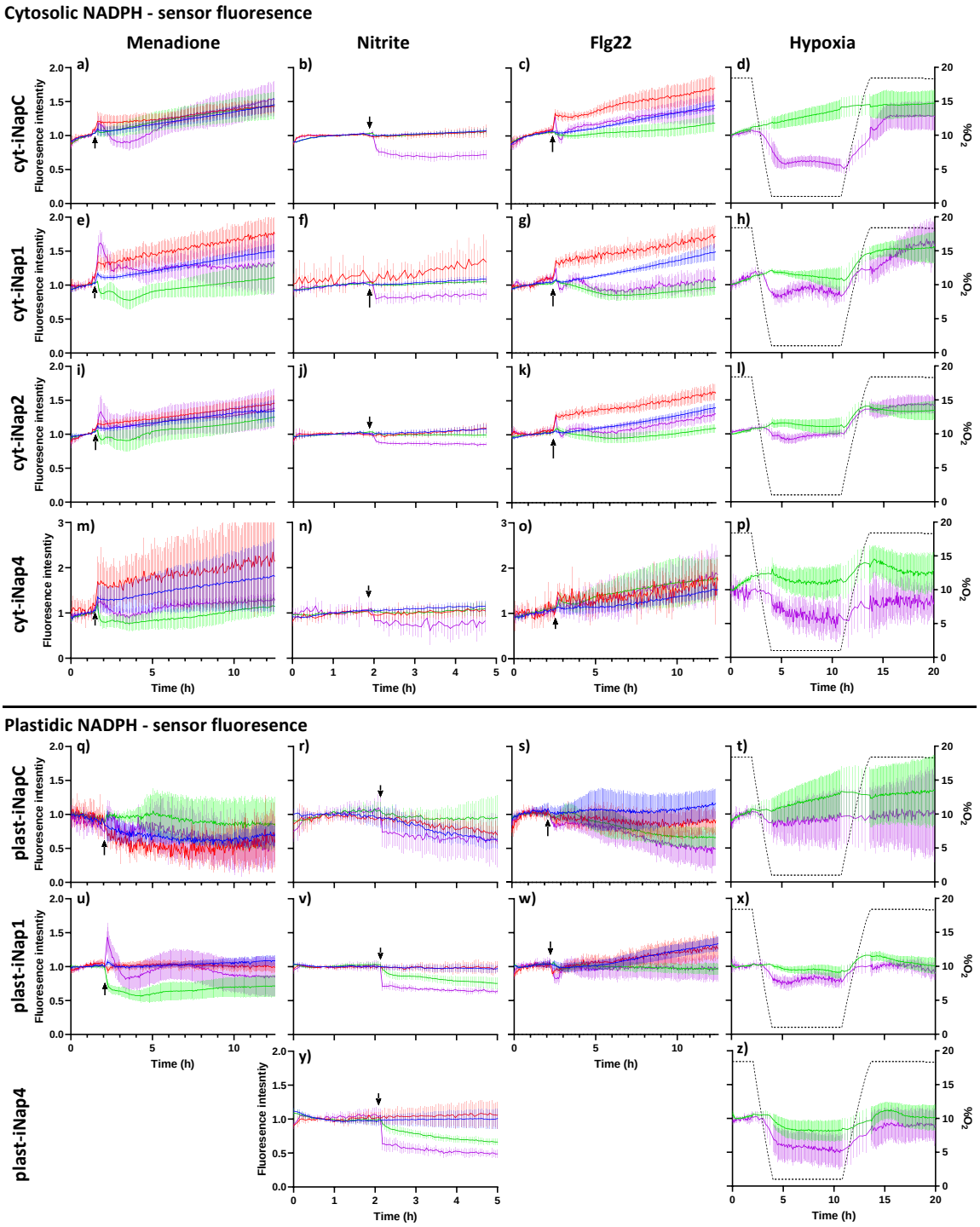

Figure 5.10. Individual fluorescence emission intensities used to calculate the fluorescence ratio of iNap expressed in the cytosol and plastids of leaf disks from 4- to 6-week-old *Arabidopsis*. Fluorescence was measured from emission at 520 ± 20 nm from excitation at 420 ± 15 nm (control-blue[—] , treatment-green [—]) and 482 ± 8 nm (control-red [—], treatment-purple [—]). Leaf disks were analysed in 96 well plates in a fluorescent plate reader. iNapC, iNap1, iNap2 and iNap4 were expressed in the cytosol. iNapC, iNap1 and iNap4 were expressed in the plastids. Menadione concentration was 60 µM, nitrite concentration was 2 mM, flg22 concentration was 1 µM. Oxygen concentration was reduced by flushing the plate reader with

nitrogen regulated by an atmospheric control unit. Black arrows indicate the time treatment, or an equivalent control, was added to leaf disks. Values are the mean ± SD n = 5

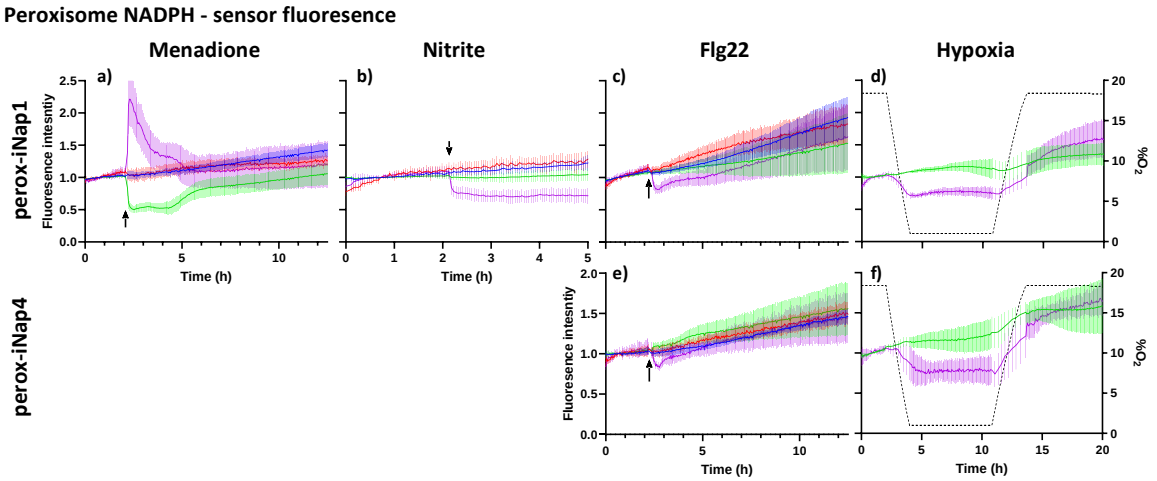

Figure 5.11 Individual fluorescence emission intensities used to calculate the fluorescence ratio of iNap expressed in the peroxisome of leaf disks from 4- to 6-week-old *Arabidopsis*. Fluorescence was measured from emission at 520 ± 20 nm from excitation at 420 ± 15 nm (control-blue[—] , treatment-green [—]) and 482 ± 8 nm (control-red [—], treatment-purple [—]) Leaf disks were analysed in 96 well plates in a fluorescent plate reader. Menadione concentration was 60 µM, nitrite concentration was 2 mM, flg22 concentration was 1 µM. Oxygen concentration was reduced by flushing the plate reader with nitrogen regulated by an atmospheric control unit. Black arrows indicate the time treatment, or an equivalent control, was added to leaf disks. Values are the mean ± SD n = 5

Similar fluorescence ratios for the same sensor were measured before treatments, despite experiments being conducted on different days and with different plants ranging in age from 4- to 6-weeks old (Figure 5.8, 5.9). This suggests that ratiometric measurement was effective at normalising any differences in fluorescent protein expression between individual leaves or plants. The initial fluorescence ratios were also consistent with the different binding affinities of the iNap sensor variants with the lower affinity iNap4 showing a lower $R_{420/482}$ compared to the higher affinity iNap1 or iNap2 sensors (Figure 5.8, 5.9) (Table 5.1).

iNap was able to detect decreases in NADPH caused by menadione, nitrite, and hypoxia in both the cytosol and plastids (Figure 5.7). Flg22 induced changes in sensor fluorescence (Figure 5.10, c, g, k, o, s, w) but after pH correction using iNapC, no change in NADPH concentration was measured (Figure 5.7, c, g, k, n). The fluorescence ratio $R_{420/482}$ increased in

cytosolic iNapC for all treatments (Figure 5.8, a-d), suggesting the treatments caused a decrease in cytosolic pH. The fluorescence ratio $R_{420/482}$ also increased in plast-iNapC following treatment with nitrite, flg22 and hypoxia (Figure 5.8, r, s, t) suggesting these treatments also caused a decrease in plastidic pH. Perox-iNapC was not sufficiently fluorescent above background to be used for pH correction of perox-iNap1 or perox-iNap4. The importance of pH correction is exemplified for nitrite treated leaf disks as the uncorrected sensor ratios increased (Figure 5.9, f, j, n, v, y) but after pH correction with iNapC, a decrease in NADPH was observed (Figure 5.7, b, f, m, p).

The intensity changes of the two individual fluorescence intensity signals relative to each other contains information about the technical reliability of the measured ratio changes. Emission from excitation at 420 nm decreases with decreasing NADPH concentration and emission from excitation at 482 nm increases (Lim et al., 2020; Tao et al., 2017). Only emission from excitation at 482 nm is sensitive to pH (Tao et al., 2017) and therefore changes in fluorescence from excitation at 420 nm (green lines Figure 5.10, 5.11) gives a pH insensitive indication of changes in NADPH levels albeit at the loss of a ratiometric signal. The changes in the pH corrected fluorescence ratio were generally consistent with the signal from excitation at 420 nm, suggesting pH correction was effective across the different treatments.

5.2.5 SoNar and Peredox-mCherry detect changes in NADH:NAD^+ ratio

To quantify changes in cytosolic and plastidic NADH:NAD^+ ratio, individual fluorescence intensities were measured for SoNar (Figure 5.12q-x), the ratio of fluoresce was calculated (Figure 5.12i-p), and pH effects were corrected by normalising the fluorescence ratio to the pH insensitive control sensor iNapC (Figure 5.12a-h). Cytosolic NADH:NAD^+ was also measured in parallel using Peredox-mCherry which does not require any pH correction (Figure 5.13).

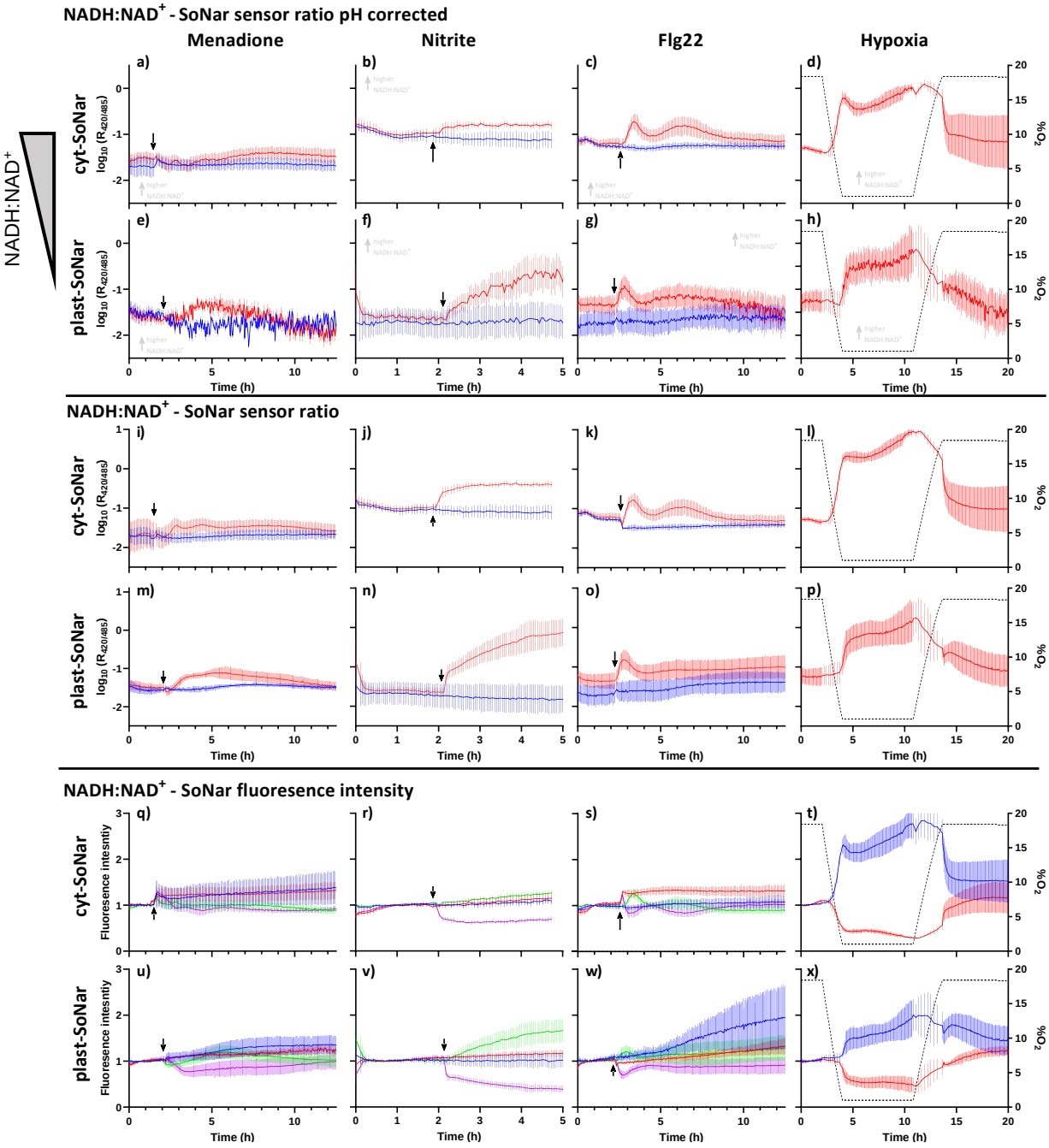

Figure 5.12 NADH:NAD$^+$ measured by SoNar expressed in the cytosol or plastids of leaf disks from 4- to 6-week-old *Arabidopsis*. **a-h)** Relative NADH:NAD$^+$ ratio measured by SoNAr sensors after pH correction. Red lines (—) represent treated leaf disks, blue lines (—) represent an equivalent control. **i-p)** Fluorescence ratio ($R_{420}/_{482}$) of SoNar before pH correction with iNapC. Red lines (—) represent treated leaf disks, blue lines (—) represent an equivalent control. **q-x)** Individual fluorescence emission intensities used to calculate the fluorescence ratio of SoNar. Fluorescence was measured from emission at 520 ± 20 nm from excitation at 420 ± 15 nm (control-blue[—] , treatment-green [—]) and 482 ± 8 nm (control-red [—], treatment-purple [—]). Leaf disks were analysed in 96 well plates in a fluorescent plate reader. Menadione concentration was 60 µM, nitrite concentration was 2 mM, flg22 concentration was 1 µM. Oxygen concentration was reduced by flushing the plate reader with nitrogen regulated by an atmospheric

control unit. Black arrows indicate the time treatment, or an equivalent control, was added to leaf disks. Values are the mean ± SD n = 5

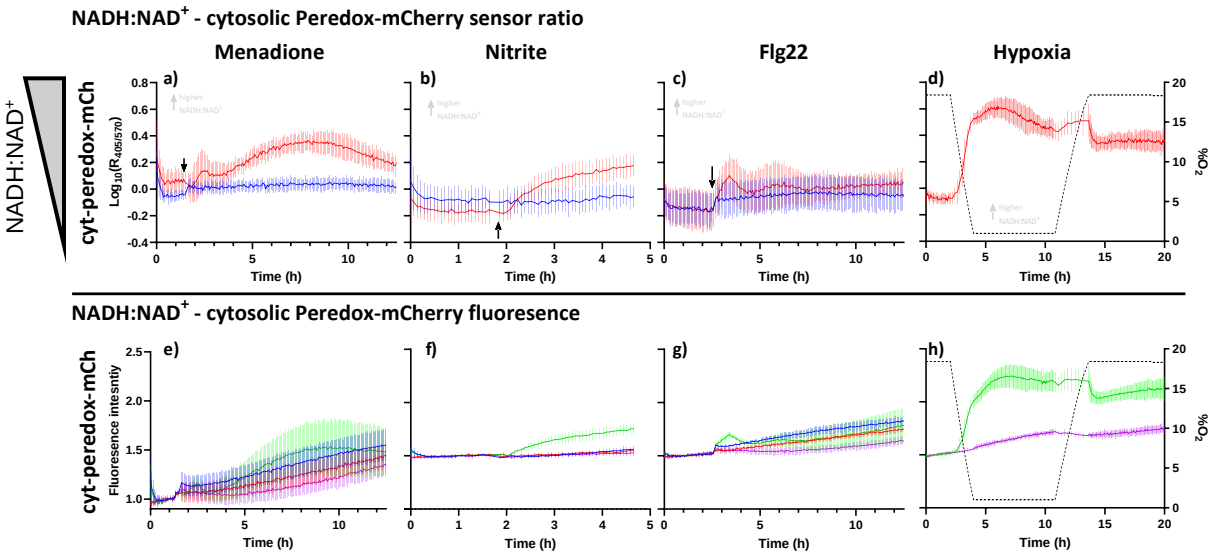

Figure 5.13 Relative NADH:NAD$^+$ ratio measured by peredox-mCherry expressed in the cytosol of leaf disks from 4- to 6-week old *Arabidopsis*. **a-d**) Fluorescence ratio of tSapphire/mCherry, red lines (—) represent treated leaf disks, blue lines (—) represent an equivalent control. **e-h**) Individual fluorescence intensities used to calculate the fluorescence ratio of peredox-mCherry. tSapphire fluorescence was measured by emission at 530 ± 20 nm from excitation at 400 ± 8 nm (control-blue[—] , treatment-green [—]), mCherry fluorescence was measured by emission at 610 ± 8 nm from excitation at 570 ± 10 nm (control-red [—], treatment-purple [—]). Leaf disks were analysed in 96 well plates in a fluorescent plate reader. Menadione concentration was 60 µM, nitrite concentration was 2 mM, flg22 concentration was 1 µM. Oxygen concentration was reduced by flushing the plate reader with nitrogen regulated by an atmospheric control unit. Black arrows indicate the time treatment, or an equivalent control, was added to leaf disks. Values are the mean ± SD n = 5

The four treatments tested all increased in the NADH:NAD$^+$ ratio as measured by both SoNar and Peredox-mCherry (Figure 5.12a-g, 5.13a-d). SoNar and peredox-mCherry showed qualitatively similar changes in cytosolic NADH:NAD$^+$ across the four treatments. Comparison of quantitative measurements of NADH:NAD$^+$ ratio was not possible without calibration of the sensors. Peredox-mCherry is insensitive to changes in pH and therefore the fact that SoNar shows similar changes in NADH:NAD$^+$ across the different treatments suggests pH correction of SoNar was effective.

Plastidic and cytosolic changes in NADH:NAD$^+$ measured by SoNar were similar suggesting either the applied treatments had direct affects in both the cytosol and plastids or cytosolic and plastidic pools of NADH are coordinated.

The individual fluorescence intensities of SoNar showed inverse behaviour, consistent with the sensitivity of the individual signals to the NADH:NAD$^+$ ratio (Figure 5.12q-x). Individual fluorescence intensities of Peredox-mCherry also changed as expected with the mCherry fluorescence similar between treatment and control samples and tSapphire fluorescence changing with the NADH:NAD$^+$ ratio (Figure 5.13e-h).

5.2.6 GRX1-roGFP2 detects changes in glutathione redox potential

To quantify changes in glutathione redox potential and correlate these with changes in pyridine nucleotides, fluorescence of GRX1-roGFP2 was quantified in parallel with other biosensors (Figure 5.14).

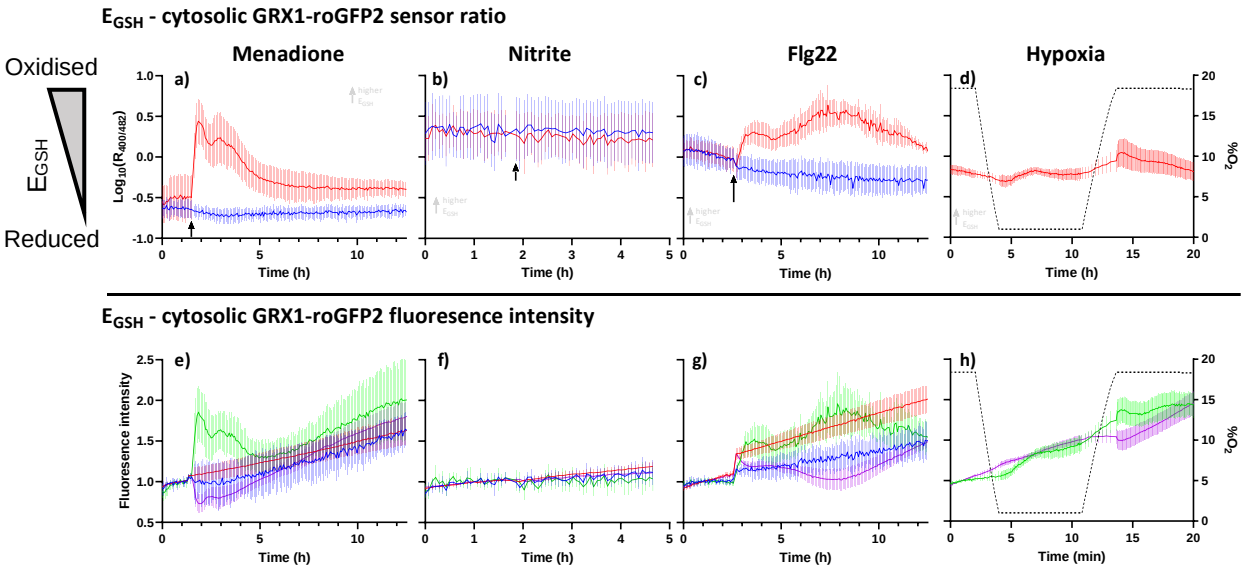

Figure 5.14 Glutathione redox potential (E_{GSH}) measured by GRX1-roGFP2 expressed in the cytosol of leaf disks from 4- to 6-week old *Arabidopsis*. **a-d**) Fluorescence ratio $R_{400/482}$, red lines (—) represent treated leaf disks, blue lines (—) represent an equivalent control. **e-h**) Individual fluorescence intensities used to calculate the fluorescence ratio of GRX1-roGFP2. Fluorescence was measured from emission at 530 ± 20 nm from excitation at 400 ± 8 nm (control-blue[—] , treatment-green [—]) and 482 ± 8 nm (control-red [—], treatment-purple [—]). Leaf disks were analysed in 96 well plates in a fluorescent plate reader. Menadione concentration was 60 µM, nitrite concentration was 2 mM, flg22 concentration was 1 µM. Oxygen concentration was reduced by flushing the plate reader with nitrogen regulated by an atmospheric control unit. Black arrows indicate the time treatment, or an equivalent control, was added to leaf disks. Values are the mean ± SD n = 5

GRX1-roGFP2 was able to detect changes in cytosolic glutathione redox potential (E_{GSH}) caused by the applied treatments. Glutathione became more oxidised following treatment with menadione, flg22 and hypoxia (Figure 5.14a,c,d). Nitrite treatment did not affect E_{GSH} (Figure 5.14b). Changes in sensor fluorescence ratio were validated by changes in the individual fluorescence intensities which show the expected opposing changes as glutathione became oxidised (Figure 5.14e).

5.2.7 Hypoxia decreased $MgATP^{2-}$ concentration

To compare the effect of hypoxia on redox metabolites with the effect on ATP, the $MgATP^{2-}$ sensor ATeam was applied in parallel with other sensors (Figure 5.15).

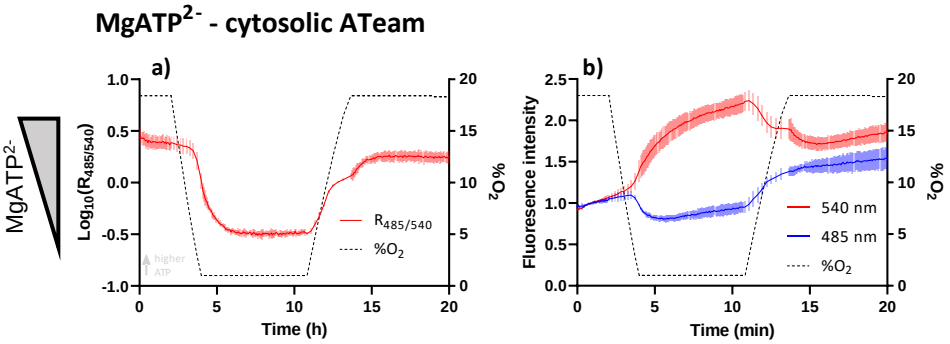

Figure 5.15. $MgATP^{2-}$ measured by cytosolic ATeam expressed in 4- to 6-week old *Arabidopsis* leaf disks. **a**) Fluorescence ratio ($R_{485/540}$) of ATeam. **b**) Individual fluorescence intensities used to calculate fluorescence ratio. Fluorescence was measured from excitation at 435 ± 10 nm by emission at 452 ± 10 nm (red lines [—]) and 540 ± 8 nm (blue lines [—]). Oxygen concentration was reduced by flushing the plate reader with nitrogen regulated by an atmospheric control unit. Values are the mean ± SD n = 5.

The cytosolic $MgATP^{2-}$ concentration measured by cyt-ATeam decreased rapidly after the onset of hypoxia reaching a plateau after 4 h (Figure 5.15a). $MgATP^{2-}$ concentration recovered to near pre-hypoxia levels as the oxygen concentration was increased. The individual fluorescence signals showed an opposing change in intensity supporting the validity of the ratiometric measurement (Figure 5.15b).

5.2.8 Investigating the cause of flg22 induced increase in NADH:NAD$^+$ ratio

Both hypoxia and flg22 treatment caused increases in the NADH:NAD$^+$ ratio (Figure 5.12c, d, g, h, Figure 5.13c,d). The activity of NADPH oxidases activated by flg22 may consume oxygen at a sufficient rate to create local areas of hypoxia, particularly as leaf disks are submerged in buffer during the fluorescence assay. To test if the change in NADH:NAD$^+$ ratio is caused by NADPH oxidases, the NADPH oxidase inhibitor diphenyleneiodonium (DPI) was applied prior to flg22 treatment and the change in NADH:NAD$^+$ quantified using cyt-peredox-mCherry (Figure 5.16).

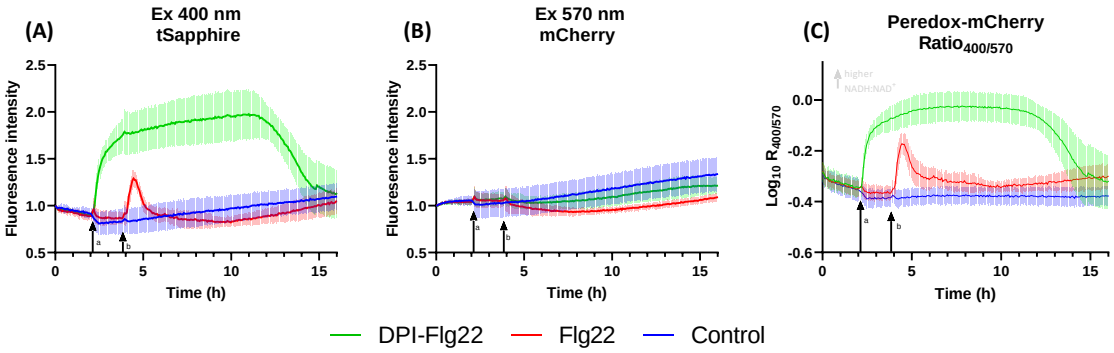

Figure 5.16. The effect of 50 µM diphenyleneiodonium (DPI) and 1 µM flg22 on NADH:NAD$^+$ measured by cytosolic Peredox-mCherry in leaf disks of 4- to 6-week old *Arabidopsis* measured in parallel in a 96 well plate using a fluorescent plate reader. Fluorescence intensity was measured from **A**) excitation at 400 ± 8 nm, emission 530 ± 20 nm for tSapphire and **B**) excitation 570 ± 10 nm, emission 610 nm for mCherry. **C**) Log_{10} transformed ratio of tSapphire/mCherry fluorescence. Treatments were added at times indicated by black arrows, **a**-50 µM DPI or DMSO control added, **b**-1 µM Flg22 added. DPI + Flg22 – green, Flg22 – red, control – blue. Values are mean ± SD n = 8.

Addition of DPI caused a rapid increase in the NADH:NAD$^+$ ratio potentially saturating Peredox-mCherry (Figure 5.16c). The individual fluorescence signals of tSapphire and mCherry show the ratio change in Peredox-mCherry was driven by the NAD(H) sensitive tSapphire (Figure 5.16A,B). DPI is an uncompetitive flavoenzyme inhibitor commonly used to inhibit NADPH oxidases but can also have off target effects on other flavoenzymes such as NADH ubiquinone oxidoreductase (Complex I) in the mitochondrial electron transport chain (Aldieri et al., 2008; Majander et al., 1994). The observed increase in NADH:NAD$^+$ is likely caused by inhibition of mitochondrial electron transport and subsequent inhibition of NADH oxidation.

Unfortunately, the effect of DPI masked any subsequent effect of flg22 in DPI treated leaf disks as Peredox-mCherry was likely already saturated. DPI is therefore not a useful inhibitor for testing the involvement of NADPH oxidases in the observed increase in NADH:NAD^+. Leaf disks treated with flg22 in the absence of DPI showed a similar response to previous experiments (Figure 5.13c) with an initial rapid increase in NADH:NAD^+ followed by a recovery before a secondary more gradual increase and recovery (Figure 5.16c).

To test if oxygen availability affected the increase in NADH:NAD^+ following flg22 treatment, the effect of increasing the oxygen availability by supplementing the leaf disk buffer with perfluoredaclin (PFD) was investigated (Figure 5.17). PFD is a fluorocarbon with very high oxygen solubility (49ml/100ml) and can therefore increase the availability of oxygen to the leaf disks in the assay.

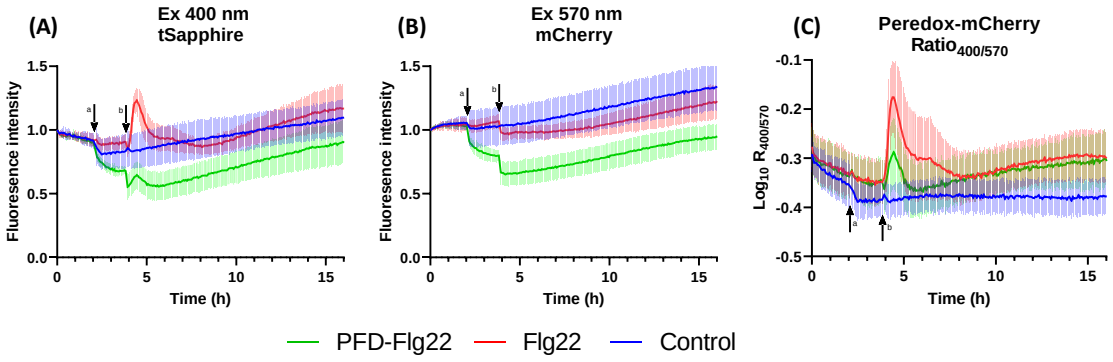

Figure 5.17. The effect of perfluorodecalin (PFD) and 1 µM flg22 on NADH:NAD^+ measured by cytosolic Peredox-mCherry in leaf disks of 4-6 week old *Arabidopsis* measured in parallel in a 96 well plate using a fluorescence plate reader. Fluorescence intensity was measured from **A**) excitation at 400 ± 8 nm, emission 530 ± 20 nm for tSapphire and **B**) excitation 570 ± 10 nm, emission 610 nm for mCherry. **C**) Log_{10} transformed ratio of tSapphire/mCherry fluorescence. Treatments were added at times indicated by black arrows **a**-20 µl PFD or buffer control added, **b**-1 µM flg22 + 10 µl PFD or buffer control added. PFD + Flg22 – green, Flg22 – red, control – blue. Values are mean ± SD n = 8.

Perfluorodecalin alone did not affect the NADH:NAD^+ ratio measured by cytosolic Peredox-mCherry (Figure 5.17C). PFD deceased the fluorescence intensity of both tSapphire and mCherry but their ratio was unaffected, highlighting the advantage of ratiometric measurement (Figure 5.17A,B). The NADH:NAD^+ ratio increased following addition of flg22 in both PFD

treated and control samples. The peak increase in $R_{400/570}$ was significantly smaller for PFD treated leaf disks compared to control samples (t-test $P<0.05$), consistent with an increase in gas diffusion and subsequent increased capacity of cells to oxidise NADH. This observation is consistent with the hypothesis that the increase in NADH:NAD^+ ratio following flg22 treatment is caused by a decreased capacity for NADH oxidation, potentially due to decreased oxygen availability.

5.3 Discussion

Redox metabolism can be highly dynamic with rapid changes in concentrations or redox states of metabolites in response to external stimuli or internal signalling pathways. Analytical methods can be limited in spatial and temporal resolution, and although subcellular fractionation has provided useful estimates of dynamic changes in NAD(P)(H), it remains technically challenging and has not been widely applied. Quantifying redox metabolites with subcellular resolution using fluorescent biosensors could provide insight into redox metabolism in plants.

5.3.1 Genetically encoded fluorescent biosensors allow simultaneous quantification of redox metabolites across multiple subcellular compartments

The fluorescent biosensors for NADPH and NADH:NAD^+ used in this chapter have previously been characterised in plants (Lim et al., 2020; Steinbeck et al., 2020). However, the analysis by Lim et al., (2020) of the NADPH sensor iNap and NADH:NAD^+ sensor SoNar was limited to cotyledons of seedlings using confocal microscopy. In this chapter, I applied plate reader-based multiwell fluorometry to analyse multiple sensors in parallel. This approach is well suited for the analysis of external treatments on specific tissues and organs and has previously been applied to leaves, whole seedlings and seeds (De Col et al., 2017; Nietzel et al., 2019a; Steinbeck et al., 2020; Wagner et al., 2019). The advantage of multiwell fluorometry compared to confocal microscopy is the high throughput and ability to analyse replicate samples in parallel. However, this is at the cost of the cell type specificity and potentially higher signal to noise ratios of confocal microscopy.

Analysis of the fluorescence spectra of the iNap and SoNar sensors showed they were fluorescent at the expected wavelengths (Figure 5.2-5.4) but there was variability in signal intensity and signal to noise ratios between different sensors (Figure 5.6). Transgenic *Arabidopsis* plants expressing iNap sensors were transformed with different vectors. Cyt-iNapC-A (from MS) had a much larger signal:noise ratio than cyt-iNapC-B (from BL) which was not used for further analysis (Figure 5.6). Both sensors are expressed by the same CaMV 35S promoter and differences may be due to the insertion site in the genome. However, the signal:noise ratios of all the iNap sensors donated by BL were lower than the cyt-iNap2 and cyt-iNapC-A donated by ML suggesting the transformation vector could be optimised for better expression. Perox-iNapC was not sufficiently fluorescent for analysis of leaf discs using a fluorescence plate reader. Confocal analysis of perox-iNapC showed fluorescence in roots but not in other tissues (Appendix B.1.7) suggesting expression may be silenced in leaves. Despite this Lim et al., (2020) reported sufficient fluorescent signal for analysis of perox-iNapC and subsequent pH correction of perox-iNap1 and perox-iNap4 in cotyledons of 10-d-old seedlings. Fluorescence intensity was variable between leaves of the same plant as well as between different plants. Effort was made to use leaves of a similar age and to equally distribute leaves from different plants between treatment and control. However, a more thorough characterisation of differences in fluorescence intensity based on precise leaf age would be useful for future analysis.

To accurately measure NAD(P)(H) concentrations in plants, biosensors must have binding affinities that match the physiology to be monitored. The binding affinity as well as the Hill coefficient set the operational range of the sensor defined as the range of ligand concentrations which cause a change in fluorescence signal until a plateau is reached. Quantification becomes increasingly difficult as the signal plateaus due to the decreased response of the sensor to variation in ligand concentration, and therefore a range between 5%-95% of the maximum and minimum signal is often used. Subcellular fractionation gives the current best estimates of NAD(P)(H) concentrations in different compartments (Table 5.2) and these values could be used to choose biosensors with appropriate binding affinities. However, subcellular

fractionation provides a measurement of the total metabolite concentration including both protein bound and free metabolites (assuming the extraction method liberates metabolites from proteins). Fluorescence lifetime imaging has been used to show that up to 75% of NADH and 30-50% of NAD^+ may be bound to proteins in isolated plant mitochondria (Kasimova et al., 2006). Estimation of the actual free concentration of NAD(P)(H) can therefore be challenging and empirical testing of biosensors is required to identify an optimal sensor for a specific compartment or condition.

Table 5.2. Estimates of subcellular total NAD(P)(H) concentrations. Data modified from (Gakière et al., 2018b).

	Min (µM)	**Max (µM)**
Cytosol		
NAD^+	320	460
NADH	80	190
$NADP^+$	83	140
NADPH	150	230
Plastids		
NAD^+	140	280
NADH	60	110
$NADP^+$	230	330
NADPH	300	490
Mitochondria		
NAD^+	1060	2240
NADH	90	430
$NADP^+$	80	270
NADPH	50	240

Four iNap variants have been developed with various affinities for NADPH. Tao et al., (2017) report *in vitro* K_d of 2.0 µM, 6.0 µM, 25 µM and 120 µM for iNap1, 2, 3 and 4 respectively whereas Lim et al., (2020) report the k_d of iNap1 as 0.3 µM and iNap4 as 30 µM. The differences in K_d may be due to the temperature of analysis with Tao et al., (2017) studying animal systems at 37 °C and Lim et al., (2020) analysing plant samples and therefore using 22 °C. Previous analysis by Lim et al., (2020) showed different iNap variants were required in different compartments to avoid saturation of the sensor in *Arabidopsis* cotyledons, with the

higher affinity iNap1 being suited to the cytosol and lower affinity iNap4 being suited to plastids and peroxisomes, consistent with the higher NADPH concentration expected in these compartments (Heineke et al., 1991; Herber and Santarius, 1965; Igamberdiev and Gardeström, 2003; Szal et al., 2008; Wigge et al., 1993). In the analysis presented in this chapter the treatments used were expected to cause decreases in NADPH, making the higher affinity iNap1 and iNap2 variants more useful than the lower affinity iNap4, which consistently showed smaller changes than iNap1 or iNap2 in the same compartment (Figure 5.7). The estimated concentrations of NADPH from subcellular fractionation (Table 5.2) are substantially larger than the *in vitro* K_d values of the iNap sensors, and yet decreases in sensor ratio were observed following treatment with menadione, KNO_2 or hypoxia. This suggests that there is a substantial amount of NADPH bound to proteins and the free NADPH concentration is likely much lower than the estimates from subcellular fractionation. *In vivo* calibration of biosensors will be required to confirm this and precisely compare values to those from subcellular fractionation methods.

SoNar has a large operational range and can measure changes in NADH:NAD^+ ratio from 0.0005 to 1.25 (Zhao et al., 2015, 2016b). SoNar was able to quantify increases in NADH:NAD^+ following the treatments applied in this chapter confirming it was not saturated under physiological conditions (in the absence of any treatments) and has an appropriate affinity for measuring increases in the NADH:NAD^+ ratio in the cytosol and plastids of *Arabidopsis* leaves. Peredox-mCherry was also able to detect increases in NADH:NAD^+ in the cytosol suggesting it is not saturated under physiological conditions in the dark. However, peredox-mCherry has a higher affinity for NADH compared to SoNar and has been shown to become saturated following supply of exogenous sucrose (Hung et al., 2011; Steinbeck et al., 2020; Zhao et al., 2015). A lower affinity variant, peredox-mCherry DS has been developed to overcome this and was previously used to confirm that flg22 treatment and hypoxia do not cause saturation of peredox-mCherry (Steinbeck et al., 2020).

5.3.2 Calibration of fluorescent biosensors for redox metabolites

Comparing measurements between different experiments or incorporating data into models requires absolute quantification of NAD(P)(H) concentrations and ratios rather than just relative changes. Sensors are typically calibrated by measuring the dissociation constant in conditions which match those *in vivo* as closely as possible and identifying the fluorescent signal which equates to completely saturated or desaturated sensor *in vivo*. However, driving the *in vivo* concentration of NAD(P)(H) to specific values required for calibration can be challenging because of the ability of metabolism to buffer changes in metabolite concentration and the fact that NAD(P)(H) are not readily membrane permeable. To saturate the sensor, cells may be first permeabilised with digitonin and supplied with exogenous ligand, whilst complete desaturation relies on chemical treatment to decrease the NAD(P)(H) concentration (Lim et al., 2020; Moon et al., 2020; Zhao et al., 2015). Recently, direct microinjection has been used to calibrate an inorganic phosphate biosensor in *Arabidopsis* roots (Sahu et al., 2020) and a similar approach could be attempted for NAD(P)(H). The lack of absolute quantification is a weakness in the current application of many fluorescent biosensors particularly if the data are to be compared between independent systems or incorporated into computational models. The development of meaningful calibration protocols will be a necessary next step for the sensors to realise their full potential.

5.3.3 pH sensitivity of SoNar and iNap adds noise and uncertainty to measurements

pH differs between compartments and cell types and can change markedly (up to 1.5 pH units) during fluctuations in photosynthesis, hypoxia or calcium signalling (Behera et al., 2018; Lim et al., 2020; Wagner et al., 2019). Fluorescent proteins can be intrinsically pH sensitive due to protonation/de-protonation of phenolic groups in the chromophore (Kneen et al., 1998). The fluorescent protein variants used in biosensors can be particularly susceptible to changes in pH since the chromophore is exposed to the medium as a result of the circular permutation (Quatresous et al., 2012; Schwarzländer et al., 2011, 2014). Therefore, when measuring NAD(P)(H), any confounding effect of pH on biosensor readout must be considered. iNap and

SoNar are strongly affected by pH when excited at 482 nm whereas excitation at 420 nm is relatively insensitive to pH (Lim et al., 2020; Tao et al., 2017; Zhao et al., 2015). To overcome this pH sensitivity, an NAD(P)(H)-insensitive control sensor with a similar pH response, iNapC, was expressed in separate transgenic plants under the same conditions to correct for changes in pH. pH correction was not possible for peroxisomal iNap sensors as the fluorescence intensity of perox-iNapC was not sufficiently above background fluorescence. Fluorescence intensity of plast-iNapC was also low leading to a large amount of noise being introduced to plast-iNap and plast-SoNar after correction with plast-iNapC. The validity of the pH correction can be evaluated by examining the fluorescence intensity from excitation at 420 nm which is unaffected by changes in pH (Tao et al., 2017). In general, the changes observed in fluorescence intensity from excitation at 420 nm were consistent with the pH corrected $R_{420/482}$. However, treatment with KNO_2 in the cytosol did not affect fluorescence from excitation at 420 nm in cyt-iNap1, cyt-iNap2 or cyt-iNap4 (Figure 5.10f,j,n) but the pH corrected $R_{420/482}$ showed a decrease in NADPH (Figure 5.7b,f). This could be caused by slightly different pH responses of iNapC to other iNap variants although this was shown not to be the case using *in vitro* assays of purified iNapC and iNap1 or iNap4 (Lim et al., 2020; Tao et al., 2017). An iNap-mCherry construct has been created to avoid use of the pH sensitive fluorescence signal when quantifying NADPH levels, but this sensor shows a lower dynamic range and is yet to be tested in plants (Tao et al., 2017).

Compared to SoNar, peredox-mCherry has the advantage of being largely unaffected by pH over a physiologically relevant range, relying on a pH-insensitive variant of the tSapphire fluorescent protein and an additional mutagenesis of the Rex domains to produce the final pH-insensitive sensor (Hung et al., 2011; Steinbeck et al., 2020). Comparing the response of cyt-peredox-mCherry to the corrected $R_{420/482}$ of cyt-SoNar suggests pH correction using iNapC is effective as they showed similar responses across different treatments. Peredox-mCherry is more suited to making cell specific maps of NADH:NAD^+ as precise alignment to a pH control sensor is not necessary as it would be for SoNar (Steinbeck et al., 2020).

The application of fluorescent biosensors in this chapter relies on fluorescence intensity measurement to quantify metabolite concentrations. However, fluorescence lifetime imaging (FLIM) can be used as an orthogonal readout to quantify sensor responses with strengths and limitations that complement those of fluorescence intensity measurements. Typically FLIM relies on measuring the time between excitation and emission of fluorescence rather than the overall intensity (Datta et al., 2020). A further feature of FLIM applied to fluorescent biosensors is based on the deconvolution of fluorescence decay into multiple components (Chang et al., 2017; Li et al., 2019, 2020). The ratio of these decay components can produce a robust signal that is independent of sensor concentration and relies on only a single fluorescence excitation/emission wavelength. Therefore, time resolved fluorescence allows the single pH-independent fluorescent signal upon excitation at 420 nm of iNap and SoNar to be used, eliminating the need for correction with separate transgenic plants expressing iNapC (Chang et al., 2017; Li et al., 2019, 2020). The dynamic range of time resolved fluorescence measurements can also be greater than intensity-based measurements which can potentially improve signal-to-noise ratios. For example, the dynamic range of Peredox increased from 3-fold to 7-fold when time resolved fluorescence was used (Chang et al., 2017). Since FLIM is independent of sensor abundance, fusion of Peredox to mCherry is no longer necessary, reducing the size of the protein with potential advantages for expression and subcellular targeting. Engineering new sensors focusing on fluorescence lifetime properties rather than fluorescence intensities might open new possibilities for sensor designs that have previously been overlooked (Li et al., 2020).

5.3.4 Menadione induced oxidative stress

Menadione caused a decrease in the NADPH concentration across all compartments measured (Figure 5.7a,e,i, 5.1u, 5.11a), an increase in the NADH:NAD^+ ratio in the cytosol and plastids (Figure 5.12a,e, 5.13a), and oxidation of glutathione in the cytosol (Figure 5.14a). The changes in NADPH concentration are consistent with previous analysis of iNap sensors in *Arabadopsis* cotyledons which showed a decrease in NADPH after 5 min following 30 µM menadione treatment (Lim et al., 2020). The initial decrease in NADPH concentration over time

means that the demand for NADPH must be greater than the supply. The NADPH concentration recovered after 9 h but it is not possible to know to what extent this is caused by adaptation of the metabolic network i.e. increased supply, or degradation of menadione over time, i.e. decreased demand. This highlights the limitation of quantifying the concentration of metabolites alone, as it does not inform about the underlying fluxes into or out of a metabolic pool.

Menadione affected the NADH:NAD^+ ratio in both the cytosol and plastids consistent with previous analysis of *Arabidopsis* cotyledons which showed an initial decrease in NADH:NAD^+ after 5 min (Lim et al., 2020). However, previous analysis did not capture the dynamics of the response over time, and therefore the more pronounced increase in the NADH:NAD^+ ratio after ~2.5 h of treatment (Figure 5.12a,e, 5.13a), was not previously observed (Lim et al., 2020). This highlights the importance of quantifying changes over time as redox metabolites can fluctuate dynamically. The initial decrease in NADH:NAD^+ could be caused by mitochondrial consumption of NADH by NADH: ubiquinone reductase (complex I) which can reduce menadione with electrons from NADH (Hatefi and Stempel, 1969; Ruzicka and Crane, 1971; Thor et al., 1982). The subsequent reduction of the NAD pool is similar to the effect of antimycin A (Steinbeck et al., 2020; Wagner et al., 2019), a complex III inhibitor, suggesting that menadione or the subsequent production of ROS may inhibit oxidation of NADH by mitochondria.

5.3.5 Nitrite affected pyridine nucleotide metabolism across multiple compartments

Nitrite increases the demand for NAPDH specifically in the plastids via nitrite reductase (Joy and Hageman, 1966; Ramaro et al., 1981). As expected, the NADPH concentration decreased in the plastids (Figure 5.7m,p). Interestingly, a decrease was also observed in the cytosol, although this was not as pronounced (Figure 5.7b,f), suggesting coupling between plastidic and cytosolic NADPH pools or a direct cytosolic target of nitrite treatment. Previous analysis of maize root tips showed decreases in NADPH concentration following nitrite treatment although this was using whole cell extraction and therefore lacked the subcellular resolution achieved here using fluorescent biosensors (Marks, 2000). The coordinated change in cytosolic

and plastidic NADPH suggests reductant can be transported from the cytosol to plastids when plastidic demand is increased and that solely plastidic sources could not meet the increased NADPH demand alone. Evidence from knockout mutants of cytosolic 6-phosphogluconate dehydrogenase in maize also support this as they showed decreased nitrogen assimilation from nitrite into proteins suggesting cytosolic oxPPP, which produces NADPH, supports the plastidic steps of nitrogen assimilation (Marks, 2000).

Surprisingly, nitrite treatment also caused an increase in the NADH:NAD^+ ratio in both the cytosol and plastids with a larger increase in the plastid (Figure 5.12,b,f, Figure 5.13b). Nitrite reductase is specific to NADPH and therefore the increase in NADH:NAD^+ is likely caused by a secondary effect not directly related to the activity of nitrite reductase. The largest demand for NADH is from the mitochondrial electron transport chain (mETC) and therefore the increase in NADH:NAD^+ is likely to be caused by inhibition of mitochondrial electron transport. However, it is not clear how nitrite could cause this inhibition and the subsequent increase in NADH:NAD^+ observed.

KNO_2 is the salt of a permeable weak acid and can diffuse into cells. Because leaf disks were submerged in MES buffer at pH 5.8, this results in the import of protons and a decrease in pH. Changes in fluorescence of iNapC were consistent with a decrease in pH in the cytosol and plastids (Figure 5.8b,r)following nitrite treatment highlighting the importance of pH correction. A decrease in pH has previously been observed using phosphorus NMR measurements which showed a drop from pH 7.4 to 7.0 following treatment of maize root tips with 2 mM $NaNO_2$ (Marks, 2000). To confirm the effects observed here are due to nitrite and not pH, a similar weak acid such as acetic acid could be applied and the effect on NADPH and NADH:NAD^+ quantified.

5.3.6 Hypoxia affected pyridine nucleotide metabolism

Hypoxia affected all the redox metabolites measured across all compartments with an overall increase in NADH:NAD^+ ratio (Figure 5.12d,h, 5.13d), decrease in NADPH concentration (Figure 5.7d,h,i,o) and oxidation of the glutathione pool (Figure 5.14d). Changes in NADH:NAD^+ observed using cyt-peredox-mCherry are consistent with previous analysis in

Arabidopsis leaves with an increase in the NADH:NAD^+ ratio following the onset of hypoxia (Steinbeck et al., 2020; Wagner et al., 2019). However, cyt-SoNar and cyt-perdox-mCherry differed after 3 h where cyt-peredox-mCherry showed a decreasing NADH:NAD^+ ratio and cyt-SoNar showed an increasing NADH:NAD^+ ratio. The difference in sensor response could be caused by differences in maturation of the fluorescent proteins which requires oxygen (Tsien, 1998), although ratiometric measurement should account for this and the difference in sensor response requires further investigation.

NADPH concentration clearly decreased in the cytosol with the effect on plastids and peroxisomes more difficult to interpret due to poor pH correction with plast- or perox-iNapC. Demand for NADPH could increase during hypoxia to both generate ROS via NADPH oxidases (Liu et al., 2017; Pucciariello et al., 2012; Yang and Hong, 2015) as well as protect against ROS by maintaining glutathione and ascorbate reduction. The glutathione pool became more oxidised during hypoxia (Figure 5.14d) consistent with an increase in ROS production and previous analyses of *Arabidopsis* leaf disks (Wagner et al., 2019). Increased ROS production under hypoxia is counterintuitive as ROS production is dependent on oxygen, although the oxygen concentration was maintained at 1% which may still be sufficient for generating ROS (Pucciariello and Perata, 2017, 2021). ROS production during low oxygen availability has been proposed to have important signalling roles, with an RBOH mediated oxidative burst following the onset of hypoxia important for activating transcription factors which trigger adaptation to low oxygen (Pucciariello and Perata, 2017, 2021). Additionally, the glutathione redox potential could have increased during hypoxia due to a decrease in the total glutathione concentration caused by glutathione turnover and decreased synthesis due to lack of ATP supply (Joshi et al., 2019) (Figure 5.15)The glutathione oxidation was not directly correlated with the decrease in NADPH as glutathione gradually became more reduced after 3 h whereas NADPH concentration continued to decrease. This suggests the change in NADPH concentration was not solely due to increased demand for glutathione reduction. NADPH concentration continually decreased over the 7 h leaves were maintained at 1% oxygen suggesting any metabolic adaptations to hypoxia

could not meet the demand for NADPH. Prolonged exposure to 1% oxygen may cause a more permanent affect and it would need to be empirically tested if leaves could recover from exposure to hypoxia for more than 7 h.

The effect of reoxygenation after the period of hypoxia was also assessed. In real world situations as flood water recedes oxygen concentration can increase rapidly, potentially causing oxidative damage to plant cells which have adapted to hypoxic conditions (Yeung et al., 2018). Glutathione became more oxidised as soon as the oxygen concentration was increased (Figure 5.14d) consistent with increased ROS production following reoxygenation. However, the NADPH concentration gradually recovered as oxygen concentration was increased (Figure 5.7d,h,j,o,r) indicating NADPH supply was able to meet any increased demands from ROS detoxification and RBOH activity. Optimal balancing of ROS is necessary for effective recovery from submergence (Yeung et al., 2018) and an adequate NADPH supply is necessary for this. Enhancement of NADPH supply may therefore offer a strategy to improve flood tolerance in crops.

Quantifying the precise demands for NADPH from RBOH would be informative for understanding how the NADPH concentration can both decrease and increase in situations where RBOH activity is reported to increase. Quantifying H_2O_2 levels using the fluorescent biosensor roGFP2-Orp1 (Nietzel et al., 2019a) could provide some indication of RBOH activity but still cannot quantify actual fluxes from NADPH to H_2O_2. The decrease in NADPH concentration during hypoxia may be driven more by a decrease in supply than increased demand. This could be caused by the diversion of flux through glycolysis rather than the oxPPP to meet the ATP demands of the cell. Deuterium labelling in mammalian cells revealed changes in NADPH supply during hypoxia with a switch from malic enzyme to the oxPPP (Liu et al., 2016). Unfortunately, assessment of changes in NADPH production using similar deuterium labelling strategies is not effective in plants (Chapter 4).

5.3.7 Immune elicitation differentially affected redox metabolites

Immune elicitation using 1 µM flg22 caused an increase in the NADH:NAD^+ ratio (Figure 5.12c,g, 5.13c) and oxidation of the glutathione pool (Figure 5.14c) but did not appear to affect NADPH concentrations (Figure 5.7,c,g,k,n). Flg22 induces a well characterised oxidative burst triggered by a calcium signalling cascade (Ma et al., 2013) and resulting in activation of NADPH oxidases (Kadota et al., 2015; Marino et al., 2012). NADPH oxidases consume NADPH to generate extracellular H_2O_2 which can then enter cells via aquaporins (Bestetti et al., 2018; Bienert and Chaumont, 2014; Nietzel et al., 2019b; Rodrigues et al., 2017). Cyt-GRX1-roGFP2 showed the cytosolic glutathione pool was oxidised following flg22 treatment consistent with an increase in cytosolic H_2O_2 (Figure 5.14c). However, no change in NADPH concentration was observed in the cytosol (Figure 5.7,c,g,k), where plasma membrane bound NADPH oxidases are located. A possible decrease in plastidic NADPH was indicated by plast-iNap1 (Figure 5.7n) but pH correction added considerable variability to the measurement (Figure 5.8s). An increase in the $R_{420/482}$ of iNapC suggested a decrease in pH following flg22 treatment (Figure 5.8c,s), which could be caused by release of protons from cytosolic NAPDH oxidation. NMR data following elicitor treatment of Tobacco or *Phaseolus vulgaris* cell cultures also showed decreases in cytoplasmic pH from 7.5 to 7.05 and 7.46 to 7.28 respectively (Ojalvo et al., 1987; Pugin et al., 1997). The lack of change in NADPH concentration means that NADPH supply and demand remained balanced but there could still have been a change in overall flux through NADPH. Measurement of underlying fluxes is required to identify if this is the case, highlighting the weakness of measuring metabolite concentrations alone.

In contrast to the stable NADPH levels, the NADH:NAD^+ ratio increased following flg22 treatment observed with both SoNar and peredox-mCherry (Figure 5.12c,g, 5.13c), consistent with previous analysis (Steinbeck et al., 2020). The increase in NADH:NAD^+ ratio could be driven by calmodulin/Ca^{2+} NAD kinases causing depletion of NAD^+ as it is converted to $NADP^+$ as well as the NADase activity of Toll/interleukin-1 receptor (TIR) domains (Dell'Aglio et al., 2019; Wan et al., 2019). Decreased oxygen availability driven by NADPH oxidase activity may

also cause an increase in NADH:NAD^+ ratio due to inhibition of mitochondrial electron transport, as observed when external oxygen concentration is decreased (Figure 5.13d) (Steinbeck et al., 2020; Wagner et al., 2019). Addition of perflurodecalin which can increase gas diffusion and oxygen availability of submerged leaf disks (Wagner et al., 2019), significantly decreased the peak in NADH:NAD^+ ratio caused by flg22 treatment (Figure 5.17C). However further analysis using larger proportions of perfluorodecalin or manipulating the external oxygen concentration are needed to test this further. Chemical inhibition of RBOH using DPI was not effective for testing the link between RBOH activity and the increase in NADH:NAD^+ ratio as DPI is a non-specific inhibitor of flavoenzymes and therefore caused reduction of NAD likely via complex I inhibition (Figure 5.16). Future work could make use of genetic knock outs of RBOH genes to assess the role of NADPH oxidases on the changes in NADH:NAD^+.

5.3.8 The flow of reducing power between redox metabolites

Pyridine nucleotides are not in thermodynamic equilibrium as indicated by the different ratios of NADH:NAD^+ and NADPH:$NADP^+$ measured in plant cells (Heineke et al., 1991; Herber and Santarius, 1965; Igamberdiev and Gardeström, 2003; Szal et al., 2008; Wigge et al., 1993). This is vital for allowing the opposing roles of NADPH and NAD^+ as the primary cellular reductant and oxidant respectively, to function within the same subcellular compartments. Following all the treatments applied in this chapter the NADH:NAD^+ ratio increased while the NADPH concentration decreased or remained constant. If NADH and NADPH were in equilibrium, then similar changes would have been observed in both metabolites. The direction of possible reductant transfer between pyridine nucleotides is influenced by their relative redox potentials and therefore sensor calibration is required before this can be reliably estimated (see section 5.3.3).

The glutathione redox potential must be ultimately dependent on the supply of NADPH as GSSG is reduced to GSH by glutathione reductase using NADPH (Kubo et al., 1993). However, the cytosolic glutathione redox potential was not consistently correlated with the NADPH concentration following the treatments applied in this chapter. For example, nitrite

treatment decreased the concentration of NADPH (Figure 5.7b,f,m,p) but the glutathione redox potential was unaffected (Figure 5.14b), whereas flg22 treatment caused oxidation of the glutathione pool (Figure 5.14c) but NADPH concentration was unaffected (Figure 5.7,c,g,k,n). In contrast, menadione treatment caused a closely correlated decrease in NADPH concentration (Figure 5.7a,e,i) and oxidation of the glutathione pool (Figure 5.14a). The changes in glutathione redox state appear to be more closely associated with increases in ROS, which occur following flg22 or menadione treatment, than changes in NADPH supply. The redox potentials of these metabolites are defined by the net activity of all the enzymes or processes which contribute to their production or consumption. Ultimately, the concentrations or redox potentials of NADPH or glutathione alone are uninformative for identifying the flow of reductant.

5.3.9 Reducing power can be exchanged between subcellular compartments

Although reduced pyridine nucleotides do not directly move between compartments the reducing equivalents can be indirectly transported via metabolite shuttles (Figure 1.1). Shuttling of reducing power has been well documented during illumination during which reductant from NADPH generated in the chloroplasts is transported to the cytosol via the malate valve (Shameer et al., 2019), resulting in an increased cytosolic NADH:NAD^+ ratio (Elsässer et al., 2020; Lim et al., 2020; Steinbeck et al., 2020). Photorespiration can also transport reducing power between compartments with reductant from the chloroplasts being released in the mitochondria as NADH from the reaction catalysed by glycine decarboxylase (Lim et al., 2020). The changes in pyridine nucleotide concentration observed following treatment with menadione, flg22, nitrite and hypoxia also support the idea that redox metabolism is coordinated between subcellular compartments and demand for reductant in one compartment can be met by supply in another. This is also consistent with analyses of coenzymes by metabolic flux analyses of *Arabidopsis* cell cultures (Masakapalli et al., 2013)(Chapter 3). Menadione primarily targets the mitochondria but NADPH concentration decreased in the cytosol (Figure 5.7a,e,i), plastid (Figure 5.10u) and peroxisomes (Figure 5.11a), and the NADH:NAD^+ ratio increased in both the cytosol and plastids (Figure 5.12a,e 5.13a). Nitrite is reduced by nitrite reductase which is localised specifically to the

plastids (Miflin, 1974; Ramaro et al., 1981), and yet changes in NADPH were also seen in the cytosol and peroxisomes (Figure 5.7b,f) and NADH:NAD^+ increased in both the cytosol and plastids (Figure 5.12b,f, 5.13b). Flg22 did not affect NAPDH in any of the compartments measured (Figure 5.7,c,g,k,n) but the NADH:NAD^+ ratio increased in both the cytosol and plastids (Figure 5.12b,f, 5.13b)). However, it is also possible that these treatments simultaneously affect multiple compartments in the same way without any exchange of redox metabolites between compartments. To change reductant demands in specific compartments, water forming NAD(P)H oxidases could be expressed with subcellular localisation tags (Cracan et al., 2017; Titov et al., 2016).

The direction of reductant flow is ultimately dependent on the thermodynamic driving force but also the activity of any transporters and enzymes involved in shuttles. Plastidic NADP-malate dehydrogenase expression and activity is regulated by light levels to facilitate export of reductant from the chloroplast during the day (Scheibe, 1987; Yokochi et al., 2021). However, plastidic NADP-MDH knock outs showed elevated cytosolic NADH:NAD^+ ratio in leaves in the dark compared to WT plants, suggesting plastidic NADP-MDH also has a role in transporting reducing equivalents in the dark (Elsässer et al., 2020). Understanding how reducing power is distributed to different compartments depending on specific cellular demands, and how this is controlled, could identify opportunities for optimisation and future genetic engineering strategies for enhanced crops (Kramer and Evans, 2011).

5.3.10 An NAD^+ specific sensor is needed for plants

Changes in the NADH:NAD^+ ratio can be caused by differences in the rate of oxidation and reduction of NAD(H) and also by direct synthesis or breakdown of NADH or NAD^+. Measuring the NADH:NAD^+ ratio alone cannot distinguish between these possibilities and therefore separate measurements of NADH and NAD^+ or the total pool of NAD(H) are required. Alternative sensors are available that have yet to be expressed in plants including Frex, an NADH sensor, and LigA-cpVenus, an NAD^+ specific sensor (Cambronne et al., 2016; Zhao et al., 2011). However, these sensors have limitations for application to plants. Frex is highly pH sensitive,

similar to other cpYFP based sensors SoNar and iNap (Zhao et al., 2011). Unfortunately FLIM of Frex relies on the pH-sensitive excitation at 485 nm and therefore pH correction would still be required to use this sensor in plants (Chang et al., 2017; Li et al., 2020). Similarly the NAD^+ sensor LigA-cpVenus is pH-sensitive and would require separate transgenic plants expressing cpVenus for pH correction akin to SoNar and iNap (Cambronne et al., 2016). Moreover the *in vitro* K_d of Frex and LigA-cpVenus suggest these sensors could be saturated in plants. However, ultimately, their suitability for quantifying changes in NAD(H) concentration will need to be tested empirically since *in vitro* and *in vivo* binding affinities can differ (Cambronne et al., 2016).

5.3.11 An NADPH:$NADP^+$ and/or an $NADP^+$ sensor is needed for plants

Whilst NADPH sensing using iNap can be informative, the actual redox potentials of the subcellular NADP(H) pools are dependent on the ratios of reduced to oxidised forms. Therefore, a more meaningful definition of the system could be achieved with an NADPH:$NADP^+$ ratio sensor, or an $NADP^+$ specific sensor in combination with the current iNap NADPH sensor in plants. Currently the only available NADPH:$NADP^+$ ratio sensor, NADP-Snifit, is based on a semisynthetic sensor design which requires a chemical probe to be infiltrated into cells expressing the sensor protein (Sallin et al., 2018). Permeability of plant tissues may affect the application of NADP-Snifit to plants and will require empirical testing and optimisation. Two $NADP^+$ sensors have been developed and used in bacteria and mammalian cells, Apollo-$NADP^+$ and NADPsor, although both suffer from small dynamic ranges and the binding affinity of NADPsor is likely too weak to be useful *in planta* (Cameron et al., 2016; Zhao et al., 2016a). Therefore, these existing $NADP^+$ biosensors would require modification before they can be applied to plants.

As well as extending the use of existing biosensors to plants, completely new sensors also need to be developed. An NADPH:$NADP^+$ ratio sensor to directly report on the NADPH redox potential would be useful and could be constructed as a ligand binding sensor, similar to SoNar or Peredox. Alternatively, consideration should be given to a thiol-based redox sensor, which is directly oxidised or reduced by NADP(H). One such sensor could be created by fusing

an NADP-specific glutathione reductase to roGFP3 (Hanson et al., 2004), analogous to the glutathione redox sensors that are based on fusion of glutaredoxin and roGFP2 (Schwarzländer et al., 2016). Since NAD-specific glutathione reductase isoforms have also been described (Reiter et al., 2014), the same sensor design with a different glutathione reductase domain could allow sensing of the NAD(H) redox potential.

5.4 Conclusion

In conclusion, I have demonstrated that iNap, SoNar and Peredox-mCherry function as effective NADPH and NADH:NAD^+ ratio sensors in plants, and can report on dynamic changes in redox metabolism. Multiwell parallel fluorometry allowed multiple redox metabolites in multiple compartments to be analysed simultaneously revealing distinct changes between redox metabolites but coordinated responses between subcellular compartments. Future work using fluorescent biosensors should focus on calibration to calculate absolute concentrations and redox potentials as well as overcoming issues with pH correction either with entirely new sensors, application of FLIM to iNap and SoNar sensors or simply by optimising the expression of iNapC. Calibration and accurate pH correction will allow concentrations measured by fluorescent biosensors to be incorporated into kinetic models of redox metabolism, helping to gain mechanistic understanding of the changes observed. Ultimately, fluorescent biosensors cannot measure the flow of reductant between different metabolites, but they can still identify conditions in which redox metabolism has been perturbed and be used to formulate hypothesis for further testing.

Chapter 6: General discussion

6.1 Quantifying redox metabolism in plants

The aim of this thesis was to develop and evaluate methods for quantifying redox metabolism in plants. To do this I explored the application of INST-MFA in heterotrophic *Arabidopsis* cells under oxidative stress, evaluated deuterium labelling strategies for quantifying specific coenzyme production rates, and applied fluorescent biosensors for quantifying subcellular redox metabolites *in planta* (Table 6.1). The fundamental problem with previous approaches to understanding redox metabolism in plants has been a lack of, quantitative measurement, specificity between different coenzymes and subcellular resolution. The methods I developed and evaluated in this thesis aimed to address these issues and increase our understanding of redox metabolism in plants.

6.1.1 Deuterium labelling is limited in quantifying redox metabolism in plants

Ambiguity in analysing coenzyme production and consumption comes from unknown contributions of enzymes to NADPH and NADH production, as well as unknown costs for maintenance processes such as ROS detoxification. Deuterium labelling is a potential strategy to resolve both these issues by quantifying the relative contribution of different pathways to total NADPH production and subsequently the total NADPH production/consumption rate (assuming a metabolic steady state) (Chen et al., 2019a; Fan et al., 2014; Ghergurovich et al., 2020; Lewis et al., 2014; Liu et al., 2016; Zhang et al., 2017). However, the application of deuterium labelling to heterotrophic *Arabidopsis* cell cultures was limited by the rapid exchange of the redox active hydrogen of NADPH with water, likely catalysed by flavin enzymes which are highly abundant in plants (Smith et al., 2019). The subsequent requirement for correction with a water-exchange fraction was affected by the underlying structure of the plant metabolic network which contains confounding routes of label incorporation from water onto NADPH. It is likely that similar issues will be encountered across multiple plant species and that flavin enzyme abundance will be high in other autotrophs due to the presence of Fd-NADPH oxidoreductase. Finally, duplication of

NADPH producing pathways in multiple compartments, a common feature of plant metabolism, was also found to lead to measurement inaccuracy. Taken together, these factors ultimately rule out deuterium labelling as an effective strategy for quantifying redox metabolism in plants.

Table 6.1. Comparison of methods for quantifying redox metabolism in plants.

	^{13}C INST-MFA	**^{2}H labelling**	**Fluorescent biosensors**
Information provided	Subcellular carbon fluxes through central metabolism, including redox reactions	Relative fluxes from different coenzyme producing reactions, specific to NAD(P)H	Relative metabolite concentrations or ratios in specific subcellular compartments
Advantages	Describes *in vivo* metabolism Network wide approach avoids bias of individual pathway analyses Also resolves non-redox fluxes which might still be relevant to redox metabolism	Describes *in vivo* metabolism Coenzyme specific unlike ^{13}C analysis Could potentially quantify total coenzyme production rates for estimating maintenance costs	Describes *in vivo* metabolism in whole plants and tissues Subcellular compartment specific Can compare multiple metabolites in parallel using plate reader fluorometry Captures dynamic changes not at metabolic steady state
Limitations	Limited to metabolic steady state Lack of specificity for different coenzymes	Rapid exchange between NADPH and water abolishes required labelling of redox active hydride Plant metabolic network structure with duplication of pathways and flux through gluconeogenesis prevent accurate measurement	Biosensors require further development including better pH correction for NADPH sensors Concentrations cannot directly inform on fluxes or mechanistic interactions

6.1.2 Fluorescent biosensors are useful but do not provide flux information

Genetically encoded fluorescent biosensors were applied to quantify relative changes in NADH:NAD^+ ratios, NADPH concentration, and glutathione redox potential. To investigate the possible interactions between redox metabolites, treatments were applied that would be expected to alter the demand for NADPH, including menadione, hypoxia, nitrite and flg22. In general, these treatments caused decreases in the NADPH concentration and increases in the NADH:NAD^+ ratio with similar responses in the cytosol, plastids and peroxisome. pH correction introduced additional error in estimations of relative metabolite levels using SoNar and iNap, particularly for sensors in the plastids and peroxisomes, but overall the sensors were effective in quantifying relative changes in metabolite concentrations in real time *in planta*. The observed variation in the NADH:NAD^+ ratio was somewhat surprising, particularly following treatment with nitrite and flg22 in which the direct cause of the change in NADH:NAD^+ is not clear and requires further investigation. By measuring changes in metabolite concentrations over time, the fluorescent biosensors used in this thesis allowed insight into pyridine nucleotides that has not been previously possible, even with subcellular fractionation methods. However, changes in metabolite concentration alone are not sufficient to describe the underlying flux phenotype.

6.1.3 INST-MFA is the most promising method for quantifying redox metabolism in plants

The flux maps generated using INST-MFA in Chapter 3 demonstrate that fluxes in central plant metabolism including glycolysis, pentose phosphate pathway, TCA cycle, anaplerosis and amino acid biosynthesis can be precisely determined in heterotrophic *Arabidopsis* cell cultures using a single [$^{13}C_6$]glucose labelling experiment over a period of 4 h. INST-MFA was able to quantify the effect of oxidative stress induced by menadione treatment on these fluxes at a network level, providing a more quantitative and global analysis compared to previous studies which only indirectly inferred qualitative information about fluxes (Baxter et al., 2007b, 2007a). The results showed the major effect of menadione treatment was bypassing of pyruvate kinase and an increase in flux through PEP carboxylase generating OAA and malate which was

imported into the mitochondria and used to maintain TCA cycle flux. The plastidic oxPPP and ME flux also increased following menadione treatment, possibly as a mechanism to increase NADPH production, although the magnitude of these fluxes remained very small relative to TCA cycle fluxes. Analysis of coenzyme production and consumption suggested sources of NADPH in addition to NADP-IDH and the oxPPP are required to meet the biosynthetic demand, particularly if GOGAT consumes NADPH rather than NADH for nitrogen assimilation. These findings are consistent with previous work based on both flux analysis (Masakapalli et al., 2010, 2013, 2014) and genetic knock outs (Chai et al., 2006; Mhamdi and Noctor, 2015; Mhamdi et al., 2010; Voll et al., 2012; Wakao et al., 2008) showing that despite the common assertion that the oxPPP is the major source of NADPH in heterotrophic plant cells, other sources must make a substantial contribution to total supply. INST-MFA based on ^{13}C labelling cannot avoid ambiguity in coenzyme specificity, but the quantitative flux information provided makes it the most powerful technique for understanding metabolic phenotypes.

6.1.4 Relevance of experimental systems to whole plant metabolism

The methods explored in this thesis used two experimental systems, heterotrophic *Arabidopsis* cell cultures (in both liquid culture and on solid media), and transgenic *Arabidopsis* plants expressing fluorescent biosensors. Plant cell cultures represent an ideal system for isotope labelling and flux analysis which relies on the rapid introduction of labelled substrates to a homogenous population of cells. Heterotrophic *Arabidopsis* cells have been used previously for SS-MFA as well as analysis of oxidative stress, providing a useful comparison for the INST-MFA analyses in Chapter 3 (Baxter et al., 2007a; Kruger et al., 2012; Masakapalli et al., 2010, 2013, 2014; Williams et al., 2008). Furthermore, understanding the metabolism of plant cell cultures themselves can be directly relevant to biotechnological applications which use plant cell suspensions for producing high value chemicals or recombinant proteins (Arya et al., 2020; Santos et al., 2016).

Biosensors were expressed in whole plants providing insight into redox metabolism *in planta.* I focused on studying leaf disks, but other tissues such as roots and seeds are also

amenable to the multiwell fluorometry methods described in Chapter 5 (Nietzel et al., 2020). Leaf disks are submerged in buffer for analysis which may affect gas exchange, although the effects of decreasing the atmospheric oxygen concentration demonstrate that submergence does not cause hypoxia, consistent with previous analyses (Wagner et al., 2019). Future work could analyse leaf disks submerged in perfluorodecalin which improves gas exchange while maintaining favourable optical properties for fluorescence measurements. Analysis of whole plants with fluorescent imaging could also provide insight into differences in redox metabolites at the whole plant level in repose to external stimuli such as wounding or herbivory, analogous to the imaging of calcium biosensors (Toyota et al., 2018). If appropriate sensors could be expressed in the apoplast, whole plant imaging may be particularly useful for understanding the potential extracellular signalling roles of pyridine nucleotides (Wang et al., 2019).

All the analyses in this thesis explored heterotrophic metabolism. Understanding heterotrophic metabolism is important as plants spend half their lives in darkness and heterotrophic sink tissues are the major harvestable products of crops, with the relationship between source and sink metabolism acting as a major driver of crop productivity (Beevers, 1969; Bush, 2020; Rossi et al., 2015; Smith et al., 2018; White et al., 2016). Studying heterotopic metabolism also had several technical advantages for the methods studied in this thesis. The use of heterotrophic cells was a necessity for the application of deuterium labelling for studying NADPH metabolism as in photosynthesising cells, protons from water are directly transferred onto NADPH by ferredoxin-NADP reductase preventing accurate calculation of the water exchange fraction. INST-MFA in heterotrophic plant cells presents a novel application of INST-MFA to plants as the few other published reports on plants have focused exclusively on photosynthetic metabolism in leaves (Ma et al., 2014; Xu et al., 2021). Leaf disks expressing biosensors were all analysed in darkness due to the limitations of the fluorescence plate reader. Analysis of fluorescent biosensors in pseudo-continuous light using confocal microscopy has recently been described allowing rapid switching between illumination and fluorescence measurement (15-30 s illumination, 1.6 s scan cycles) (Elsässer et al., 2020). Integrating a similar

system into a fluorescence plate reader could also be possible, making use of low profile LEDs to illuminate plates from below (Baillargeon et al., 2019; Serôdio et al., 2018). Such a system could also be used to quantify chlorophyl fluorescence parameters in parallel to estimate rates of photosynthetic election flux alongside concentrations or redox potentials of NAD(P)(H). Ultimately measurements of both heterotrophic and autotrophic systems will be necessary to understand redox metabolism in plants, and further work will be needed to extend the methods explored in this thesis to autotrophic metabolism.

6.1.5 The relative contributions of different sources of reducing power

A question often raised when discussing NADPH production in plants is the unknown contribution of different sources of NAPDH to the total supply (Corpas and Barroso, 2014; Gorelova et al., 2017a; Schwender et al., 2003). The discussion of Chapter 3 highlights the challenge of quantifying coenzyme production and consumption using ^{13}C based labelling due to the unknown relative contribution of isozymes which produce different coenzymes by identical carbon transformations. The deuterium labelling strategy explored in Chapter 4 aimed to resolve this problem but was limited by the rate of hydrogen exchange between NADPH and water and the fundamental structure of the plant metabolic network. Analysis of the coenzyme demands for biosynthesis suggest some variable contribution to total supply could be made by sources such as IDH, ME, np-G3PDH, MTHFDH and ALDH. In studies of mammalian and bacterial metabolism, including photoautotrophic cyanobacteria, imbalances in NADPH and NADH production are often reconciled by invoking the activity of transhydrogenases which can transfer the redox active hydride between NADP(H) and NAD(H) (Fuhrer and Sauer, 2009; Rydström, 2006; Sauer et al., 2004; Wijker et al., 2019). Both soluble and membrane bound transhydrogenases exist, with the membrane bound form using the mitochondrial proton motive force to drive reduction of NADP from NADH (Rydström, 2006; Sauer et al., 2004) . Plants do not possess the genes for the transhydrogenases identified in other organisms but transhydrogenase-like activity can occur through the action of isozymes with multiple coenzyme specificity, as in the malate/OAA shuttle or via isoforms of IDH (Bykova and Møller, 2001;

Bykova et al., 1999). Flux balance analyses of plants often identifies transhydrogenation cycles, sometimes at the expense of ATP, which are generally removed from models or excluded as infeasible based on measurements of the relative NADPH:$NADP^+$ and NADH:NAD^+ ratios (Cheung et al., 2013). It is true that transhydrogenation will only occur in a thermodynamically feasible direction, but this can vary depending on the conditions and concentration of any coupled reactants and products. In Chapter 5 I identified three conditions which transiently decrease the NADPH concentration while the NADH:NAD^+ ratio increased; menadione, nitrite and hypoxia treatment. Without accurate calibration of biosensors, as well as measurement of $NADP^+$ concentration it is not possible to determine the thermodynamic feasibility of transhydrogenation from NADH to $NADP^+$, but it is possible that under the right circumstances such a reaction does occur. Transhydrogenation between NADP(H) and NAD(H) would provide plants with additional flexibility to rapidly meet changing demands for specific reduced coenzymes although the regulation of flux through NADPH and NADH producing reactions may be sufficient to produce an optimal coenzyme balance without the need for interconversion between coenzymes.

6.2 Future work

6.2.1 INST-MFA could be refined with positional isotopomer information

The application of INST-MFA to plants remains limited to date (Ma et al., 2014; Xu et al., 2021) and there is scope for optimisation of experimental methods and software applications. Currently only two software packages are available for INST-MFA, INCA (Young, 2014) (used in Chapter 3) and OpenMebius (Kajihata et al., 2014). However, neither of these software packages can incorporate positional labelling information into INST-MFA. Positional information produced by NMR or tandem MS can improve the precision of flux estimation and resolve certain fluxes that are otherwise indeterminable (Choi and Antoniewicz, 2019; Rühl et al., 2012b; Wang et al., 2021). Software packages for SS-MFA such as 13C-Flux2 (Weitzel et al., 2013) and Metran can incorporate these measurements but they cannot perform INST-MFA. All currently available software is based on the elementary metabolite units framework which can be

expanded to include positional information (Choi and Antoniewicz, 2019). This represents a missed opportunity to improve flux precision with relatively little additional experimental or computational effort.

6.2.2 Calibrated biosensors could facilitate thermodynamic or kinetic modelling

Integrating measurements of compartment-specific concentrations and ratios from fluorescent biosensors should improve the accuracy of computational models. Such models could be kinetic, based on dynamic concentration information and enzyme parameters (Baghalian et al., 2014; Nägele et al., 2010), or stoichiometric, based on flux balance analysis with additional thermodynamic parameters that could be constrained by metabolite concentrations (Hamilton et al., 2013). A kinetic model of mammalian mitochondrial redox metabolism incorporating data from a mitochondrially targeted iNap3 sensor and ^{13}C-flux analysis was recently used to investigate mitochondrial NADPH production rate and NADPH:$NADP^+$ ratios under H_2O_2 redox stress (Moon et al., 2020). By measuring biosensor dynamics at various rates of H_2O_2 production, data were fitted to a kinetic model (Moon et al., 2020). Methods using whole cell extracts are unable to provide the required data for kinetic modelling, demonstrating the advantage of *in vivo* biosensors. A similar approach could be taken to study dynamic changes in plant metabolism currently inaccessible to steady state flux analysis, such as during pathogen infection.

Parameters for thermodynamically constrained FBA models could also be provided by *in vivo* measurement of NAD(P)(H) concentrations or redox states using fluorescent biosensors helping, for example, to resolve the directionality of metabolite shuttles between organelles (Hamilton et al., 2013; Shameer et al., 2019). The direction of readily reversible reactions such as the mitochondrial malate/OAA shuttle is influenced by the relative concentrations of NAD(H) and malate/OAA in different compartments. Therefore, quantitative measurement of subcellular NADH:NAD^+ ratios in the cytosol and mitochondria using fluorescent biosensors would provide some of the necessary information to quantify the direction of reductant flow between compartments. SoNar and iNap fluorescent biosensors have already been used to measure the comparative differences in the amount of redox coenzymes in different compartments, supporting

hypotheses of reductant flow during photosynthesis and photorespiration (Lim et al., 2020). However, sensor calibration and quantification of absolute concentrations or ratios will be required for incorporation into models for flux prediction.

6.2.3 Better quantification of redox metabolism could facilitate metabolic engineering

Engineering metabolism for biotechnological aims requires that the host organism can support any modification being introduced. Specific modifications to redox metabolism are commonplace when engineering microorganisms (de Arroyo Garcia and Jones, 2020; Chemler et al., 2010; Chen et al., 2014; King and Feist, 2014; Qiao et al., 2017; Wang et al., 2013; Yukawa et al., 2020; Zhao et al., 2017a) but specific manipulation of coenzyme metabolism is less common in plants. Manipulating redox metabolism in plants has been demonstrated to enhance tolerance to biotic and abiotic stresses (Jin et al., 2021; Kawai-Yamada et al., 2005; Scharte et al., 2009). Potential metabolic engineering strategies include isozyme replacement or engineering altered coenzyme specificity for specific dehydrogenases (Cahn et al., 2017; King and Feist, 2014). The methods evaluated in this thesis could be applied to assess and develop these metabolic engineering strategies in plants. For example, extending the INST-MFA methodology developed in Chapter 3 to high throughput flux analyses of genetically modified plant cell cultures could allow rational metabolic engineering analogous to methods applied to microorganisms (Heux et al., 2017). INST-MFA should also be applied to leaves of whole plants which have been genetically engineered to gain mechanistic insight into the effect of any genetic changes. Fluorescent biosensors for redox metabolites could be integrated into genetic engineering pipelines to screen strains for altered redox metabolism. Flux prediction using models which incorporate data from biosensors could also be used to identify optimal modifications that would enhance redox metabolism for improved yield or stress tolerance.

6.3 Conclusion

Three methods were developed and evaluated for quantifying redox metabolism in plants. Deuterium labelling was a promising strategy for quantify specific redox coenzyme fluxes but was limited by confounding routes of label transfer found in plants. Fluorescent biosensors provided specific information about relative concentrations of redox carriers *in planta* but still require accurate calibration to realise their full potential. INST-MFA was able to measure fluxes under conditions of changing reductant demand and provided quantitative information about how the metabolic network can balance redox metabolism. Although ^{13}C-INST-MFA still cannot resolve fluxes through specific coenzymes, the compartment specific and network wide flux information provided make this the most promising method for further investigation of redox metabolism in plants. Taken together, the methods evaluated in this thesis provide a set of tools for quantifying redox metabolism that can be applied to improve our fundamental understanding of plant biology and meet biotechnological aims.

References

Adebiyi, A.O., Jazmin, L.J., and Young, J.D. (2015). ^{13}C flux analysis of cyanobacterial metabolism. Photosynth. Res. *126*, 19–32.

Agrawal, S., Kumar, S., Sehgal, R., George, S., Gupta, R., Poddar, S., Jha, A., and Pathak, S. (2019). El-MAVEN: A Fast, Robust, and User-Friendly Mass Spectrometry Data Processing Engine for Metabolomics. In High-Throughput Metabolomics: Methods and Protocols, A. D'Alessandro, ed. (New York, NY: Springer New York), pp. 301–321.

Agrimi, G., Russo, A., Pierri, C.L., and Palmieri, F. (2012). The peroxisomal NAD^+ carrier of Arabidopsis thaliana transports coenzyme A and its derivatives. J. Bioenerg. Biomembr. *44*, 333–340.

Aldieri, E., Riganti, C., Polimeni, M., Gazzano, E., Lussiana, C., Campia, I., and Ghigo, D. (2008). Classical inhibitors of NOX NAD(P)H oxidases are not specific. Curr. Drug Metab. *9*, 686–696.

Allen, D.K., and Young, J.D. (2013). Carbon and nitrogen provisions alter the metabolic flux in developing soybean embryos. Plant Physiol. *161*, 1458–1475.

Allen, D.K., Shachar-Hill, Y., and Ohlrogge, J.B. (2007). Compartment-specific labeling information in ^{13}C metabolic flux analysis of plants. Phytochemistry *68*, 2197–2210.

Aller, I., Rouhier, N., and Meyer, A.J. (2013). Development of roGFP2-derived redox probes for measurement of the glutathione redox potential in the cytosol of severely glutathione-deficient rml1 seedlings. Front. Plant Sci. *4*.

Alonso, A.P., Val, D.L., and Shachar-Hill, Y. (2011). Central metabolic fluxes in the endosperm of developing maize seeds and their implications for metabolic engineering. Metab. Eng. *13*, 96–107.

Anderson, J.M., Chow, W.S., and Park, Y.I. (1995). The grand design of photosynthesis:

Acclimation of the photosynthetic apparatus to environmental cues. Photosynth. Res. *46*, 129–139.

Antoniewicz, M.R. (2013). Dynamic metabolic flux analysis-tools for probing transient states of metabolic networks. Curr. Opin. Biotechnol. *24*, 973–978.

Antoniewicz, M.R., Kelleher, J.K., and Stephanopoulos, G. (2006). Determination of confidence intervals of metabolic fluxes estimated from stable isotope measurements. Metab. Eng. *8*, 324–337.

Arrivault, S., Guenther, M., Ivakov, A., Feil, R., Vosloh, D., Van Dongen, J.T., Sulpice, R., and Stitt, M. (2009). Use of reverse-phase liquid chromatography, linked to tandem mass spectrometry, to profile the Calvin cycle and other metabolic intermediates in Arabidopsis rosettes at different carbon dioxide concentrations. Plant J. *59*, 824–839.

de Arroyo Garcia, L., and Jones, P.R. (2020). In silico co-factor balance estimation using constraint-based modelling informs metabolic engineering in Escherichia coli. PLoS Comput. Biol. *16*, 1–32.

Arya, S.S., Rookes, J.E., Cahill, D.M., and Lenka, S.K. (2020). Next-generation metabolic engineering approaches towards development of plant cell suspension cultures as specialized metabolite producing biofactories. Biotechnol. Adv. *45*, 107635.

Austin, P.C., and Hux, J.E. (2002). A brief note on overlapping confidence intervals. J. Vasc. Surg. *36*, 194–195.

Baghalian, K., Hajirezaei, M.R.M.-R., and Schreiber, F. (2014). Plant metabolic modeling: achieving new insight into metabolism and metabolic engineering. Plant Cell *26*, 3847–3866.

Baillargeon, P., Coss-Flores, K., Singhera, F., Shumate, J., Williams, H., DeLuca, L., Spicer, T.P., and Scampavia, L. (2019). Design of Microplate-Compatible Illumination Panels for a Semiautomated Benchtop Pipetting System. SLAS Technol. Transl. Life Sci. Innov. *24*, 399–

407.

Baker, N.R. (2008). Chlorophyll fluorescence: A probe of photosynthesis in vivo. Annu. Rev. Plant Biol. *59*, 89–113.

Baker, P.J., Britton, K.L., Rice, D.W., Rob, A., and Stillman, T.J. (1992). Structural consequences of sequence patterns in the fingerprint region of the nucleotide binding fold: Implications for nucleotide specificity. J. Mol. Biol. *228*, 662–671.

Bateman, A., Martin, M.J., O'Donovan, C., Magrane, M., Alpi, E., Antunes, R., Bely, B., Bingley, M., Bonilla, C., Britto, R., et al. (2017). UniProt: The universal protein knowledgebase. Nucleic Acids Res. *45*, D158–D169.

Baxter, C.J., Schauer, N., Redestig, H., Fernie, A.R., Liu, J., Patil, K.R., Repsilber, D., Nielsen, J., Sweetlove, L.J., Selbig, J., et al. (2007a). The metabolic response of heterotrophic Arabidopsis cells to oxidative stress. Plant Physiol. *143*, 312–325.

Baxter, C.J., Liu, J.L., Fernie, A.R., and Sweetlove, L.J. (2007b). Determination of metabolic fluxes in a non-steady-state system. Phytochemistry *68*, 2313–2319.

Beard, D.A., and Qian, H. (2007). Relationship between thermodynamic driving force and one-way fluxes in reversible processes. PLoS One *2*, 1–4.

Beevers, H. (1969). Metabolic Sinks. In Physiological Aspects of Crop Yield, pp. 169–180.

Behera, S., Xu, Z., Luoni, L., Bonza, M.C., Doccula, F.G., De Michelis, M.I., Morris, R.J., Schwarzländer, M., and Costa, A. (2018). Cellular Ca^{2+} signals generate defined pH signatures in plants. Plant Cell *30*, 2704–2719.

Ben-Yoseph, O., Kingsley, P.B., and Ross, B.D. (1994). Metabolic loss of deuterium from isotopically labeled glucose. Magn. Reson. Med. *32*, 405–409.

Berrisford, J.M., and Sazanov, L.A. (2009). Structural basis for the mechanism of

respiratory complex I. J. Biol. Chem. *284*, 29773–29783.

Bestetti, S., Medraño-Fernandez, I., Galli, M., Ghitti, M., Bienert, G.P., Musco, G., Orsi, A., Rubartelli, A., and Sitia, R. (2018). A persulfidation-based mechanism controls aquaporin-8 conductance. Sci. Adv. *4*, 1–9.

Bhonwong, A., Stout, M.J., Attajarusit, J., and Tantasawat, P. (2009). Defensive role of tomato polyphenol oxidases against cotton bollworm helicoverpa armigera and beet armyworm spodoptera exigua. J. Chem. Ecol. *35*, 28–38.

Bienert, G.P., and Chaumont, F. (2014). Aquaporin-facilitated transmembrane diffusion of hydrogen peroxide. Biochim. Biophys. Acta - Gen. Subj. *1840*, 1596–1604.

Blacker, T.S., and Duchen, M.R. (2016). Investigating mitochondrial redox state using NADH and NADPH autofluorescence. Free Radic. Biol. Med. *100*, 53–65.

Blacker, T.S., Mann, Z.F., Gale, J.E., Ziegler, M., Bain, A.J., Szabadkai, G., and Duchen, M.R. (2014). Separating NADH and NADPH fluorescence in live cells and tissues using FLIM. Nat. Commun. *5*, 3936.

Buchanan, B.B., and Balmer, Y. (2005). Redox regulation: A broadening horizon. Annu. Rev. Plant Biol. *56*, 187–220.

Buescher, J.M., Moco, S., Sauer, U., and Zamboni, N. (2010). Ultrahigh performance liquid chromatography-tandem mass spectrometry method for fast and robust quantification of anionic and aromatic metabolites. Anal. Chem. *82*, 4403–4412.

Bush, D.R. (2020). Identifying the pathways that control resource allocation in higher plants. Proc. Natl. Acad. Sci. U. S. A. *117*, 8669–8671.

Büttner, M. (2007). The monosaccharide transporter(-like) gene family in Arabidopsis. FEBS Lett. *581*, 2318–2324.

Bykova, N. V., and Møller, I.M. (2001). Involvement of matrix NADP turnover in the

oxidation of NAD^+-linked substrates by pea leaf mitochondria. Physiol. Plant. *111*, 448–456.

Bykova, N. V, Rasmusson, A.G., Igamberdiev, A.U., Gardestrîm, P., and Moller, I. (1999). Two separate transhydrogenase activities are preset in plant mitochondria. Biochem.Biophys.Res.Commun. *265*, 106–111.

Cahn, J.K.B., Werlang, C.A., Baumschlager, A., Brinkmann-Chen, S., Mayo, S.L., and Arnold, F.H. (2017). A general tool for engineering the NAD/NADP cofactor preference of oxidoreductases. ACS Synth. Biol. *6*, 326–333.

Calvin, M., and Benson, A.A. (1948). The path of carbon in photosynthesis. Science *107*, 476–480.

Cambronne, X.A., Stewart, M.L., Kim, D., Jones-Brunette, A.M., Morgan, R.K., Farrens, D.L., Cohen, M.S., and Goodman, R.H. (2016). Biosensor reveals multiple sources for mitochondrial NAD^+. Science *352*, 1474–1477.

Cameron, W.D., Bui, C. V., Hutchinson, A., Loppnau, P., Gräslund, S., and Rocheleau, J. V. (2016). Apollo-$NADP^+$: A spectrally tunable family of genetically encoded sensors for $NADP^+$. Nat. Methods *13*, 352–358.

Chai, M.F., Chen, Q.J., An, R., Chen, Y.M., Chen, J., and Wang, X.C. (2005). NADK2, an Arabidopsis chloroplastic NAD kinase, plays a vital role in both chlorophyll synthesis and chloroplast protection. Plant Mol. Biol. *59*, 553–564.

Chai, M.F., Wei, P.C., Chen, Q.J., An, R., Chen, J., Yang, S., and Wang, X.C. (2006). NADK3, a novel cytoplasmic source of NADPH, is required under conditions of oxidative stress and modulates abscisic acid responses in Arabidopsis. Plant J. *47*, 665–674.

Chance, B., Legallais, V., and Schoener, B. (1962). Metabolically linked changes in fluorescence emission spectra of cortex of rat brain, kidney and adrenal gland. Nature *195*, 1073–1075.

Chang, M., Li, L., Hu, H., Hu, Q., Wang, A., Cao, X., Yu, X., Zhang, S., Zhao, Y., Chen,

J., et al. (2017). Using fractional intensities of time-resolved fluorescence to sensitively quantify NADH/NAD^+ with genetically encoded fluorescent biosensors. Sci. Rep. *7*, 4209.

Chaudhuri, B., Hörmann, F., Lalonde, S., Brady, S.M., Orlando, D.A., Benfey, P., and Frommer, W.B. (2008). Protonophore- and pH-insensitive glucose and sucrose accumulation detected by FRET nanosensors in *Arabidopsis* root tips. Plant J. *56*, 948–962.

Chemler, J.A., Fowler, Z.L., McHugh, K.P., and Koffas, M.A.G. (2010). Improving NADPH availability for natural product biosynthesis in Escherichia coli by metabolic engineering. Metab. Eng. *12*, 96–104.

Chen, L., Zhang, Z., Hoshino, A., Zheng, H.D., Morley, M., Arany, Z., and Rabinowitz, J.D. (2019a). NADPH production by the oxidative pentose-phosphate pathway supports folate metabolism. Nat. Metab. *1*, 404–415.

Chen, Q., Wang, B., Ding, H., Zhang, J., and Li, S. (2019b). Review: The role of NADP-malic enzyme in plants under stress. Plant Sci. 0–1.

Chen, X., Li, S., and Liu, L. (2014). Engineering redox balance through cofactor systems. Trends Biotechnol. *32*, 337–343.

Cheung, C.Y.M., Williams, T.C.R., Poolman, M.G., Fell, D.A., Ratcliffe, R.G., and Sweetlove, L.J. (2013). A method for accounting for maintenance costs in flux balance analysis improves the prediction of plant cell metabolic phenotypes under stress conditions. Plant J. *75*, 1050–1061.

Chida, H., Nakazawa, A., Akazaki, H., Hirano, T., Suruga, K., Ogawa, M., Satoh, T., Kadokura, K., Yamada, S., Hakamata, W., et al. (2007). Expression of the algal cytochrome c6 gene in Arabidopsis enhances photosynthesis and growth. Plant Cell Physiol. *48*, 948–957.

Choi, J., and Antoniewicz, M.R. (2019). Tandem mass spectrometry for ^{13}C metabolic flux analysis: methods and algorithms based on EMU framework. Front. Microbiol. *10*, 1–8.

Chong, J., Wishart, D.S., and Xia, J. (2019). Using MetaboAnalyst 4.0 for

comprehensive and integrative metabolomics data analysis. Curr. Protoc. Bioinforma. *68*, e86.

Clough, S.J., and Bent, A.F. (1998). Floral dip: a simplified method for Agrobacterium - mediated transformation of Arabidopsis thaliana. Plant J. *16*, 735–743.

De Col, V., Fuchs, P., Nietzel, T., Elsässer, M., Voon, C.P., Candeo, A., Seeliger, I., Fricker, M.D., Grefen, C., Møller, I.M., et al. (2017). ATP sensing in living plant cells reveals tissue gradients and stress dynamics of energy physiology. Elife *6*, e26770.

Comelli, R.N., and Gonzalez, D.H. (2007). Conserved homeodomain cysteines confer redox sensitivity and influence the DNA binding properties of plant class III HD-Zip proteins. Arch. Biochem. Biophys. *467*, 41–47.

Corpas, F.J., and Barroso, J.B. (2014). NADPH-generating dehydrogenases: their role in the mechanism of protection against nitro-oxidative stress induced by adverse environmental conditions. Front. Environ. Sci. *2*, 55.

Costa, A., Drago, I., Behera, S., Zottini, M., Pizzo, P., Schroeder, J.I., Pozzan, T., and Schiavo, F. Lo (2010). H2O2 in plant peroxisomes: An *in vivo* analysis uncovers a Ca^{2+}-dependent scavenging system. Plant J. *62*, 760–772.

Couturier, J., Chibani, K., Jacquot, J.-P., and Rouhier, N. (2013). Cysteine–based redox regulation and signaling in plants. Front. Plant Sci. *4*, 1–7.

Cracan, V., Titov, D. V., Shen, H., Grabarek, Z., and Mootha, V.K. (2017). A genetically encoded tool for manipulation of $NADP^+$/NADPH in living cells. Nat. Chem. Biol. *13*, 1088–1095.

Datta, R., Heaster, T.M., Sharick, J.T., Gillette, A.A., and Skala, M.C. (2020). Fluorescence lifetime imaging microscopy: fundamentals and advances in instrumentation, analysis, and applications. J. Biomed. Opt. *25*, 071203.

Dell'Aglio, E., Giustini, C., Kraut, A., Couté, Y., Costa, A., Decros, G., Gibon, Y., Mazars, C., Matringe, M., Finazzi, G., et al. (2019). Identification of the Arabidopsis calmodulin-

dependent NAD1 kinase that sustains the elicitor-induced oxidative BURST. Plant Physiol. *181*, 1449–1458.

Dietz, K.J. (2014). Redox regulation of transcription factors in plant stress acclimation and development. Antioxid. Redox Signal. *21*, 1356–1372.

Dietz, K.J. (2017). Subcellular metabolomics: The choice of method depends on the aim of the study. J. Exp. Bot. *68*, 5695–5698.

Elsässer, M., Feitosa-Araujo, E., Lichtenauer, S., Wagner, S., Fuchs, P., Giese, J., Kotnik, F., Hippler, M., Meyer, A.J., Maurino, V.G., et al. (2020). Photosynthetic activity triggers pH and NAD redox signatures across different plant cell compartments. BioRxiv doi: 10.1101/2020.10.31.363051.

Esposito, S., Guerriero, G., Vona, V., Di Martino Rigano, V., Carfagna, S., and Rigano, C. (2005). Glutamate synthase activities and protein changes in relation to nitrogen nutrition in barley: The dependence on different plastidic glucose-6P dehydrogenase isoforms. J. Exp. Bot. *56*, 55–64.

Fan, J., Ye, J., Kamphorst, J.J., Shlomi, T., Thompson, C.B., and Rabinowitz, J.D. (2014). Quantitative flux analysis reveals folate-dependent NADPH production. Nature *510*, 298–302.

Feitosa-Araujo, E., De Souza Chaves, I., Florian, A., Da Fonseca-Pereira, P., Condori Apfata, J.A., Heyneke, E., Medeiros, D.B., Pires, M.V., Mettler-Altmann, T., Neuhaus, H.E., et al. (2020a). Downregulation of a Mitochondrial NAD^+Transporter (NDT2) Alters Seed Production and Germination in Arabidopsis. Plant Cell Physiol. *61*, 897–908.

Feitosa-Araujo, E., da Fonseca-Pereira, P., Miranda Pena, M., Medeiros, D.B., Souza, L.P. de, Yoshida, T., Weber, A.P., Araújo, W.L., Fernie, A.R., Schwarzländer, M., et al. (2020b). Changes in intracellular NAD status affect stomatal development in an abscisic acid-dependent manner. Plant J. *104*, 1149–1168.

Fell, D.A. (2005). Enzymes, metabolites and fluxes. J. Exp. Bot. *56*, 267–272.

Fernie, A.R., and Stitt, M. (2012). On the discordance of metabolomics with proteomics and transcriptomics: Coping with increasing complexity in logic, chemistry, and network interactions. Plant Physiol. *158*, 1139–1145.

Fernie, A.R., Roscher, A., Ratcliffe, R.G., and Kruger, N.J. (2001). Fructose 2,6-bisphosphate activates pyrophosphate: fructose-6-phosphate 1-phosphotransferase and increases triose phosphate to hexose phosphate cycling in heterotrophic cells. Planta *212*, 250–263.

Fletcher, S.J., Herlihy, J.M., Knowles, J.R., and Albery, W.J. (1976). Energetics of triosephosphate isomerase: the appearance of solvent tritium in substrate glyceraldehyde 3-phosphate and in product. Biochemistry *15*, 5612–5617.

Foyer, C.H., and Halliwell, B. (1976). The presence of glutathione and glutathione reductase in chloroplasts: A proposed role in ascorbic acid metabolism. Planta *133*, 21–25.

Foyer, C.H., and Noctor, G. (2009). Redox regulation in photosynthetic organisms: signaling, acclimation, and practical implications. Antioxid. Redox Signal. *11*, 861–905.

Foyer, C.H., and Noctor, G. (2011). Ascorbate and glutathione: the heart of the redox hub. Plant Physiol. *155*, 2–18.

Foyer, C.H., and Noctor, G. (2020). Redox homeostasis and signaling in a higher-CO_2 world. Annu. Rev. Plant Biol. *71*, 157–182.

Foyer, C.H., Theodoulou, F.L., and Delrot, S. (2001). The functions of inter- and intracellular glutathione transport systems in plants. Trends Plant Sci. *6*, 486–492.

Foyer, C.H., Noctor, G., and Hodges, M. (2011). Respiration and nitrogen assimilation: targeting mitochondria-associated metabolism as a means to enhance nitrogen use efficiency. J. Exp. Bot. *62*, 1467–1482.

Friso, G., and Van Wijk, K.J. (2015). Posttranslational protein modifications in plant

metabolism. Plant Physiol. *169*, 1469–1487.

Fuhrer, T., and Sauer, U. (2009). Different biochemical mechanisms ensure network-wide balancing of reducing equivalents in microbial metabolism. J. Bacteriol. *191*, 2112–2121.

Fukuyama, K. (2004). Structure and function of plant-type ferredoxins. Photosynth. Res. *81*, 289–301.

Gakière, B., Fernie, A.R., and Pétriacq, P. (2018a). More to NAD^+ than meets the eye: a regulator of metabolic pools and gene expression in Arabidopsis. Free Radic. Biol. Med. *122*, 86–95.

Gakière, B., Hao, J., de Bont, L., Pétriacq, P., Nunes-Nesi, A., and Fernie, A.R. (2018b). NAD^+ biosynthesis and signaling in plants. Crit. Rev. Plant Sci. *37*, 259–307.

Garlick, A.P. (2002). Carbohydrate metabolism during oxidative stress in plants. University of Oxford.

Garlick, A.P., Moore, C., and Kruger, N.J. (2002). Monitoring flux through the oxidative pentose phosphate pathway using [1-^{14}C]gluconate. Planta *216*, 265–272.

Gauthier, P.P.G., Battle, M.O., Griffin, K.L., and Bender, M.L. (2018). Measurement of gross photosynthesis, respiration in the light, and mesophyll conductance using $H_2{}^{18}O$ labeling. Plant Physiol. *177*, 62–74.

Gerhardt, R., Stitt, M., and Heldt, H.W. (1987). Subcellular metabolite levels in spinach leaves: regulation of sucrose synthesis during diurnal alterations in photosynthetic partitioning. Plant Physiol. *83*, 399–407.

Ghergurovich, J.M., García-Cañaveras, J.C., Wang, J., Schmidt, E., Zhang, Z., TeSlaa, T., Patel, H., Chen, L., Britt, E.C., Piqueras-Nebot, M., et al. (2020). A small molecule G6PD inhibitor reveals immune dependence on pentose phosphate pathway. Nat. Chem. Biol. *16*, 731–739.

Gil, A., Siegel, D., Permentier, H., Reijngoud, D.J., Dekker, F., and Bischoff, R. (2015). Stability of energy metabolites-an often overlooked issue in metabolomics studies: A review. Electrophoresis *36*, 2156–2169.

Gill, S.S., Anjum, N.A., Hasanuzzaman, M., Gill, R., Trivedi, D.K., Ahmad, I., Pereira, E., and Tuteja, N. (2013). Glutathione and glutathione reductase: A boon in disguise for plant abiotic stress defense operations. Plant Physiol. Biochem. *70*, 204–212.

Giró, M., Ceccoli, R.D., Poli, H.O., Carrillo, N., and Lodeyro, A.F. (2011). An in vivo system involving co-expression of cyanobacterial flavodoxin and ferredoxin-$NADP^+$ reductase confers increased tolerance to oxidative stress in plants. FEBS Open Bio *1*, 7–13.

Gjetting, K.S.K., Ytting, C.K., Schulz, A., and Fuglsang, A.T. (2012). Live imaging of intra-and extracellular pH in plants using pHusion, a novel genetically encoded biosensor. J. Exp. Bot. *63*, 3207–3218.

Gomes, A., Fernandes, E., and Lima, J.L.F.C. (2005). Fluorescence probes used for detection of reactive oxygen species. J. Biochem. Biophys. Methods *65*, 45–80.

González-Bosch, C. (2018). Priming plant resistance by activation of redox-sensitive genes. Free Radic. Biol. Med. 0–1.

Gorelova, V., De Lepeleire, J., Van Daele, J., Pluim, D., Meï, C., Cuypers, A., Leroux, O., Rébeillé, F., Schellens, J., Blancquaert, D., et al. (2017a). Dihydrofolate reductase/thymidylate synthase fine-tunes the folate status and controls redox homeostasis in plants. Plant Cell *29*, 2831–2853.

Gorelova, V., Ambach, L., Rébeillé, F., Stove, C., and Van Der Straeten, D. (2017b). Folates in Plants: Research Advances and Progress in Crop Biofortification. Front. Chem. *5*, 1–20.

Grüning, N.-M., Rinnerthaler, M., Bluemlein, K., Mülleder, M., Wamelink, M.M.C., Lehrach, H., Jakobs, C., Breitenbach, M., and Ralser, M. (2011). Pyruvate kinase triggers a

metabolic feedback loop that controls redox metabolism in respiring cells. Cell Metab. *14*, 415–427.

Gutscher, M., Pauleau, A.-L., Marty, L., Brach, T., Wabnitz, G.H., Samstag, Y., Meyer, A.J., and Dick, T.P. (2008). Real-time imaging of the intracellular glutathione redox potential. Nat. Methods *5*, 553–559.

Haber, Z., and Rosenwasser, S. (2020). Resolving the dynamics of photosynthetically produced ROS by high-resolution monitoring of chloroplastic EGSH in Arabidopsis. BioRxiv doi: 10.1101/2020.03.04.976092.

Halliwell, B., and Gutteridge, J.M.C. (2015a). Oxygen: boon yet bane—introducing oxygen toxicity and reactive species. In Free Radicals in Biology and Medicine, (Oxford: Oxford University Press), p.

Halliwell, B., and Gutteridge, J.M.C. (2015b). Oxidative stress and redox regulation: adaptation, damage, repair, senescence, and death. In Free Radicals in Biology and Medicine, (Oxford: Oxford University Press), p.

Hamilton, J.J., Dwivedi, V., and Reed, J.L. (2013). Quantitative assessment of thermodynamic constraints on the solution space of genome-scale metabolic models. Biophys. J. *105*, 512–522.

Hanke, G., and Mulo, P. (2013). Plant type ferredoxins and ferredoxin-dependent metabolism. Plant, Cell Environ. *36*, 1071–1084.

Hanson, A.D., Gage, D.A., and Shachar-hill, Y. (2000). Plant one-carbon metabolism and its engineering. Trends Plant Sci. *5*, 206–213.

Hanson, G.T., Aggeler, R., Oglesbee, D., Cannon, M., Capaldi, R.A., Tsien, R.Y., and Remington, S.J. (2004). Investigating mitochondrial redox potential with redox-sensitive green fluorescent protein indicators. J. Biol. Chem. *279*, 13044–13053.

Harth, S., Wagner, J., Sens, T., Choe, J. yong, Benz, J.P., Weuster-Botz, D., and Oreb,

M. (2020). Engineering cofactor supply and NADH-dependent d-galacturonic acid reductases for redox-balanced production of l-galactonate in Saccharomyces cerevisiae. Sci. Rep. *10*, 1–12.

Hashida, S.N., Takahashi, H., and Uchimiya, H. (2009). The role of NAD biosynthesis in plant development and stress responses. Ann. Bot. *103*, 819–824.

Hatefi, Y., and Stempel, K.E. (1969). Isolation and enzymatic properties of the mitochondrial reduced diphosphopyridine nucleotide dehydrogenase. J. Biol. Chem. *244*, 2350–2357.

Heineke, D., Riens, B., Grosse, H., Hoferichter, P., Peter, U., Flugge, U., and Heldt, H.W. (1991). Redox transfer across the inner chloroplast envelope membrane. Plant Physiol. *95*, 1131–1137.

Heise, R., Fernie, A.R., Stitt, M., and Nikoloski, Z. (2015). Pool size measurements facilitate the determination of fluxes at branching points in non-stationary metabolic flux analysis: the case of Arabidopsis thaliana. Front. Plant Sci. *6*, 386.

Herber, U.W., and Santarius, K.A. (1965). Compartmentation and reduction of pyridine nucleotides in relation to photosynthesis. Biochim. Biophys. Acta *9*, 390–408.

Herud-Sikimic, O., Stiel, A.C., Ortega-Perez, M., Shanmugaratnam, S., Höcker, B., and Jürgens, G. (2020). Design of a biosensor for direct visualisation of auxin. BioRxiv doi: 10.1101/2020.01.19.911735.

Heux, S., Bergès, C., Millard, P., Portais, J.C., and Létisse, F. (2017). Recent advances in high-throughput ^{13}C-fluxomics. Curr. Opin. Biotechnol. *43*, 104–109.

Höhner, R., Pribil, M., Herbstová, M., Lopez, L.S., Kunz, H.H., Li, M., Wood, M., Svoboda, V., Puthiyaveetil, S., Leister, D., et al. (2020). Plastocyanin is the long-range electron carrier between photosystem II and photosystem I in plants. Proc. Natl. Acad. Sci. U. S. A. *117*, 15354–15362.

Hong, S., Chen, T., Liu, L., Cao, C., Lv, F., Rabinowitz, J.D., Huang, Y., and Chen, X.

(2020). Live-Cell Imaging of NADPH Production from Specific Pathways. CCS Chem. 1642–1648.

Horn, P.J. (2021). Where do the electrons go? How numerous redox processes drive phytochemical diversity: Redox processes in phytochemistry. Phytochem. Rev.

Horsch, R.B., King, J., and Jones, G.E. (1980). Measurement of cultured plant cell growth on filter paper discs. Can. J. Bot. *58*, 2402–2406.

Hossain, M.A., Nakano, Y., and Asada, K. (1984). Monodehydroascorbate reductase in spinach chloroplasts and its participation in regeneration of ascorbate for scavenging hydrogen peroxide. Plant Cell Physiol. *25*, 385–395.

Hossain, M.A., Bhattacharjee, S., Armin, S.M., Qian, P., Xin, W., Li, H.Y., Burritt, D.J., Fujita, M., and Tran, L.S.P. (2015). Hydrogen peroxide priming modulates abiotic oxidative stress tolerance: Insights from ROS detoxification and scavenging. Front. Plant Sci. *6*, 1–19.

Hu, C., Wang, P., Zhang, P., Nie, X., Li, B., Tai, L., Liu, W.-T., Li, W.-Q., and Chen, K.-M. (2020). NADPH Oxidases: The Vital Performers and Center Hubs during Plant Growth and Signaling. Cells *9*, 437.

Hung, Y.P., Albeck, J.G., Tantama, M., and Yellen, G. (2011). Imaging cytosolic NADH-NAD^+ redox state with a genetically encoded fluorescent biosensor. Cell Metab. *1071*, 83–95.

Hunt, L., Lerner, F., and Ziegler, M. (2004). NAD - New roles in signalling and gene regulation in plants. New Phytol. *163*, 31–44.

Hýsková, V.D., Miedzińska, L., Dobrá, J., Vankova, R., and Ryšlavá, H. (2014). Phosphoenolpyruvate carboxylase, NADP-malic enzyme, and pyruvate, phosphate dikinase are involved in the acclimation of *Nicotiana tabacum L.* to drought stress. J. Plant Physiol. *171*, 19–25.

Igamberdiev, A.U. (2020). Citrate valve integrates mitochondria into photosynthetic

metabolism. Mitochondrion *52*, 218–230.

Igamberdiev, A.U., and Gardeström, P. (2003). Regulation of NAD- and NADP-dependent isocitrate dehydrogenases by reduction levels of pyridine nucleotides in mitochondria and cytosol of pea leaves. Biochim. Biophys. Acta - Bioenerg. *1606*, 117–125.

Iyer, V. V., Sriram, G., Fulton, D.B., Zhou, R., Westgate, M.E., and Shanks, J. V. (2008). Metabolic flux maps comparing the effect of temperature on protein and oil biosynthesis in developing soybean cotyledons. Plant, Cell Environ. *31*, 506–517.

Jacoby, R.P., Millar, A.H., and Taylor, N.L. (2015). Assessment of respiration in isolated plant mitochondria using clark-type electrodes. In Plant Mitochondria: Methods and Protocols, pp. 1–303.

Jacquot, J.P., Rivera-Madrid, R., Marinho, P., Kollarova, M., Le Maréchal, P., Miginiac-Maslow, M., and Meyer, Y. (1994). Arabidopsis thaliana NAPHP thioredoxin reductase: cDNA characterization and expression of the recombinant protein in Escherichia coli. J. Mol. Biol. *235*, 1357–1363.

Jamaï, A., Tommasini, R., Martinoia, E., and Delrot, S. (1996). Characterization of glutathione uptake in broad bean leaf protoplasts. Plant Physiol. *111*, 1145–1152.

Jazmin, L.J., Xu, Y., Cheah, Y.E., Adebiyi, A.O., Johnson, C.H., and Young, J.D. (2017). Isotopically nonstationary ^{13}C flux analysis of cyanobacterial isobutyraldehyde production. Metab. Eng. *42*, 9–18.

Jin, J., Li, K., Qin, J., Yan, L., Wang, S., Zhang, G., Wang, X., and Bi, Y. (2021). The response mechanism to salt stress in Arabidopsis transgenic lines over-expressing of GmG6PD. Plant Physiol. Biochem.

Jinich, A., Flamholz, A., Ren, H., Kim, S.-J.J., Sanchez-Lengeling, B., Cotton, C.A.R.R., Noor, E., Aspuru-Guzik, A., and Bar-Even, A. (2018). Quantum chemistry reveals thermodynamic principles of redox biochemistry. PLOS Comput. Biol. *14*, e1006471.

Joshi, N.C., Meyer, A.J., Bangash, S.A.K., Zheng, Z.L., and Leustek, T. (2019). Arabidopsis γ-glutamylcyclotransferase affects glutathione content and root system architecture during sulfur starvation. New Phytol. *221*, 1387–1397.

Journet, E.-P., Neuburger, M., and Douce, R. (1981). Role of glutamate-oxaloacetate transaminase and malate dehydrogenase in the regeneration of NAD^+ for glycine oxidation by spinach leaf mitochondria. Plant Physiol. *67*, 467–469.

Joy, K.W., and Hageman, R.H. (1966). The purification and properties of nitrite reductase from higher plants, and its dependence on ferredoxin. Biochem. J. *100*, 263–273.

Kadota, Y., Shirasu, K., and Zipfel, C. (2015). Regulation of the NADPH Oxidase RBOHD during Plant Immunity. Plant Cell Physiol. *56*, 1472–1480.

Kajihata, S., Furusawa, C., Matsuda, F., and Shimizu, H. (2014). OpenMebius: an open source software for isotopically nonstationary ^{13}C-based metabolic flux analysis. Biomed Res. Int. *2014*, 627014.

Kappelmann, J., Wiechert, W., and Noack, S. (2016). Cutting the Gordian Knot: Identifiability of anaplerotic reactions in Corynebacterium glutamicum by means of ^{13}C-metabolic flux analysis. Biotechnol. Bioeng. *113*, 661–674.

Karimi, M., Inzé, D., and Depicker, A. (2002). GATEWAY^{TM} vectors for Agrobacterium-mediated plant transformation. Trends Plant Sci. *7*, 193–195.

Kasimova, M.R., Grigiene, J., Krab, K., Hagedorn, P.H., Flyvbjerg, H., Andersen, P.E., and Møller, I.M. (2006). The free NADH concentration is kept constant in plant mitochondria under different metabolic conditions. Plant Cell *18*, 688–698.

Kawai-Yamada, M., Yu, L.-H., Huang, J., Hayashi, M., Takahashi, H., Uchimiya, H., Tezuka, T., and Tamura, K. (2005). Enhanced dihydroflavonol-4-reductase activity and NAD homeostasis leading to cell death tolerance in transgenic rice. Proc. Natl. Acad. Sci. *102*, 7020–7025.

Kazuki, S., Akihiko, K., Shigenobu, O., Yousuke, S., and Tamio, Y. (1980). Incorporation of hydrogen atoms from deuterated water and stereospecifically deuterium-labeled nicotinamide nucleotides into fatty acids with the Escherichia coli fatty acid synthetase system. Biochim. Biophys. Acta *618*, 202–213.

King, Z.A., and Feist, A.M. (2014). Optimal cofactor swapping can increase the theoretical yield for chemical production in Escherichia coli and Saccharomyces cerevisiae. Metab. Eng. *24*, 117–128.

Kneen, M., Farinas, J., Li, Y., and Verkman, A.S. (1998). Green fluorescent protein as a noninvasive intracellular pH indicator. Biophys. J. *74*, 1591–1599.

Knol, M.J., Pestman, W.R., and Grobbee, D.E. (2011). The (mis)use of overlap of confidence intervals to assess effect modification. Eur. J. Epidemiol. *26*, 253–254.

Köhler, E., Barrach, H.-J., and Neubert, D. (1970). Inhibition of NADP dependent oxidoreductases by the 6-aminonicotinamide analogue of NADP. FEBS Lett. *6*, 225–228.

Kojima, S., Konishi, N., Beier, M.P., Ishiyama, K., Maru, I., Hayakawa, T., and Yamaya, T. (2014). NADH-dependent glutamate synthase participated in ammonium assimilation in Arabidopsis root. Plant Signal. Behav. *9*, 1–4.

Koller, D. (1990). Light-driven leaf movements. Plant. Cell Environ. *13*, 615–632.

Krall, L., Huege, J., Catchpole, G., Steinhauser, D., and Willmitzer, L. (2009). Assessment of sampling strategies for gas chromatography-mass spectrometry (GC-MS) based metabolomics of cyanobacteria. J. Chromatogr. B Anal. Technol. Biomed. Life Sci. *877*, 2952–2960.

Kramer, D.M., and Evans, J.R. (2011). The importance of energy balance in improving photosynthetic productivity. Plant Physiol. *155*, 70–78.

Kruger, N.J., and Ratcliffe, R.G. (2009). Insights into plant metabolic networks from steady-state metabolic flux analysis. Biochimie *91*, 697–702.

Kruger, N.J., and Ratcliffe, R.G. (2015). Fluxes through plant metabolic networks: measurements, predictions, insights and challenges. Biochem. J. *465*, 27–38.

Kruger, N.J., and von Schaewen, A. (2003). The oxidative pentose phosphate pathway: structure and organisation. Curr. Opin. Plant Biol. *6*, 236–246.

Kruger, N.J., Le Lay, P., and Ratcliffe, R.G. (2007). Vacuolar compartmentation complicates the steady-state analysis of glucose metabolism and forces reappraisal of sucrose cycling in plants. Phytochemistry *68*, 2189–2196.

Kruger, N.J., Masakapalli, S.K., and Ratcliffe, R.G. (2012). Strategies for investigating the plant metabolic network with steady-state metabolic flux analysis: Lessons from an Arabidopsis cell culture and other systems. J. Exp. Bot. *63*, 2309–2323.

Kubo, A., Sano, T., Saji, H., Tanaka, K., Kondo, N., and Tanaka, K. (1993). Primary structure and properties of glutathione reductase from arabidopsis thaliana. Plant Cell Physiol. *34*, 1259–1266.

Lambers, H. (1982). Cyanide-resistant respiration: A non-phosphorylating electron transport pathway acting as an energy overflow. Physiol. Plant. *55*, 478–485.

Lancien, M., Martin, M., Hsieh, M.H., Leustek, T., Goodman, H., and Coruzzi, G.M. (2002). Arabidopsis glt1-T mutant defines a role for NADH-GOGAT in the non-photorespiratory ammonium assimilatory pathway. Plant J. *29*, 347–358.

Lanquar, V., Grossmann, G., Vinkenborg, J.L., Merkx, M., Thomine, S., and Frommer, W.B. (2014). Dynamic imaging of cytosolic zinc in *Arabidopsis* roots combining FRET sensors and RootChip technology. New Phytol. *202*, 198–208.

Lee, R.B. (1980). Sources of reductant for nitrate assimilation in non-photosynthetic tissue: a review. Plant. Cell Environ. *3*, 65–90.

Lehmann, M., Schwarzlä Nder B, M., Obata, T., Sirikantaramas, S., Burow, M., Olsen, C.E., Tohge, T., Fricker, M.D., Lindberg Møller, B., Fernie, A.R., et al. (2009). The metabolic

response of Arabidopsis roots to oxidative stress is distinct from that of heterotrophic cells in culture and highlights a complex relationship between the levels of transcripts, metabolites, and flux. Mol. Plant *2*, 390–406.

Lehmann, M., Laxa, M., Sweetlove, L.J., Fernie, A.R., and Obata, T. (2012). Metabolic recovery of Arabidopsis thaliana roots following cessation of oxidative stress. Metabolomics *8*, 143–153.

Leterrier, M., Barroso, J.B., Valderrama, R., Palma, J.M., and Corpas, F.J. (2012). NADP-dependent isocitrate dehydrogenase from Arabidopsis roots contributes in the mechanism of defence against the nitro-oxidative stress induced by salinity. Sci. World J. *2012*, 1–9.

Levenberg, K. (1944). A method for the solution of certain non-linear problems in least squares. Q. Appl. Math. *2*, 164–168.

Lewis, C.A., Parker, S.J., Fiske, B.P., McCloskey, D., Gui, D.Y., Green, C.R., Vokes, N.I., Feist, A.M., Vander Heiden, M.G., and Metallo, C.M. (2014). Tracing compartmentalized NADPH metabolism in the cytosol and mitochondria of mammalian cells. Mol. Cell *55*, 253–263.

Li, B.-B., Wang, X., Tai, L., Ma, T.-T., Shalmani, A., Liu, W.-T., Li, W.-Q., and Chen, K.-M. (2018). NAD kinases: metabolic targets controlling redox co-enzymes and reducing power partitioning in plant stress and development. Front. Plant Sci. *9*, 379.

Li, L., Zhou, J.S., Wang, P., Ma, C.Q., Zhu, Z.W., Gu, J., Zhu, C., Chen, G.Q., Zhang, S.J., and Xu, J.H. (2019). pH resistant ratiometric measurement of nicotinamide adenine dinucleotide levels by time-resolved fluorescence spectroscopy. Chinese J. Anal. Chem. *47*, e19009–e19013.

Li, L., Cheng, Y., Shen, S., Zhou, J., Wang, A., Chen, G., Xu, J., Yang, Y., Zhao, Y., Zhang, S., et al. (2020). Sensitive detection via the time-resolved fluorescence of circularly permuted yellow fluorescent protein biosensors. Sensors Actuators, B Chem. *321*, 128614.

Lim, S., Voon, C.P., and Lim, B.L. (2020). In planta study of photosynthesis and photorespiration using NADPH and NADH/NAD^+ fluorescent protein sensors. Nat. Commun. *11*, 3238.

Liu, M., and Lu, S. (2016). Plastoquinone and ubiquinone in plants: Biosynthesis, physiological function and metabolic engineering. Front. Plant Sci. *7*, 1–18.

Liu, B., Sun, L., Ma, L., and Hao, F.S. (2017). Both AtrbohD and AtrbohF are essential for mediating responses to oxygen deficiency in Arabidopsis. Plant Cell Rep. *36*, 947–957.

Liu, J., Li, H., Zhao, G., Caiyin, Q., and Qiao, J. (2018). Redox cofactor engineering in industrial microorganisms: strategies, recent applications and future directions. J. Ind. Microbiol. Biotechnol. *45*, 313–327.

Liu, L., Shah, S., Fan, J., Park, J.O., Wellen, K.E., and Rabinowitz, J.D. (2016). Malic enzyme tracers reveal hypoxia-induced switch in adipocyte NADPH pathway usage. Nat. Chem. Biol. *12*, 345–352.

Lonien, J., and Schwender, J. (2009). Analysis of metabolic flux phenotypes for two Arabidopsis mutants with severe impairment in seed storage lipid synthesis. Plant Physiol. *151*, 1617–1634.

López-Calcagno, P.E., Brown, K.L., Simkin, A.J., Fisk, S.J., Vialet-Chabrand, S., Lawson, T., and Raines, C.A. (2020). Stimulating photosynthetic processes increases productivity and water-use efficiency in the field. Nat. Plants *6*, 1054–1063.

Lorenzen, I., Aberle, T., and Plieth, C. (2004). Salt stress-induced chloride flux: A study using transgenic *Arabidopsis* expressing a fluorescent anion probe. Plant J. *38*, 539–544.

Lu, W., Wang, L., Chen, L., Hui, S., and Rabinowitz, J.D. (2018). Extraction and quantitation of NAD(P)(H). Antioxid. Redox Signal. *28*, 167–179.

Lu, Y.P., Li, Z.S., Drozdowicz, Y.M., Hörtensteiner, S., Martinoia, E., and Rea, P.A. (1998). AtMRP2, an Arabidopsis ATP binding cassette transporter able to transport glutathione

S-conjugates and chlorophyll catabolites: Functional comparisons with AtMRP1. Plant Cell *10*, 267–282.

Luo, L., He, Y., Zhao, Y., Xu, Q., Wu, J., Ma, H., Guo, H., Bai, L., Zuo, J., Zhou, J.M., et al. (2019). Regulation of mitochondrial NAD pool via NAD^+ transporter 2 is essential for matrix NADH homeostasis and ROS production in Arabidopsis. Sci. China Life Sci. *62*, 991–1002.

Luo, L., He, Y., Xu, Q., Lyu, W., Yan, J., Xin, P., Zhang, D., Chu, J., Li, J., and Yu, H. (2020). Rapid and specific isolation of intact mitochondria from *Arabidopsis* leaves. J. Genet. Genomics *47*, 65–68.

Ma, F., Jazmin, L.J., Young, J.D., and Allen, D.K. (2014). Isotopically nonstationary ^{13}C flux analysis of changes in Arabidopsis thaliana leaf metabolism due to high light acclimation. Proc. Natl. Acad. Sci. *111*, 16967–16972.

Ma, Y., Zhao, Y., Walker, R.K., and Berkowitz, G.A. (2013). Molecular steps in the immune signaling pathway evoked by plant elicitor peptides: Ca^{2+}-dependent protein kinases, nitric oxide, and reactive oxygen species are downstream from the early $Ca2^+$ signal. Plant Physiol. *163*, 1459–1471.

Mairinger, T., Wegscheider, W., Peña, D.A., Steiger, M.G., Koellensperger, G., Zanghellini, J., and Hann, S. (2018). Comprehensive assessment of measurement uncertainty in ^{13}C-based metabolic flux experiments. Anal. Bioanal. Chem. *410*, 3337–3348.

Maister, S.G., Pett, C.P., Knowles, J.R., and Albery, W.J. (1976). Energetics of triosephosphate isomerase: the appearance of solvent tritium in substrate dihydroxyacetone phosphate and in product. Biochemistry *15*, 5607–5612.

Majander, A., Finel, M., and Wikström, M. (1994). Diphenyleneiodonium inhibits reduction of iron-sulfur clusters in the mitochondrial NADH-ubiquinone oxidoreductase (Complex I). J. Biol. Chem. *269*, 21037–21042.

Marino, D., Dunand, C., Puppo, A., and Pauly, N. (2012). A burst of plant NADPH oxidases. Trends Plant Sci. *17*, 9–15.

Marks, A.J. (2000). The role of cytosolic 6-phosphogluconate dehydrogenase in maize primary roots. University of Oxford.

Martí, M.C., Jiménez, A., and Sevilla, F. (2020). Thioredoxin network in plant mitochondria: cysteine S-posttranslational modifications and stress conditions. Front. Plant Sci. *11*, 1–20.

Masakapalli, S.K., Le Lay, P., Huddleston, J.E., Pollock, N.L., Kruger, N.J., and Ratcliffe, R.G. (2010). Subcellular flux analysis of central metabolism in a heterotrophic Arabidopsis cell suspension using steady-state stable isotope labeling. Plant Physiol. *152*, 602–619.

Masakapalli, S.K., Kruger, N.J., and Ratcliffe, R.G. (2013). The metabolic flux phenotype of heterotrophic Arabidopsis cells reveals a complex response to changes in nitrogen supply. Plant J. *74*, 569–582.

Masakapalli, S.K., Bryant, F.M., Kruger, N.J., and Ratcliffe, R.G. (2014). The metabolic flux phenotype of heterotrophic Arabidopsis cells reveals a flexible balance between the cytosolic and plastidic contributions to carbohydrate oxidation in response to phosphate limitation. Plant J. *78*, 964–977.

Massey, V. (2000). The chemical and biological versatility of riboflavin. Biochem. Soc. Trans. *28*, 283.

Matoh, T.T.T., and Takahashi, E. (1982). Changes in the activities of ferredoxin- and NADH-glutamate synthase during seedling development of peas. Planta *154*, 289–294.

Maughan, S.C., Pasternak, M., Cairns, N., Kiddle, G., Brach, T., Jarvis, R., Haas, F., Nieuwland, J., Lim, B., Müller, C., et al. (2010). Plant homologs of the Plasmodium falciparum chloroquine-resistance transporter, PfCRT, are required for glutathione homeostasis and stress

responses. Proc. Natl. Acad. Sci. U. S. A. *107*, 2331–2336.

McDonagh, B., Ogueta, S., Lasarte, G., Padilla, C.A., and Bárcena, J.A. (2009). Shotgun redox proteomics identifies specifically modified cysteines in key metabolic enzymes under oxidative stress in Saccharomyces cerevisiae. J. Proteomics *72*, 677–689.

Mergner, J., Frejno, M., List, M., Papacek, M., Chen, X., Chaudhary, A., Samaras, P., Richter, S., Shikata, H., Messerer, M., et al. (2020). Mass-spectrometry-based draft of the Arabidopsis proteome. Nature *579*, 409–414.

Mescam, M., Vinnakota, K.C., and Beard, D.A. (2011). Identification of the catalytic mechanism and estimation of kinetic parameters for fumarase. J. Biol. Chem. *286*, 21100–21109.

Mevik, B.-H., and Wehrens, R. (2007). The pls package: principal component and partial least squares regression in R. J. Stat. Software; Vol 1, Issue 2.

Meyer, A.J., May, M.J., and Fricker, M. (2001). Quantitative in vivo measurement of glutathione in Arabidopsis cells. Plant J. *27*, 67–78.

Meyer, Y., Belin, C., Delorme-Hinoux, V., Reichheld, J.P., and Riondet, C. (2012). Thioredoxin and glutaredoxin systems in plants: Molecular mechanisms, crosstalks, and functional significance. Antioxid. Redox Signal. *17*, 1124–1160.

Mhamdi, A., and Noctor, G. (2015). Analysis of the roles of the Arabidopsis peroxisomal isocitrate dehydrogenase in leaf metabolism and oxidative stress. Environ. Exp. Bot. *114*, 22–29.

Mhamdi, A., Mauve, C., Gouia, H., Saindrenan, P., Hodges, M., and Noctor, G. (2010). Cytosolic NADP-dependent isocitrate dehydrogenase contributes to redox homeostasis and the regulation of pathogen responses in Arabidopsis leaves. Plant Cell Environ. *33*, 1112–1123.

Miflin, B.J. (1974). The location of nitrite reductase and other enzymes related to amino acid biosynthesis in the plastids of root and leaves. Plant Physiol. *54*, 550–555.

Miflin, B.J., and Lea, P.J. (1976). The pathway of nitrogen assimilation in plants.

Phytochemistry *15*, 873–885.

Millar, A.H., and Leaver, C.J. (2000). The cytotoxic lipid peroxidation product, 4-hydroxy-2-nonenal, specifically inhibits decarboxylating dehydrogenases in the matrix of plant mitochondria. FEBS Lett. *481*, 117–121.

Millard, P., Letisse, F., Sokol, S., and Portais, J.C. (2012). IsoCor: Correcting MS data in isotope labeling experiments. Bioinformatics *28*, 1294–1296.

Miller, G., Schlauch, K., Tam, R., Cortes, D., Torres, M.A., Shulaev, V., Dangl, J.L., and Mittler, R. (2009). The plant NADPH oxidase RBOHD mediates rapid systemic signaling in response to diverse stimuli. Sci. Signal. *2*.

Missihoun, T.D., Kotchoni, S.O., and Bartels, D. (2018). Aldehyde dehydrogenases function in the homeostasis of pyridine nucleotides in arabidopsis thaliana. Sci. Rep. *8*, 4–11.

Mittler, R. (2017). ROS are good. Trends Plant Sci. *22*, 11–19.

Miyake, C. (2010). Alternative electron flows (water-water cycle and cyclic electron flow around PSI) in photosynthesis: Molecular mechanisms and physiological functions. Plant Cell Physiol. *51*, 1951–1963.

Mock, H.P., and Dietz, K.J. (2016). Redox proteomics for the assessment of redox-related posttranslational regulation in plants. Biochim. Biophys. Acta - Proteins Proteomics *1864*, 967–973.

Moon, S.J., Dong, W., Stephanopoulos, G.N., and Sikes, H.D. (2020). Oxidative pentose phosphate pathway and glucose anaplerosis support maintenance of mitochondrial NADPH pool under mitochondrial oxidative stress. Bioeng. Transl. Med. *5*, e10184.

Müller-Schüssele, S.J., Wang, R., Gütle, D.D., Romer, J., Rodriguez-Franco, M., Scholz, M., Lüth, V.M., Kopriva, S., Dörmann, P., Schwarzländer, M., et al. (2020). Chloroplasts require glutathione reductase to balance reactive oxygen species and maintain efficient photosynthesis. Plant J. 1–15.

Müller-Schüssele, S.J., Schwarzländer, M., and Meyer, A.J. (2021). Live monitoring of plant redox and energy physiology with genetically encoded biosensors. Plant Physiol. 1–36.

Nägele, T., Henkel, S., Hörmiller, I., Sauter, T., Sawodny, O., Ederer, M., and Heyer, A.G. (2010). Mathematical modeling of the central carbohydrate metabolism in arabidopsis reveals a substantial regulatory influence of vacuolar invertase on whole plant carbon metabolism. Plant Physiol. *153*, 260–272.

Nelson, N., and Junge, W. (2015). Structure and energy transfer in photosystems of oxygenic photosynthesis. Annu. Rev. Biochem. *84*, 659–683.

Niehaus, M., Straube, H., Künzler, P., Rugen, N., Hegermann, J., Giavalisco, P., Eubel, H., Witte, C.P., and Herde, M. (2020). Rapid affinity purification of tagged plant mitochondria (Mito-AP) for metabolome and proteome analyses. Plant Physiol. *182*, 1194–1210.

Nietzel, T., Elsässer, M., Ruberti, C., Steinbeck, J., Ugalde, J.M., Fuchs, P., Wagner, S., Ostermann, L., Moseler, A., Lemke, P., et al. (2019a). The fluorescent protein sensor roGFP2-Orp1 monitors in vivo H_2O_2 and thiol redox integration and elucidates intracellular H_2O_2 dynamics during elicitor-induced oxidative burst in Arabidopsis. New Phytol. *221*, 1649–1664.

Nietzel, T., Elsässer, M., Ruberti, C., Steinbeck, J., Ugalde, J.M., Fuchs, P., Wagner, S., Ostermann, L., Moseler, A., Lemke, P., et al. (2019b). The fluorescent protein sensor roGFP2-Orp1 monitors in vivo H_2O_2 and thiol redox integration and elucidates intracellular H_2O_2 dynamics during elicitor-induced oxidative burst in Arabidopsis. New Phytol. *221*, 1649–1664.

Nietzel, T., Mostertz, J., Ruberti, C., Née, G., Fuchs, P., Wagner, S., Moseler, A., Müller-Schüssele, S.J., Benamar, A., Poschet, G., et al. (2020). Redox-mediated kick-start of mitochondrial energy metabolism drives resource-efficient seed germination. Proc. Natl. Acad. Sci. U. S. A. *117*, 741–751.

Noctor, G., and Foyer, C.H. (1998). Ascorbate and glutathione: keeping active oxygen under control. Annu. Rev. Plant Physiol. Plant Mol. Biol *49*, 249–279.

Noctor, G., Queval, G., and Gakière, B. (2006). NAD(P) synthesis and pyridine nucleotide cycling in plants and their potential importance in stress conditions. J. Exp. Bot. *57*, 1603–1620.

Noctor, G., Mhamdi, A., Chaouch, S., Han, Y., Neukermans, J., Marquez-Garcia, B., Queval, G., and Foyer, C.H. (2012). Glutathione in plants: An integrated overview. Plant, Cell Environ. *35*, 454–484.

Nogués, I., Campos, L.A., Sancho, J., Gómez-Moreno, C., Mayhew, S.G., and Medina, M. (2004). Role of neighboring FMN side chains in the modulation of flavin reduction potentials and in the energetics of the FMN:apoprotein interaction in Anabaena flavodoxin. Biochemistry *43*, 15111–15121.

Nöh, K., and Wiechert, W. (2006). Experimental design principles for isotopically instationary ^{13}C labeling experiments. Biotechnol. Bioeng. *94*, 234–251.

Nöh, K., Wahl, A., and Wiechert, W. (2006). Computational tools for isotopically instationary ^{13}C labeling experiments under metabolic steady state conditions. Metab. Eng. *8*, 554–577.

Obata, T., Matthes, A., Koszior, S., Lehmann, M., Araújo, W.L., Bock, R., Sweetlove, L.J., and Fernie, A.R. (2011). Alteration of mitochondrial protein complexes in relation to metabolic regulation under short-term oxidative stress in Arabidopsis seedlings. Phytochemistry *72*, 1081–1091.

Ohnishi, M., Anegawa, A., Sugiyama, Y., Harada, K., Oikawa, A., Nakayama, Y., Matsuda, F., Nakamura, Y., Sasaki, R., Shichijo, C., et al. (2018). Molecular components of Arabidopsis intact vacuoles clarified with metabolomic and proteomic analyses. Plant Cell Physiol. *59*, 1353–1362.

Ojalvo, I., Rokem, J.S., Navon, G., and Goldberg, I. (1987). ^{31}P NMR study of elicitor treated phaseolus vulgaris cell suspension cultures. Plant Physiol. *85*, 716–719.

Palmieri, F., Rieder, B., Ventrella, A., Blanco, E., Do, P.T., Nunes-Nesi, A., Trauth, A.U., Fiermonte, G., Tjaden, J., Agrimi, G., et al. (2009). Molecular identification and functional characterization of Arabidopsis thaliana mitochondrial and chloroplastic NAD^+ carrier proteins. J. Biol. Chem. *284*, 31249–31259.

Pandey, P., Singh, J., Achary, V.M.M., and Mallireddy Reddy, K. (2015). Redox homeostasis via gene families of ascorbate-glutathione pathway. Front. Environ. Sci. *3*, 1–14.

Papageorgiou, G.C., and Govindjee (2014). The Non-Photochemical Quenching of the Electronically Excited State of Chlorophyll a in Plants: Definitions, Timelines, Viewpoints, Open Questions. In Non-Photochemical Quenching and Energy Dissipation in Plants, Algae and Cyanobacteria, B. Demmig-Adams, G. Garab, W. Adams III, and Govindjee, eds. (Dordrecht: Springer Netherlands), pp. 1–44.

Park, J., and Choi, Y. (2017). Cofactor engineering in cyanobacteria to overcome imbalance between NADPH and NADH: A mini review. Front. Chem. Sci. Eng. *11*, 66–71.

Piattoni, C. V., Guerrero, S.A., and Iglesias, A.A. (2013). A differential redox regulation of the pathways metabolizing glyceraldehyde-3-phosphate tunes the production of reducing power in the cytosol of plant cells. Int. J. Mol. Sci. *14*, 8073–8092.

Ponsero, A.J., Igbaria, A., Darch, M.A., Miled, S., Outten, C.E., Winther, J.R., Palais, G., D'Autréaux, B., Delaunay-Moisan, A., and Toledano, M.B. (2017). Endoplasmic Reticulum Transport of Glutathione by Sec61 Is Regulated by Ero1 and Bip. Mol. Cell *67*, 962-973.e5.

Potters, G., Horemans, N., and Jansen, M.A.K. (2010). The cellular redox state in plant stress biology - A charging concept. Plant Physiol. Biochem. *48*, 292–300.

Press, W.H., and Vetterling, W.T. (1992). Numerical recipes in C : the art of scientific computing (Cambridge: Cambridge University Press).

Pucciariello, C., and Perata, P. (2017). New insights into reactive oxygen species and nitric oxide signalling under low oxygen in plants. Plant Cell Environ. *40*, 473–482.

Pucciariello, C., and Perata, P. (2021). The oxidative paradox in low oxygen stress in plants. Antioxidants *10*, 1–14.

Pucciariello, C., Parlanti, S., Banti, V., Novi, G., and Perata, P. (2012). Reactive oxygen species-driven transcription in Arabidopsis under oxygen deprivation. Plant Physiol. *159*, 184–196.

Pucker, B., Rückert, C., Stracke, R., Viehöver, P., Kalinowski, J., and Weisshaar, B. (2019). Twenty-five years of propagation in suspension cell culture results in substantial alterations of the Arabidopsis thaliana genome. Genes (Basel). *10*, 1–13.

Pugin, a., Frachisse, J.M., Tavernier, E., Bligny, R., Gout, E., Douce, R., and Guern, J. (1997). Early events induced by the elicitor cryptogein in tobacco cells: involvement of a plasma membrane NADPH oxidase and activation of glycolysis and the pentose phosphate pathway. Plant Cell *9*, 2077–2091.

Qiao, K., Wasylenko, T.M., Zhou, K., Xu, P., and Stephanopoulos, G. (2017). lipid production inYarrowia lipolytica maximized by engineering cytosolic redox metabolism. Nat. Biotechnol. *35*, 173–177.

Quatresous, E., Legrand, C., and Pouvreau, S. (2012). Mitochondria-targeted cpYFP: PH or superoxide sensor? J. Gen. Physiol. *140*, 567–570.

Queval, G., Jaillard, D., Zechmann, B., and Noctor, G. (2011). Increased intracellular H_2O_2 availability preferentially drives glutathione accumulation in vacuoles and chloroplasts. Plant, Cell Environ. *34*, 21–32.

R Core Team (2020). R: A Language and Environment for Statistical Computing.

Ramaro, C.S., Srinivasan, C.., and Naik, M.S. (1981). Origin of reductant for reduction of nitrate and nitrite in rice and wheat leaves in vivo. New Phytol. *87*, 517–525.

Rao, S.T., and Rossmann, M.G. (1973). Comparison of super-secondary structures in proteins. J. Mol. Biol. *76*, 241–256.

Rasmusson, A.G., Soole, K.L., and Elthon, T.E. (2004). Alternative NAD(P)H dehydrogenases of plant mitochondria. Annu. Rev. Plant Biol. *55*, 23–39.

Ratcliffe, R.G., and Shachar-Hill, Y. (2006). Measuring multiple fluxes through plant metabolic networks. Plant J. *45*, 490–511.

Rawsthorne, S. (2002). Carbon flux and fatty acid synthesis in plants. Prog. Lipid Res. *41*, 182–196.

Reiter, J., Pick, A., Wiemann, L., Schieder, D., and Sieber, V. (2014). A novel natural NADH and NADPH dependent glutathione reductase as tool in biotechnological applications. JSM Biotechnol. Biomed. Eng. *2*, 1028.

Rich, P.R., and Maréchal, A. (2012). Electron transfer chains: Structures, mechanisms and energy coupling. Compr. Biophys. *8*, 72–93.

Richards, A. (2015). University of Oxford Advanced Research Computing.

Rius, S.P., Casati, P., Iglesias, A.A., and Gomez-Casati, D.F. (2006). Characterization of an Arabidopsis thaliana mutant lacking a cytosolic non-phosphorylating glyceraldehyde-3-phosphate dehydrogenase. Plant Mol. Biol. *61*, 945–957.

Rizza, A., Walia, A., Lanquar, V., Frommer, W.B., and Jones, A.M. (2017). In vivo gibberellin gradients visualized in rapidly elongating tissues. Nat. Plants *3*, 803–813.

Rodrigues, O., Reshetnyak, G., Grondin, A., Saijo, Y., Leonhardt, N., Maurel, C., and Verdoucq, L. (2017). Aquaporins facilitate hydrogen peroxide entry into guard cells to mediate ABA- and pathogen-triggered stomatal closure. Proc. Natl. Acad. Sci. U. S. A. *114*, 9200–9205.

Rontein, D., Dieuaide-Noubhani, M., Dufourc, E.J., Raymond, P., and Rolin, D. (2002). The metabolic architecture of plant cells. Stability of central metabolism and flexibility of anabolic pathways during the growth cycle of tomato cells. J. Biol. Chem. *277*, 43948–43960.

Rossi, M., Bermudez, L., and Carrari, F. (2015). Crop yield: Challenges from a metabolic

perspective. Curr. Opin. Plant Biol. *25*, 79–89.

Rühl, M., Le Coq, D., Aymerich, S., and Sauer, U. (2012a). ^{13}C-flux analysis reveals NADPH-balancing transhydrogenation cycles in stationary phase of nitrogen-starving Bacillus subtilis. J. Biol. Chem. *287*, 27959–27970.

Rühl, M., Rupp, B., Nöh, K., Wiechert, W., Sauer, U., and Zamboni, N. (2012b). Collisional fragmentation of central carbon metabolites in LC-MS/MS increases precision of ^{13}C metabolic flux analysis. Biotechnol. Bioeng. *109*, 763–771.

Ruiz-May, E., Segura-Cabrera, A., Elizalde-Contreras, J.M., Shannon, L.M., and Loyola-Vargas, V.M. (2019). A recent advance in the intracellular and extracellular redox post-translational modification of proteins in plants. J. Mol. Recognit. *32*, 1–13.

Ruzicka, F.J., and Crane, F.L. (1971). Quinone interaction with the respiratory chain-linked NADH dehydrogenase of beef heart mitochondria. BBA - Bioenerg. *226*, 221–233.

Rydström, J. (2006). Mitochondrial NADPH, transhydrogenase and disease. Biochim. Biophys. Acta - Bioenerg. *1757*, 721–726.

Sagi, M., and Fluhr, R. (2006). Production of reactive oxygen species by plant NADPH oxidases. Plant Physiol. *141*, 336–340.

Sahu, A., Banerjee, S., Raju, A.S., Chiou, T.-J., Garcia, L.R., and Versaw, W.K. (2020). Spatial profiles of phosphate in roots indicate developmental control of uptake, recycling, and sequestration. Plant Physiol. *184*, 2064–2077.

Sallin, O., Reymond, L., Gondrand, C., Raith, F., Koch, B., and Johnsson, K. (2018). Semisynthetic biosensors for mapping cellular concentrations of nicotinamide adenine dinucleotides. Elife *7*, e32638.

Santos, R.B., Abranches, R., Fischer, R., Sack, M., and Holland, T. (2016). Putting the spotlight back on plant suspension cultures. Front. Plant Sci. *7*, 1–12.

Sauer, M., and Friml, J. (2010). Immunolocalization of proteins in plants. In Plant Developmental Biology: Methods and Protocols, L. Hennig, and C. Köhler, eds. (Totowa, NJ: Humana Press), pp. 253–263.

Sauer, U., Canonaco, F., Heri, S., Perrenoud, A., and Fischer, E. (2004). The soluble and membrane-bound transhydrogenases UdhA and PntAB have divergent functions in NADPH metabolism of Escherichia coli. J. Biol. Chem. *279*, 6613–6619.

Schaedler, T.A., Thornton, J.D., Kruse, I., Schwarzländer, M., Meyer, A.J., Van Veen, H.W., and Balk, J. (2014). A conserved mitochondrial ATP-binding cassette transporter exports glutathione polysulfide for cytosolic metal cofactor assembly. J. Biol. Chem. *289*, 23264–23274.

Schaefer, P.M., Kalinina, S., Rueck, A., von Arnim, C.A.F., and von Einem, B. (2019). NADH Autofluorescence—A Marker on its Way to Boost Bioenergetic Research. Cytom. Part A *95*, 34–46.

Scharte, J., Schön, H., Tjaden, Z., Weis, E., and von Schaewen, A. (2009). Isoenzyme replacement of glucose-6-phosphate dehydrogenase in the cytosol improves stress tolerance in plants. Proc. Natl. Acad. Sci. *106*, 8061–8066.

Scheibe, R. (1987). $NADP^+$-malate dehydrogenase in C3-plants: Regulation and role of a light-activated enzyme. Physiol. Plant. *71*, 393–400.

Scheibe, R. (2004). Malate valves to balance cellular energy supply. Physiol. Plant. *120*, 21–26.

Scheibe, R. (2019). Maintaining homeostasis by controlled alternatives for energy distribution in plant cells under changing conditions of supply and demand. Photosynth. Res. *139*, 81–91.

Scheibe, R., Backhausen, J.E., Emmerlich, V., and Holtgrefe, S. (2005). Strategies to maintain redox homeostasis during photosynthesis under changing conditions. J. Exp. Bot. *56*, 1481–1489.

Schertl, P., and Braun, H.P. (2014). Respiratory electron transfer pathways in plant mitochondria. Front. Plant Sci. *5*, 163.

Schläpfer, P., Zhang, P., Wang, C., Kim, T., Banf, M., Chae, L., Dreher, K., Chavali, A.K., Nilo-Poyanco, R., Bernard, T., et al. (2017). Genome-wide prediction of metabolic enzymes, pathways, and gene clusters in plants. Plant Physiol. *173*, 2041–2059.

Schleucher, J., Vanderveer, P., Markley, J.L., and Sharkey, T.D. (1999). Intramolecular deuterium distributions reveal disequilibrium of chloroplast phosphoglucose isomerase. Plant Cell Environ. *22*, 525–533.

Schneider, A., Martini, N., and Rennenberg, H. (1992). Reduced glutathione (GSH) transport into cultured tobacco cells. Plant Physiol. Biochem. *30*, 29–38.

Schneider, M., Knuesting, J., Birkholz, O., Heinisch, J.J., and Scheibe, R. (2018). Cytosolic GAPDH as a redox-dependent regulator of energy metabolism. BMC Plant Biol. *18*, 1–14.

Scholten, H.J. (1980). A plating technique for poorly growing cell cultures of Arabidopsis thaliana. Arab. Inf. Serv. *17*, 27.

Schürmann, P., and Buchanan, B.B. (2008). The ferredoxin/thioredoxin system of oxygenic photosynthesis. Antioxid. Redox Signal. *10*, 1235–1273.

Schwarzländer, M., Fricker, M.D., Müller, C., Marty, L., Brach, T., Novak, J., Sweetlove, L.J., Hell, R., and Meyer, A.J. (2008). Confocal imaging of glutathione redox potential in living plant cells. J. Microsc. *231*, 299–316.

Schwarzländer, M., Fricker, M.D., and Sweetlove, L.J. (2009). Monitoring the in vivo redox state of plant mitochondria: Effect of respiratory inhibitors, abiotic stress and assessment of recovery from oxidative challenge. Biochim. Biophys. Acta - Bioenerg. *1787*, 468–475.

Schwarzländer, M., Logan, D.C., Fricker, M.D., and Sweetlove, L.J. (2011). The circularly permuted yellow fluorescent protein cpYFP that has been used as a superoxide probe is

highly responsive to pH but not superoxide in mitochondria: Implications for the existence of superoxide “flashes.” Biochem. J. *437*, 381–387.

Schwarzländer, M., Wagner, S., Ermakova, Y.G., Belousov, V. V., Radi, R., Beckman, J.S., Buettner, G.R., Demaurex, N., Duchen, M.R., Forman, H.J., et al. (2014). The “mitoflash” probe cpYFP does not respond to superoxide. Nature *514*, E12–E14.

Schwarzländer, M., Dick, T.P., Meyer, A.J., and Morgan, B. (2016). Dissecting redox biology using fluorescent protein sensors. Antioxid. Redox Signal. *24*, 680–712.

Schwender, J., Shachar-Hill, Y., and Ohlrogge, J.B. (2006). Mitochondrial metabolism in developing embryos of Brassica napus. J. Biol. Chem. *281*, 34040–34047.

Schwender, J.J.J., Ohlrogge, J.B., and Shachar-Hill, Y. (2003). A flux model of glycolysis and the oxidative pentosephosphate pathway in developing Brassica napus embryos. J. Biol. Chem. *278*, 29442–29453.

Selinski, J., and Scheibe, R. (2018). Malate valves: old shuttles with new perspectives. Plant Biol. *21*, 21–30.

Serôdio, J., Schmidt, W., Frommlet, J.C., Christa, G., and Nitschke, M.R. (2018). An LED-based multi-actinic illumination system for the high throughput study of photosynthetic light responses.

Shameer, S., Ratcliffe, R.G., and Sweetlove, L.J. (2019). Leaf energy balance requires mitochondrial respiration and export of chloroplast NADPH in the light. Plant Physiol. *180*, 1947–1961.

Shreve, D.S., and Levy, H.R. (1980). Kinetic mechanism of glucose-6-phosphate dehydrogenase from the lactating rat mammary gland. Implications for regulation. J. Biol. Chem. *255*, 2670–2677.

Slabas, A.R., and Fawcett, T. (1992). The biochemistry and molecular biology of plant lipid biosynthesis. Plant Mol. Biol. *19*, 169–191.

Smith, E.N., McCullagh, J.S.O., Ratcliffe, R.G., and Kruger, N.J. (2019). Limitations of deuterium-labelled substrates for quantifying NADPH metabolism in heterotrophic arabidopsis cell cultures. Metabolites *9*, 205.

Smith, M.R., Rao, I.M., and Merchant, A. (2018). Source-sink relationships in crop plants and their influence on yield development and nutritional quality. Front. Plant Sci. *9*, 1–10.

Soares, A.P., Anastasiou, D., Poulogiannis, G., Asara, J.M., Boxer, M.B., Jiang, J., Shen, M., Bellinger, G., Sasaki, A.T., Locasale, J.W., et al. (2011). Inhibition of pyruvate kinase M2 by reactive oxygen species contributes to cellular antioxidant responses. Science *334*, 1278 LP – 1283.

de Souza Chaves, I., Feitosa-Araújo, E., Florian, A., Medeiros, D.B., da Fonseca-Pereira, P., Charton, L., Heyneke, E., Apfata, J.A.C., Pires, M. V., Mettler-Altmann, T., et al. (2019). The mitochondrial NAD^+ transporter (NDT1) plays important roles in cellular NAD^+ homeostasis in Arabidopsis thaliana. Plant J. *100*, 487–504.

Sperschneider, J., Catanzariti, A.M., Deboer, K., Petre, B., Gardiner, D.M., Singh, K.B., Dodds, P.N., and Taylor, J.M. (2017). LOCALIZER: Subcellular localization prediction of both plant and effector proteins in the plant cell. Sci. Rep. *7*, 1–14.

Steinbeck, J., Fuchs, P., Negroni, Y.L., Elsässer, M., Lichtenauer, S., Stockdreher, Y., Feitosa-Araujo, E., Kroll, J.B., Niemeier, J.O., Humberg, C., et al. (2020). In vivo NADH/NAD^+ biosensing reveals the dynamics of cytosolic redox metabolism in plants. Plant Cell *32*, 3324–3345.

Su, X., Lu, W., and Rabinowitz, J.D. (2017). Metabolite spectral accuracy on orbitraps. Anal. Chem. *89*, 5940–5948.

Suarez-Mendez, C.A., Hanemaaijer, M., ten Pierick, A., Wolters, J.C., Heijnen, J.J., and Wahl, S.A. (2016). Interaction of storage carbohydrates and other cyclic fluxes with central metabolism: a quantitative approach by non-stationary ^{13}C metabolic flux analysis. Metab. Eng.

Commun. *3*, 52–63.

Sugiura, K., Yokochi, Y., Fu, N., Fukaya, Y., Yoshida, K., Mihara, S., and Hisabori, T. (2019). The thioredoxin (Trx) redox state sensor protein can visualize Trx activities in the light/dark response in chloroplasts. J. Biol. Chem. *294*, 12091–12098.

Sun, L.R., Zhao, Z.J., and Hao, F.S. (2019). NADPH oxidases, essential players of hormone signalings in plant development and response to stresses. Plant Signal. Behav. *14*, 5–9.

Suzuki, N., Miller, G., Morales, J., Shulaev, V., Torres, M.A., and Mittler, R. (2011). Respiratory burst oxidases: The engines of ROS signaling. Curr. Opin. Plant Biol. *14*, 691–699.

Sweetlove, L.J., Heazlewoo, J.L., Herald, V., Holtzapffel, R., Day, D.A., Leaver, C.J., and Millar, A.H. (2002). The impact of oxidative stress on A. thaliana mitochondria. Plant J. *32*, 891–904.

Szal, B., Dąbrowska, Z., Malmberg, G., Gardeström, P., and Rychter, A.M. (2008). Changes in energy status of leaf cells as a consequence of mitochondrial genome rearrangement. Planta *227*, 697–706.

Szecowka, M., Heise, R., Tohge, T., Nunes-Nesi, A., Vosloh, D., Huege, J., Feil, R., Lunn, J., Nikoloski, Z., Stitt, M., et al. (2013). Metabolic fluxes in an illuminated Arabidopsis rosette. Plant Cell *25*, 694–714.

Szymańska, E., Saccenti, E., Smilde, A.K., and Westerhuis, J.A. (2012). Double-check: Validation of diagnostic statistics for PLS-DA models in metabolomics studies. Metabolomics *8*, 3–16.

Tanz, S.K., Castleden, I., Small, I.D., and Harvey Millar, A. (2013). Fluorescent protein tagging as a tool to define the subcellular distribution of proteins in plants. Front. Plant Sci. *4*, 1–9.

Tao, R., Zhao, Y., Chu, H., Wang, A., Zhu, J., Chen, X., Zou, Y., Shi, M., Liu, R., Su, N., et al. (2017). Genetically encoded fluorescent sensors reveal dynamic regulation of NADPH

metabolism. Nat. Methods *14*, 720–728.

Tao, X., Yang, Z., and Tong, L. (2003). Crystal structures of substrate complexes of malic enzyme and insights into the catalytic mechanism. Structure *11*, 1141–1150.

Thor, H., Smith, M.T., Hartzell, P., Bellomo, G., Jewell, S.A., and Orrenius, S. (1982). The metabolism of menadione (2-methyl-1,4-naphthoquinone) by isolated hepatocytes. A study of the implications of oxidative stress in intact cells. J. Biol. Chem. *257*, 12419–12425.

Titov, D. V, Cracan, V., Goodman, R.P., Peng, J., Grabarek, Z., and Mootha, V.K. (2016). Complementation of mitochondrial electron transport chain by manipulation of the NAD^+/NADH ratio. Science *352*, 231 LP – 235.

Toyota, M., Spencer, D., Sawai-Toyota, S., Jiaqi, W., Zhang, T., Koo, A.J., Howe, G.A., and Gilroy, S. (2018). Glutamate triggers long-distance, calcium-based plant defense signaling. Science *361*, 1112–1115.

Tronconi, M.A., Fahnenstich, H., Gerrard Weehler, M.C., Andreo, C.S., Flügge, U.-I.I., Drincovich, M.F., and Maurino, V.G. (2008). Arabidopsis NAD-malic enzyme functions as a homodimer and heterodimer and has a major impact on nocturnal metabolism. Plant Physiol. *146*, 1540–1552.

Tsien, R.Y. (1998). The green fluorescent protein. Annu. Rev. Biochem. *67*, 509–544.

Turner, W.L., Waller, J.C., Vanderbeld, B., and Snedden, W.A. (2004). Cloning and characterization of two NAD kinases from Arabidopsis. Identification of a calmodulin binding isoform. Plant Physiol. *135*, 1243–1255.

Turner, W.L., Waller, J.C., and Snedden, W.A. (2005). Identification, molecular cloning and functional characterization of a novel NADH kinase from Arabidopsis thaliana (thale cress). Biochem. J. *385*, 217–223.

Verhagen, K.J., van Gulik, W.M., and Wahl, S.A. (2020). Dynamics in redox metabolism, from stoichiometry towards kinetics. Curr. Opin. Biotechnol. *64*, 116–123.

Verniquet, F., Gaillard, J., Neuberger, M., and Douce, R. (1991). Rapid inactivation of plant aconitase by hydrogen peroxide. Biochem. J. *276*, 643–648.

Voelker, T., and Kinney, A.J. (2001). Variations in the biosynthesis of seed-storage lipids. Annu. Rev. Plant Biol. *52*, 335–361.

Voll, L.M., Zell, M.B., Engelsdorf, T., Saur, A., Wheeler, M.G., Drincovich, M.F., Weber, A.P.M., and Maurino, V.G. (2012). Loss of cytosolic NADP-malic enzyme 2 in *Arabidopsis thaliana* is associated with enhanced susceptibility to *Colletotrichum higginsianum*. New Phytol. *195*, 189–202.

Voon, C.P., Guan, X., Sun, Y., Sahu, A., Chan, M.N., Gardeström, P., Wagner, S., Fuchs, P., Nietzel, T., Versaw, W.K., et al. (2018). ATP compartmentation in plastids and cytosol of Arabidopsis thaliana revealed by fluorescent protein sensing. Proc. Natl. Acad. Sci. U. S. A. *115*, E10778–E10787.

Waadt, R., Köster, P., Andrés, Z., Waadt, C., Bradamante, G., Lampou, K., Kudla, J., and Schumacher, K. (2020). Dual-reporting transcriptionally linked genetically encoded fluorescent indicators resolve the spatiotemporal coordination of cytosolic abscisic acid and second messenger dynamics in arabidopsis. Plant Cell *32*, 2582–2601.

Wada, M. (2013). Chloroplast movement. Plant Sci. *210*, 177–182.

Wagner, S., Steinbeck, J., Fuchs, P., Lichtenauer, S., Elsässer, M., Schippers, J.H.M., Nietzel, T., Ruberti, C., Van Aken, O., Meyer, A.J., et al. (2019). Multiparametric real-time sensing of cytosolic physiology links hypoxia responses to mitochondrial electron transport. New Phytol. *244*, 1668–1684.

Wahl, S.A., Nöh, K., and Wiechert, W. (2008). ^{13}C labeling experiments at metabolic nonstationary conditions: An exploratory study. BMC Bioinformatics *9*, 1–18.

Wakao, S., and Benning, C. (2005). Genome-wide analysis of glucose-6-phosphate dehydrogenases in Arabidopsis. Plant J. *41*, 243–256.

Wakao, S., Andre, C., and Benning, C. (2008). Functional analyses of cytosolic glucose-6-phosphate dehydrogenases and their contribution to seed oil accumulation in Arabidopsis. Plant Physiol. *146*, 277–288.

Walia, A., Waadt, R., and Jones, A.M. (2018). Genetically encoded biosensors in plants: pathways to discovery. Annu. Rev. Plant Biol. *69*, 497–524.

Walker, B.J., Kramer, D.M., Fisher, N., and Fu, X. (2020). Flexibility in the energy balancing network of changing environmental conditions. Mdpi *9*, 301.

Wallsgrove, R.M., Lea, P.J., and Miflin, B.J. (1982). The development of NAD(P)H-dependent and ferredoxin-dependent glutamate synthase in greening barley and pea leaves. Planta *154*, 473–476.

Walsby-Tickle, J., Gannon, J., Hvinden, I., Bardella, C., Abboud, M.I., Nazeer, A., Hauton, D., Pires, E., Cadoux-Hudson, T., Schofield, C.J., et al. (2020). Anion-exchange chromatography mass spectrometry provides extensive coverage of primary metabolic pathways revealing altered metabolism in IDH1 mutant cells. Commun. Biol. *3*, 1–12.

Wan, L., Essuman, K., Anderson, R.G., Sasaki, Y., Monteiro, F., Chung, E.H., Nishimura, E.O., DiAntonio, A., Milbrandt, J., Dangl, J.L., et al. (2019). TIR domains of plant immune receptors are NAD^+-cleaving enzymes that promote cell death. Science *365*, 799–803.

Wang, C., Huang, X., Li, Q., Zhang, Y., Li, J.L., and Mou, Z. (2019). Extracellular pyridine nucleotides trigger plant systemic immunity through a lectin receptor kinase/BAK1 complex. Nat. Commun. *10*, 4810.

Wang, F.-L., Tan, Y.-L., Wallrad, L., Du, X.-Q., Eickelkamp, A., Wang, Z.-F., He, G.-F., Han, J.-P., Schmitz-Thom, I., Wu, W.-H., et al. (2020). A mechanism for sensing of and adaptation to K^+ deprivation in plants. BioRxiv doi: 10.1101/2020.03.21.000570.

Wang, M., Herrmann, C.J., Simonovic, M., Szklarczyk, D., and von Mering, C. (2015). Version 4.0 of PaxDb: Protein abundance data, integrated across model organisms, tissues, and

cell-lines. Proteomics *15*, 3163–3168.

Wang, W., Chen, D., Zhang, X., Liu, D., Cheng, Y., and Shen, F. (2018). Role of plant respiratory burst oxidase homologs in stress responses. Free Radic. Res. *52*, 826–839.

Wang, Y., San, K.Y., and Bennett, G.N. (2013). Cofactor engineering for advancing chemical biotechnology. Curr. Opin. Biotechnol. *24*, 994–999.

Wang, Y., Hui, S., Wondisford, F.E., and Su, X. (2021). Utilizing tandem mass spectrometry for metabolic flux analysis. Lab. Investig. *101*, 423–429.

Waszczak, C., Akter, S., Jacques, S., Huang, J., Messens, J., and Van Breusegem, F. (2015). Oxidative post-translational modifications of cysteine residues in plant signal transduction. J. Exp. Bot. *66*, 2923–2934.

Watanabe, S., Sakai, T., Goto, S., Yaginuma, T., Hayakawa, T., and Yamaya, T. (1996). Expression of NADH-dependent glutamate synthase in response to the supply of nitrogen in rice cells in suspension culture. Plant Cell Physiol. *37*, 1034–1037.

Weitzel, M., Nöh, K., Dalman, T., Niedenführ, S., Stute, B., and Wiechert, W. (2013). 13CFLUX2-high-performance software suite for ^{13}C-metabolic flux analysis. Bioinformatics *29*, 143–145.

Welchen, E., and Gonzalez, D.H. (2016). Cytochrome c, a hub linking energy, redox, stress and signaling pathways in mitochondria and other cell compartments. Physiol. Plant. *157*, 310–321.

Westerhuis, J.A., Hoefsloot, H.C.J., Smit, S., Vis, D.J., Smilde, A.K., Velzen, E.J.J., Duijnhoven, J.P.M., and Dorsten, F.A. (2008). Assessment of PLSDA cross validation. Metabolomics *4*, 81–89.

Wheeler, M.C.G., Drincovich, F.M., Andreo, C.S., Flugge, U., Tronconi, M. a, and Maurino, V.G. (2005). A comprehensive analysis of the NADP-malic enzyme gene family of Arabidopsis. Plant Physiol. *139*, 39–51.

White, A.C., Rogers, A., Rees, M., and Osborne, C.P. (2016). How can we make plants grow faster? A source-sink perspective on growth rate. J. Exp. Bot. *67*, 31–45.

Wiechert, W. (2007). The thermodynamic meaning of metabolic exchange fluxes. Biophys. J. *93*, 2255–2264.

Wiechert, W., and Nöh, K. (2005). From stationary to instationary metabolic flux analysis. Adv. Biochem. Eng. Biotechnol. *92*, 145–172.

Wigge, B., Krömer, S., and Gardeström, P. (1993). The redox levels and subcellular distribution of pyridine nucleotides in illuminated barley leaf protoplasts studied by rapid fractionation. Physiol. Plant. *88*, 10–18.

Wijker, R.S., Sessions, A.L., Fuhrer, T., and Phan, M. (2019). 2H/1H variation in microbial lipids is controlled by NADPH metabolism. Proc. Natl. Acad. Sci. U. S. A. *116*, 12173–12182.

Williams, T.C.R., Miguet, L., Masakapalli, S.K., Kruger, N.J., Sweetlove, L.J., and Ratcliffe, R.G. (2008). Metabolic network fluxes in heterotrophic Arabidopsis cells: stability of the flux distribution under different oxygenation conditions. Plant Physiol. *148*, 704–718.

Xu, Y., Fu, X., Sharkey, T.D., Shachar-Hill, Y., and Walker, B. (2021). The metabolic origins of non-photorespiratory CO_2 release during photosynthesis: A metabolic flux analysis. Plant Physiol kiab076.

Yang, C.Y., and Hong, C.P. (2015). The NADPH oxidase Rboh D is involved in primary hypoxia signalling and modulates expression of hypoxia-inducible genes under hypoxic stress. Environ. Exp. Bot. *115*, 63–72.

Yeung, E., van Veen, H., Vashisht, D., Paiva, A.L.S., Hummel, M., Rankenberg, T., Steffens, B., Steffen-Heins, A., Sauter, M., de Vries, M., et al. (2018). A stress recovery signaling network for enhanced flooding tolerance in Arabidopsis thaliana. Proc. Natl. Acad. Sci. U. S. A. *115*, E6085–E6094.

Yokochi, Y., Yoshida, K., Hahn, F., Miyagi, A., and Wakabayashi, K. (2021). Redox regulation of NADP-malate dehydrogenase is vital for land plants under fluctuating light environment. PNAS *6*, e2016903118.

Young, J.D. (2014). INCA: A computational platform for isotopically non-stationary metabolic flux analysis. Bioinformatics *30*, 1333–1335.

Young, J.D., Shastri, A.A., Stephanopoulos, G., and Morgan, J.A. (2011). Mapping photoautotrophic metabolism with isotopically nonstationary ^{13}C flux analysis. Metab. Eng. *13*, 656–665.

Yuan, J., Bennett, B.D., and Rabinowitz, J.D. (2008). Kinetic flux profiling for quantitation of cellular metabolic fluxes. Nat. Protoc. *3*, 1328–1340.

Yukawa, T., Bamba, T., Guirimand, G., Matsuda, M., Hasunuma, T., and Kondo, A. (2020). Optimization of 1,2,4-butanetriol production from xylose in Saccharomyces cerevisiae by metabolic engineering of NADH/NADPH balance. Biotechnol. Bioeng. *118*, 175– 185.

Zaffagnini, M., Fermani, S., Costa, A., Lemaire, S.D., and Trost, P. (2013). Plant cytoplasmic GAPDH: redox post-translational modifications and moonlighting properties. Front. Plant Sci. *4*, 1–18.

Zhang, Y., Krahnert, I., Bolze, A., Gibon, Y., and Fernie, A.R. (2020). Adenine nucleotide and nicotinamide adenine dinucleotide measurements in plants. Curr. Protoc. Plant Biol. *5*, e20115.

Zhang, Z., Chen, L., Liu, L., Su, X., and Rabinowitz, J.D. (2017). Chemical basis for deuterium labeling of fat and NADPH. J. Am. Chem. Soc. *139*, 14368–14371.

Zhao, C., Zhao, Q., Li, Y., and Zhang, Y. (2017a). Engineering redox homeostasis to develop efficient alcohol-producing microbial cell factories. Microb. Cell Fact. *16*, 115.

Zhao, F.L., Zhang, C., Zhang, C., Tang, Y., and Ye, B.C. (2016a). A genetically encoded biosensor for in vitro and in vivo detection of $NADP^+$. Biosens. Bioelectron. *77*, 901–906.

Zhao, Y., Jin, J., Hu, Q., Zhou, H.M., Yi, J., Yu, Z., Xu, L., Wang, X., Yang, Y., and Loscalzo, J. (2011). Genetically encoded fluorescent sensors for intracellular NADH detection. Cell Metab. *14*, 555–566.

Zhao, Y., Hu, Q., Cheng, F., Su, N., Wang, A., Zou, Y., Hu, H., Chen, X., Zhou, H.M., Huang, X., et al. (2015). SoNar, a highly responsive NAD^+/NADH sensor, allows high-throughput metabolic screening of anti-tumor agents. Cell Metab. *21*, 777–789.

Zhao, Y., Wang, A., Zou, Y., Su, N., Loscalzo, J., and Yang, Y. (2016b). *In vivo* monitoring of cellular energy metabolism using SoNar, a highly responsive sensor for NAD^+/NADH redox state. Nat. Protoc. *11*, 1345–1359.

Zhao, Y., Zhang, Z., Zou, Y., and Yang, Y. (2017b). Visualization of nicotine adenine dinucleotide redox homeostasis with genetically encoded fluorescent sensors. Antioxid. Redox Signal. *28*, 213–229.

Zinta, G., Khan, A., AbdElgawad, H., Verma, V., and Srivastava, A.K. (2016). Unveiling the redox control of plant reproductive development during abiotic stress. Front. Plant Sci. *7*, 700.

Zuccarelli, R., and Freschi, L. (2018). Glutathione reductase: Safeguarding plant cells against oxidative damage. In Antioxidants and Antioxidant Enzymes in Higher Plants, pp. 61–82.

Appendix A

A.1 Effect of cell extraction method on metabolite peak area and recovery

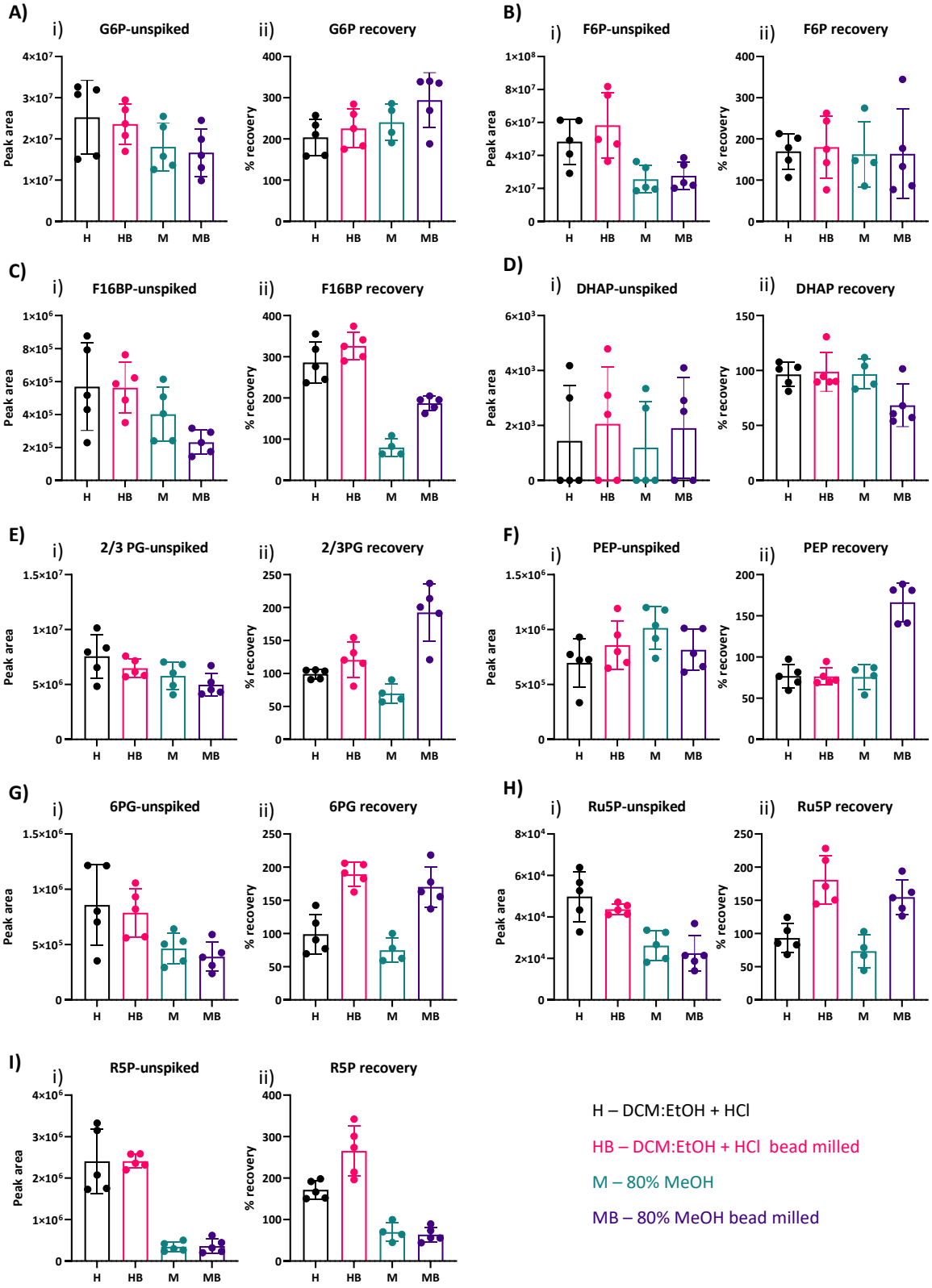

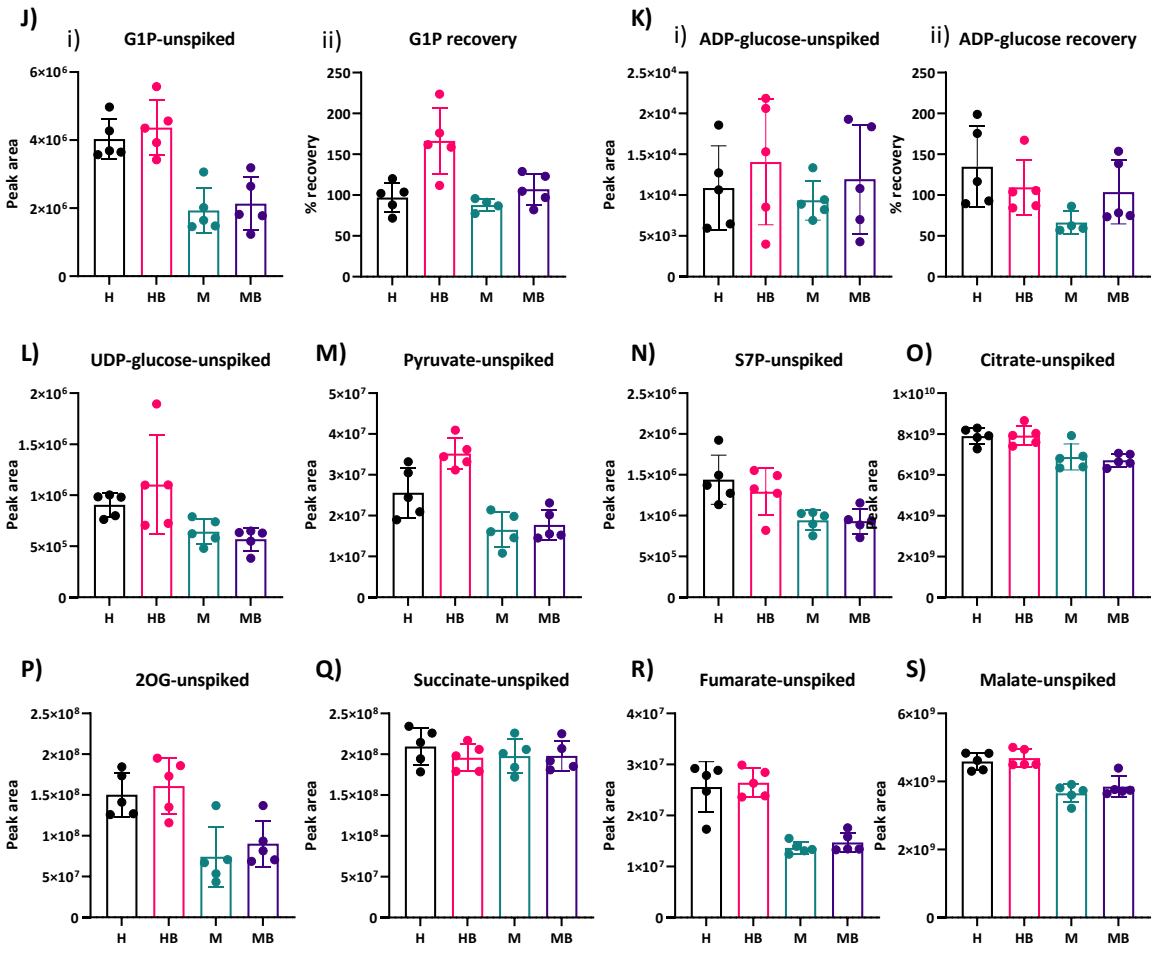

H – DCM:EtOH + HCl

HB – DCM:EtOH + HCl bead milled

M – 80% MeOH

MB – 80% MeOH bead milled

Figure A.1. Chromatographic peak area and % recovery of central carbon metabolites extracted form heterotrophic *Arabidopsis* cells using either DCM:EtOH + HCl or 80% MeOH extraction methods with or without bead milling. Samples were analysed using IE-chromatography and QExative MS. For metabolites with available standards cell samples were spiked with a mixture of standards to a final concentration of 15 µM. Recovery was calculated by (spiked-unspiked)/(standard alone). Values are the mean ± SD n = 5.

A.2 Glycosyl labelling of UDP glucose

UDP-glucose is synthesised exclusively in the cytosol from G6P via G1P therefore the glucosyl moiety of UDP-glucose can report on labelling of the cytosolic hexose phosphates. Following supply of [$^{13}C_6$]glucose, UDP incorporates ^{13}C and therefore contributes to the labelling observed in UDP-glucose. The labelling in UDP was deconvoluted from the labelling in UDP-glucose to estimate the label incorporation specifically in the glucosyl moiety of UDP-glucose.

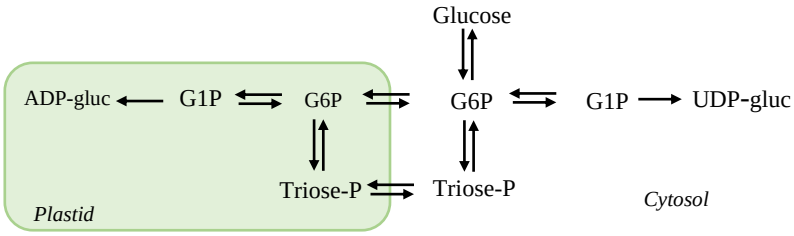

The deconvolution was performed on data corrected for natural abundance using AccuCor. Labelling in the glucosyl moiety was calculated by least squares fitting of the labelling in UDP and UDP-glucose.

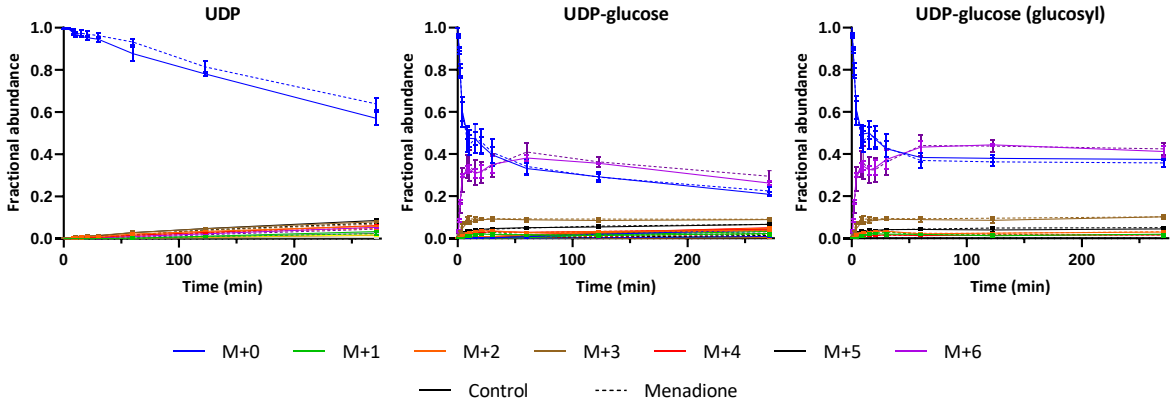

Figure A.2. Labelling time courses of UDP, UDP-glucose and the glucosyl moiety of UDP-glucose following supply of [U^{13}C]glucose. UDP-glucose glycosyl labelling was calculated by deconvoluting the UDP labelling from UDP glucose labelling after correction for natural abundance.

UDP is labelled relatively slowly compared to UDP-glucose (Figure A.2). However, as labelling in UDP becomes appreciable (> 15 min) it begins to make a significant contribution to the total labelling of UDP-glucose. Deconvolution of the UDP labelling pattern form UDP-glucose reveals the labelling in the glucosyl moiety of UDP glucose which reaches a steady state after 30 min, similar to the labelled observed in hexose phosphates.

A.3 Complete labelling timecourses

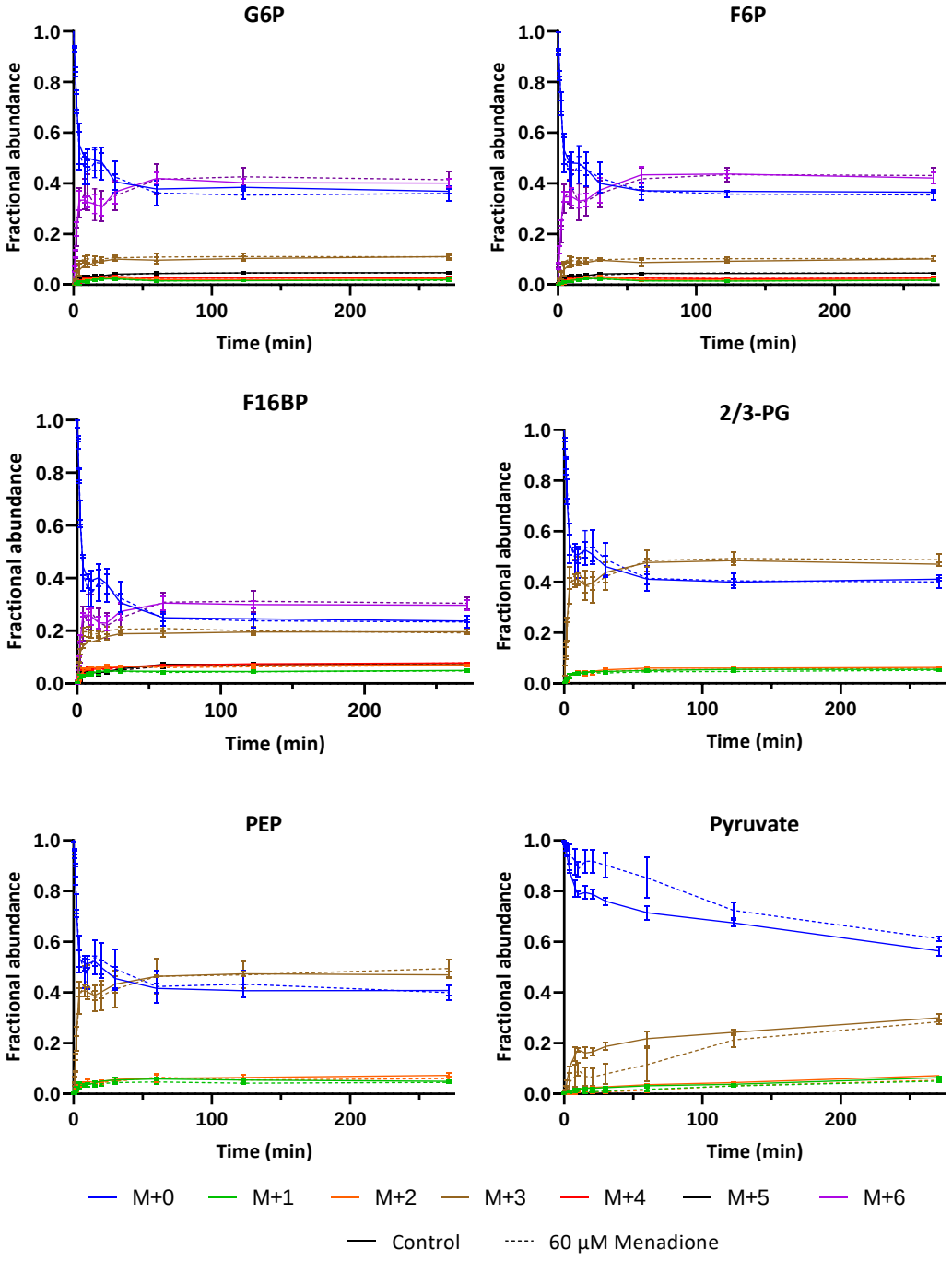

Figure A.3. Mass isotopologue distributions of glycolytic intermediates after supply of [$^{13}C_6$]glucose to heterotrophic *Arabidopsis* cell cultures following 6 h treatment with 60 µM menadione. MID's are corrected for natural abundance of heavy isotopes. Values are the mean ± SD n = 3.

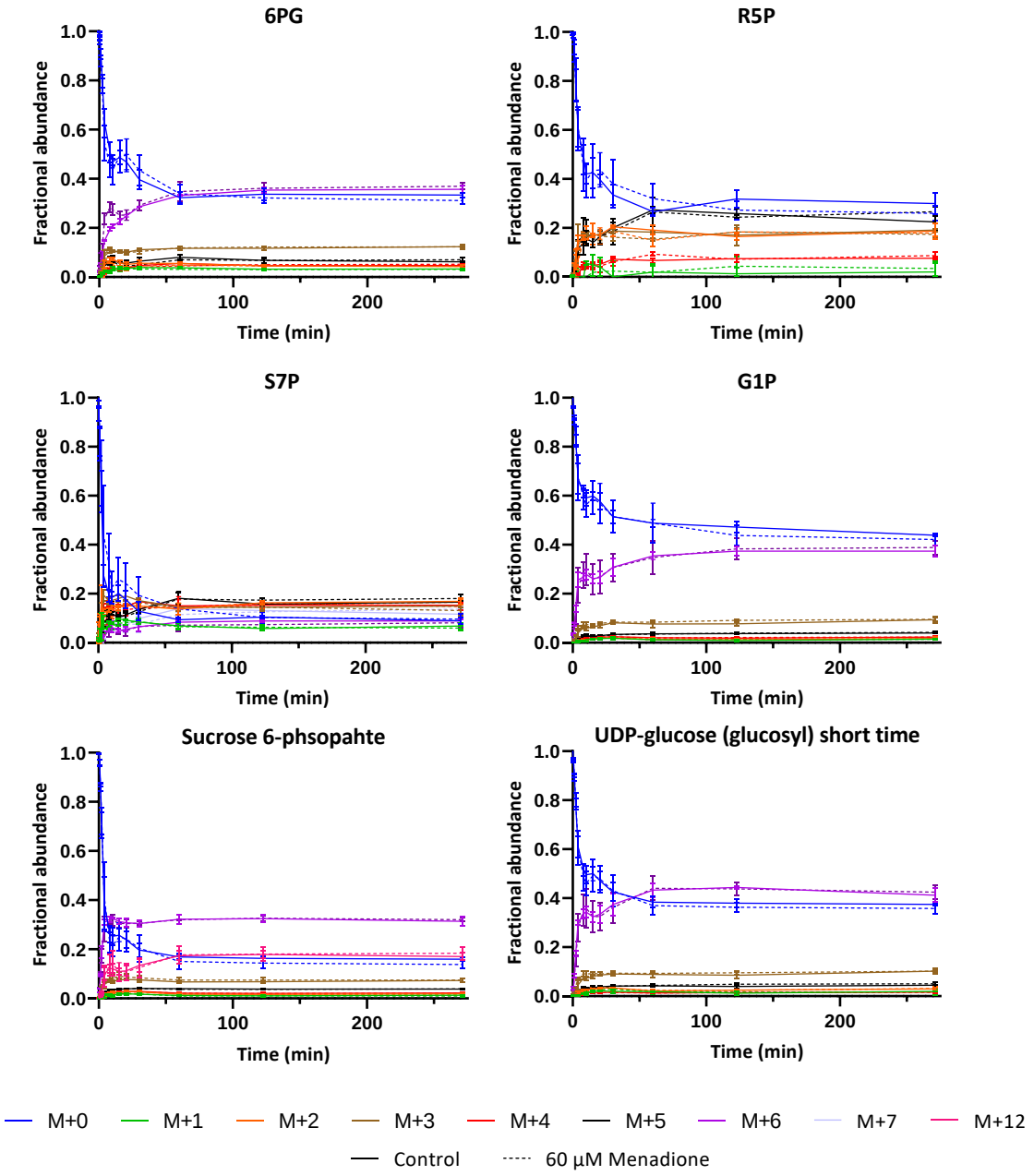

Figure A.4. Mass isotopologue distributions of pentose phosphate pathway and starch/sucrose biosynthesis intermediates following supply of [$^{13}C_6$]glucose to heterotrophic *Arabidopsis* cell cultures following 6 h treatment with 60 µM menadione. MID's are corrected for natural abundance. Values are the mean ± SD n = 3.

A.4 Relative 2-Oxoglutarate abundance

An estimate of relative 2-oxglutarate (2OG) abundance was made by summing the individual peaks for all measured mass isotopologues. Note that samples were not normalised for cell number or variance in sample preparation which may have an effect on apparent metabolite abundance.

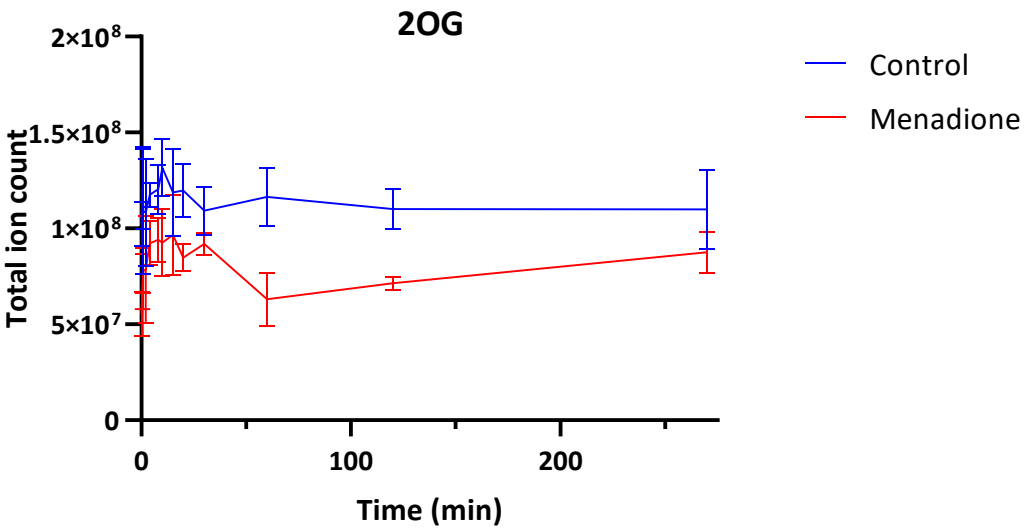

Figure A.5. Relative abundance of 2-oxoglutarate extracted from *Arabidopsis* cell cultures following 6 h treatment with 60 µM menadione or an untreated control. Samples were analysed using IC-MS. Mass isotopologues were summed to give a total abundance at each time point regardless of ^{13}C incorporation. Values are the mean ± SD n = 3.

The abundance of 2OG was significantly lower in menadione treated samples compared to an untreated control (Figure A.5) (P = 0.0069, mixed-effects analysis). A decrease in 2OG abundance could have been caused by inhibition of aconitase by increased ROS production (Baxter et al., 2007a; Millar and Leaver, 2000; Verniquet et al., 1991).

A.5 Model definition and net fluxes of heterotrophic *Arabidopsis* cell cultures

Table A.1. Model definition and net fluxes of heterotrophic *Arabidopsis* cell cultures. Flux values are global best-fit estimates for heterotrophic *Arabidopsis* cell cultures treated with 60 µM menadione for 6 h or an untreated control. Fluxes were deduced using INST-MFA following supply of [$^{13}C_6$]glucose. Fluxes are the molar flux relative to glucose uptake. The 95% confidence intervals were determined by both Monte Carlo simulation (MC) and parameter continuation (PC). Net flux is the difference between the forward and reverse fluxes for a reversible reaction. The exchange (exch) flux is the smaller of these two values, representing the amount of material flowing simultaneously in both directions. Exchange fluxes with confidence ranges from 0 – inf are deemed indeterminable.

		Control					Menadione				
			PC (95% CI)		MC (95% CI)			PC (95% CI)		MC (95% CI)	
Flux ID	**Equation**	**Value**	**LB**	**UB**	**LB**	**UB**	**Value**	**LB**	**UB**	**LB**	**UB**
upt	GLC.int (abcdef) -> G6P.c (abcdef)	1.000	1.000	1.000	1.000	1.000	1.000	1.000	1.000	1.000	1.000
chex1 net	G6P.c (abcdef) <-> F6P.c (abcdef)	0.599	0.599	0.599	0.555	0.646	0.587	0.484	0.712	0.533	0.654
chex1 exch	G6P.c (abcdef) <-> F6P.c (abcdef)	14.668			5.119	1880.579	23.596			7.498	9620.980
chex2-1 net	F6P.c (abcdef) <-> FBP.c (abcdef)	0.540	0.516	0.540	0.486	0.606	0.529	0.394	0.687	0.460	0.608
chex2-1 exch	F6P.c (abcdef) <-> FBP.c (abcdef)	5601.467			5575.231	5629.055	3223.349			2407.894	3591.919
chex2 net	FBP.c (abcdef) <-> TP.c (cba) + TP.c (def)	0.540	0.488	0.613	0.486	0.606	0.529	0.453	0.606	0.460	0.608
chex2 exch	FBP.c (abcdef) <-> TP.c (cba) + TP.c (def)	0.156	0.131	0.391	0.130	0.178	0.253			0.220	0.282
chex3-1 net	TP.c (abc) <-> 3PG.c (abc)	1.315	1.309	1.315	1.210	1.540	1.417	1.046	1.747	1.267	1.559
chex3-1 exch	TP.c (abc) <-> 3PG.c (abc)	9999999	0.000	Inf	9999998	9999999	675.248			0.000	1856.085
chex3-2 net	3PG.c (abc) <-> PEP.c (abc)	1.315	1.309	1.315	1.210	1.540	1.417	1.046	1.747	1.267	1.559
chex3-2 exch	3PG.c (abc) <-> PEP.c (abc)	0.000			0.000	903.930	0.000			0.000	2955.360
chex3	PEP.c (abc) -> PYR.c (abc)	0.477	0.420	0.670	0.380	0.633	0.173	0.084	0.382	0.090	0.342
phex1 net	G6P.p (abcdef) <-> F6P.p (abcdef)	0.237	0.229	0.237	0.199	0.279	0.246	0.143	0.345	0.182	0.291
phex1 exch	G6P.p (abcdef) <-> F6P.p (abcdef)	0.532	0.472	0.600	0.475	0.600	0.509			0.423	0.606
phex2-1	F6P.p (abcdef) -> FBP.p (abcdef)	0.233	0.229	0.234	0.196	0.274	0.243	0.144	0.343	0.184	0.291
phex2 net	FBP.p (abcdef) <-> TP.p (cba) + TP.p (def)	0.233	0.229	0.234	0.196	0.274	0.243	0.144	0.343	0.184	0.291
phex2 exch	FBP.p (abcdef) <-> TP.p (cba) + TP.p (def)	0.066	0.042	0.094	0.043	0.092	0.119			0.077	0.160
phex3-1 net	TP.p (abc) <-> 3PG.p (abc)	0.222	0.021	0.259	0.067	0.249	0.119	0.029	0.193	0.039	0.181

phex3-1 exch	TP.p (abc) <-> 3PG.p (abc)	0.000	0.000	276516	0.000	0.127	47.835			23.030	87.099
phex3-2 net	3PG.p (abc) <-> PEP.p (abc)	0.145	0.131	0.145	0.020	0.176	0.043	0.020	0.208	0.030	0.106
phex3-2 exch	3PG.p (abc) <-> PEP.p (abc)	0.049	0.000	Inf	0.019	0.182	0.000			0.000	0.794
phex3	PEP.p (abc) -> PYR.p (abc)	0.121	0.000	0.157	0.000	0.151	0.020	0.006	0.090	0.008	0.082
cppp1	G6P.c (abcdef) -> 6PG.c (abcdef) + NADPH	0.000	0.000	0.000	0.000	0.000	0.000	0.000	0.003	0.000	0.010
cppp1-1	6PG.c (abcdef) -> Ru5P.c (bcdef) + CO2 (a) + NADPH	0.000	0.000	0.000	0.000	0.000	0.000	0.000	0.003	0.000	0.010
pppp1	G6P.p (abcdef) -> 6PG.p (abcdef) + NADPH	0.004			0.002	0.022	0.007	0.004	0.038	0.004	0.043
pppp-1	6PG.p (abcdef) -> Ru5P.p (bcdef) + CO2 (a) + NADPH	0.004	0.002	0.029	0.002	0.022	0.007	0.004	0.038	0.004	0.043
R20 net	Ru5P.p (abcde) <-> X5P.p (abcde)	-0.004			-0.007	0.008	-0.003	-0.006	0.043	-0.005	0.021
R20 exch	Ru5P.p (abcde) <-> X5P.p (abcde)	0.006	0.000	0.155	0.000	0.119	0.000			0.000	0.062
R21 net	Ru5P.p (abcde) <-> R5P.p (abcde)	0.009	0.009	0.009	0.006	0.014	0.009	0.003	0.033	0.007	0.022
R21 exch	Ru5P.p (abcde) <-> R5P.p (abcde)	5447.977			5444.721	5456.009	3734.462			3713.425	3755.364
pppp2a net	R5P.p (abcde) + TKC2.p (fg) <-> S7P.p (fgabcde)	0.004			0.002	0.010	0.005	0.002	0.027	0.003	0.018
pppp2a exch	R5P.p (abcde) + TKC2.p (fg) <-> S7P.p (fgabcde)	0.000	0.000	0.002	0.000	0.001	0.000			0.000	0.002
pppp2b net	E4P.p (abcd) + TKC2.p (ef) <-> F6P.p (efabcd)	-0.008	-0.008		-0.011	-0.002	-0.007	-0.011	0.015	-0.009	0.007
pppp2b exch	E4P.p (abcd) + TKC2.p (ef) <-> F6P.p (efabcd)	0.991	0.851	1.160	0.848	1.143	0.879			0.701	1.065
R24 net	X5P.p (abcde) <-> TP.p (cde) + TKC2.p (ab)	-0.004			-0.007	0.008	-0.002	-0.005	0.043	-0.004	0.025
R24 exch	X5P.p (abcde) <-> TP.p (cde) + TKC2.p (ab)	0.029			0.000	0.806	0.045			0.000	10.947
pppp3a net	S7P.p (abcdefg) <-> E4P.p (defg) + TAC3.p (abc)	0.004			0.002	0.010	0.005	0.002	0.027	0.003	0.018
pppp3a exch	S7P.p (abcdefg) <-> E4P.p (defg) + TAC3.p (abc)	0.006	0.003	0.019	0.003	0.015	0.004			0.003	0.017
pppp3b net	TP.p (abc) + TAC3.p (def) <-> F6P.p (defabc)	0.004			0.002	0.010	0.005	0.002	0.027	0.003	0.018
pppp3b exch	TP.p (abc) + TAC3.p (def) <-> F6P.p (defabc)	1.081	0.891	1.374	0.871	1.347	0.702			0.529	0.903
cmex	PYR.c (abc) -> PYR.m (abc)	0.373	0.372	0.373	0.257	0.428	0.000	0.000	0.478	0.000	0.191
cpex	PYR.c (abc) -> PYR.p (abc)	0.000	0.000	0.094	0.000	0.143	0.070	0.000	0.157	0.000	0.109

gpt net	G6P.c (abcdef) <-> G6P.p (abcdef)	0.303	0.259	0.347	0.259	0.346	0.315	0.263	0.378	0.250	0.367
gpt exch	G6P.c (abcdef) <-> G6P.p (abcdef)	1.181	1.054	1.371	1.042	1.345	1.174			0.981	1.414
tpt net	TP.c (abc) <-> TP.p (abc)	-0.239	-0.482	-0.162	-0.428	-0.169	-0.363	-0.528	-0.224	-0.482	-0.226
tpt exch	TP.c (abc) <-> TP.p (abc)	5632	4.192	403912	5063	6215	5614			3810	20686
tca1	PYR.m (abc) -> CO2 (a) + AcCoA (bc)	0.998	0.869	1.161	0.862	1.131	1.008	0.862	1.165	0.835	1.130
tca2	AcCoA (ab) + MAL (cdef) -> CIT (fedbac)	0.972	0.854	1.157	0.858	1.111	0.982	0.844	1.172	0.842	1.144
R33 net	CIT (abcdef) <-> ICIT (abcdef)	0.943	0.921	0.964	0.829	1.083	0.953	0.685	1.290	0.812	1.115
R33 exch	CIT (abcdef) <-> ICIT (abcdef)	9736.509	0.000	Inf	9731.633	9740.911	5388.791			5327.807	5445.333
tca3	ICIT (abcdef) -> CO2 (f) + AKG (abcde) + NADPH	0.943	0.820	1.129	0.829	1.083	0.953	0.813	1.143	0.812	1.115
tca4	AKG (abcde) -> CO2 (a) + SUCCCoA (bcde)	0.811	0.693	0.996	0.695	0.953	0.821	0.682	0.975	0.680	0.982
R36 net	SUCCCoA (abcd) <-> SUCC (abcd)	0.811	0.809	0.811	0.695	0.953	0.821	0.550	1.168	0.680	0.982
R36 exch	SUCCCoA (abcd) <-> SUCC (abcd)	5.655	0.000	Inf	2.845	11.874	8.207			3.732	9.423
tca5 net	SUCC (abcd) <-> FUM (abcd)	0.801	0.800	0.801	0.684	0.941	0.811	0.539	1.148	0.670	0.976
tca5 exch	SUCC (abcd) <-> FUM (abcd)	2.501	1.191	6.238	1.434	5.610	0.777			0.000	3.548
tca6a-1 net	FUM (abcd) <-> MAL (abcd)	0.804	0.685	0.992	0.687	0.944	0.814	0.667	1.002	0.672	0.980
tca6a-1 exch	FUM (abcd) <-> MAL (abcd)	6.548	3.268	33.948	3.764	15.678	1436.364			13.700	10439.849
ana1 net	PEP.c (abc) + CO2 (d) <-> MAL (abcd)	0.838	0.764	1.005	0.769	1.026	1.243	0.995	1.422	1.001	1.401
ana1 exch	PEP.c (abc) + CO2 (d) <-> MAL (abcd)	0.000	0.000	0.003	0.000	0.028	0.000			0.000	0.036
ana2	MAL (abcd) -> PYR.m (abc) + CO2 (d)	0.625	0.543	0.735	0.541	0.769	1.008	0.676	1.165	0.741	1.116
ana3	MAL (abcd) -> PYR.p (abc) + CO2 (d) + NADPH	0.000	0.000	0.038	0.000	0.076	0.020	0.005	0.078	0.007	0.074
pdhp	PYR.p (abc) -> CO2 (a) + AcCoA.p (bc)	0.090	0.054	0.125	0.058	0.124	0.079	0.040	0.114	0.046	0.117
throx net	THR (abcd) <-> GLY (ab) + AcCoA (cd)	-0.026	-0.026	-0.025	-0.030	0.105	-0.026	-0.035	0.149	-0.030	0.128
throx exch	THR (abcd) <-> GLY (ab) + AcCoA (cd)	2953.872	0.000	Inf	2950.756	2958.417	8.511			0.001	1095.926
gly net	SER (abc) <-> GLY (ab) + CX (c)	0.026	-0.053	0.030	-0.041	0.030	0.026	-0.054	0.030	-0.051	0.029
gly exch	SER (abc) <-> GLY (ab) + CX (c)	1150.598	0.000	Inf	878.923	1446.182	5207.149			3858.159	6105.760
gly1 net	GLY (ab) <-> CO2 (a) + CX (b)	-0.022	-0.025	0.057	-0.025	0.043	-0.022	-0.025	0.058	-0.025	0.055
gly1 exch	GLY (ab) <-> CO2 (a) + CX (b)	9172	0.000	2003322	8577	9518	1587.339			52.878	6293
fas1	AcCoA.p (ab) -> AcCoA.eff (ab)	0.084			0.052	0.118	0.073	0.005	0.145	0.040	0.110
fas2	TP.c (abc) -> G3P (abc)	0.004	0.004	0.006	0.002	0.006	0.004	0.000	0.008	0.002	0.006

adh	PYR.c (abc) -> CO2 (a) + EtOH (bc)	0.005	0.001	0.009	0.001	0.009	0.005	0.001	0.009	0.001	0.009
ahdeff	EtOH (ab) -> EtOH.eff (ab)	0.005	0.005	0.005	0.001	0.009	0.005	0.000	0.012	0.001	0.009
chex4 net	G6P.c (abcdef) <-> G1P.c (abcdef)	0.098	0.063	0.124	0.068	0.125	0.097	0.064	0.128	0.067	0.130
chex4 exch	G6P.c (abcdef) <-> G1P.c (abcdef)	3.914	2.649	10.038	2.153	8.399	1.609			0.443	4.554
chex5 net	G1P.c (abcdef) <-> UDPG (abcdef)	0.098		0.098	0.068	0.125	0.097	0.035	0.156	0.067	0.130
chex5 exch	G1P.c (abcdef) <-> UDPG (abcdef)	0.000	0.000	0.130	0.000	0.472	0.000			0.000	1.982
chex6	F6P.c (abcdef) + UDPG (ghijkl) -> S6P (abcdefghijkl)	0.059	0.059	0.061	0.030	0.085	0.058	0.000	0.115	0.028	0.090
gsuc	S6P (abcdefghijkl) -> GSUC (abcdef) + FSUC (ghijkl)	0.059	0.059	0.061	0.030	0.085	0.058	0.000	0.115	0.028	0.090
fsuceff	FSUC (abcdef) -> F6P.eff (abcdef)	0.059	0.059	0.061	0.030	0.085	0.058	0.000	0.115	0.028	0.090
gsuceff	GSUC (abcdef) -> G6P.eff (abcdef)	0.059	0.059	0.061	0.030	0.085	0.058	0.000	0.115	0.028	0.090
phex4 net	G6P.p (abcdef) <-> G1P.p (abcdef)	0.061	0.051	0.061	0.032	0.089	0.063	0.005	0.121	0.033	0.092
phex4 exch	G6P.p (abcdef) <-> G1P.p (abcdef)	0.328	0.308	0.354	0.304	0.351	0.316			0.287	0.442
phex5 net	G1P.p (abcdef) <-> ADPG (abcdef)	0.061	0.051	0.061	0.032	0.089	0.063	0.005	0.121	0.033	0.092
phex5 exch	G1P.p (abcdef) <-> ADPG (abcdef)	2359.295			2359.266	2359.325	2365.341			1.170	4790.671
stsp	ADPG (abcdef) -> STA (abcdef)	0.061	0.051	0.061	0.032	0.089	0.063	0.005	0.121	0.033	0.092
sta	STA (abcdef) -> STA.eff (abcdef)	0.061	0.051	0.061	0.032	0.089	0.063	0.005	0.121	0.033	0.092
wall	UDPG (abcdef) -> WALL (abcdef)	0.031	0.029	0.036	0.025	0.037	0.031	0.019	0.043	0.025	0.037
pentan	UDPG (abcdef) -> PENTAN (abcde) + CO2 (f)	0.008	0.008	0.009	0.006	0.010	0.008	0.004	0.012	0.006	0.010
pentaneff	PENTAN (abcde) -> PENTAN.eff (abcde)	0.008	0.008	0.009	0.006	0.010	0.008	0.004	0.012	0.006	0.010
citout	CIT (abcdef) -> CIT.eff	0.029	0.029	0.029	0.025	0.033	0.029	0.021	0.037	0.025	0.033
succout	SUCC (abcd) -> SUCC.eff	0.010	0.010	0.015	0.000	0.019	0.010	0.000	0.030	0.000	0.020
malout	MAL (abcd) -> MAL.eff	0.035	0.034	0.045	0.009	0.059	0.036	0.000	0.087	0.011	0.062
gaba	GLU (abcde) -> CO2 (a) + GABA (edcb)	0.017	0.015	0.019	0.015	0.019	0.017	0.015	0.019	0.015	0.019
gabaout	GABA (abcd) -> GABA.eff (abcd)	0.017	0.017	0.019	0.015	0.019	0.017	0.013	0.021	0.015	0.019
glu net	AKG (abcde) <-> GLU (abcde)	0.129	0.129	0.135	0.121	0.136	0.129	0.115	0.143	0.122	0.136
glu exch	AKG (abcde) <-> GLU (abcde)	1.571	0.000	Inf	1.350	2.613	0.203			0.000	0.948
glueeff	GLU (abcde) -> GLX.s (abcde)	0.095	0.095	0.098	0.080	0.101	0.097	0.000	0.109	0.091	0.103
gln net	GLU (abcde) <-> GLN (abcde)	0.002	0.000	0.103	0.000	0.016	0.000	0.000	0.038	0.000	0.000
gln exch	GLU (abcde) <-> GLN (abcde)	0.006	0.000		0.000	0.009	0.000			0.000	0.000

glneff	GLN (abcde) -> GLX.s (abcde)	0.002			0.000	0.016	0.000	0.000	0.044	0.000	0.000
glxeff	GLX.s (abcde) -> GLX.eff (abcde)	0.097	0.093	0.098	0.091	0.102	0.097	0.086	0.108	0.091	0.103
pro	GLU (abcde) -> PRO (abcde)	0.015	0.011	0.019	0.011	0.019	0.015	0.011	0.019	0.011	0.019
proeff	PRO (abcde) -> PRO.eff (abcde)	0.015			0.011	0.019	0.015	0.007	0.023	0.011	0.019
asp	MAL (abcd) -> ASP (abcd)	0.000	0.000	0.159	0.000	0.131	0.000	0.000	0.161	0.000	0.155
aspeff	ASP (abcd) -> ASP.eff (abcd)	0.010	0.009	0.011	0.008	0.012	0.010	0.006	0.014	0.008	0.012
arg	AKG (abcde) + CO2 (f) + ASP (ghjk) -> ARG (abcdef) + FUM (ghjk)	0.003	0.001	0.005	0.001	0.005	0.003	0.001	0.005	0.001	0.005
argeff	ARG (abcdef) -> ARG.eff (abcdef)	0.003			0.001	0.005	0.003	0.000	0.007	0.001	0.005
ser	3PG.p (abc) -> SER (abc)	0.076	0.076	0.077	0.011	0.083	0.076	0.000	0.090	0.000	0.083
sereff	SER (abc) -> SER.eff (abc)	0.044	0.038	0.050	0.039	0.050	0.044	0.038	0.050	0.038	0.050
cys	SER (abc) -> CYS (abc)	0.003	0.003	0.006	0.001	0.005	0.003	0.000	0.007	0.001	0.005
cyseff	CYS (abc) -> CYS.eff (abc)	0.003	0.003	0.006	0.001	0.005	0.003	0.000	0.007	0.001	0.005
glyeff	GLY (ab) -> GLY.eff (ab)	0.022	0.022	0.026	0.018	0.026	0.022	0.014	0.030	0.018	0.026
ala net	PYR.c (abc) <-> ALA (abc)	0.098	0.098	0.098	0.080	0.115	0.098	0.064	0.132	0.081	0.115
ala exch	PYR.c (abc) <-> ALA (abc)	2.021			0.421	1951.854	0.004			0.000	0.022
alaeff	ALA (abc) -> ALA.eff (abc)	0.098	0.098	0.098	0.080	0.115	0.098	0.064	0.132	0.081	0.115
aro1	E4P.p (abcd) + PEP.p (efg) -> ARO (efgabcd)	0.004	0.000	0.004	0.001	0.007	0.006	0.000	0.012	0.003	0.009
aro2	E4P.p (abcd) + PEP.p (efg) -> ARO (efdcbag)	0.005	0.000	0.008	0.005	0.005	0.003	0.000	0.006	0.003	0.003
leu1	PYR.p (abc) + PYR.p (def) -> CO2 (a) + ISOVAL (debcf)	0.010	0.007	0.013	0.008	0.013	0.010	0.007	0.013	0.007	0.013
leu	ISOVAL (abcde) + AcCoA.p (fg) -> CO2 (a) + LEU (fgbcde)	0.006	0.004	0.008	0.004	0.008	0.006	0.004	0.008	0.004	0.008
leueff	LEU (abcdef) -> LEU.eff (abcdef)	0.006			0.004	0.008	0.006	0.002	0.010	0.004	0.008
val	ISOVAL (abcde) -> VAL (abcde)	0.004			0.002	0.006	0.004	0.000	0.008	0.002	0.006
valeff	VAL (abcde) -> VAL.eff (abcde)	0.004			0.002	0.006	0.004	0.000	0.008	0.002	0.006
met	ASP (abcd) + CX (e) -> MET (abcde)	0.002	0.002	0.003	0.000	0.004	0.002	0.000	0.006	0.000	0.004
meteff	MET (abcde) -> MET.eff (abcde)	0.002	0.002	0.003	0.000	0.004	0.002	0.000	0.006	0.000	0.004
thr net	ASP (abcd) <-> THR (abcd)	-0.015	-0.019	0.144	-0.018	0.116	-0.015	-0.018	0.145	-0.018	0.139
thr exch	ASP (abcd) <-> THR (abcd)	1188	0.000	142386	1100	1259	21.209			14.864	107.651

threff	THR (abcd) -> THR.eff (abcd)	0.009	0.007	0.011	0.007	0.011	0.009	0.005	0.013	0.007	0.011
asn net	ASP (abcd) <-> ASN (abcd)	0.000			0.000	0.000	0.000			0.000	0.000
asn exch	ASP (abcd) <-> ASN (abcd)	10000	0.000	Inf	10000	10000	2127.090			2127.090	2127.093
ile	PYR.p (abc) + THR (defg) -> CO2 (a) + ILE (debfgc)	0.002	0.000	0.004	0.000	0.004	0.002	0.000	0.004	0.000	0.004
ileeff	ILE (abcdef) -> ILE.eff (abcdef)	0.002			0.000	0.004	0.002	0.000	0.006	0.000	0.004
phe	ARO (abcdefg) + PEP.p (hij) -> CO2 (a) + PHE (hijbcdefg)	0.006	0.004	0.008	0.004	0.008	0.006	0.004	0.008	0.004	0.008
pheeff	PHE (abcdefghi) -> PHE.eff (abcdefghi)	0.006			0.004	0.008	0.006	0.002	0.010	0.004	0.008
tyr	ARO (abcdefg) + PEP.p (hij) -> CO2 (a) + TYR (hijbcdefg)	0.003	0.001	0.005	0.001	0.005	0.003	0.001	0.005	0.001	0.005
tyreff	TYR (abcdefghi) -> TYR.eff (abcdefghi)	0.003			0.001	0.005	0.003	0.000	0.007	0.001	0.005
lys	MAL (abcd) + PYR.p (efg) -> CO2 (e) + LYS (abcdgf)	0.011	0.000	0.017	0.000	0.016	0.011	0.000	0.017	0.000	0.017
lys1	MAL (abcd) + PYR.p (efg) -> CO2 (a) + LYS (efgdcb)	0.000	0.000	0.016	0.000	0.014	0.000	0.000	0.011	0.000	0.014
lyseff	LYS (abcdef) -> LYS.eff (abcdef)	0.011			0.006	0.017	0.011	0.000	0.023	0.005	0.017
his	R5P.p (abcde) + CX (f) -> HIS (edcbaf)	0.002	0.000	0.004	0.000	0.004	0.002	0.000	0.004	0.000	0.004
hiseff	HIS (abcdef) -> HIS.eff (abcdef)	0.002			0.000	0.004	0.002	0.000	0.006	0.000	0.004
trp	SER (abc) + R5P.p (defgh) + PEP.p (ijk) + E4P.p (lmno) + PEP.p (pqr) -> Trp (abcedklmnoj) + CO2 (i) + TP.p (fgh) + PYR.p (pqr)	0.003	0.001	0.005	0.001	0.005	0.003	0.001	0.005	0.001	0.005
trpeff	Trp (abcdefghijk) -> Trp.eff (abcdefghijk)	0.003			0.001	0.005	0.003	0.000	0.007	0.001	0.005
R109	0*G6P.c (abcdef) -> G6P.s (abcdef)	71.383			63.811	78.283	79.130	60.421	96.894	67.682	87.361
R110	0*G6P.p (abcdef) -> G6P.s (abcdef)	28.617	21.587	36.197	21.708	36.142	20.870	11.697	31.186	12.591	32.296
R111	G6P.s (abcdef) -> sink	100.000			100.000	100.000	100.000			100.000	100.000
R112	0*F6P.c (abcdef) -> F6P.s (abcdef)	100.000	100.000	100.000	98.074	100.000	100.000	92.387	100.000	96.590	100.000
R113	0*F6P.p (abcdef) -> F6P.s (abcdef)	0.000	0.000	2.789	0.000	1.848	0.000	0.000	4.664	0.000	3.276
R114	F6P.s (abcdef) -> sink	100.000			100.000	100.000	100.000			100.000	100.000
R115	0*3PG.c (abc) -> 3PG.s (abc)	99.999		100.000	99.999	99.999	100.000	0.000	100.000	100.000	100.000
R116	0*3PG.p (abc) -> 3PG.s (abc)	0.001	0.000	100.000	0.001	0.001	0.000	0.000	100.000	0.000	0.000

R117	3PG.s (abc) -> sink	100.000			100.000	100.000	100.000			100.000	100.000
R118	0*PEP.c (abc) -> PEP.s (abc)	99.999		100.000	99.999	99.999	100.000	0.000	100.000	99.999	100.000
R119	0*PEP.p (abc) -> PEP.s (abc)	0.001	0.000	100.000	0.001	0.001	0.000	0.000	100.000	0.000	0.000
R120	PEP.s (abc) -> sink	100.000			100.000	100.000	100.000			100.000	100.000
R121	0*PYR.c (abc) -> PYR.s (abc)	0.000	0.000	1.292	0.000	15.446	34.356	0.000	87.781	0.000	80.865
R122	0*PYR.p (abc) -> PYR.s (abc)	0.000	0.000	7.352	0.000	0.000	65.644			18.982	100.000
R123	0*PYR.m (abc) -> PYR.s (abc)	100.000	93.227	100.000	84.320	100.000	0.000	0.000	18.472	0.000	0.000
R124	PYR.s (abc) -> sink	100.000			100.000	100.000	100.000			100.000	100.000
R125	0*6PG.c (abcdef) -> 6PG.s (abcdef)	1.898			0.671	3.226	0.000	0.000	2.565	0.000	9.647
R126	0*6PG.p (abcdef) -> 6PG.s (abcdef)	98.102	96.836	99.552	96.773	99.324	100.000	99.075	100.000	90.297	100.000
R127	6PG.s (abcdef) -> sink	100.000			100.000	100.000	100.000			100.000	100.000
R128	0*G1P.c (abcdef) -> G1P.s (abcdef)	64.806			61.941	67.023	70.981	57.947	74.991	61.064	73.215
R129	0*G1P.p (abcdef) -> G1P.s (abcdef)	35.194	33.018	37.778	32.957	38.056	29.019	26.975	33.904	26.785	38.851
R130	G1P.s (abcdef) -> sink	100.000			100.000	100.000	100.000			100.000	100.000
R131	0*MAL (abcd) -> MAL.s (abcd)	48.069			42.449	54.018	38.670	31.133	46.717	34.617	42.231
R132	0*MAL.u (abcd) -> MAL.s (abcd)	51.931	45.052	58.026	45.958	57.528	61.330	56.962	65.167	57.747	65.357
R133	MAL.s (abcd) -> sink	100.000			100.000	100.000	100.000			100.000	100.000
R134	0*CIT (abcdef) -> CIT.s (abcdef)	12.241			9.254	15.257	6.000	0.151	11.650	2.887	8.905
R135	0*CIT.u (abcdef) -> CIT.s (abcdef)	87.759	84.580	90.877	84.739	90.742	94.000	91.080	97.029	91.079	97.105
R136	CIT.s (abcdef) -> sink	100.000			100.000	100.000	100.000			100.000	100.000
R137	0*AKG (abcde) -> AKG.s (abcde)	75.093			70.499	80.048	75.362	68.587	83.938	71.958	79.006
R138	0*AKG.u (abcde) -> AKG.s (abcde)	24.907	20.034	29.321	19.877	29.493	24.638	20.342	27.928	20.990	28.009
R139	AKG.s (abcde) -> sink	100.000			100.000	100.000	100.000			100.000	100.000
R140	0*SUCC (abcd) -> SUCC.s (abcd)	29.916			24.283	36.753	10.811	3.240	18.743	6.746	14.664
R141	0*SUCC.u (abcd) -> SUCC.s (abcd)	70.084	63.433	76.357	63.194	75.700	89.189	84.999	92.957	85.298	93.220
R142	SUCC.s (abcd) -> sink	100.000			100.000	100.000	100.000			100.000	100.000
R143	0*FUM (abcd) -> FUM.s (abcd)	20.067			15.183	24.923	14.987	8.166	21.711	11.124	18.083
R144	0*FUM.u (abcd) -> FUM.s (abcd)	79.933	74.747	84.905	74.977	84.685	85.013	81.261	88.515	81.883	88.850
R145	FUM.s (abcd) -> sink	100.000			100.000	100.000	100.000			100.000	100.000
R146	0*FBP.c (abcdef) -> FBP.s (abcdef)	47.277			44.335	49.821	39.327	31.257	46.366	34.799	42.941
R147	0*FBP.p (abcdef) -> FBP.s (abcdef)	52.723	49.878	55.579	50.179	55.659	60.673	56.668	64.570	57.040	65.196

R148	FBP.s (abcdef) -> sink	100.000			100.000	100.000	100.000			100.000	100.000
R149	0*ICIT (abcdef) -> ICIT.s (abcdef)	12.424	12.326	13.994	9.521	15.661	5.934	0.101	11.553	2.947	8.764
R150	0*ICIT.u (abcdef) -> ICIT.s (abcdef)	87.576	84.446	90.681	84.336	90.431	94.066	91.155	97.289	91.227	97.050
R151	ICIT.s (abcdef) -> sink	100.000			100.000	100.000	100.000			100.000	100.000
GLCl	GLC.ext (abcdef) -> GLC.int (abcdef)	0.838	0.836	0.841	0.832	0.844	0.887	0.869	0.905	0.878	0.898
GLGv	GLC.v (abcdef) -> GLC.int (abcdef)	0.162	0.156	0.167	0.156	0.167	0.113	0.104	0.124	0.102	0.122
NADPHout	NADPH -> NADPHout	0.951	0.922	0.965	0.838	1.118	0.987	0.836	1.174	0.867	1.187
CO2in	CO2.ex (a) + CO2 (b) -> CO2 (a) + CO2.waste (b)	0.000	0.000	0.120	0.000	0.418	0.001	0.000	1.538	0.000	1.004
CO2out	CO2 (a) -> CO2.eff (a)	2.678	2.327	3.162	2.306	3.078	2.698	2.282	3.168	2.273	3.101
CXin	CX.ex (a) + CX (b) -> CX (a) + CX.waste (b)	0.000	0.000	Inf	0.000	0.265	0.000	0.000	Inf	0.000	173.909
RPE net	Ru5P.c (abcde) <-> X5P.c (abcde)	0.000	0.000	0.000	0.000	0.000	0.000	0.000	0.023	0.000	0.010
RPE exch	Ru5P.c (abcde) <-> X5P.c (abcde)	0.035			0.031	0.039	0.004			0.000	196.676
RPI net	Ru5P.c (abcde) <-> R5P.c (abcde)	0.000			0.000	0.000	0.000			0.000	0.000
RPI exch	Ru5P.c (abcde) <-> R5P.c (abcde)	0.011			0.009	0.013	0.046			0.000	0.248
XPT net	X5P.c (abcde) <-> X5P.p (abcde)	0.000	0.000	0.000	0.000	0.000	0.000	0.000	0.023	0.000	0.010
XPT exch	X5P.c (abcde) <-> X5P.p (abcde)	0.000	0.000	Inf	0.000	0.000	0.368			0.016	196.537
R152	0*R5P.c (abcde) -> R5P.s (abcde)	30.460	24.939	30.783	19.927	44.936	49.541	44.084	100.000	35.651	100.000
R153	0*R5P.p (abcde) -> R5P.s (abcde)	69.540	45.332	78.459	54.998	79.874	50.459	0.000	54.846	0.000	64.321
R154	R5P.s -> sink	100.000			100.000	100.000	100.000			100.000	100.000

A.6 Coenzyme stoichiometries

Table A.2. Coenzyme stoichiometries of internal reactions (excluding biomass outputs). Values are based on stoichiometries defined in AraCyc (Schläpfer et al., 2017). Values in italics represent potential stoichiometries discussed in the main text for glyceraldehyde 3-phsophate dehydrogenase (chex3-1), isocitrate dehydrogenase (tca3), and methylenetetrahydrofolate metabolism (CX, gly net).

		Coenzyme stoichiometry		
Flux	Equation	ATP	NADH	NADPH
upt	GLC.int -> G6P.c	-1	0	0
chex2-1 net	F6P.c <-> FBP.c	-1	0	0
chex3-1 net	TP.c <-> 3PG.c	1	1	*1*
chex3	PEP.c -> PYR.c	1	0	0
phex2-1	F6P.p -> FBP.p	-1	0	0
phex3-1 net	TP.p <-> 3PG.p	1	1	0
phex3	PEP.p -> PYR.p	1	0	0
cppp1	G6P.c -> 6PG.c + NADPH	0	0	1
cppp1-1	6PG.c -> Ru5P.c + CO2 + NADPH	0	0	1
pppp1	G6P.p -> 6PG.p + NADPH	0	0	1
pppp-1	6PG.p -> Ru5P.p + CO2 + NADPH	0	0	1
tca1	PYR.m -> CO2 + AcCoA	0	1	0
tca2	AcCoA + MAL -> CIT	0	1	0
tca3	ICIT -> CO2 + AKG + NADPH	0	*1*	1
tca4	AKG -> CO2 + SUCCCoA	0	1	0
R36 net	SUCCCoA <-> SUCC	1	0	0
tca5 net	SUCC <-> FUM	0	0.6	0
ana1 net	PEP.c + CO2 <-> MAL	0	-1	0
ana2	MAL -> PYR.m + CO2	0	1	0
ana3	MAL -> PYR.p + CO2 + NADPH	0	0	1
pdhp	PYR.p -> CO2 + AcCoA.p	0	1	0
gly net	SER <-> GLY + CX	0	0	*1*
gly1 net	GLY <-> CO2 + CX	0	1	0

Table A.3. Coenzyme stoichiometries and biomass output fluxes of heterotrophic *Arabidopsis* cell cultures. Stoichiometries are based on the AraCyc database (Schläpfer et al., 2017). The conenzyme requirements for synthesising the carbon skeleton are separated from the requirements for any amino group assimilation to allow evaluation of differning costs of nitrogen asismilation depending on GOGAT specificity (see Table A.4). Values for the molar flux to biomass outputs are taken from analyses of identical cell cultures by Masakapalli et al., 2014. Fluxes were determined realtive to the glucose uptake rate from the distribution of radioactivity following supply of [$^{14}C_6$]glucose. Values are the mean ± SD, n = 3.

				Carbon skeleton			**Amino group**		
Product	**Precursor**	**Flux**	**Molar flux**	**ATP**	**NADH**	**NADPH**	**Glutamate**	**Glutamine**	**ATP**
Starch	Hexose-P	sta	0.069 ± 0.015	1	0	0	0	0	0
Cell wall hexosyl unit	Hexose-P	wall	0.031 ± 0.003	1	0	0	0	0	0
Cell wall pentosyl unit	Hexose-P	pentaneff	0.008 ± 0.001	1	-2	0	0	0	0
Sucrose	2(Hexose-P)	gsuceff	0.065 ± 0.022	1	0	0	0	0	0
Lipid - acyl chain	AcCoA	fas1	0.072 ± 0.018	1	1	1	0	0	0
Lipid - glycerol unit	Triose-P	fas2	0.004 ± 0.001	0	1	0	0	0	0
Ethanol	Pyr	adh	0.005 ± 0.002	0	1	0	0	0	0
Ala	Pyr	alaeff	0.098 ± 0.009	0	0	0	1	0	0
Arg	AKG + 2(AcCoA)	argeff	0.003 ± 0.001	7	0	1	2	1	0
Asn	OAA	aspeff	0.005 ± 0.001	2	0	0	1	1	0
Asp	OAA	aspeff	0.005 ± 0.001	0	0	0	1	0	0
Cys	3PGA + AcCoA + SO_4^{2-}	cyseff	0.003 ± 0.001	4	-1	4	1	0	0
Glu	αKG	glxeff	0.049 ± 0.003	0	0	0	1	0	0
Gln	αKG	glxeff	0.049 ± 0.003	0	0	0	1	0	1
Gly	3PGA	glyeff	0.022 ± 0.002	0	-1	0	1	0	0
His	Rib-5-P + ATP	hiseff	0.002 ± 0.001	4	-2	0	1	1	0
Ile	OAA + Pyr	ileeff	0.002 ± 0.001	2	1	2	2	0	0
Leu	2(Pyr) + AcCoA	leueff	0.006 ± 0.001	0	-1	1	1	0	0
Lys	OAA + Pyr	lyseff	0.011 ± 0.003	1	0	2	2	0	0
Met	OAA + SO_4^{2-}	meteff	0.002 ± 0.001	7	0	5	2	0	0
Phe	2(PEP) + E4P	pheeff	0.006 ± 0.001	1	0	1	1	0	0

Pro	αKG	proeff	0.015 ± 0.002	1	0	2	1	0	0
Ser	3PGA	proeff	0.044 ± 0.002	0	-1	0	1	0	0
Thr	OAA	threff	0.009 ± 0.001	2	1	1	1	0	0
Trp	2(E4P) + PEP + R5PP + 3PGA	trpeff	0.003 ± 0.001	3	0	1	1	1	0
Tyr	2(PEP) + E4P	tyreff	0.003 ± 0.001	1	0	0	1	0	0
Val	2(Pyr)	valeff	0.004 ± 0.001	0	0	1	1	0	0
GABA	αKG	gabaout	0.017 ± 0.001	0	0	1	0	0	0

Table A.4. Potential coenzyme stoichiometries of glutamate and glutamine biosynthesis depending on the NADP(H) specificity of GOGAT and the nitrogen source. Uptake of 50:50 ammonium:nitrate was assumed for all INST-MFA calculations. Note the cost of making glutamine from glutamate does not include the cost of making glutamate as biosynthetic reactions described in Table A.3 which use glutamine as an amino donor regenerate glutamate. Nitrate reductase is considered to require 1 NADH and nitrite reductase is considered to require 3 NADPH to produce the 6 ferredoxin required for nitrite reduction in heterotrophic cells.

Product	GOGAT-specificity	Nitrogen source	ATP	NADH	NADPH
Glu	NADH-GOGAT	Ammonium	1	1	0
Glu	NADPH-GOGAT	Ammonium	1	0	1
Glu	NADH-GOGAT	Nitrate	1	2	3
Glu	NADPH-GOGAT	Nitrate	1	1	4
Glu	NADH-GOGAT	50:50 Ammonium:Nitrate	1	2	2
Glu	NADPH-GOGAT	50:50 Ammonium:Nitrate	1	1	3
Gln	NAD(P)H-GOGAT	Ammonium	1	0	0
Gln	NAD(P)H-GOGAT	Nitrate	1	1	3
Gln	NAD(P)H-GOGAT	50:50 Ammonium:Nitrate	1	1	2

A.7 Comparison of predicted and measured isotopologue abundances

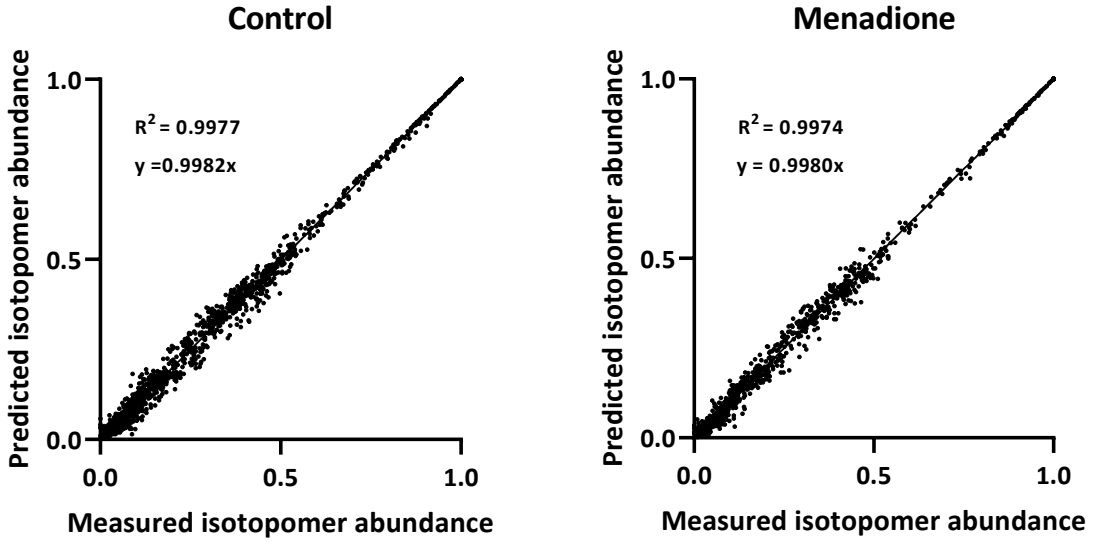

Figure A.6. Comparison of measured and simulated mass isotopologue abundances from INST-MFA across all measured metabolites and all timepoints following [$^{13}C_6$]glucose labelling of *Arabidopsis* cell cultures either treated with 60 µM menadione for 6 h or an untreated control. The line of best fit was

determined by linear regression and the equation of the line is reported together with the coefficient of determination (R^2)

A.8 Validation of PLSDA

To ensure the PLSDA model was not overfitting the data a cross-validation (Figure A.7) and permutation testing (Figure A.8) were performed to quantify how good the PLSDA model was at predicting the grouping of samples.

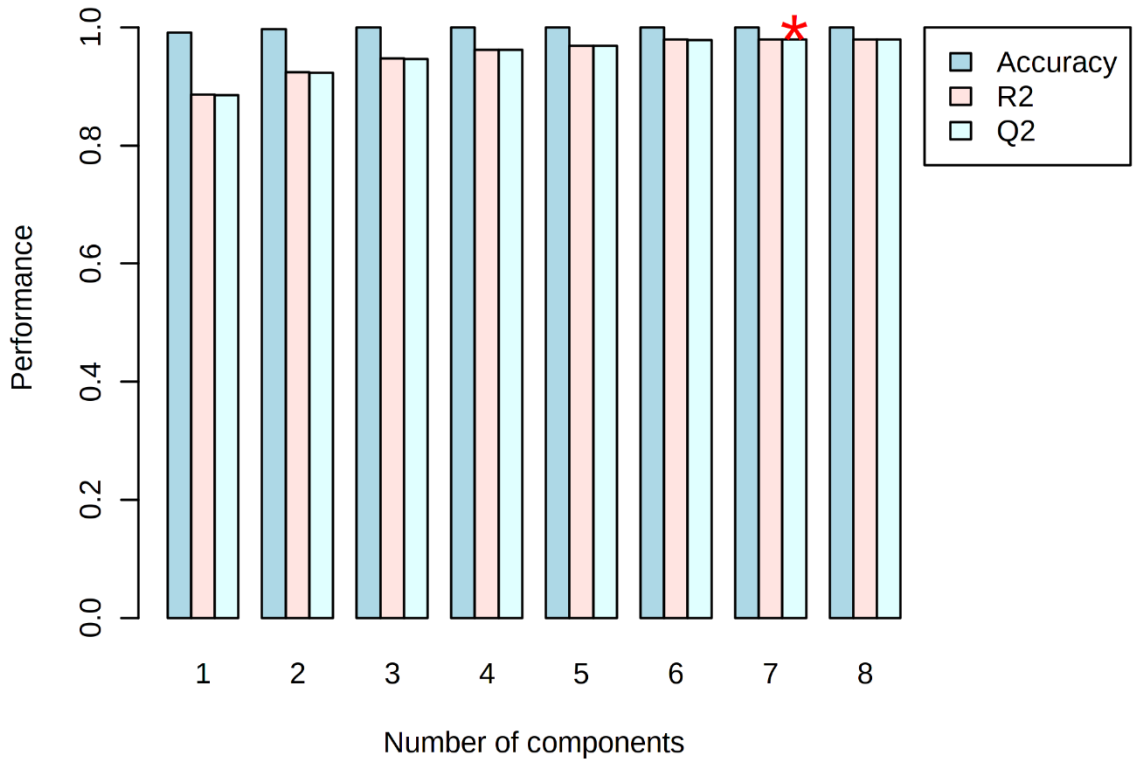

Figure A.7. Validation testing of PLSDA analysis by leave-one-out cross-validation. Performance measures included the prediction accuracy (Accuracy), sum of squares captured by the model (R^2) and the cross-validated R^2 (Q^2).

Cross-validation can identify the optimal number of components required for the PLSDA model (Szymańska et al., 2012; Westerhuis et al., 2008). In each cross validation the predicted data are compared with the original data and sum of squared errors calculated. Assessing the

performance measures showed that a seven-component model was optimal in terms of accuracy (100%), R^2 (0.98) and Q^2 (0.98) Figure A.7.

To confirm the statistical significance of the performance measures permutation testing was performed to compare the trained model to a model generated with randomly permuted data (Figure A.8). In each permutation the labels of the samples are randomly assigned, and a new classification model is calculated using the optimal number of components calculated previously (Figure A.7.). The trained classification model should outperform the randomly permuted model if there is a significant difference between the menadione and control samples and separation is not due to random chance.

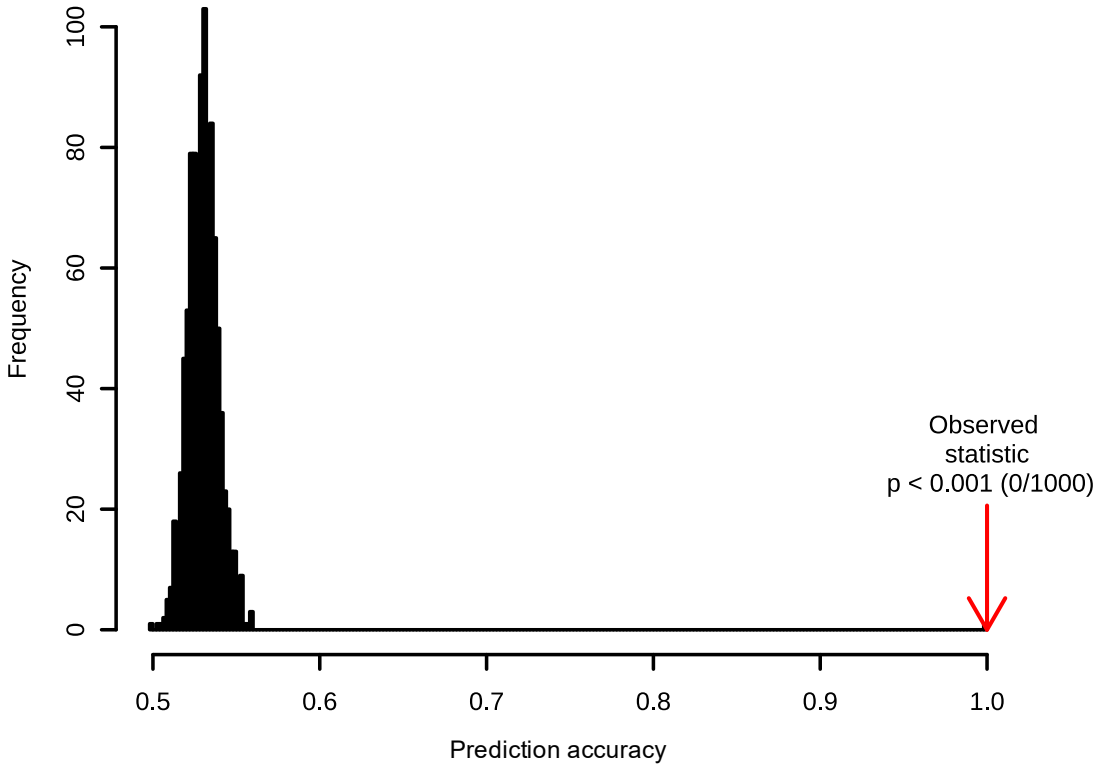

Figure A.8. Prediction accuracy of randomly permutation PLSDA model (histogram, blue bars) compared to the optimal trained model (red arrow).

The randomly permuted data performed significantly worse that the optimally trained PLSDA model as none of the randomly permuted models performed better than the optimally

trained model Figure A.8. Therefore, the model performs significantly better than random chance ($P<0.001$) and the separation between control and menadione treated flux distributions is statistically significant.

A.9 Flux map of control vs menadione treated *Arabidopsis* cell cultures

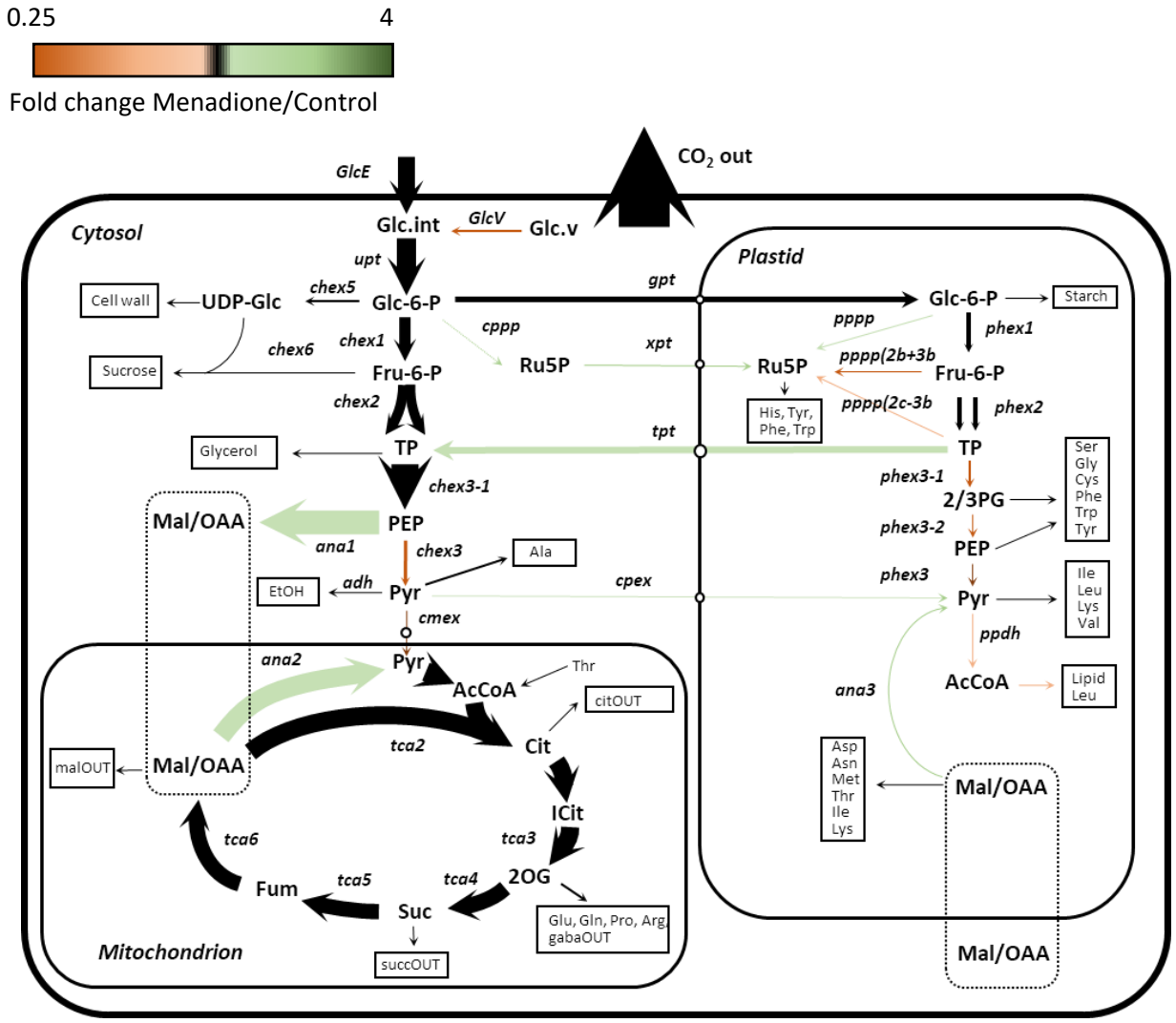

Figure A.9. Flux map of central carbon metabolism in heterotrophic *Arabidopsis* cell cultures treated with 60 µM menadione for 6 h or an untreated control. Flux arrows are coloured based on the fold change of menadione/control cells. The arrow thickness is proportional to relative molar flux in menadione treated cells. Fluxes were deduced using INST-MFA following supply of [$^{13}C_6$]glucose. Fluxes < 1% of glucose uptake rate are indicated by dashed arrows.

A.10 Net flux probability distributions

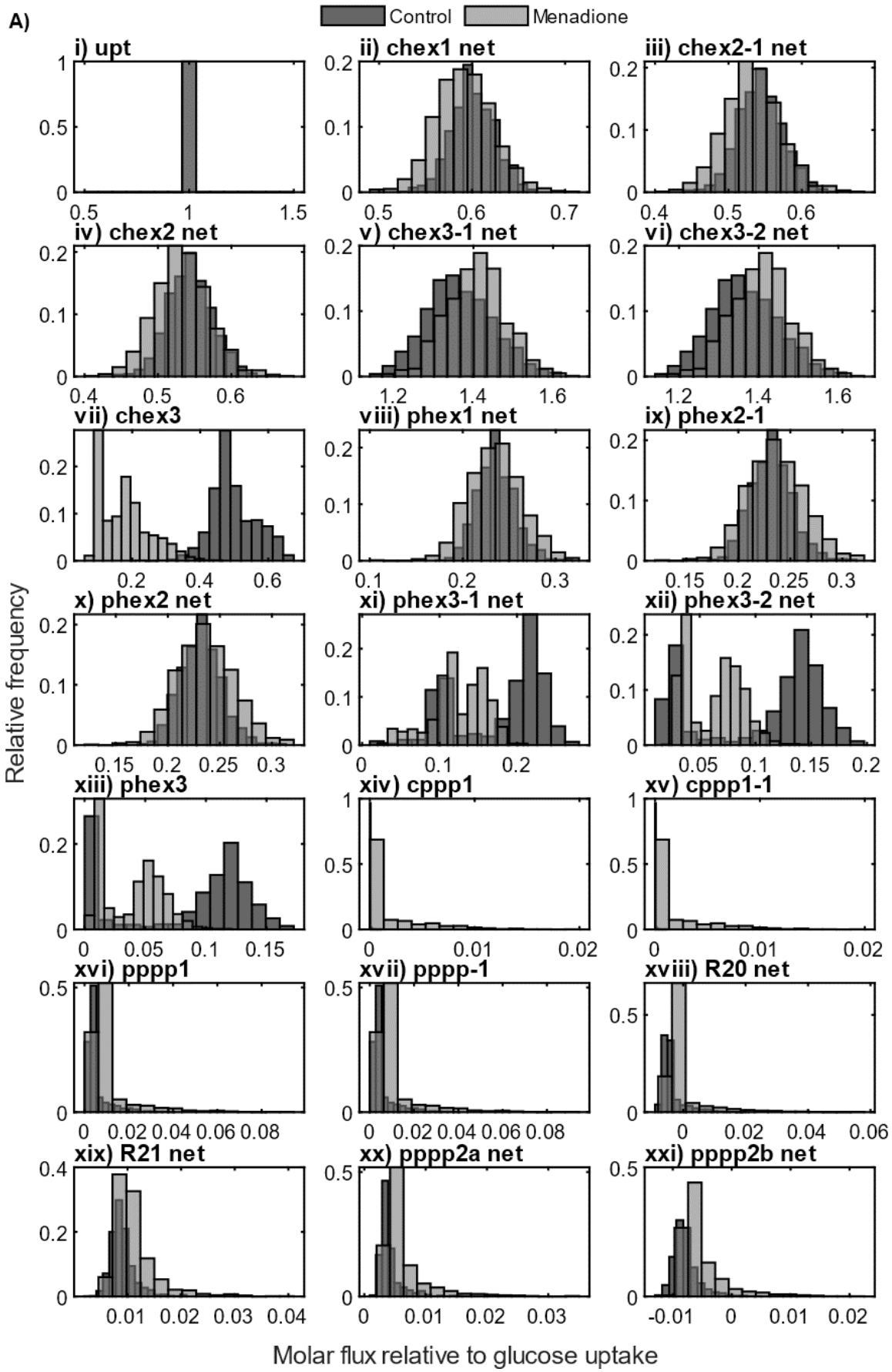

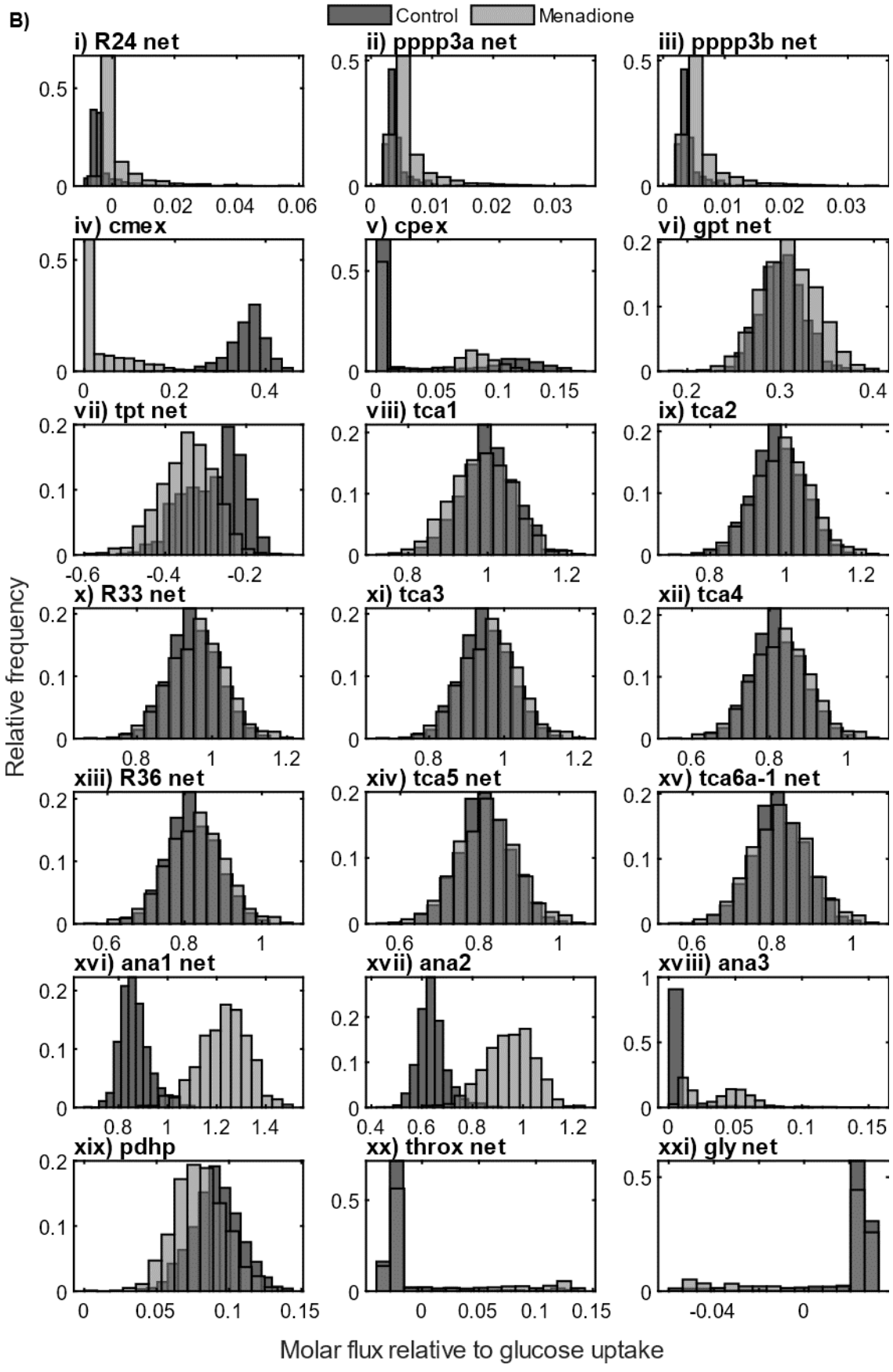
B)
Control
Menadione
i) R24 net
ii) pppp3a net
iii) pppp3b net
iv) cmex
v) cpex
vi) gpt net
vii) tpt net
viii) tca1
ix) tca2
x) R33 net
xi) tca3
xii) tca4
xiii) R36 net
xiv) tca5 net
xv) tca6a-1 net
xvi) ana1 net
xvii) ana2
xviii) ana3
xix) pdhp
xx) throx net
xxi) gly net
Relative frequency
Molar flux relative to glucose uptake

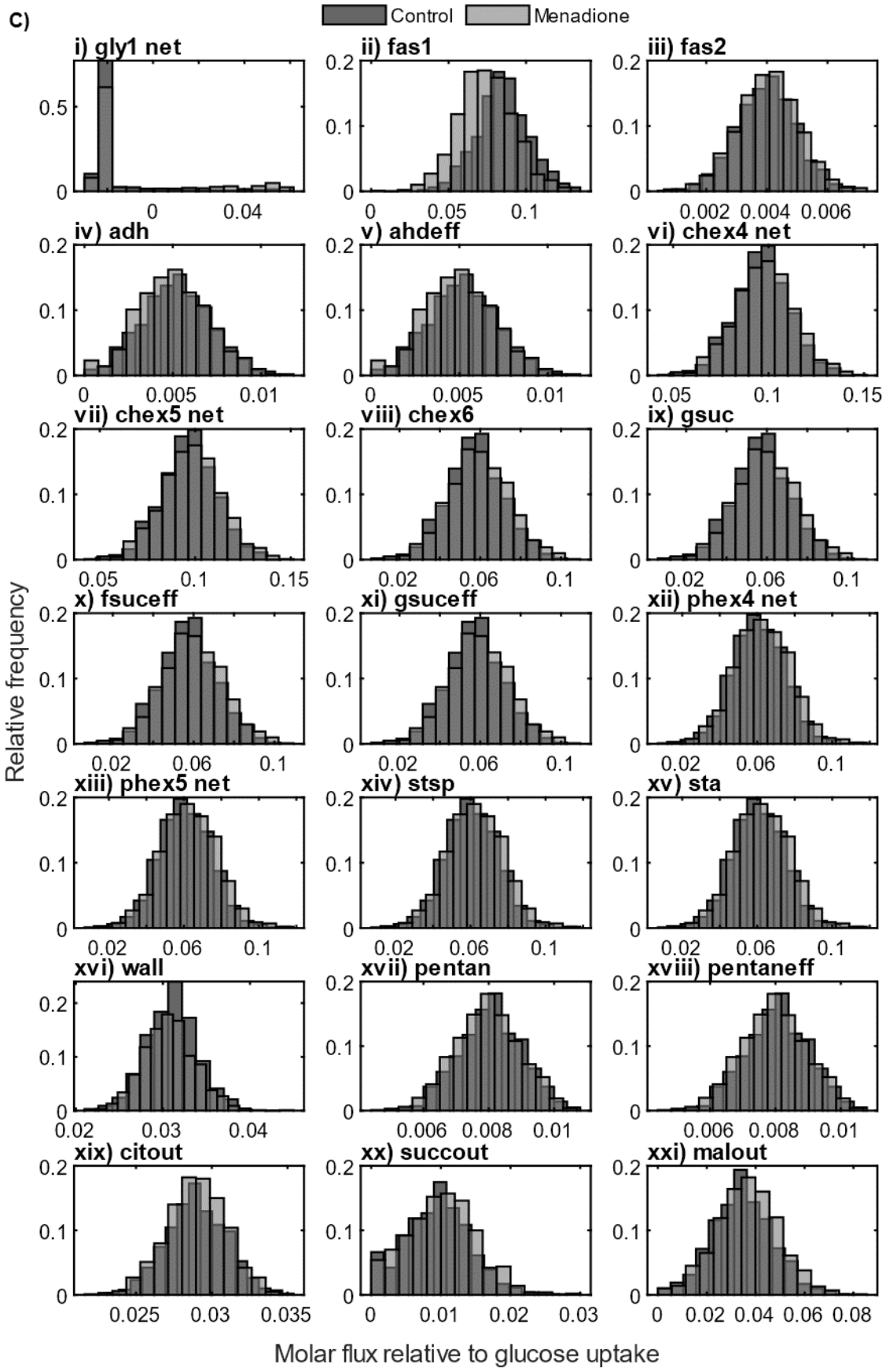
C)
Control
Menadione
i) gly1 net
ii) fas1
iii) fas2
iv) adh
v) ahdeff
vi) chex4 net
vii) chex5 net
viii) chex6
ix) gsuc
x) fsuceff
xi) gsuceff
xii) phex4 net
xiii) phex5 net
xiv) stsp
xv) sta
xvi) wall
xvii) pentan
xviii) pentaneff
xix) citout
xx) succout
xxi) malout
Relative frequency
Molar flux relative to glucose uptake

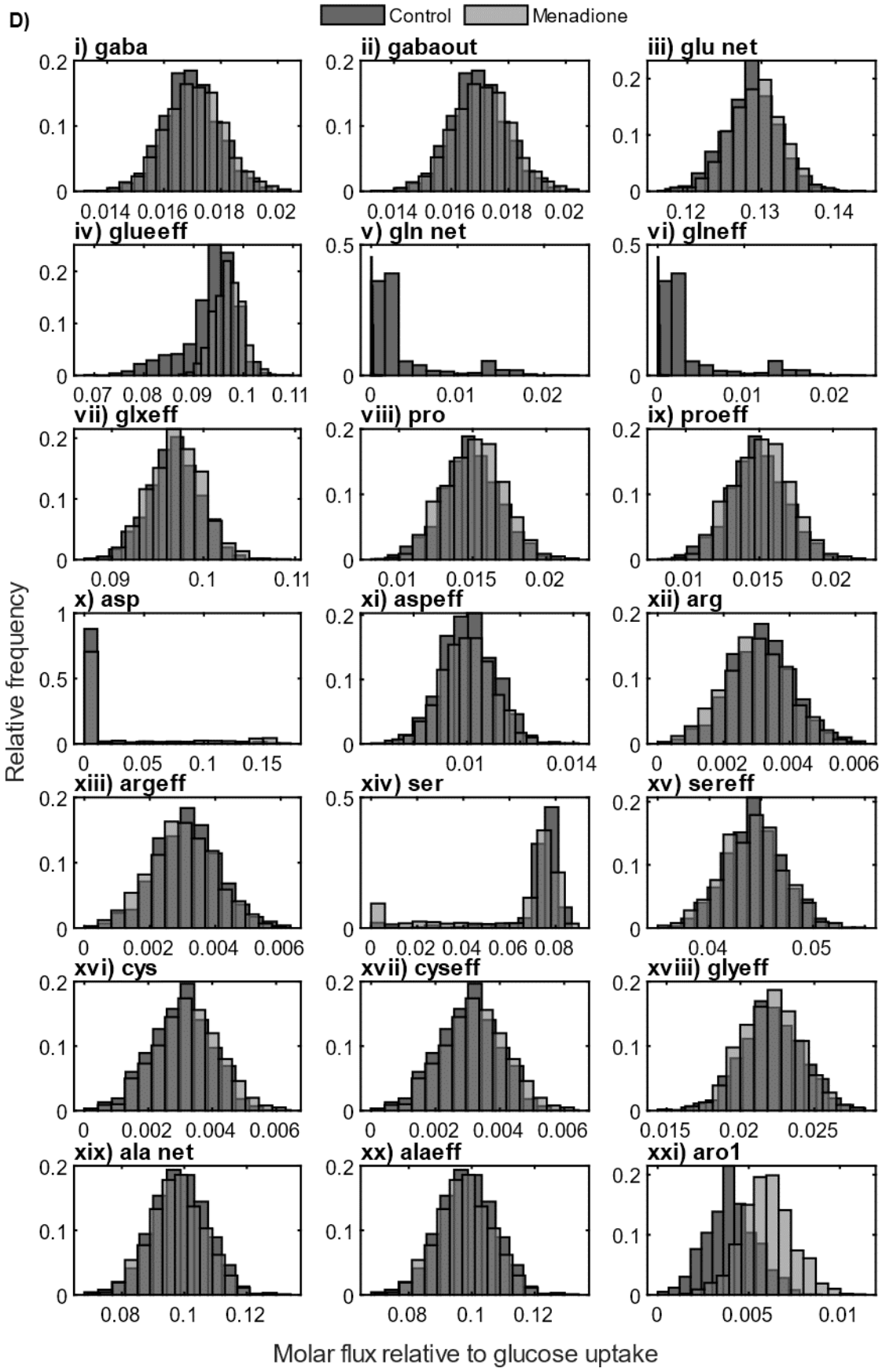
D)
Control
Menadione
i) gaba
ii) gabaout
iii) glu net
iv) glueeff
v) gln net
vi) glneff
vii) glxeff
viii) pro
ix) proeff
x) asp
xi) aspeff
xii) arg
xiii) argeff
xiv) ser
xv) sereff
xvi) cys
xvii) cyseff
xviii) glyeff
xix) ala net
xx) alaeff
xxi) aro1
Relative frequency
Molar flux relative to glucose uptake

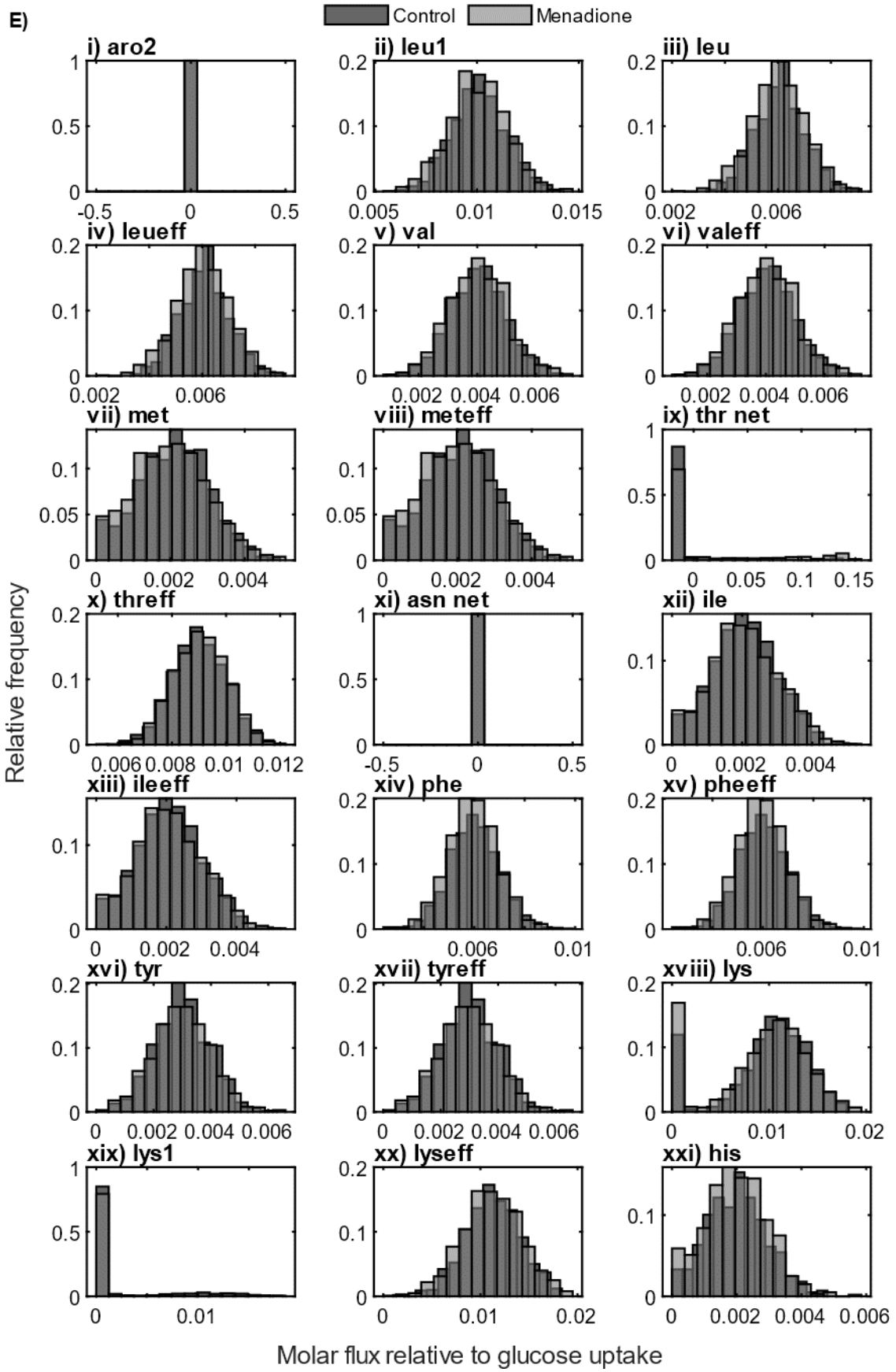
E)
Control
Menadione
i) aro2
ii) leu1
iii) leu
iv) leueff
v) val
vi) valeff
vii) met
viii) meteff
ix) thr net
x) threff
xi) asn net
xii) ile
xiii) ileeff
xiv) phe
xv) pheeff
xvi) tyr
xvii) tyreff
xviii) lys
xix) lys1
xx) lyseff
xxi) his
Relative frequency
Molar flux relative to glucose uptake

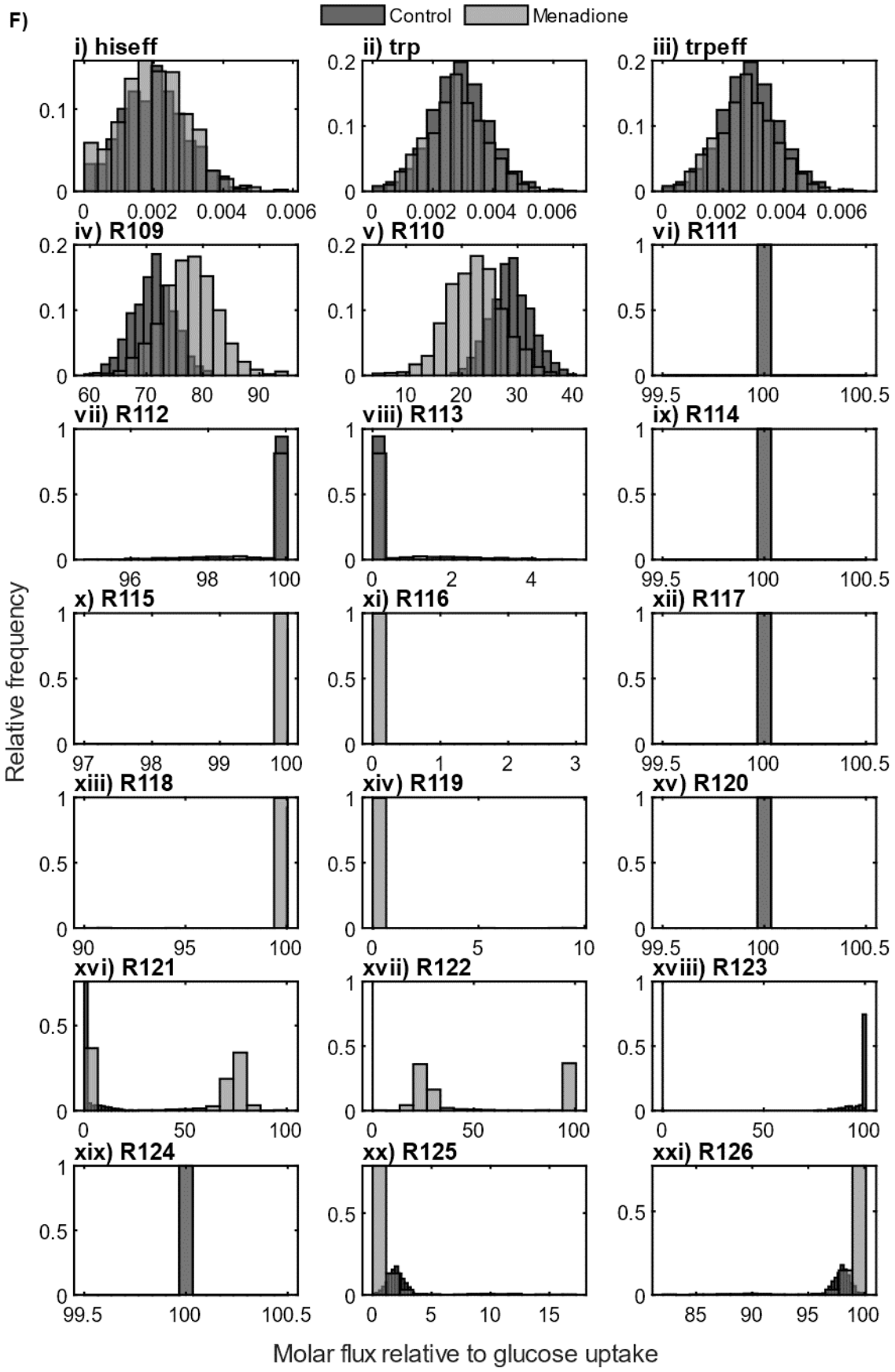
F)
Control
Menadione
i) hiseff
ii) trp
iii) trpeff
iv) R109
v) R110
vi) R111
vii) R112
viii) R113
ix) R114
x) R115
xi) R116
xii) R117
xiii) R118
xiv) R119
xv) R120
xvi) R121
xvii) R122
xviii) R123
xix) R124
xx) R125
xxi) R126
Relative frequency
Molar flux relative to glucose uptake

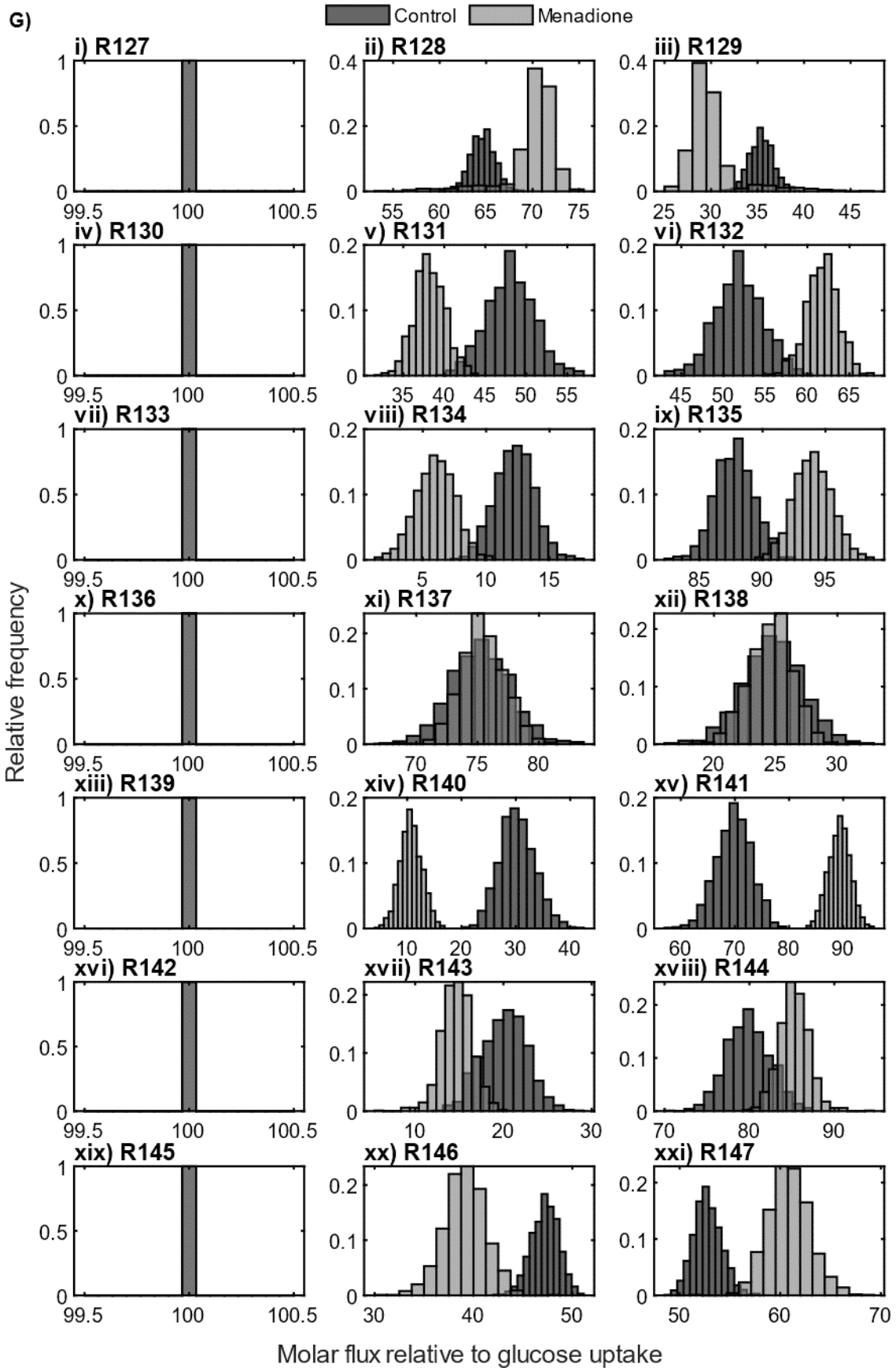
G)
Control
Menadione
i) R127
ii) R128
iii) R129
iv) R130
v) R131
vi) R132
vii) R133
viii) R134
ix) R135
x) R136
xi) R137
xii) R138
xiii) R139
xiv) R140
xv) R141
xvi) R142
xvii) R143
xviii) R144
xix) R145
xx) R146
xxi) R147
Relative frequency
Molar flux relative to glucose uptake

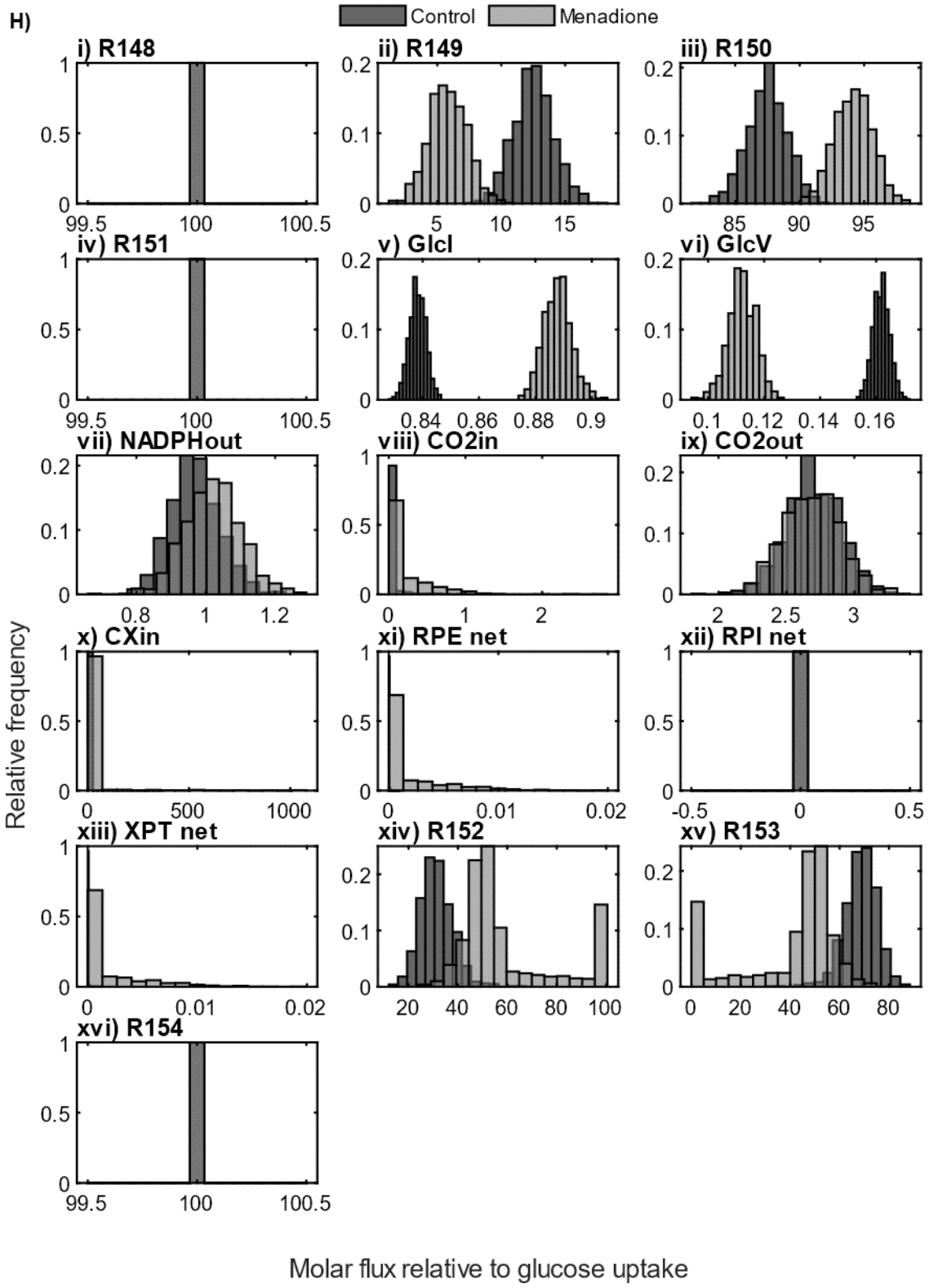

Figure A.10. Flux distributions from 1000 Monte Carlo simulation of best fit flux maps of heterotrophic *Arabidopsis* cell cultures treated with 60 µM menadione (light grey) or an untreated control (dark grey).

A.11 Comparison of SS-MFA vs INST-MFA

Table A.5. Comparison of fluxes between INST-MFA and SS-MFA of heterotrophic *Arabidopsis* cell cultures. Only directly comparable fluxes are displayed. 95% CI were calculated by parameter continuation. Non-linear confidence intervals were not reported for all fluxes in previous SS-MFA.

	INST-MFA Control			Masakapalli et al., 2010			Masakapalli et al., 2013			Masakapalli et al., 2014		
		95% CI			95% CI			95% CI			95% CI	
Flux ID	Value	LB	UB	Value	LB	UB	Value	LB	UB	Value	LB	UB
upt	1.00	1.00	1.00	1.00			1.00			1.00		
chex1	0.60	0.60	0.60	0.19			-1.53	0.25	0.09	0.19	0.12	0.26
chex2	0.54	0.52	0.54	0.12			-0.23			0.12		
chex3	0.48	0.42	0.67	0.79			0.93			1.01		
phex1	0.24	0.23	0.24	0.21			0.67			0.36		
phex2	0.23	0.23	0.23	0.44			0.86			0.54		
cppp1	0.00	0.00	0.00	0.37			0.08	0.00	0.16	0.13	0.06	0.22
pppp1	0.00	0.00	0.02	0.00			0.21	0.15	0.32	0.16	0.05	0.24
pppp2a	0.00	0.00	0.01	0.13			0.10			0.10		
pppp2b	-0.01	-0.01	0.00	0.11			0.09			0.09		
pppp2c	0.00	-0.01	0.01	0.23			0.19			0.18		
pppp3a	0.12	0.00	0.16	0.13			0.10			0.10		
pppp3b	0.00	0.00	0.01	0.13			0.10			0.10		
cmex	0.37	0.37	0.37	0.62			0.89			0.85		
cpex	0.00	0.00	0.09	0.11			0.00	0.00	0.03	0.06	0.04	0.08
gpt	0.30	0.26	0.35	0.25			0.96			0.58		
tpt	-0.24	-0.48	-0.16	0.80			1.67			-1.03		
tca1	1.00	0.87	1.16	0.66			0.95			0.86		
tca2	0.97	0.85	1.16	0.66			0.95			0.86		
tca3	0.94	0.82	1.13	0.64			0.92			0.83		
tca4	0.81	0.69	1.00	0.58			0.82			0.70		
tca5	0.80	0.80	0.80	0.58			0.82			0.69		
tca6a+b	0.80	0.69	0.99	0.58			0.82			0.69		
ana1	0.84	0.76	1.01	0.24			0.27			0.26		
ana2	0.62	0.54	0.73	0.04			0.06	0.04	0.09	0.01	0.00	0.02
ana3	0.00	0.00	0.04	0.03			0.01			0.01		
CO2 out	2.68	2.33	3.16	2.35			2.70			2.58		

Appendix B

B.1 Confocal images of biosensor subcellular localisation

B.1.1 Cyt-iNapC-A

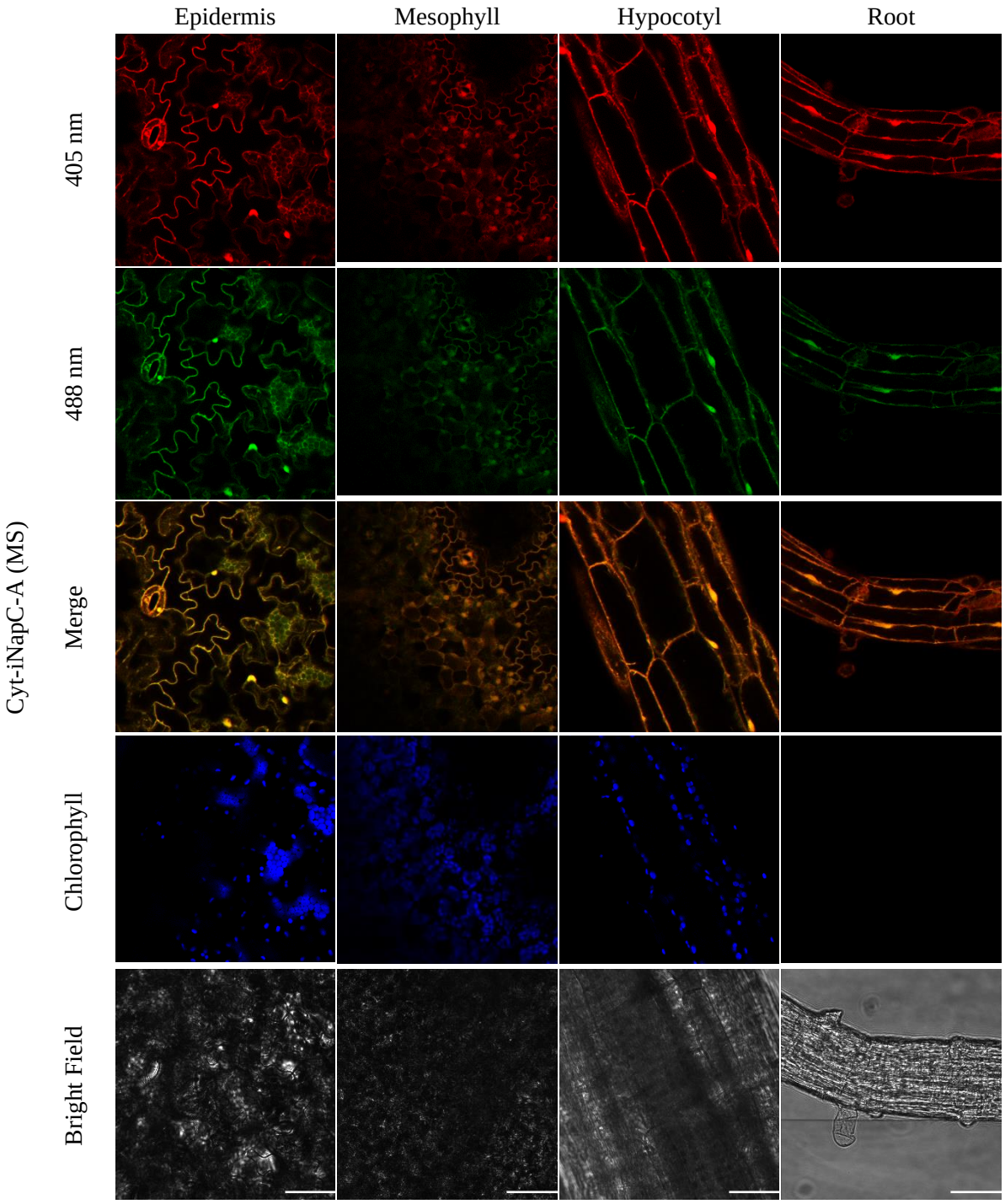

B.1.2 Cyt-iNapC-B

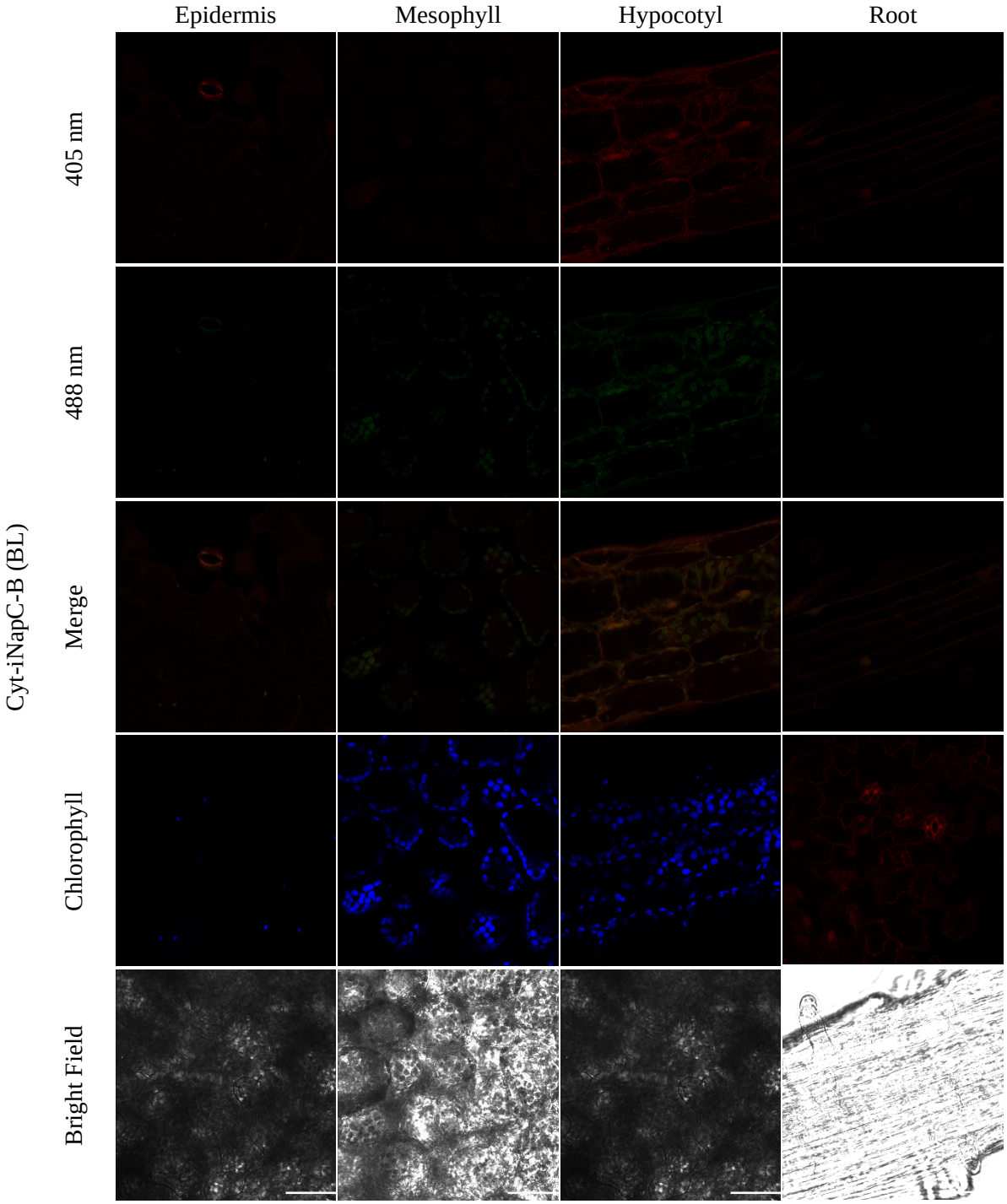

B.1.3 Cyt-iNap1

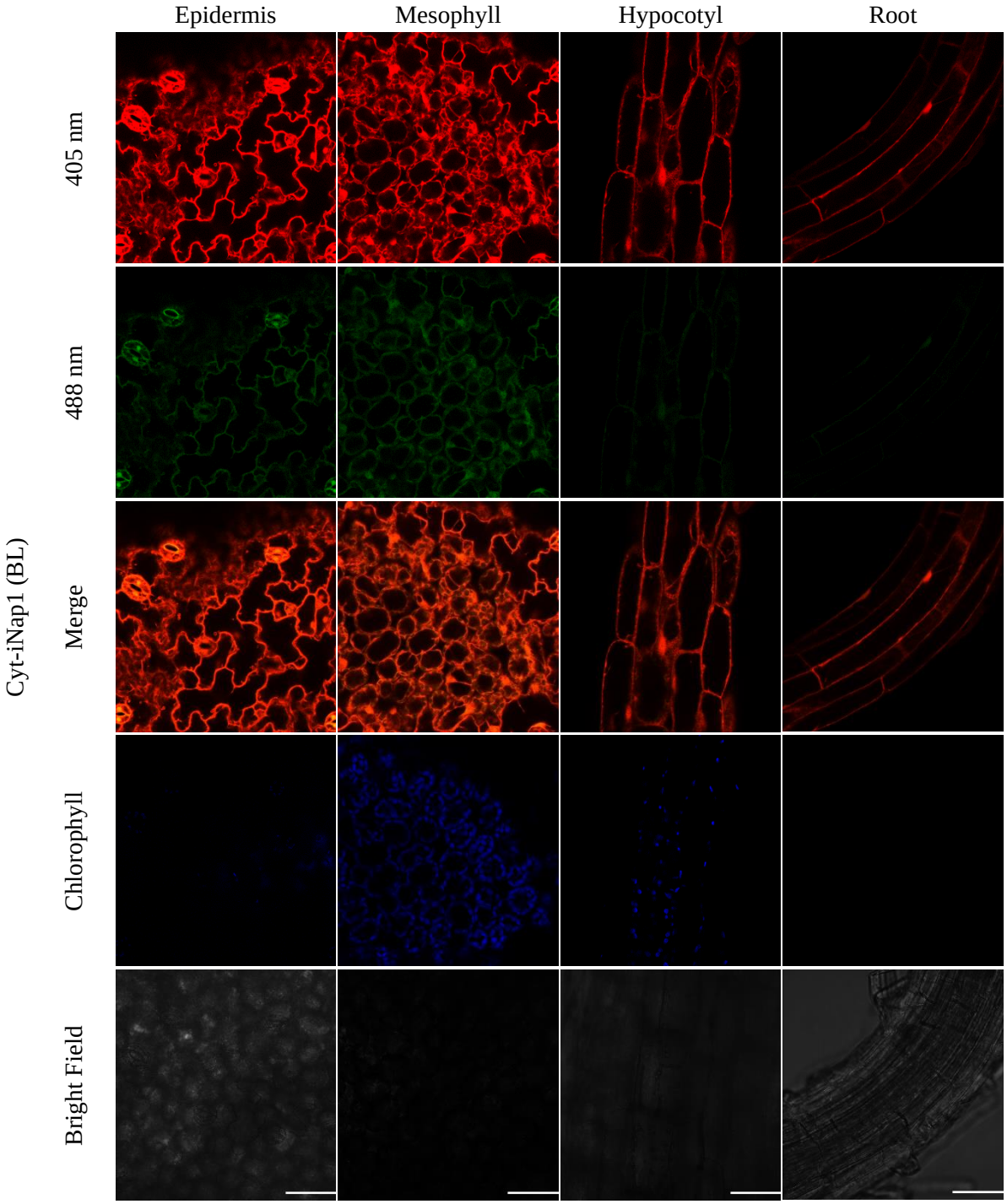

B.1.4 Cyt-iNap2

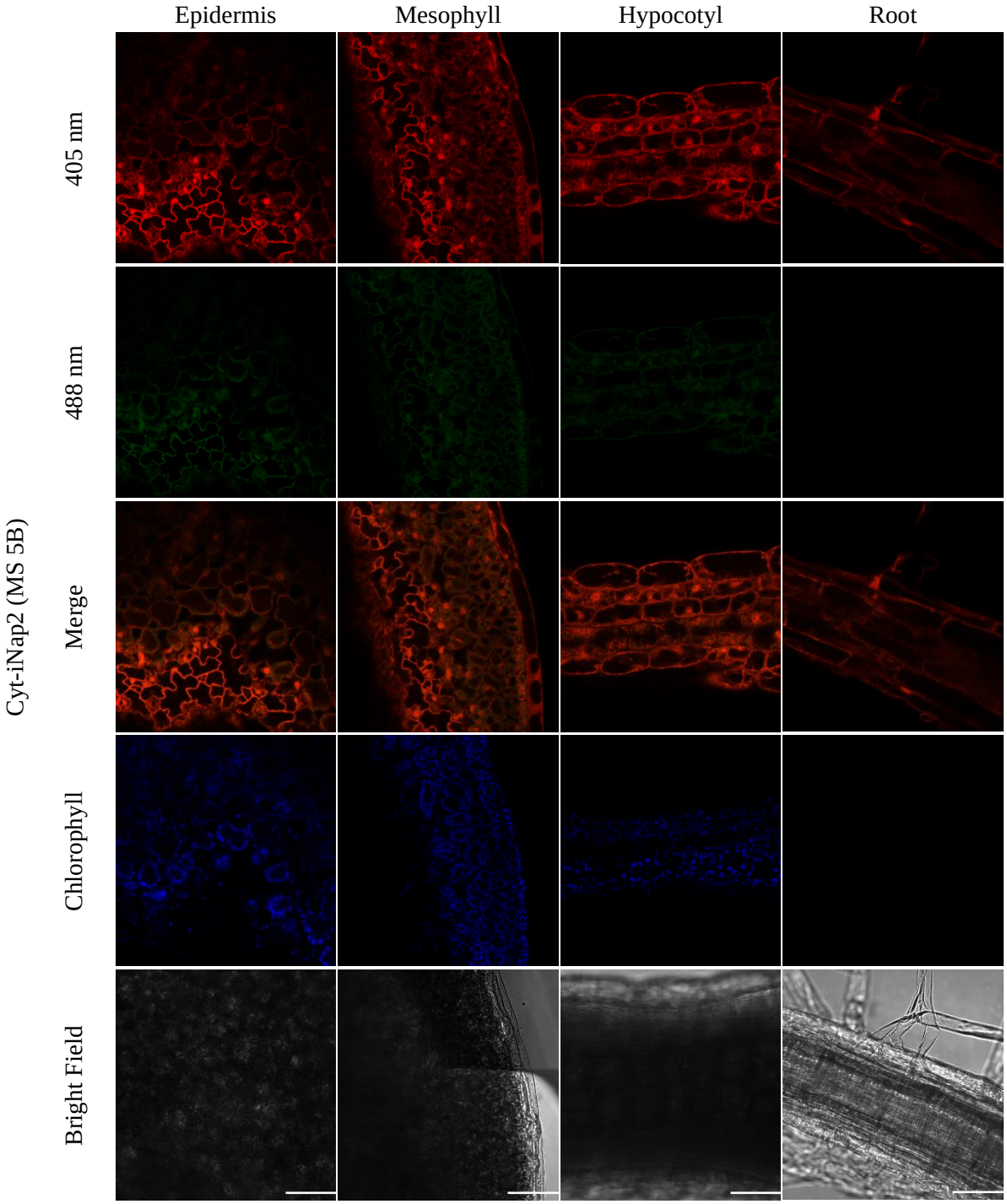

B.1.5 Cyt-iNap4

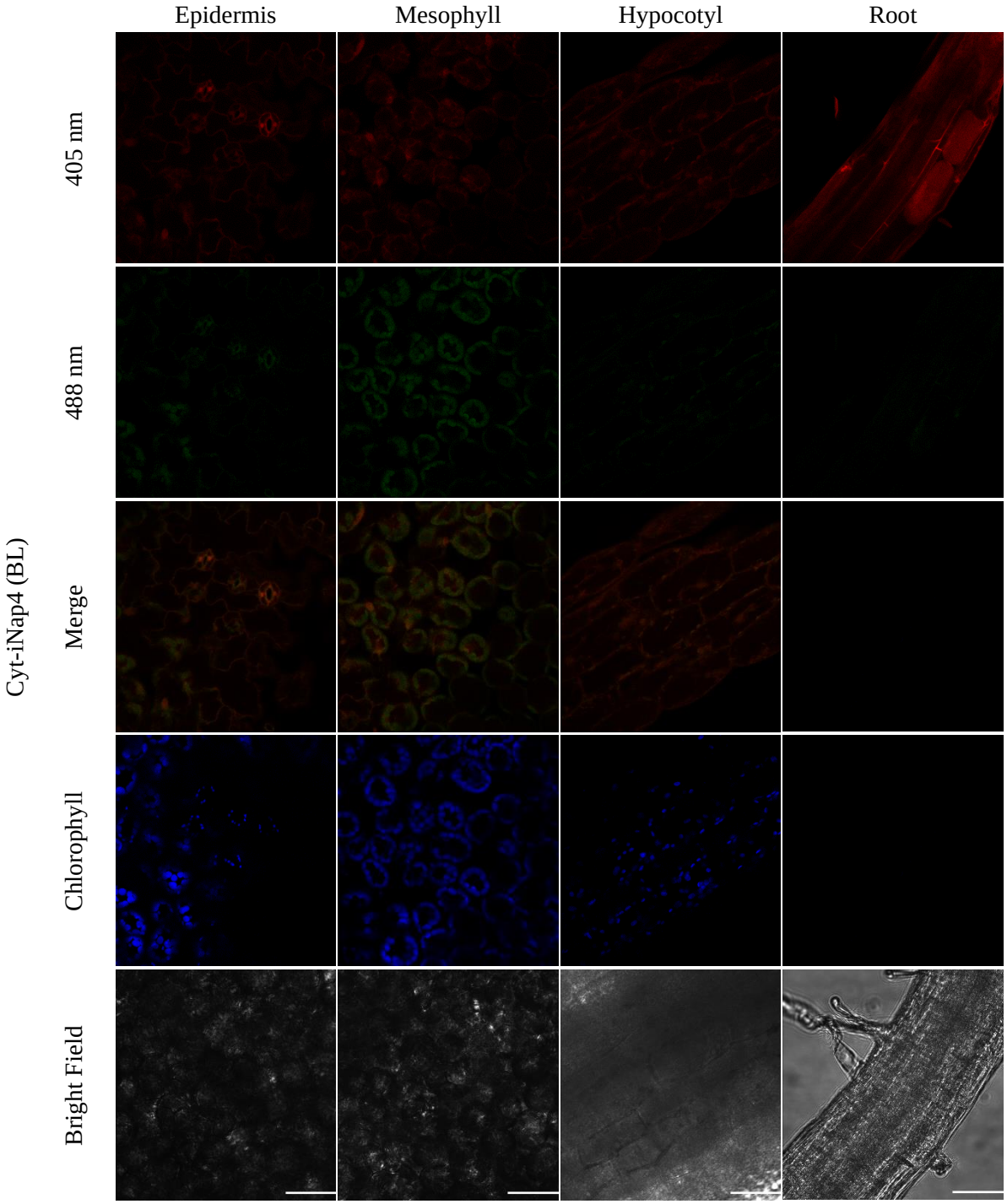

B.1.6 Cyt-SoNar

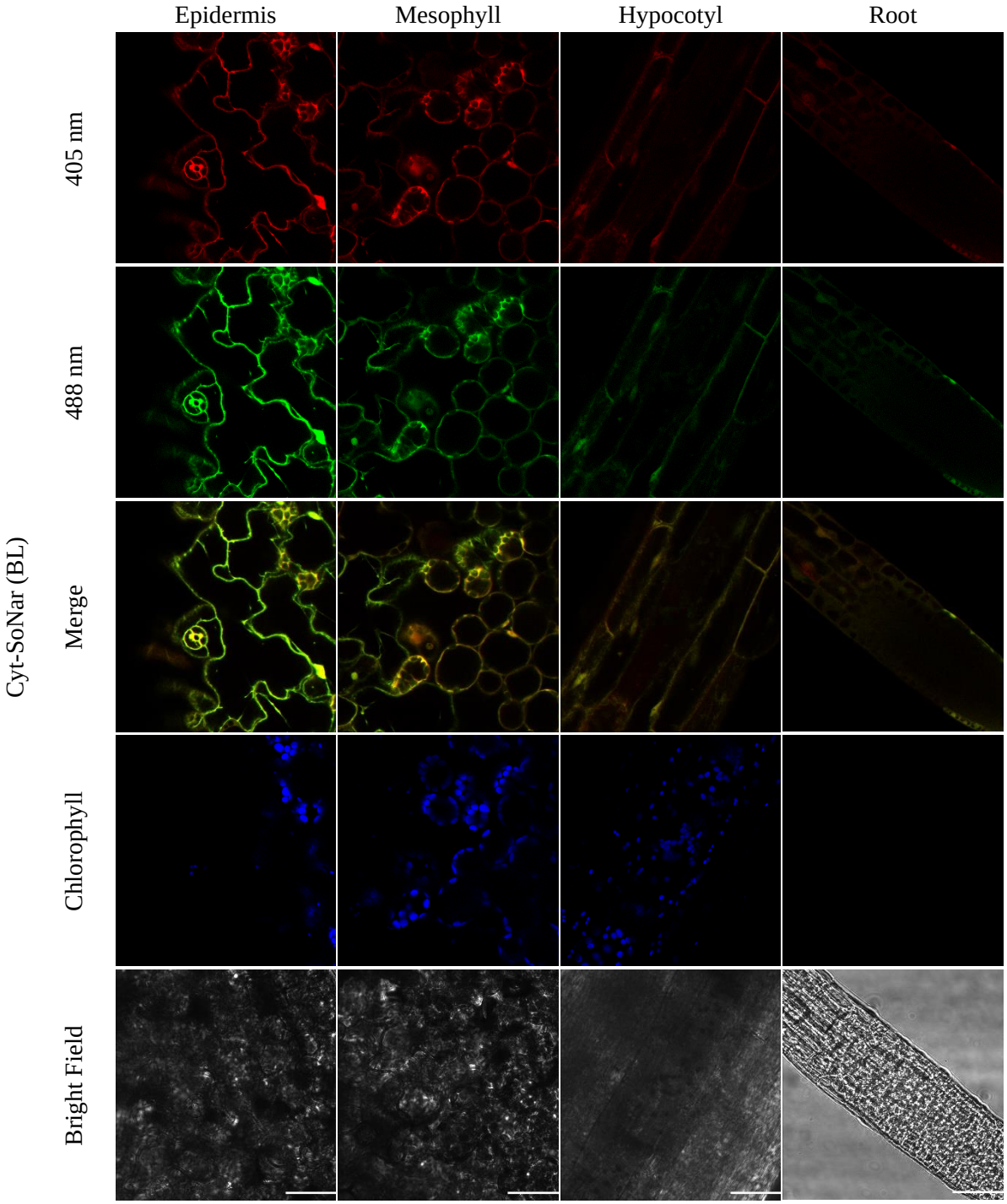

B.1.7 Perox-iNapC

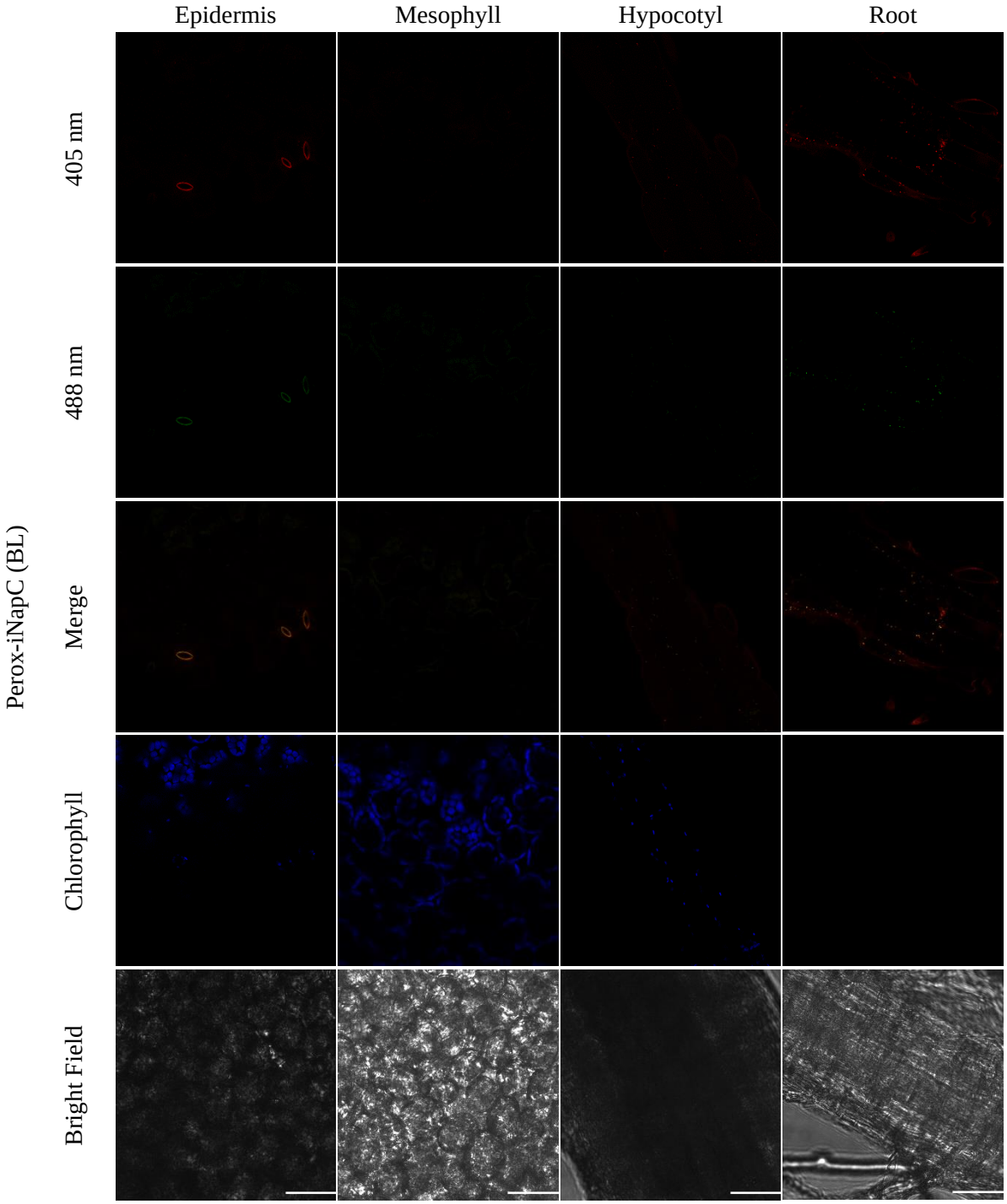

B.1.8 Perox-iNap1

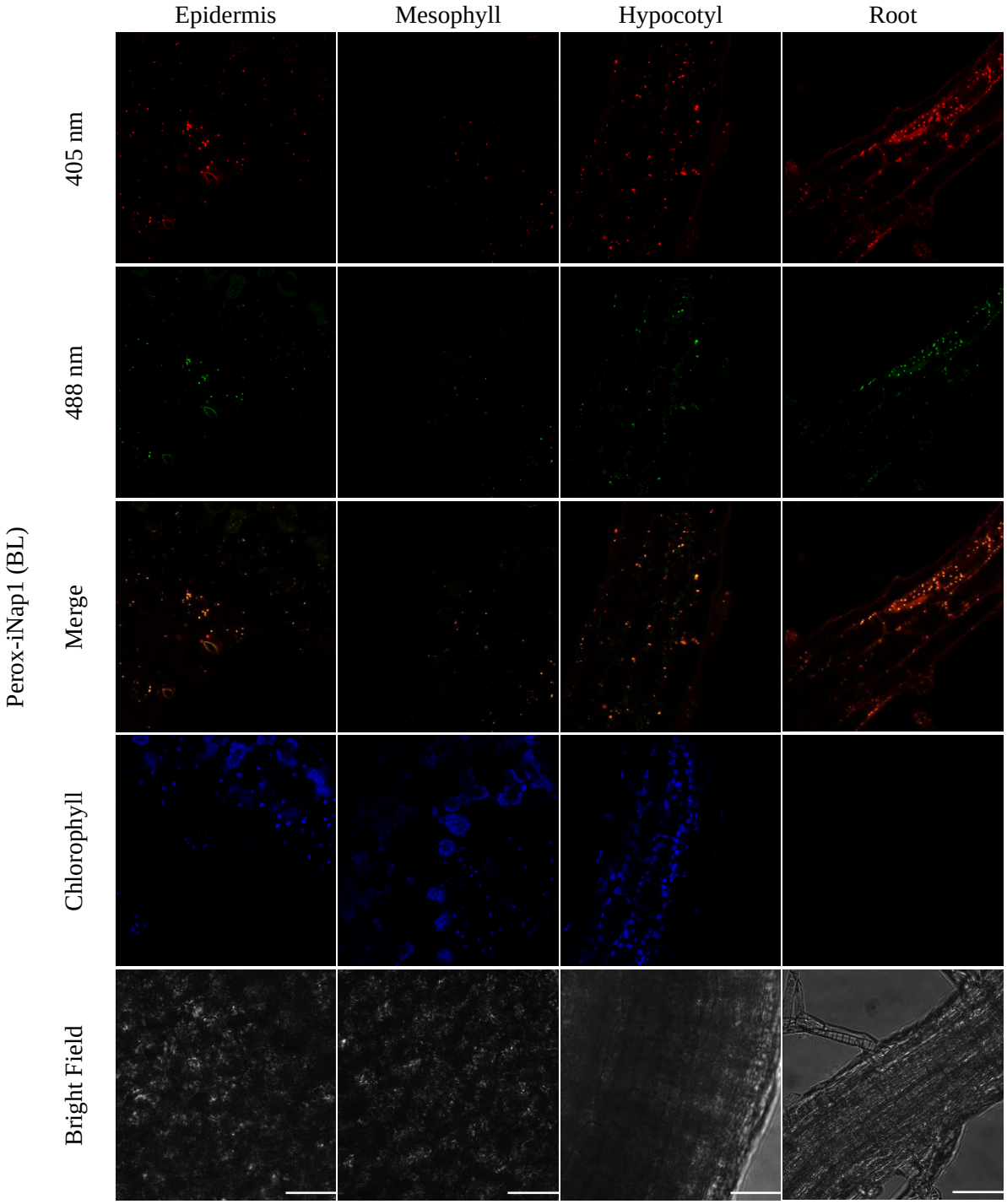

B.1.9 Perox-iNap4

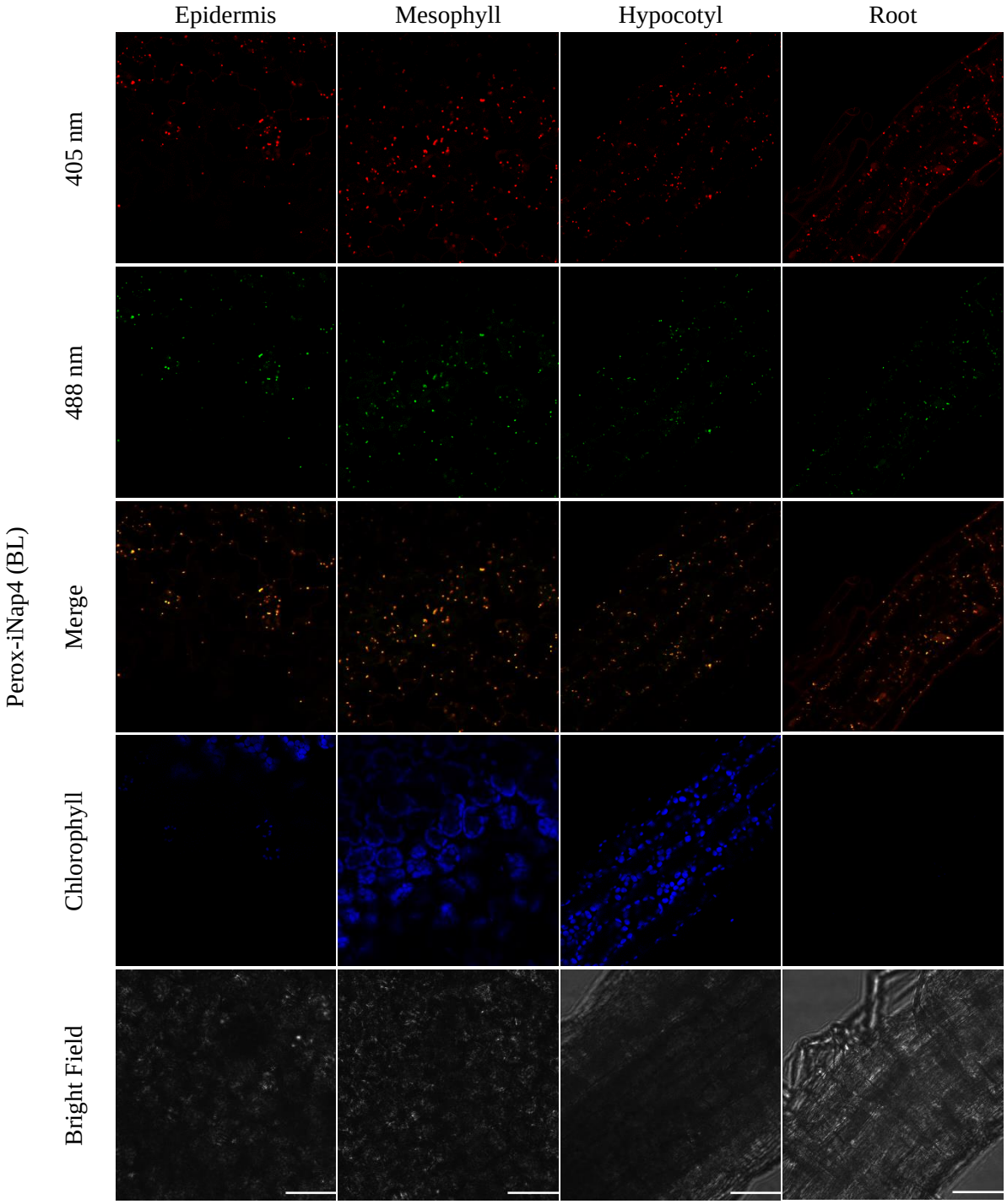

B.1.10 Plast-iNapC

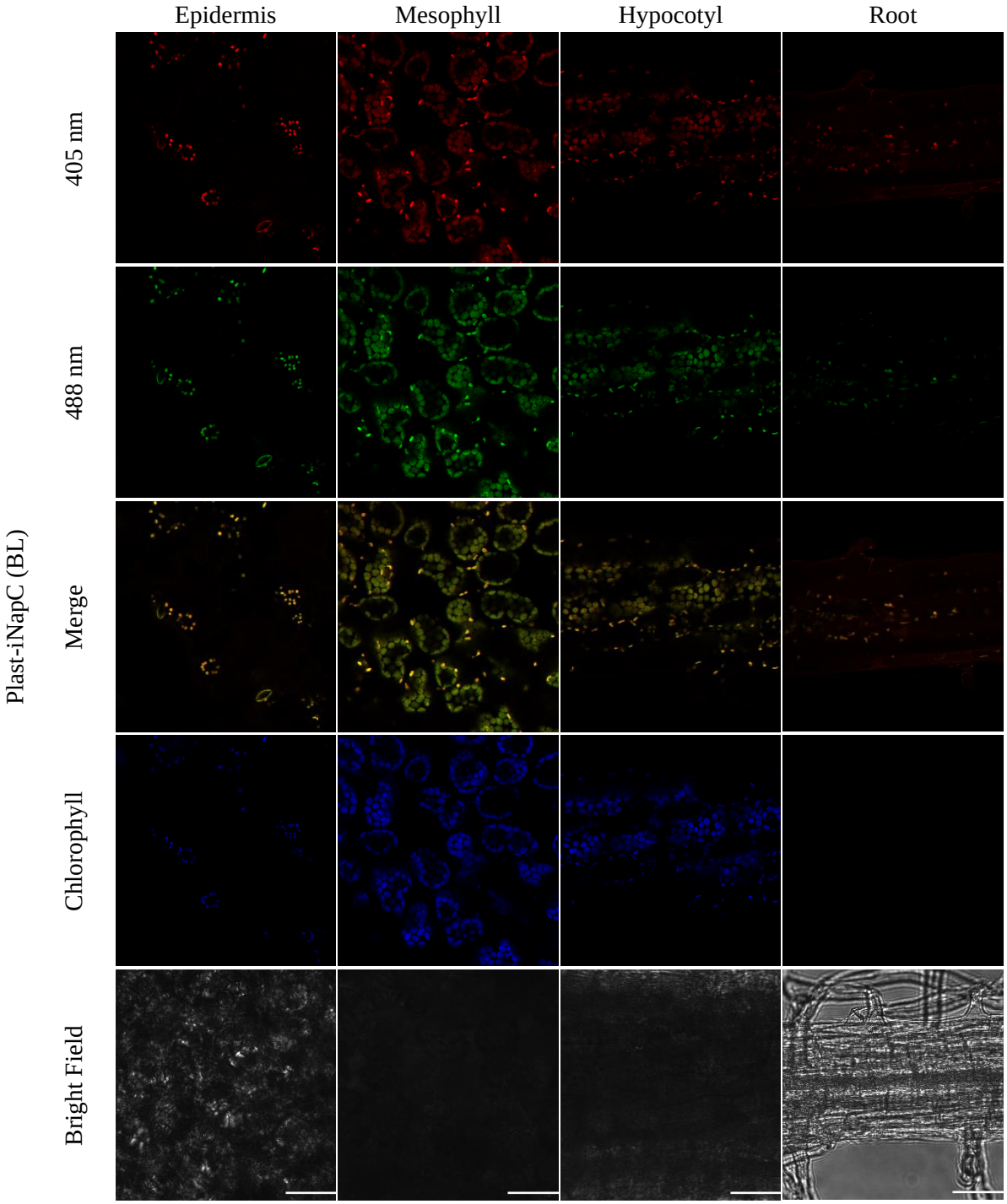

B.1.11 Plast-iNap1

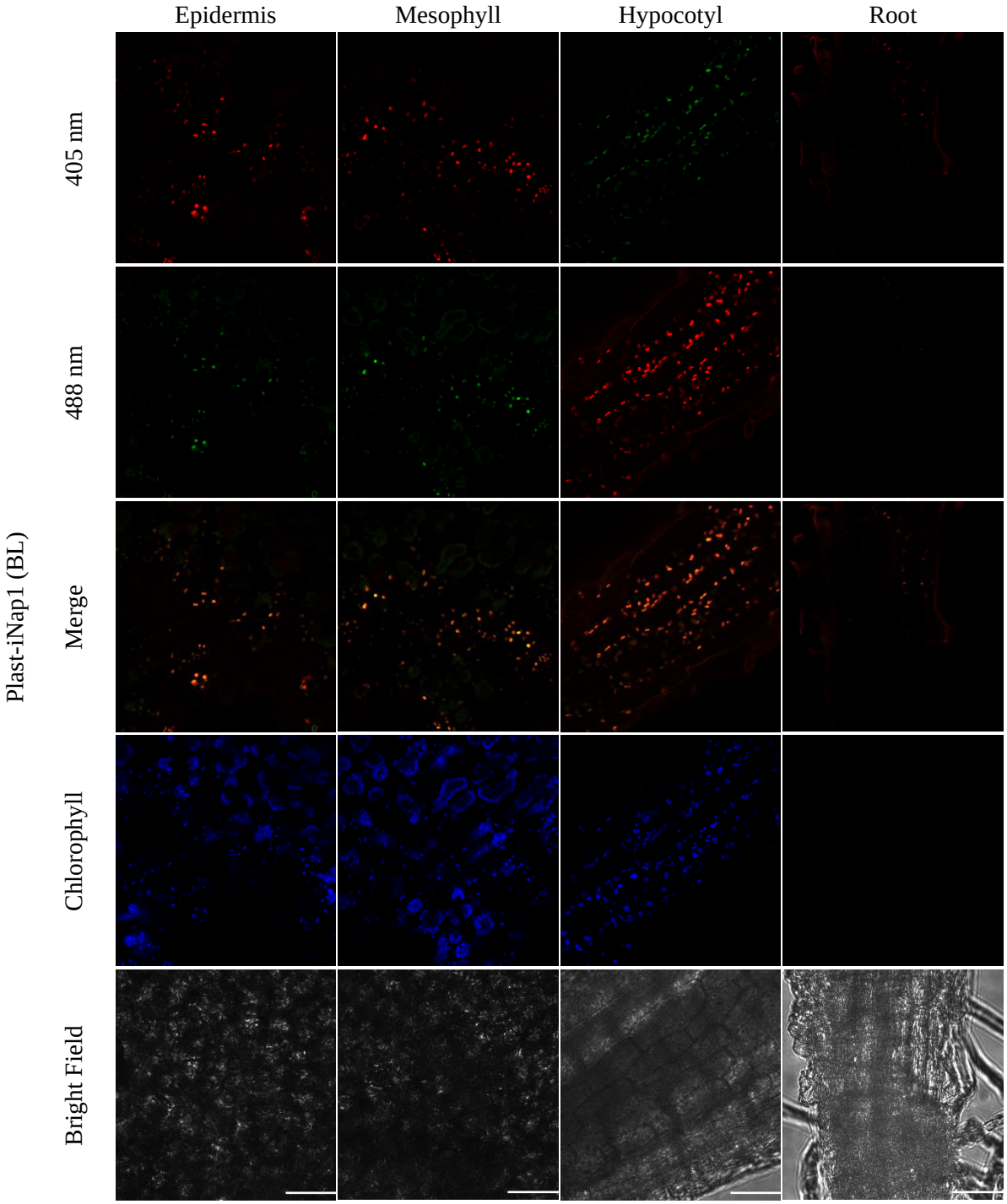

B.1.12 Plast-iNap4

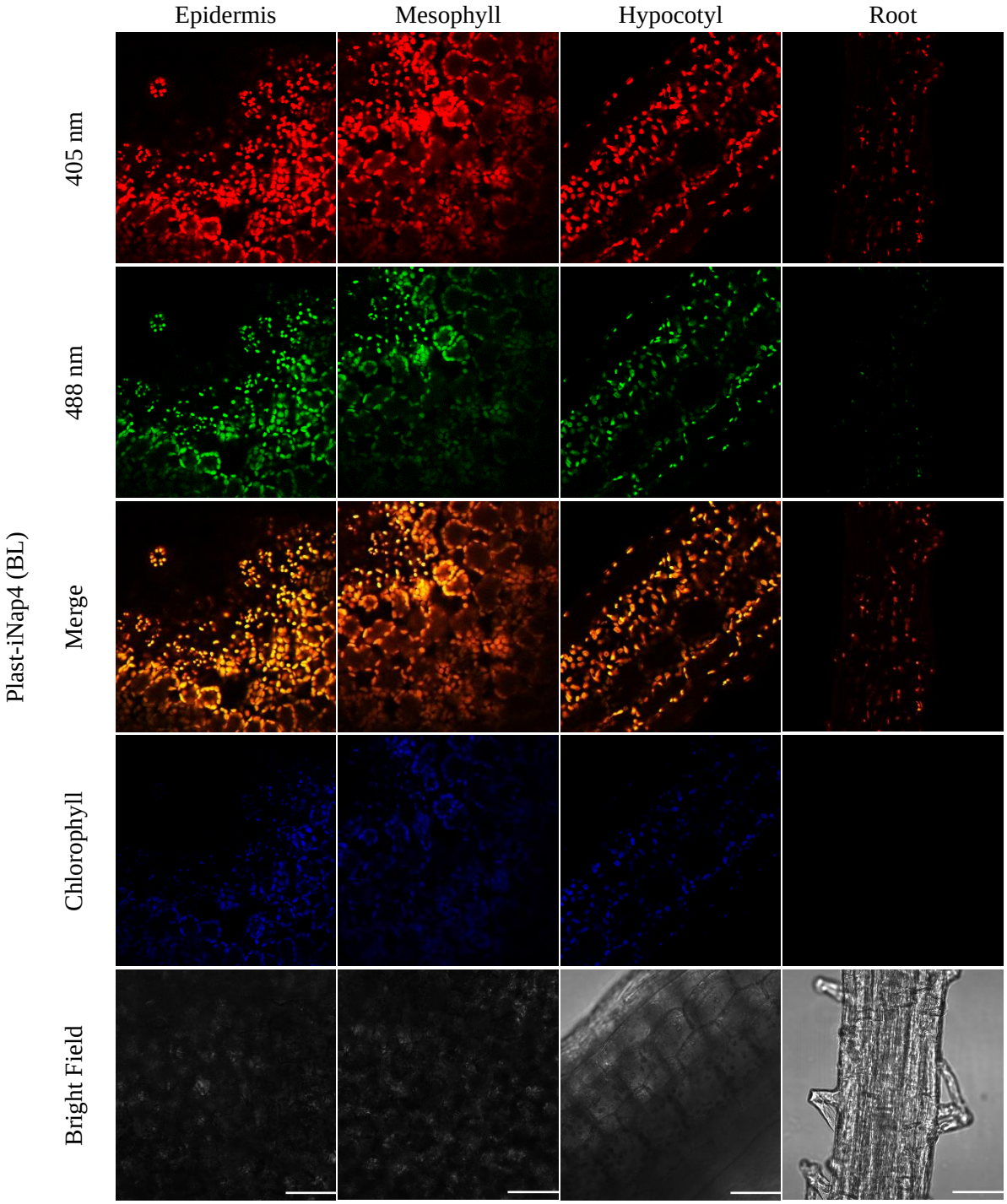

B.1.13 Plast-SoNar

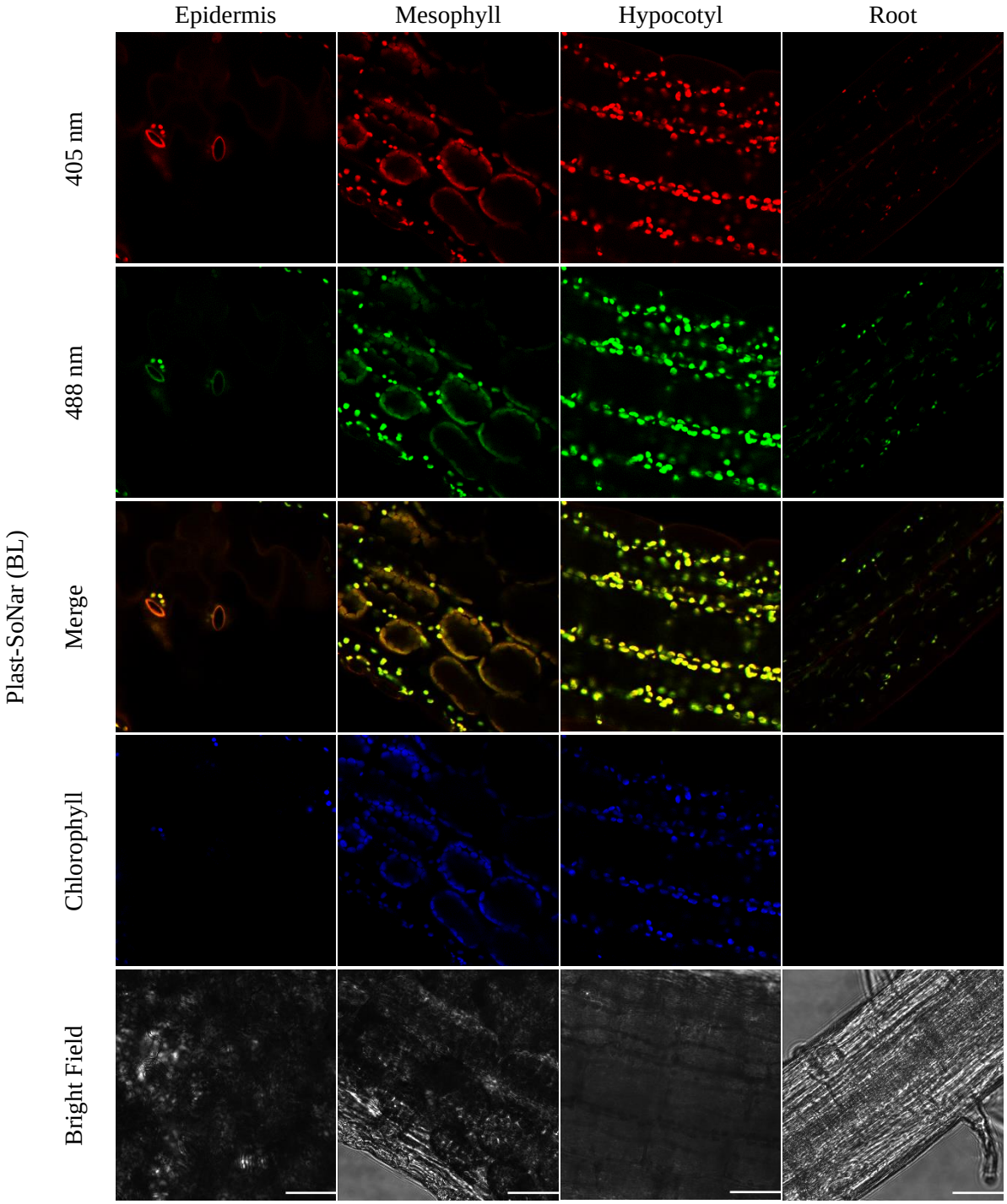

B.1.14 Col-0 WT

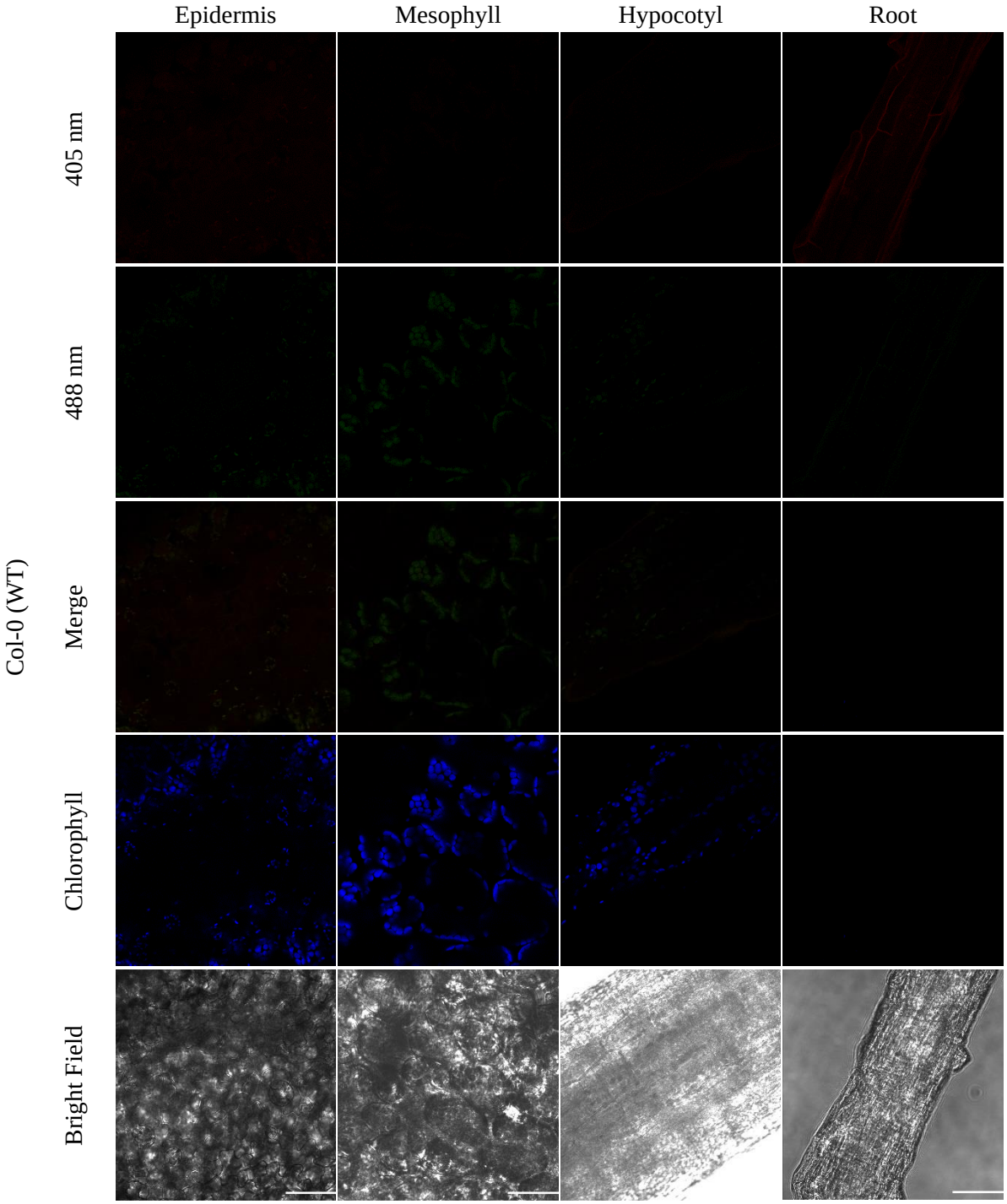
Epidermis
Mesophyll
Hypocotyl
Root
405 nm
488 nm
Merge
Chlorophyll
Bright Field
Col-0 (WT)

B.1.15 Mt-iNap2

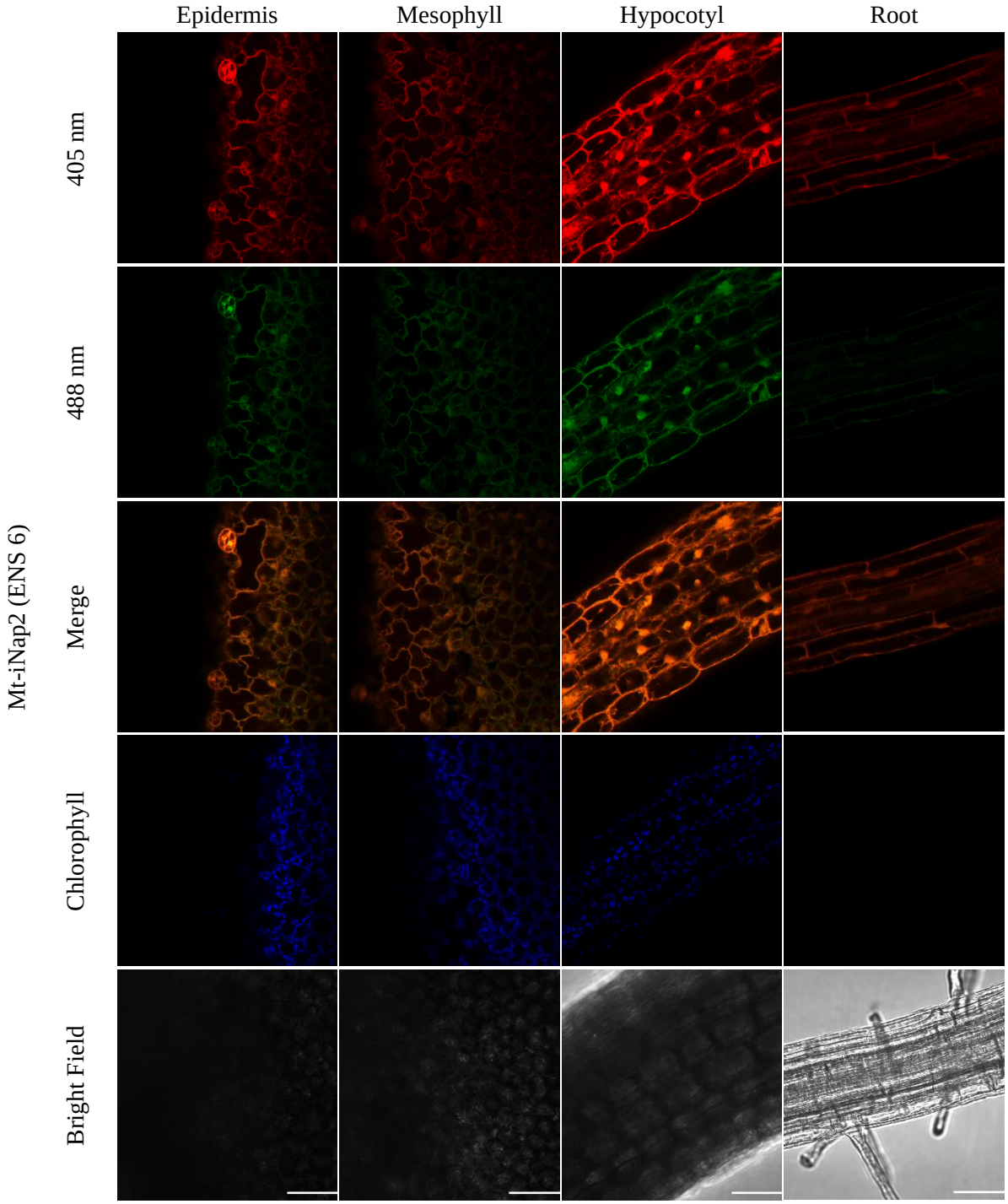

Figure B.1. Confocal images of 3-day-old *Arabidopsis* seedlings expressing iNap and SoNar sensors. iNap sensors for NADPH include, cyt-iNapC, cyt-iNap1, cyt-iNap2, cyt-iNap4, plast-iNapC, plast-iNap1, plast-iNap4, perox-iNapC, perox-iNap1, perox-iNap4. SoNar sensors for NADH:NAD^+ include cyt-SoNar and plast-SoNar. Images are displayed in pseudocolours for individual fluorescence signals. Fluorescence from excitation at 405 nm was measured at emission 500-540 nm (red). Fluorescence from excitation at 488 nm was measured at emission 500-540 nm (green). Merge represents the overlay of these two images. Chlorophyl fluorescence was recorded from emission at 627-700 nm from excitation at 488 nm (blue). Scale bars on bright field images are representative of all images and represent 50 µm.

B.1.16 Mt-iNap2 (MitoTracker staining)

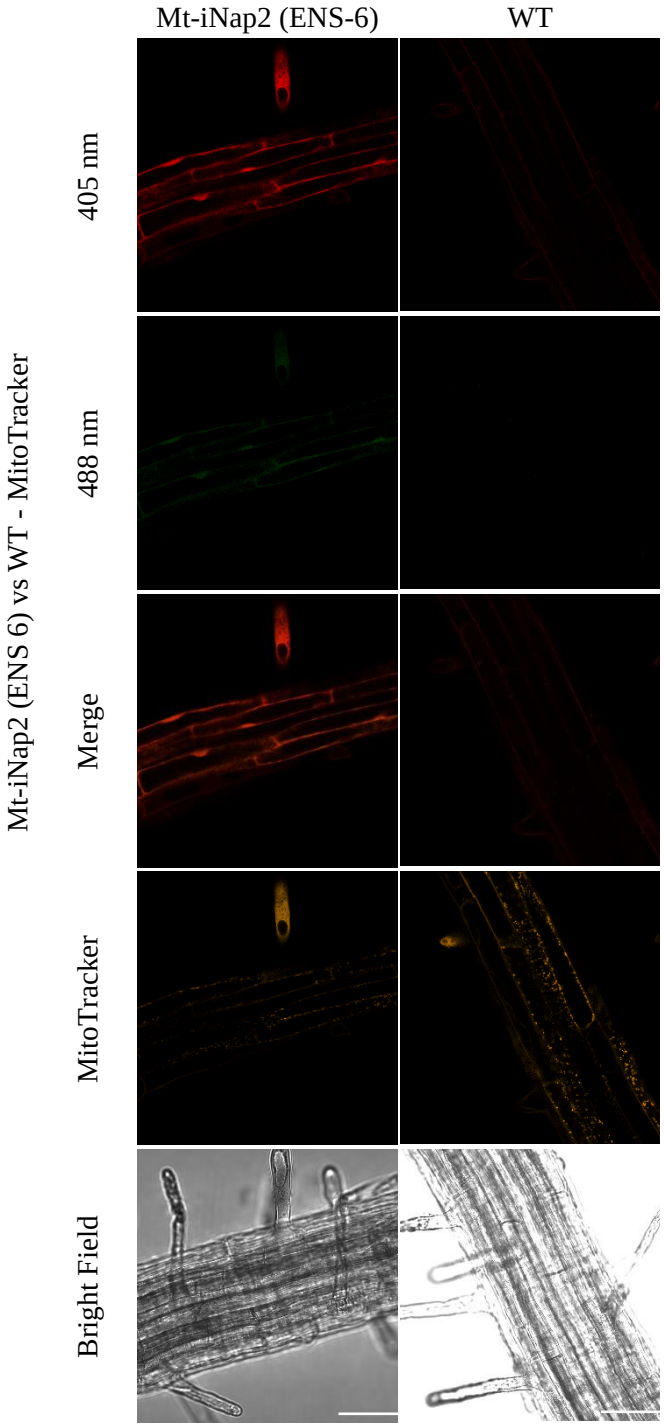

Figure B.2. Confocal images of roots of 3-day-old *Arabidopsis* seedlings expressing mt-iNap1 or WT control (Col-0) stained with MitoTracker Orange. Images are displayed in pseudocolours for individual fluorescence signals. Fluorescence from excitation at 405 nm was measured at emission 500-540 nm (red). Fluorescence from excitation at 488 nm was measured at emission 500-540 nm (green). Merge represents the overlay of these two images. MitoTracker fluorescence was recorded from emission at 566-611 nm by excitation at 561 nm (orange). Scale bars on bright field images are representative of all images and represent 50 µm. Seedlings were stained with 250 nM MitoTracker Orange in ½ MS media (pH 5.8) for 10 minutes and washed with fresh media before imaging.